Additive Manufacturing and Characterization of Mini-Devices for Oral Drug Delivery

Vaut, Lukas

Publication date:
2019

Document Version
Publisher's PDF, also known as Version of record

PH.D. THESIS

Additive Manufacturing and Characterization of Mini-Devices for Oral Drug Delivery

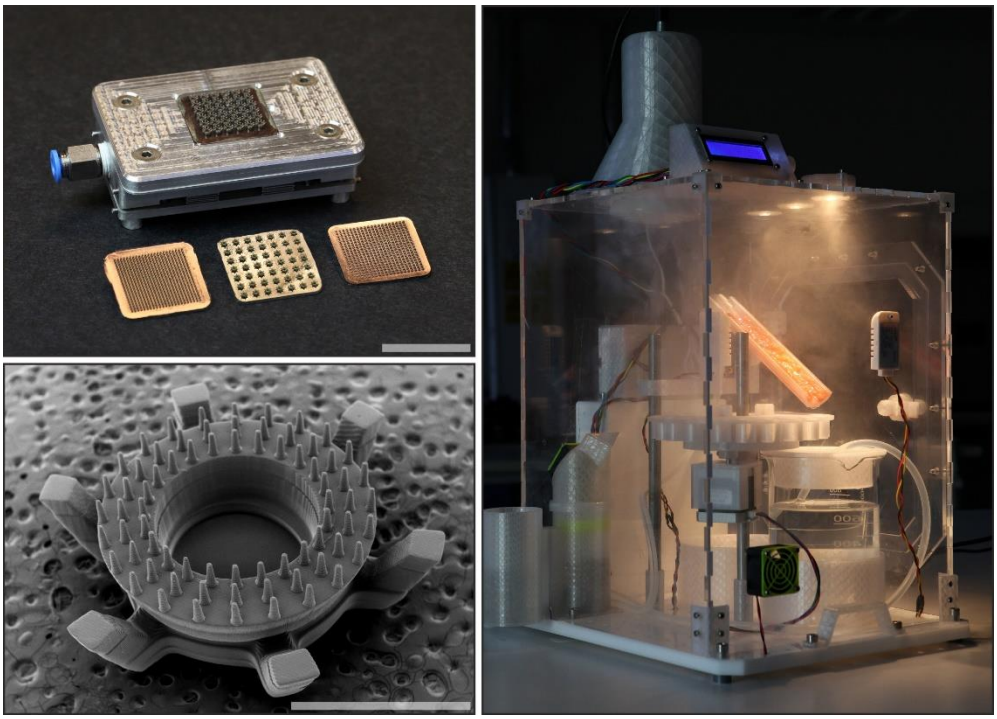

Lukas Vaut

February 2019

Danmarks Grundforskningsfond
Danish National Research Foundation

IDÜN

VILLUM FONDEN

Cover image

Top left: Mini-devices for oral drug delivery, additively manufactured with different geometries and sizes on sacrificial release substrates, and customized vacuum-actuated holder for additive manufacturing instrument. Scale bar corresponds to 25 mm. *Bottom left:* Additively manufactured bio-inspired phage-style design of mini-devices for oral drug delivery. Scale bar is equal to 2 mm. *Right:* Replicable mostly additively manufactured automated retention model setup for evaluation of bioadhesion of e.g. oral drug delivery devices.

I dedicate the work on my Ph.D. project as well as the resulting Ph.D. thesis to my parents, who in turn have dedicated their lives to my siblings and me.

Their hard work and eternal support allowed me to strive for a Ph.D. degree.

Additive Manufacturing and Characterization of Mini-Devices for Oral Drug Delivery

A Thesis presented to the Academic Faculty

by

Lukas Vaut

Submitted in Partial Fulfillment
of the Requirements for the Degree of

Doctor of Philosophy

Department of Health Technology,
Technical University of Denmark,
Denmark

February 2019

Title of the Ph.D. Thesis
Additive Manufacturing and Characterization of Mini-Devices for Oral Drug Delivery

Name of Author
Lukas Vaut

Research Project Duration
March 2016 – March 2019

Supervisors
Principal Supervisor
Professor Anja Boisen
Department of Health Technology
Technical University of Denmark

Co-Supervisor
Associate Professor Guido Tosello
Department of Mechanical Engineering
Technical University of Denmark

Co-Supervisor (March 2016 – April 2018)
Dr. Kristian Ejlebjærg Jensen
Formerly Department of Micro- and Nanotechnology
Technical University of Denmark
Currently COMSOL A/S Denmark

Faculty
Life Science

Preface

This thesis has been written to constitute a partial fulfillment of the requirements for obtaining the Ph.D. degree from the faculty of Life Science at the Technical University of Denmark during the period from 1st of March 2016 to 28th of February 2019.

The project was carried out in the Nanoprobes group at the Department of Micro- and Nanotechnology (03/2016 – 12/2018), later Department of Health Technology (01/2019 – 02/2019), Technical University of Denmark, under principal supervision of group leader Professor Anja Boisen. As a part of the Intelligent Drug delivery and sensing Using microcontainers and Nanomechanics (IDUN) center of excellence, the work was funded by the Danish National Research Foundation (DNRF122) and Villum Foundation (Grant No. 9301).

During this Ph.D. study, courses equivalent to 29 ECTS points were attended. Among those the "Drug delivery PhD summer school 2016" at the Technical University of Denmark, the "Micro mechanical systems design and manufacture PhD summer school 2016" at the Technical University of Denmark and the "ESSON'17 European School On Nanosciences & Nanotechnologies" in Grenoble, France.

A one-month external research stay at Yamagata University in Yonezawa, Japan, under the supervision of Prof. Ajit Khosla and Prof. Hidemitsu Furukawa (Department of Mechanical Systems Engineering, Graduate School of Science and Engineering) was accomplished in July 2016.

Within the research project, the supervision of a Master of Science thesis project with a duration of 5 months was undertaken. The practical work, conducted as part of the project, contributed to the characterization of oral drug delivery mini-devices with various geometries.

Results obtained within the frame of the Ph.D. project were presented orally as external guest speaker at the Nano3Bio Young Researcher Symposium, taking place at the Technical University of Denmark in April 2016, and presented in the form of a poster both at the 44th Annual Meeting and Exposition of the Controlled Release Society in Boston, USA in July 2017 and the 44th International conference on Micro and Nano Engineering in Copenhagen in September 2018.

Moreover, an application was filed for a patent on an additive manufacturing-related method.

Lukas Vaut

Kongens Lyngby,
28th of February 2019

Acknowledgements

First and foremost, I would like to thank my principal supervisor Prof. Anja Boisen, not only for giving me the opportunity to face the challenges of an exciting Ph.D. project, but also for being an inspirational character, a care-taking and responsible supervisor, and for encouraging me to believe in my own strengths.

In the same regard, I would like to express my gratitude to my co-supervisors Prof. Guido Tosello and Dr. Kristian Ejlebjærg Jensen. I highly appreciate the numerous meetings we had and the practical guidance I received to solve the various problems I encountered. I especially want to thank Guido for supporting me with the patent application.

I would also like to thank Prof. Hidemitsu Furukawa and Prof. Ajit Khosla as well as all members of the Soft & Wet matter Engineering Lab, for hosting me in Yonezawa during my external research stay. The stay was an amazing experience for me, both professionally and personally, and I will always gladly think back to this time.

Further acknowledgements go to my collaborators Dr. Guanghong Zeng, Ermes Scarano, Nesma El-Sayed and Khorshid Kamguyan, for their professional way of working, their open attitude and problem-solving abilities. At the same time, I would like to thank my Master Thesis student Julia Juszczyk for being such an enthusiastic, uncomplicated student and for contributing to this work.

Special thanks also go to Prof. Stephan Sylvest Keller for helpful advices and interesting conversations, Dr. Kinga Zór for fruitful discussions about data treatment and Dr. Tommy Sonne Alstrøm for many great conversations about statistics and reproducible research.

Furthermore, I would like to thank all the people who helped me to cope with everyday lab challenges. Among those, especially Prof. En Te Hwu, Per Thor Jonassen, Dr. Danilo Quagliotti, Dr. Yang Zhang, Klaus Liltorp and Francesco Regi. I also greatly appreciate the administrative support from Christina Fog Schouw, Lars Schulte, Louise Søby Møller, Pia Levin Marloth, Jette Rasmussen, Dorthe Foss Lillelund, Dr. Julie Rasmussen and Dr. Sanne Enok Lauridsen. At this point, I would also like to thank Jesper Scheel who helped me with photography.

It has been my pleasure to work in the Nanoprobes group, in which every member contributed to my professional and personal development. I would like to thank my friends within and outside of the group. The foosball crew: Kuldeep, Onur, Rokon and Zarmeena, the Friday Bar crew: Chen, Nastasia, Jing and Tanja, crazy office mates and neighbors: Varadarajan, Morten, Sriram, Khorshid, Laura, Sarvesh and Maks.

Above all, I want to sincerely thank my dear Buket and my awesome family for laying out and preserving the foundation of my inner strength, and for carrying the extra weight I could not carry on my own.

Abstract

The complex nature of the human gastro-intestinal system, by the presence of digestive enzymes, harsh changes in pH, presence of thick mucus layers, etc., often accounts for low bioavailability of orally ingested drugs. In contrast to alternative routes of drug administration, the oral route is preferred, due to a combination of simplicity, safety and patient compliance. Hence, many strategies for increasing bioavailability of orally administered drugs have been developed within the pharmaceutical and related research areas. Among those is the application of drug transporting and protecting delivery platforms, which include engineered microdevices featuring a reservoir and consequent unidirectional drug release. These devices have been a subject of intensive research since almost two decades and have been shown potent as universal carrier platforms with promising oral drug delivery performance. While the fabrication of microdevices could be demonstrated by means of various fabrication protocols with different materials, it remained largely associated with elaborated and costly microfabrication techniques with limited capacity for geometrical complexity.

In this Ph.D. thesis, the implementation of additive manufacturing (3D printing) as an alternative fabrication method with increased simplicity, cost-efficiency and geometrical design freedom is demonstrated and evaluated.

Within the frame of a feasibility study, the process of using state-of-the-art micro stereolithography additive manufacturing was thoroughly characterized and associated limitations and opportunities were unveiled. A laser spot size of 30 µm, limiting the fabrication of microdevices to millimeter scale, and the lack of the possibility to fabricate individual releasable devices, were found to be the main challenges.

The implementation of pre-fabricated sacrificial release substrates in photopolymerization-based digital light processing additive manufacturing has been realized and it enabled the fabrication of patterns of delicate microstructures and their subsequent release.

Using those sacrificial release substrates for the fabrication of microdevices for oral drug delivery allows additive manufacturing to be fully integrated into potential workflows of microdevice fabrication in which various processing steps, such as drug loading and coating, are connected. Microdevices were fabricated on sacrificial release substrates and were successfully released. The rapid prototyping potential of additive manufacturing was employed to fabricate devices with alternative geometries with the aim of improving oral drug delivery performance. Characterization of different designs with use of a retention model showed that distinct surface structures led to an enhancement of mucoadhesion, while favorizing the reservoir-containing side to the intestinal wall, thus indicating a potential for their self-orientation.

Finally, the used retention model has been improved for increased physiological relevance and experimental reproducibility. A fully integrated instrumentation based on open labware and a detailed corresponding documentation for simple replication using rapid prototyping techniques such as additive manufacturing and CO_2 laser cutting have been developed.

Dansk Resumé

Kompleksiteten af det humane gastrointestinale system, fordøjelsesenzymer, et tykt mucus-lag og drastiske ændringer i pH, er ofte årsag til lav biotilgængelighed af oralt administrerede lægemidler. En oral administrationsvej er at foretrække på grund af simpelhed, sikkerhed og patient compliance og derfor er der, inden for de farmaceutiske og beslægtede forskningsområder, udviklet mange strategier for at øge biotilgængeligheden af oralt administrerede lægemidler. Blandt disse er anvendelsen af leveringsplatforme, som både beskytter lægemidlet og facilitere transporten gennem det gastrointestinale system. Dette omfatter blandt andet mikrostrukturer med reservoirs, som sikrer en retningsbestemt frigivelse af lægemidlet. Disse strukturer har dannet baggrund for intens forskning gennem de seneste to årtier, og de har vist sig at være velegnede som universelle leveringsplatforme med en lovende frigivelse mekanisme. På trods af at disse mikrostrukturer kan fremstilles ved hjælp af flere fabrikationsprotokoller og af forskellige materialer, er fabrikationen stadig forbundet med komplicerede og omkostningsfulde teknikker, med begrænset kapacitet for geometrisk kompleksitet.

Med denne PhD afhandling demonstreres og evalueres implementeringen af additivfremstilling (3D-printning) som en alternativ fremstillingsmetode, med øget simplicitet, omkostningseffektivitet og geometrisk designfrihed.

Ved en forundersøgelse er processen for anvendelsen af state-of-the-art mikro-stereolitografi additiv fremstilling blevet grundigt karakteriseret, og tilhørende begrænsninger og muligheder er blevet afdækket. En laserpunktstørrelse på 30 μm, som begrænser fremstillingen af millimeter-små mikro-strukturer samt den manglende mulighed for at fremstille individuelle strukturer, viste sig at være hovedudfordringerne.

Ved implementering af præfabrikerede opløselige frigivelsessubstrater blev 'fotopolymeriserings-baseret digital light processing' additivfremstilling realiseret, hvilket muliggør fremstilling af mønstre af fine mikrostrukturer og deres efterfølgende frigivelse.

Ved anvendelse af disse opløselige frigivelsessubstrater tillader additivfremstilling fuld integration af potentielle arbejdsgange i mikrostruktur-fremstilling, hvor forskellige behandlingstrin såsom lægemiddelindlæsning og coating, er forbundet. Mikrostrukturer blev fremstillet på opløselige frigivelsessubstrater og frigivet succesfuldt. Det hurtige prototypefremstillings-potentiale ved additivfremstilling er blevet anvendt til fremstilling af strukturer med alternative geometrier, med det formål at forbedre oral administration. Karakterisering af forskellige design ved brug af en retentionsmodel viste, at specifikke overfladestrukturer førte til en forbedring af mucoadhæsion, og en samtidig tendens til at ende med åbningen mod tarmvæggen, hvilket viser potentiale for selvorientering.

Endelig er den anvendte retentionsmodel blevet forbedret for at øge fysiologisk relevans og eksperimentel reproducerbarhed. En fuldt integreret instrumentering baseret på 'open labware' og detaljeret dokumentation, for simpel replikation ved hjælp af hurtige prototypeteknikker som additivfremstilling og CO2-laserskæring, er blevet udviklet.

Contents

List of Scientific Contributions

Scientific contributions as part of the Ph.D. thesis:

Manuscript I

Additive Manufacturing of Microreservoir Devices for Oral Drug Delivery using an Acculas BA-30 Micro-Stereolithography Instrument: A feasibility study

Lukas Vaut, Kristian E. Jensen, Guido Tosello, Ajit Khosla, Hidemitsu Furukawa, Anja Boisen

Contributions: Formulation of the scientific question, design of experiments, analysis and interpretation of results, writing and revision of the manuscript

Manuscript II

Sacrificial Polymer Substrates in Photopolymerization-based Micro 3D Printing for Fabrication and Release of Complex Micro Components

Lukas Vaut, Guanghong Zeng, Guido Tosello, Anja Boisen

Contributions: Formulation of the scientific question, design of experiments, execution of all experiments, analysis and interpretation of results, writing and revision of the manuscript

Manuscript III

3D Printing of Reservoir Devices for Oral Drug Delivery and Enhanced Mucoadhesion

Lukas Vaut, Julia J. Juszczyk, Khorshid Kamguyan, Kristian E. Jensen, Guido Tosello, Anja Boisen

Contributions: Formulation of the scientific question, design of experiments, execution of the majority of experiments, analysis and interpretation of results, writing and revision of the manuscript

Manuscript IV

Fully replicable and automated retention measurement setup for characterization of bio-adhesion

Lukas Vaut, Ermes Scarano, Guido Tosello, Anja Boisen

Contributions: Formulation of scientific question, design of instrumentation and experiments, execution of the majority of experiments, analysis and interpretation of results, writing and revision of the manuscript

Other scientific contributions:

Scientific Article

Microneedles prepared with the help of 3D printing allowing for a simple tunable design and loading of nanoparticles

Nesma El-Sayed, Lukas Vaut, Marc Schneider

Manuscript in preparation

Scientific article

Polymeric Lids for Microcontainers for Oral Protein Delivery

Chiara Mazzoni, Rasmus D. Jacobsen, Jacob Mortensen, Jacob R. Jørgensen, Lukas Vaut, Jette Jacobsen, Carsten Gundlach, Anette Müllertz, Line H. Nielsen, Anja Boisen

Submitted to Macromolecular Bioscience

Scientific article

Biodegradable microcontainers: a new platform for oral drug delivery

Zarmeena Abid, Madeeha M. Javed, Sophie Andersen, Chiara Mazzoni, Line Hagner Nielsen, Carsten Gundlach, Lukas Vaut, Ritika Singh Petersen, Annette Müllertz, Anja Boisen, Stephan S. Keller

Manuscript in preparation

Scientific Article

High-throughput aberration-corrected Raman spectrometer integrated with a smartphone

Oleksii Ilchenko, Roman Slipets, Lukas Vaut, Anja Boisen

Manuscript in preparation

Conference contribution

Geometric Optimization of Microcontainers for Oral Drug Delivery

Kristian E. Jensen, Lukas Vaut, Anja Boisen

Modelling and experiments in drug delivery systems, Coimbra, Portugal 2016

Conference contribution

Geometrically Optimized 3D Printed Mini-Devices for Oral Drug Delivery

Lukas Vaut, Julia J. Juszczyk, Kristian E. Jensen, Alina J. Andersen, Guido Tosello, Anja Boisen

44th Annual Meeting & Exposition of the Controlled Release Society, Boston, United States, 2017

Conference contribution

Use of a polymeric sacrificial release layer in photopolymer-based micro-3D printing

Lukas Vaut, Kristian E. Jensen, Guanghong Zeng, Guido Tosello, Anja

44th International conference on Micro and Nano Engineering, Copenhagen, Denmark, 2018

Conference contribution

FDM-based 3D Printing of Microfluidic Discs with Multilayered Microchannels

Rokon Uddin*, Lukas Vaut*, Anja Boisen

44th International conference on Micro and Nano Engineering, Copenhagen, Denmark, 2018

* equal contribution

Conference contribution

Solvent-free fabrication and loading of polycaprolactone microcontainers for oral drug delivery

Zarmeena Abid, Madeeha M. Javed, Lukas Vaut, Ritika S. Petersen, Anja Boisen, Stephan S. Keller

44th International conference on Micro and Nano Engineering, Copenhagen, Denmark, 2018

List of Abbreviations

2PP:	Two-Photon-Polymerization
3DP:	3-Dimensional Printing
AM:	Additive Manufacturing
ASTM:	American Society for Testing and Materials
AUC:	Area Under the Curve
BCS:	Biopharmaceuticals Classification System
BSE:	BackScattered Electron
CAD:	Computer Aided Design
CAM:	Computer Aided Manufacturing
CCD:	Charge Coupled Device
CLIP:	Continuous Liquid Interface Production
DIY:	Do-It-Yourself
DLP:	Digital Light Processing
DMD:	Digital Micromirror Device
EBW:	Electron Beam Welding
ENS:	Enteric Nervous System
FDA:	U.S. Food and Drug Administration
FDM:	Fused Deposition Modeling
FFF:	Fused Filament Fabrication
FOSS:	Free and Open-Source Software
GALT:	Gut Associated Lymphoid Tissue
GI:	Gastro-Intestinal
ISO:	International Organization for Standardization
LOM:	Laminated Object Manufacturing
MEMS:	MicroElectroMechanical Systems
MMA:	Methyl-MethAcrylate
MPSL:	Mask Projection StereoLithography
MZPL:	Minimum Zone reference PLane
ODD:	Oral Drug Delivery

PAA:	Poly(Acrylic Acid)
PCL:	PolyCaproLactone
PEGDMA:	Poly(Ethylene Glycol Di-MethAcrylate)
PEGMA:	Poly(Ethylene Glycol MethAcrylate)
PLGA:	Poly(Lactic-co-Glycolic Acid)
PMMA:	Poly(Methyl MethAcrylate)
PRINT:	Particle Replication In Non-wetting Templates
PVA:	Poly(Vinyl Alcohol)
PVP:	PolyVinylPyrrolidone
RP:	Rapid Prototyping
SE:	Secondary Electron
SEAL:	StampEd Assembly of polymer Layers
SEM:	Scanning Electron Microscopy
SL:	StereoLithography
SLM:	Selective Laser Melting
SLS:	Selective Laser Sintering
SM:	Subtractive Manufacturing
STL:	Standard Tesselation Language or STereoLithography
TA:	Texture Analyzer
TL:	Tomato Lectin
WOA:	Work Of Adhesion

List of Figures

1 | Introduction

1.1 Motivation

This Ph.D. project was carried out as a part of the Intelligent Drug delivery and sensing Using microcontainers and Nanomechanics (IDUN) center of excellence with the goal to investigate small microfabricated reservoir devices, termed microcontainers, as a universal platform for the oral delivery of drugs.

Among the different routes of administration for systemic delivery of drugs to the human body, the oral route represents the preferred one. Oral administration, most commonly referred to as oral drug delivery (ODD), is defined as the procedure when a medication is ingested and absorbed within the gastro-intestinal (GI) system. With respect to other administration routes, such as parenteral injection, the preference is justified by the ease of use and low invasiveness, thus resulting in higher patient compliance and increased safety [1–3]. Furthermore, ODD can be advantageous, because orally administered sustained-release formulations are absorbed more slowly as they are not directly entering the blood stream, thus leading to a slower and prolonged effect of the drug [4]. Aside from that, oral drug formulations can be used to specifically target diseases of the GI tract, such as inflammatory bowel disease [5].

Most oral dosage forms are fabricated in a cost-efficient manufacturing process from a dry powder of drug and are applied in the shape of tablets after employing a compaction process or in the shape of polymeric capsules, which are filled with the powder or pellets [6].

One major drawback of oral drug formulations in many cases is the low bioavailability when compared to parenteral drug administration [1]. Bioavailability is defined as the fraction of drug that enters the systemic circulation unchanged and is expressed as the systemic drug concentration over time relative to the one reached through intravenous administration, which, in turn, is regarded as 100% [7]. Especially biomolecular drugs, such as peptides and proteins (e.g. insulin), often have too low bioavailability when administered orally [2].

The efficient digestive and barrier functions of the GI tract are vital for life but also cause low bioavailability of drugs. The GI tract is one of the interfaces between the body and the environment and its functions are to take up water as well as nutrients via ingestion and absorption, and to excrete waste products. As a natural protection mechanism against

potentially harmful pathogens and substances, such as bacteria, toxins and drugs, most contents are chemically and/or enzymatically degraded to their elementary building blocks. Moreover, the intestinal mucosa is constructed as an efficient barrier that hinders unrecognized intestinal contents (e.g. drugs) from being absorbed.

Given the complex nature of the GI tract and low bioavailability of drugs, conventional drug formulations (e.g. tablets) are not always suitable for oral delivery. In this context, the concept of drug carriers was developed. The function of a drug carrier is to physically contain the drug, thereby protecting the drug from external influences (acid, enzymes etc.), transporting it to the desired target site and promoting absorption [8,9]. So far, many different types of drug carriers have been developed, however, they all have advantages and disadvantages with regards to their application.

This work investigates the use of polymeric microcontainers as a carrier platform in ODD. Microcontainers are small cylindrical devices that consist of a base-layer and an edge that builds up on the side to form a cavity (Figure 1).

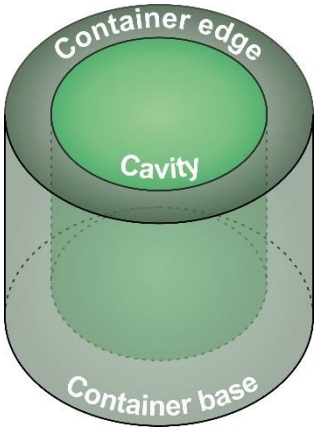

Figure 1 Schematic illustration of the microcontainer design.

The cavity of microcontainers serves to be filled with drug or a drug/polymer matrix. To protect the drug from the harsh gastric environment, a lid may be applied to the opening of the cavity. Moreover, to release the drug from the cavity, the applied lid may be composed of a pH-sensitive polymer in order to realize a targeted intestinal release. In contrast to other carrier platforms, such as particulate systems, the encapsulated drug can only be released through the opening of the cavity. Once reaching the target site for delivery, which in ODD most commonly is the intestinal mucosa, a unidirectional release of drug from the carrier can limit the drug loss to the intestinal lumen. This helps to concentrate the drug at the surface of the intestinal mucosa, under the premise that the drug is released in close proximity and in

the direction of it (Figure 2) [10–12]. A unidirectional drug release towards the intestinal mucosa may be promoted by a surface functionalization of the cavity-side, which can facilitate the formation of a chemical bond between functional groups and molecules present at the intestinal mucosa [10–16].

All in all, microcontainers represent a universal drug delivery system, which can be explored for the delivery of various drugs.

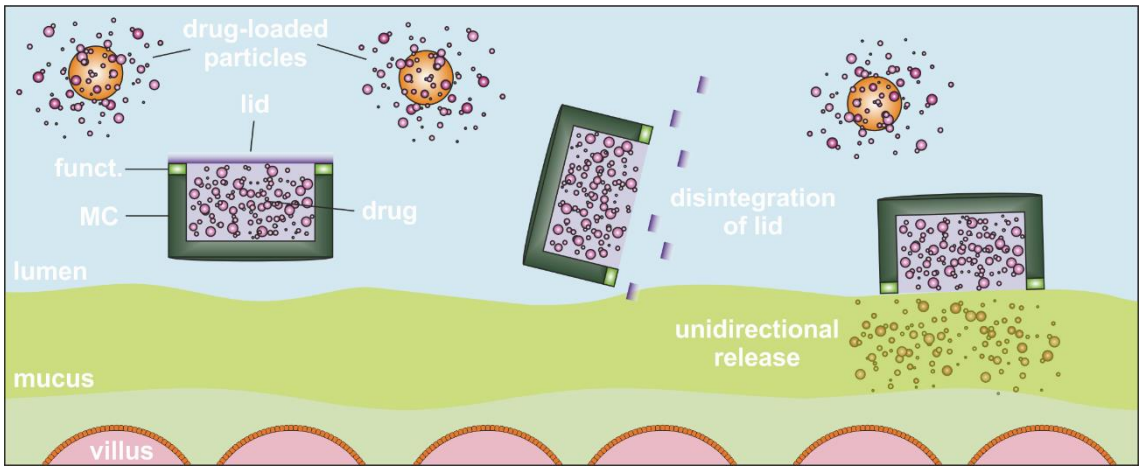

Figure 2 Schematic illustration of unidirectional drug release from microcontainers (cross-section) with pH-sensitive lid and surface functionalization in contrast to omni-directional release from particulate systems. Modified from [10].

1.2 Aim of the Ph.D. Project

Motivated by the potential impact of unidirectional drug release, the main aim of this work was to promote the attachment of microcontainers, specifically with the correct orientation, to the intestinal mucosa. Provided that a microcontainer reveals a flat aspect-ratio and is loaded with a drug, the likelihood of attaching with either the cavity side or the bottom side should be equal as both sides can be seen as two equal faces. To promote adhesion of the cavity-side, chemical surface modification has been suggested [13]. Adhesion is defined as a process of attachment of a substance to the surface of another substance and might be of either chemical or physical nature [17]. As opposed to a chemical approach, the presented project aimed at promoting the adhesion of microcontainers with their cavity side by altering their shape. The intestinal mucosa is lined with mucus, a gel-like protective layer composed mainly of mucin glycoproteins and water [18]. Mucoadhesion is the term for adhesion to the mucosa and different theories for the explanation of this phenomenon have been formulated [18].

One fundamental constraint in this work was that microcontainers are not self-propelling and therefore entirely dependent on passive movement caused by intestinal motility and flow of

intestinal contents. Previous studies on the performance of microcontainers as ODD systems have shown that non-functionalized microcontainers were engulfed by the intestinal mucus layer upon application in *in situ* intestinal perfusion studies [19]. This suggests that microcontainers, despite recurring flow and lacking surface functionalization, will eventually come into contact with the intestinal mucosa.

Consequently, the motivation was to design microcontainers in a way that facilitates strong adherence to the intestinal mucosa but at the same time creates a bias that favors only the adhesion of the cavity side and thereby the correct orientation as they adhere.

This work aimed at exploiting phenomena described by the *mechanical theory* of muco-adhesion (mechanical-based mucoadhesion), in which adhesion is presumably enhanced by an increase in surface area of the microcontainer to mucosa interface, thus increasing the viscoelastic dissipation of energy during the breakage of the interface [18]. For this reason, microcontainers with surface area-increasing anchor-like structures on the cavity side should be designed and fabricated. The anchors were expected to interact with the mucosal surface and thereby ensure a localized mucosa-oriented drug release (Figure 3).

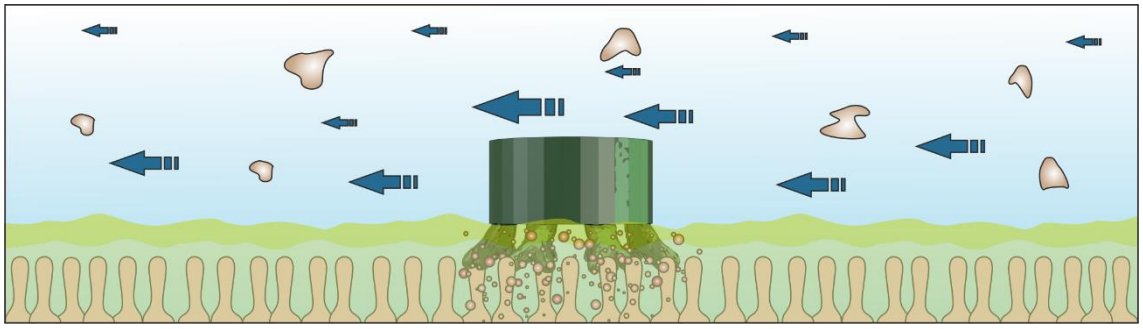

Figure 3 Schematic illustration of microcontainer featuring edge-anchors for mucosa-oriented drug release.

To allow for maximum geometrical flexibility, additive manufacturing (AM) was chosen as a fabrication technology. In summary, the following objectives should be accomplished:

- Implementation of AM as a method for fabrication of microcontainers
- Demonstration of the prototyping potential of AM with respect to ODD device fabrication by fabricating various shapes and sizes of microcontainers
- Establishment of a characterization method to determine mechanical-based mucoadhesion as well as bias in mucoadhesion
- Design, fabrication and characterization of microcontainers with edge-anchors for increased mucoadhesion and mucosa-directed drug release

1.3 Outline of the Ph.D. Thesis

The following chapters of this thesis will provide the necessary information and will guide the reader through the process of the entire project. While most of the chapters represent a synopsis of the conducted research, the last chapter contains the article manuscripts as the main part of the experimental research. In the following paragraphs, an overview of the content of the different chapters is presented.

1.3.1 Chapter 2 | Introductions to Manuscripts

The second chapter introduces the different publications attached to the thesis and succinctly describes their content as well as the current state of the publishing process.

1.3.2 Chapter 3 | Theory

This chapter gives a brief introduction to the theoretical concepts and background knowledge underlying this work. Starting with the pharmaceutical and physiological aspects of oral drug delivery, the chapter narrows down to the state-of-the-art of microfabricated oral drug delivery devices. It also gives an overview of additive manufacturing technology and its impact as well as use in drug delivery and open labware. Furthermore, the use of polyvinyl alcohol was a key enabling factor in this work. Consequently, a summary of its properties and applications is provided.

1.3.3 Chapter 4 | Fabrication and Characterization Methods

In this chapter, the development and fabrication processes that were undertaken to receive the acquired results are explained. Moreover, the employed experimental methods are described.

1.3.4 Chapter 5 | Conclusions and Outlook

Here, the conclusions derived from the entire Ph.D. project are stated and an outlook for the future impact of this research is provided.

1.3.5 Chapter 6 | References

This chapter contains the bibliography with all references used in the previous chapters.

1.3.6 Chapter 7 | Appendix

The appendix includes four different manuscripts that form the main part of this thesis.

2 | Introductions to Manuscripts

2.1 Manuscript I

This manuscript with the title *"Additive Manufacturing of Microreservoir Devices for Oral Drug Delivery using an Acculas BA-30 Micro-Stereolithography Instrument: A feasibility study"* describes the analysis of results obtained during a one-month external research stay at Yamagata University in Japan. Here, microcontainers for oral drug delivery are fabricated for the first time with various shapes and sizes using a state-of-the-art high-resolution additive manufacturing system. The manuscript aims at demonstrating the technical limitations associated with this specific fabrication technology and discusses further requirements which are needed to implement additive manufacturing as a method to fabricate microcontainers. Among those requirements are the preservation of the geometrical pattern of microcontainers after removing them from the build surface and the release of individual microcontainers upon completion of fabrication.

The manuscript has been submitted for publication as of 11 February 2019.

2.2 Manuscript II

The manuscript termed *"Sacrificial Polymer Substrates in Photopolymerization-based Micro 3D Printing for Fabrication and Release of Complex Micro Components"* represents a logic continuation of the work presented in the previous manuscript as it addresses specific problems that were encountered in the context of that work. Herein, the development and characterization process of a specific method for micro-additive manufacturing is described. The method makes use of pre-fabricated polyvinyl alcohol substrates as build surfaces in photopolymerization-based additive manufacturing. The method thereby allows for the preservation of any geometrical pattern as well as a convenient manipulation and mild release of additively manufactured micro-structures. Moreover, the method is compatible with automation and thus removes one of the main obstacles for industrial scalability of additive manufacturing of micro-components.

The manuscript has been submitted for publication as of 19 February 2019.

2.3 Manuscript III

In the manuscript with the title *"3D Printing of Reservoir Devices for Oral Drug Delivery and Enhanced Mucoadhesion"*, the method presented in Manuscript II is utilized for the implementation of additive manufacturing as a method to fabricate microcontainers (microreservoirs) for oral drug delivery. Defined arrays of microcontainers are additively manufactured on sacrificial poly(vinyl alcohol) substrates, therefore making the fabrication procedure compatible with other processing methods (e.g. drug-loading), which are employed in the development of microcontainers. Also, the fabrication and characterization of devices representing scaled-up versions of microcontainers with alternative geometries and anchor-like structures are presented. The characterization of mucoadhesion of the devices was carried out using the flow retention method [20].

The manuscript has been submitted for publication as of 20 February 2019.

2.4 Manuscript IV

As mentioned before, results presented for mucoadhesion characterization of devices for oral drug delivery in Manuscript III were obtained by use of the flow retention method [20]. To use the flow retention method, an experimental setup had to be constructed. In the course of designing and constructing such a setup, it became obvious that no common standard did exist up to that point. The motivation to develop a very versatile but reproducible setup for this experiment brought about Manuscript IV, which bears the title *"Fully replicable and automated retention measurement setup for characterization of bio-adhesion".* The manuscript describes the use of rapid prototyping techniques such as additive manufacturing and laser cutting to fully replicate the setup. Contained in the manuscript are full build instructions and references to all required components. The setup is also characterized and the performance of automated experiments demonstrated.

The manuscript has been submitted for publication as of 4 February 2019.

3 | Theory

3.1 Oral Drug Delivery

3.1.1 Routes of Drug Administration

Drugs can be administered to the body via different routes to realize therapeutic treatment (Figure 4). Drug administration routes can be divided into various categories. One common classification separates existing routes into enteral, referring to administration via the GI tract, and parenteral routes, which include all other routes of administration [4]. Consequently, the enteral route of administration includes the oral sublingual (under the tongue), oral buccal (cheeks), oral enteric (stomach or intestine) via ingestion and the rectal route. Further, routes of administration can be categorized whether the effect of administered drugs is systemic or localized.

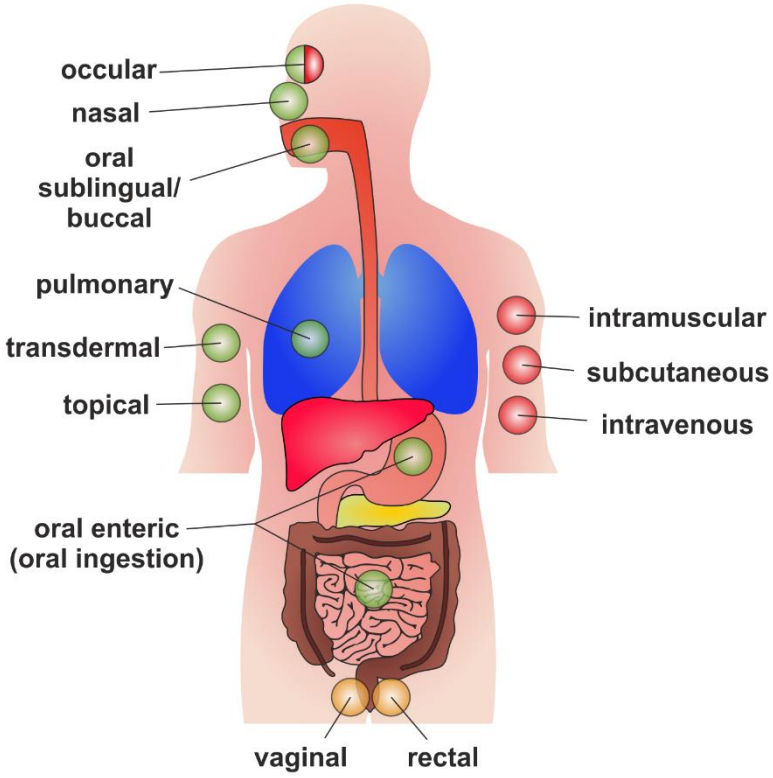

Figure 4 Routes of drug administration. Green: non-invasive, orange: non-invasive with reduced patient compliance, red: invasive.

Each route of administration has certain advantages, but also bears certain disadvantages. In this regard, invasiveness is a very important separation criterion. Invasive routes of administration include intravenous, subcutaneous and intramuscular injections, which involve the use of needles [1]. Non-invasive routes on the contrary encompass all enteral

routes as well as e.g. nasal, pulmonary, transdermal, topical and vaginal routes of administration [2,4]. Drugs can be delivered to the eye, non-invasively and invasively, but usually only for ophthalmic treatment as systemic delivery is difficult [21]. The invasiveness is a crucial criterion as it directly relates to patient compliance, synonymous with patient adherence, which is defined as the patient's tendency to abide by the recommendations given by healthcare professionals [22]. It must be noted though that invasiveness is not the only determining factor for patient compliance. In this regard, the rectal as well as vaginal routes of drug administration, for example, are also associated with decreased patient compliance due to discomfort during application [23]. Therefore, patient compliance and the route of administration are factors that highly influence the success of a therapy.

ODD usually refers to the oral enteric route of administration, in which the drug absorbing entity most commonly is the intestine as it constitutes the largest absorptive area of the GI tract [24]. In contrast to other routes of administration, ODD has the highest patient compliance. This is because it is non-invasive, therefore free of pain, and easy to administer without the need for healthcare professionals [1–3]. Other advantages include the possibility to achieve slow and sustained drug release, the potential to locally treat diseases of the GI tract as well as certain functional advantages, such as drug uptake into portal blood circulation in oral insulin delivery and thereby mimicking the physiological secretion pattern of endogenously produced insulin [4,5,25].

On the downside, as mentioned in section 1.1, ODD is often associated with low bioavailability of drugs. This is partially caused by environmental factors present before the absorption of the drug has taken place and also by environmental factors present after the drug has been absorbed. While the first can be summarized as the complex physiology of the GI tract, the latter can be attributed to the *hepatic first pass metabolism* in which drugs can be inactivated [26]. Further disadvantages are unpredictable absorption rates that increase the difficulty to estimate systemic effects, impermeability of the intestinal epithelial barrier for larger and polar molecules, potential irritation of the GI tract and the impossibility to target specific organs other than those directly connected to the GI tract [26].

To fully understand the challenges associated with ODD, the nature of the GI tract needs to be considered.

3.1.2 The Physiological Environment of the Gastro-Intestinal Tract

The natural function of the GI tract is to take up, process and absorb nutrients, electrolytes and water. The GI tract resembles a fragmented tubular system leading along the longitudinal axis through the body, with the mouth and the anus as openings (Figure 5). Different fragments account for specific organs with distinct functions. Whereas the main components of the GI tract can be summed up as oral cavity, esophagus, stomach, small intestine and large intestine, the GI tract is associated with further entities that assist digestion and absorption, which are the salivary glands, liver, gall bladder and pancreas.

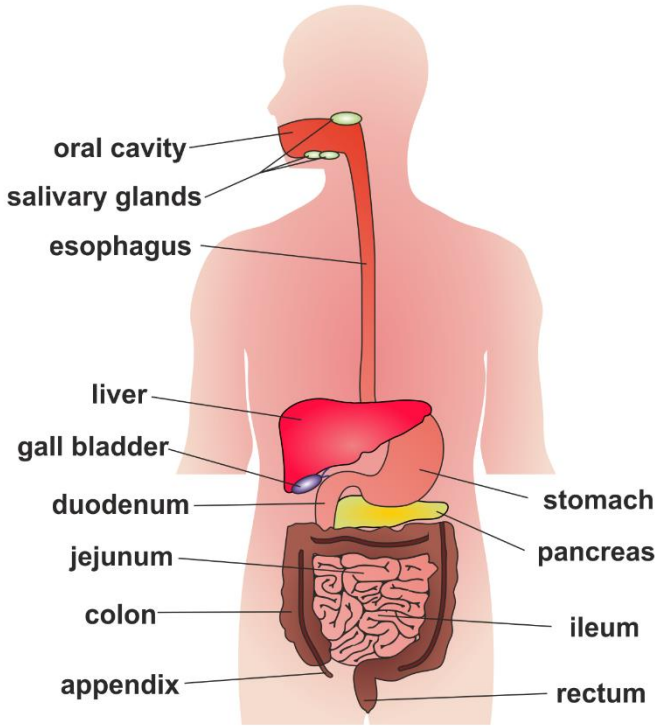

Figure 5 The human gastro-intestinal tract.

Upon ingestion of food, the chewing produces a thick mass of mashed contents, a bolus, that is mixed with saliva secreted from the salivary glands. Saliva among other things contains digestive enzymes that initiate the chemical breakdown of carbohydrate chains and fats. After swallowing, the bolus, assisted by peristaltic contractions, quickly passes through the esophagus, which connects the oral cavity and the stomach.

The stomach accounts for storage, digestive and protective purposes. A combination of mechanical and chemical degradation, facilitated through muscular contractions and mixing with gastric acid (HCl) and digestive enzymes, transforms the bolus into pre-digested chyme, which by the action of the pyloric sphincter is admitted to enter the beginning section of the

small intestine in a step-by-step fashion [27]. Through the secretion of gastric acid into the lumen of the stomach, pH-values down to 1 can occur [28]. This does not only cause chemical degradation of nutritional contents, e.g. by disruption of hydrogen bridges and disulfide bonds in proteins but also leads to elimination of potential pathogens, such as bacteria and other microorganisms, that were taken up (e.g. along with food) [27].

Most of the digestion and absorption takes place in the small intestine as it constitutes the largest absorptive area as well as the largest interface between the body and the external environment. Although the small intestine does not occupy too much space within the abdominal cavity, it has a surface area of 30 m^2 [29]. This is possible due to the hierarchical architecture of the small intestine (Figure 6). The small intestine, with a length of about 3 m, is arranged in the form of folded loops that are held in place by mesenteric tissue [27,30]. The surface area of the intestinal wall facing the luminal side of the small intestine, the mucosa, is increased through the occurrence of circular folds and small finger-like structures, the villi, which in turn are lined with epithelial cells that exhibit microvilli at their apical side [27].

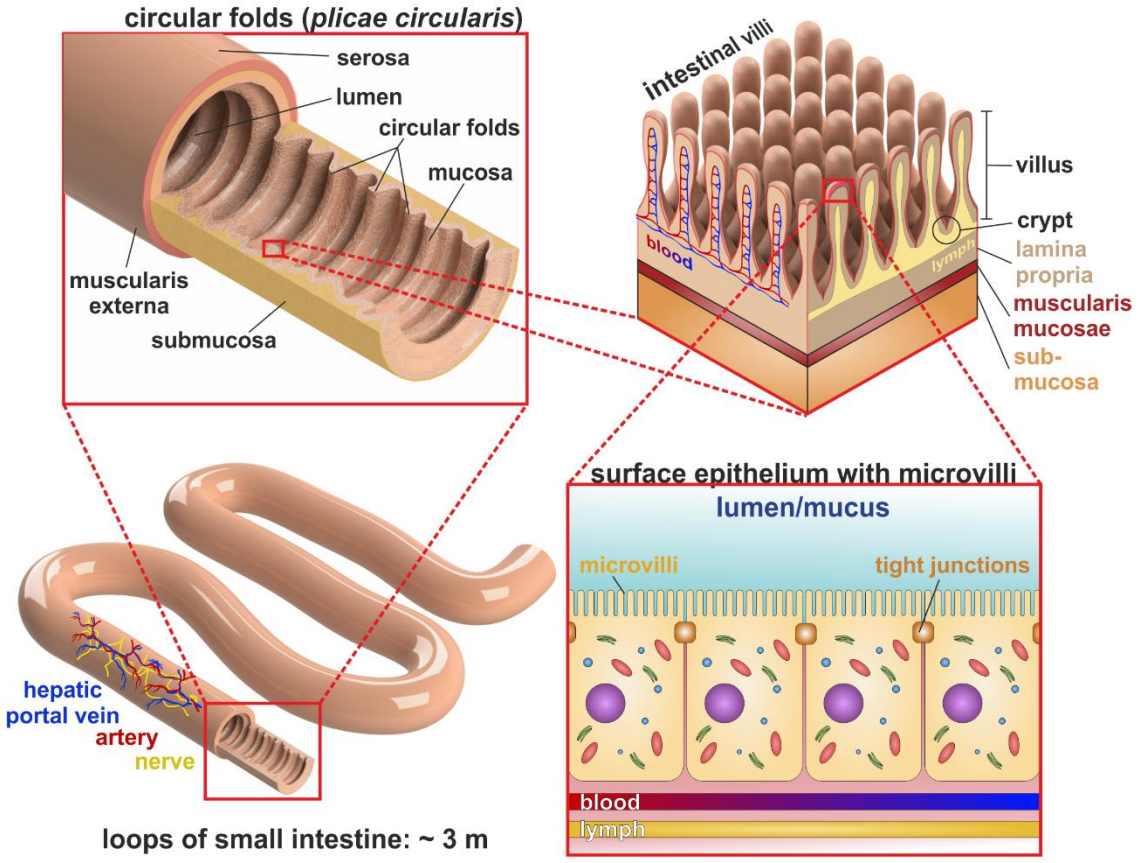

Figure 6 Hierarchical architecture of the human small intestine.

The small intestine consists of three consecutive parts, namely the duodenum, the jejunum and the ileum. The duodenum, with a length of about 25 cm, is the shortest fragment of the small intestine but is of crucial importance to the digestive process as it connects the small intestine to the pancreas as well as the gall bladder via the pancreatic duct and the common bile duct, respectively. Sodium bicarbonate is secreted from the pancreas into the duodenum, acting as a pH buffer, thus resulting in a neutralization of the chyme's acidic pH caused by mixing with gastric acid [27]. Along with bicarbonate, the pancreas secretes a mixture of digestive enzymes into the duodenum, thereby facilitating the continuation of chemical breakdown of food contents, such as proteins, carbohydrates and fats. The bile, which is secreted from the gall bladder into the duodenum, contains waste products coming from the liver that are intended for excretion, but also bile salts that act as detergents, thus stabilizing fats in the form of small particles and thereby promoting their enzymatic degradation [27]. Since the duodenum is rather short, most of the digestion and absorption takes place in the jejunum and ileum.

The intestinal wall consists of four different layers. The mucosa acts as the interface to the luminal content of the intestine and has several hierarchical levels of surface-area-increasing structural organization. The submucosa is an innervated connective tissue layer traversed by lymph and blood vessels, the *muscularis externa* consists of layers of circular and longitudinal smooth muscles, and the serosa forms the outermost layer of the intestine. As mentioned before, the intestinal villi are finger-like evaginations of the mucosa and are separated by crypts, which are invaginations. While most of the absorption happens through the villi, the crypts facilitate secretion of e.g. sodium chloride solution and renewal of epithelial cells [27]. The epithelial cell layer of the mucosa comprises specialized cell types, such as mucus-secreting *Goblet cells* or cells with membrane-bound enzymes for digestion and absorption [27]. Apart from the mucosal epithelium, the mucosa consists of two more layers, the *lamina propria* and the *muscularis mucosae*. The *lamina propria* is a connective tissue containing nerve fibers as well as blood and lymph capillaries, which serve to transport absorbed nutrients to the larger blood and lymph vessels found in the submucosa. The *muscularis mucosae* is a thin layer of smooth muscles that, by contraction, can actuate the intestinal villi, thus bringing the epithelial surface into contact with a higher number of nutrients and thereby increasing absorption [27].

The muscle-controlled movement of the intestine is referred to as intestinal motility and encompasses further types of movement apart from the actuation of intestinal villi. The contraction of circular smooth muscles within the *muscularis externa* of the intestinal wall leads to a reduction of the diameter, whereas the contraction of longitudinal smooth muscles shortens the length of the intestine. The controlled combination of these movements can result in alternating segmental contractions that facilitate the mixing of luminal contents or in sequential segmental contractions, which enable a steady forward movement of the chyme.

The orchestrated control of intestinal motility and other coordinated digestive processes is possible due to the dense enervation of the GI tract, forming the enteric nervous system (ENS). Based on reflexes, the ENS acts largely autonomously but is also connected to the central nervous system. Further control is achieved by the function of hormones, which are secreted by enteroendocrine cells present in different sections of the GI tract [27].

Nutrients absorbed in the process of digestion are transported further within the body. While fats absorbed by the mucosal epithelium are redirected to the lymphatic capillaries and connected lymph vessels, other digestion products, such as amino acids, peptides and monosaccharides, are transported into the blood capillaries that lead to the liver via the hepatic portal vein [27].

As the chyme reaches the large intestine, no further digestion, other than the one facilitated through the residential microbiota, will take place. In the large intestine most of the electrolytes and water are absorbed, resulting in the concentration of non-absorbed contents as well as waste products and the formation of feces, which eventually are excreted.

The fact that the GI tract, especially the small intestine, is the largest interface to the outer world and consequentially subjected to many pathogens and harmful substances, elucidates the occurrence of a multitude of protection mechanisms. While the protective feature of gastric acid has been mentioned already, there are several more mechanisms that need to be addressed. Throughout the GI tract, the epithelial surface reveals to be a tight barrier. This is due to the existence of so-called *tight junctions*. The latter refers to intercellular junctions between epithelial cells, in which membrane proteins (e.g. *claudins* and *occludins*) tightly connect the membranes of neighboring cells [31]. *Tight junctions* can, however, be “leaky”, meaning that in specific situations they are caused to open, for example, to let solutes pass through the intercellular space [32]. Apart from that, the GI tract is interconnected with the largest lymphatic tissue of the body, namely, the *gut-associated-lymphoid-tissue* (GALT),

which comprises immune cells scattered throughout the intestinal mucosa, immune cells residing in mesenteric lymph nodes and *Peyer's patches* [31]. While epithelial *M-cells* in the *Peyer's patches* sample the luminal content for potentially pathogenic antigens, *Paneth cells* mainly found in the crypts secrete anti-microbial *defensin* peptides [33]. Furthermore, *Goblet cells* present in the intestinal mucosa secrete a substantial amount of mucus that lines the surface and thereby protects it from harmful particles and entraps potential pathogens. A feedback mechanism induced by *cytokine*-secretion from immune cells can lead to the increased secretion of mucus, which helps to flush pathogens out of the intestine [27]. Finally, if pathogens or toxic substances reached the absorptive blood vessels and subsequently the liver via the hepatic portal vein, further detoxification processes occur.

When considering the overall complex conditions in the GI tract, several implications on ODD can be determined. As the medication, in form of a capsule, tablet or solution is usually swallowed immediately after ingestion and not chewed, thus resulting in a fast passage, the effect of the oral cavity and the esophagus can be neglected. The residence of any dosage form in the stomach, on the other hand, is usually longer and the harsh environmental conditions can have a major impact on the integrity of the drug. Hydrochloric acid present in the stomach can lead to chemical degradation, while peptide drugs are especially threatened by enzymatic degradation. Furthermore, drugs can become insoluble due to the low pH of the stomach and are therefore not absorbable any longer [26]. As the small intestine represents the largest absorptive area in the GI tract, it is usually the target of drug absorption in ODD. The barrier functions of the intestinal epithelium along with the vast occurrence of immune cells and mucus secretion can drastically limit the bioavailability of drugs. Moreover, the inter- and intraindividual variabilities in GI tract physiology, e.g. intestinal transit times, can lead to significant variations in drug bioavailability [34]. Lastly, after absorption, drugs usually enter portal circulation, thus leading to the *hepatic first pass effect*, in which many drugs are efficiently degraded within the liver [26]. The careful consideration of these challenges during the design of drug candidates and delivery platforms can result in more successful solutions, in which the mentioned implications may even be exploited for specific purposes. In this regard, the development of enteric coatings exploited the harsh pH gradient along the GI tract to target specific sections of it [34,35]. Transport mechanisms of the intestinal epithelium, including modulation of *tight junctions*, can be targeted and exploited for drug absorption and the abundance of lymphatic tissue may be exploited for lymphatic delivery in order to

avoid the *hepatic first pass effect* [32,34,36]. Finally, the thick layer of secreted mucus, which aims to shield the mucosa from particles and harmful substances, can be targeted with mucoadhesive materials for increased intestinal residence time and consequent increased possibility for absorption. The next section will elaborate on this topic.

3.1.3 Mucus and Mucoadhesion

As mentioned in the previous section, mucus is secreted from *Goblet cells* at the mucosal surface of the intestine and thereby lubricates as well as protects the epithelium against harmful particles and substances. Mucus is a soft and slimy substance composed mainly of mucin glycoproteins, lipids, salts and water [18]. The amount of mucus secretion in the human GI tract can add up to 10 l daily [37]. Reliable figures on intestinal mucus clearance rates are not available, but it can be assumed that mucus clearance is a variable process depending on the physiological state (nutrition, stress, disease etc.) of the GI tract. However, mucus turnover times have been estimated as 47 up to 270 min for the rat intestine and 10 min for the human nasal mucus, which gives the impression that the renewal of mucus layers is probably within the frame of minutes up to hours, rather than days [38,39]. The intestinal mucus layer consists of two layers, one unstirred layer, which firmly adheres to the epithelial cell surface, and one layer that loosely protrudes into the lumen [37,40]. Both layers have been reported to vary in thickness in the different intestinal sections and values have been determined for the intestine of rats (Figure 7) [40]. Accordingly, the thicknesses of both layers are the highest in the colon, followed by the ileum and duodenum and are the thinnest in the jejunum. Although a difference in mucus thickness between rat and human mucus can be assumed, the thicknesses observed in rats might not be too much different as measurements on thickness of the adherent mucus at the site of human *antrum* mucosa suggest. There, the thickness varies between 50 and 450 µm, thus limiting deviations to micrometer scale [41].

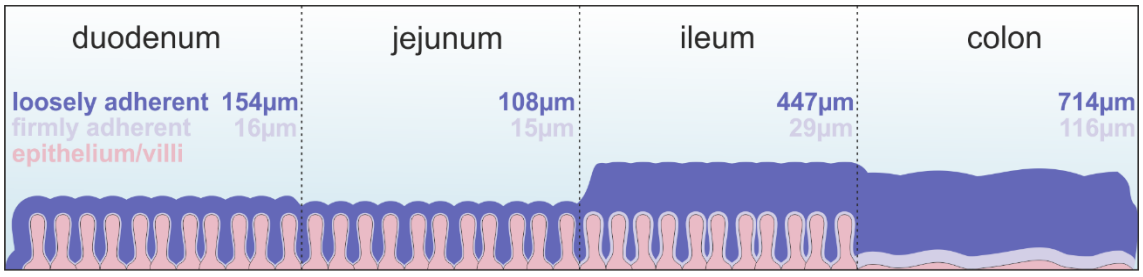

Figure 7 Mucus thicknesses in different sections of the rat intestine [40].

The molecular structure of mucus, which is responsible for its unique properties, is mainly based on an interconnected network of mucin fibers. There are two categories of mucins: gel-forming mucins and membrane-bound mucins [37]. Gel-forming mucins are elongated proteins consisting of alternating hydrophilic regions that are heavily glycosylated and folded cysteine-rich hydrophobic domains (Figure 8a) [37]. The amino acid cysteine contains a residual thiol group and hence is often involved in the formation of intra- and intermolecular disulfide bridges. Mucins build multimeric constructs through the formation of disulfide bonds between cysteine-rich domains of at least two N-termini as well as two C-termini of the proteins, respectively (Figure 8b) [42]. These constructs represent the molecular backbone of dense meshes of mucus. Mucins can further bind to one another through low-affinity hydrophilic or hydrophobic associations [37]. Membrane-bound mucins form the so-called glycocalyx layer which is firmly bound to the epithelial cell surfaces via transmembrane anchors (Figure 8c) [37]. The presumed functions of the glycocalyx comprise protection of the cell surface and binding of the firmly adherent mucus layer [37].

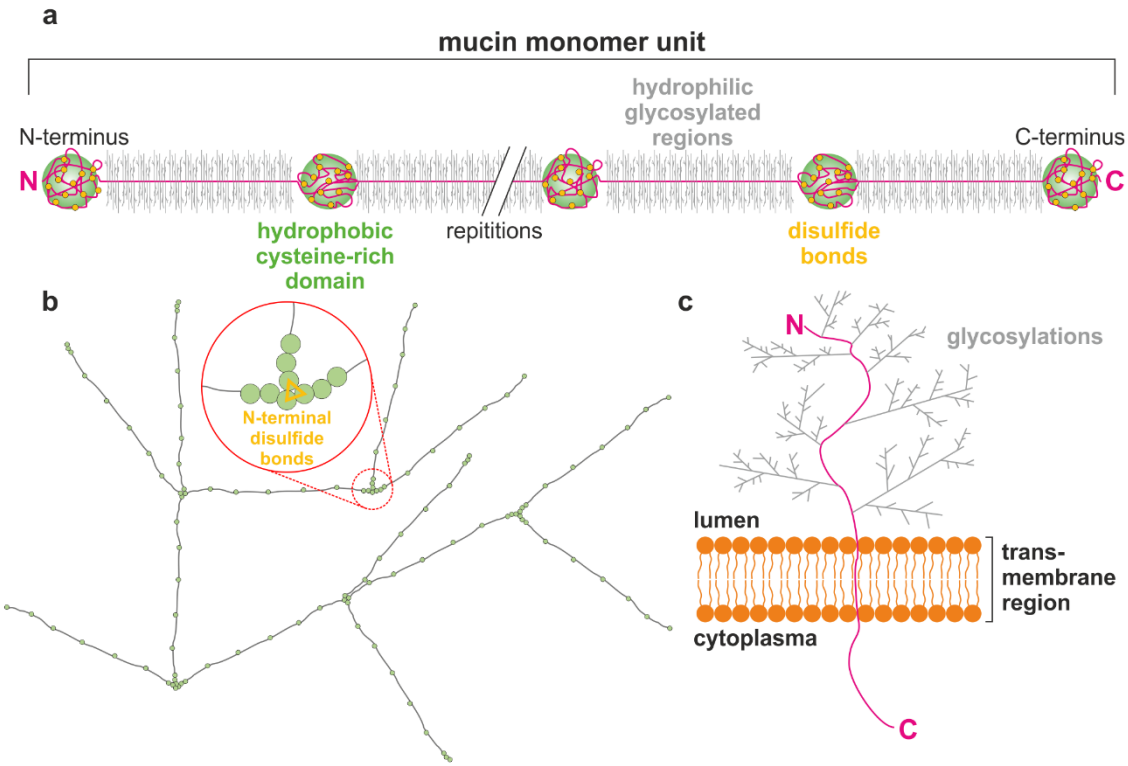

Figure 8 Molecular structure of mucus. (a) Gel-forming mucin glycoprotein monomer composed of peptide backbone with cysteine-rich domains and glycosylated regions. (b) Macromolecular structure of mucus based on low-affinity bonds between gel-forming mucins. (c) Membrane-bound mucin forming the basis of the epithelium-protecting glycocalyx. (a) and (b) modified from [37] *and (c) modified from* [43].

The nature of the macromolecular structure of mucus leads to several physiologically relevant properties. Disulfide bridges provided by cysteines are known to increase the stability of proteins and their constructs, which is exemplified by the high cysteine contents of keratins, a family of structural proteins that form the elementary building blocks of hair, nail and horn structures. When shear stress is induced to mucus, up to a certain threshold, the mucin fibers rather bend instead of breaking the intermolecular bond, thus leading to the elasticity of the mucus [37]. This phenomenon can, at least in part, be attributed to the occurrence of disulfide bridges within the intermolecular bonds [44]. However, an increase of shear stress over the threshold will cause the breaking of the bonds and consequently result in viscous behavior [37]. These circumstances render mucus a shear-thinning gel with viscoelastic properties, which consequently make mucus a good lubricant. The viscosity of mucus is negatively correlated with shear rate and can reach values as low as that of water under physiological stress conditions [37]. Albeit, mucus yields the ability to re-anneal as the mucin fibers can re-establish disulfide and low-affinity bonds after shear stress [44]. Mucus usually consists up to 95 % of water and it has to be noted that the viscoelasticity of mucus is highly dependent on the water content, with higher viscoelasticity in less hydrated state and lower viscoelasticity in a more hydrated state [18,37].

In accordance with its function to protect the intestinal mucosa from pathogens, the viscoelasticity of mucus can efficiently hinder the movement of bacteria and trap them [37]. Considering the importance of this feature and the fact that viscoelasticity highly depends on the water content of mucus, one can assume that a regulation feedback for mucus hydration is required. It is assumed that this regulation happens indirectly through the regulation of ionic gradients at the mucosal surface [37]. In fact, an imbalance in hydration-regulation leads to severe infections of the airway mucosa in cystic fibrosis patients [45]. Mucus can, in general, be regarded as a semipermeable barrier, which is permeable for nutrients, metabolites and wastes, while hindering pathogens, particles and drug molecules from traveling towards the epithelium [37,46]. One theory about how mucus prevents the passage of particles is that additionally to entanglement within the mesh structure, low-affinity bonds between a multitude of mucins and the particle surface are established and broken alternately, so that, despite low energy of the bonds, efficient retention can occur [37]. The adhesiveness of mucus to particles and other materials, and the other way around, is subject to intense research as a better understanding can help within the development of more efficient ODD formulations.

The adhesion to mucosal surfaces, termed mucoadhesion, is strategically exploited in order to design mucoadhesive drug delivery systems with increased retention time for increased drug release and potentially increased drug absorption [47]. On the contrary, it has been proposed to design non-mucoadhesive particulate delivery systems for enhanced passage of the mucus barrier and consequentially higher drug absorption [37,48]. The mechanism of mucoadhesion is not properly understood as it probably involves a magnitude of different processes. But nevertheless, a collection of several possible explanations exists, and in reality, a combination of those might be applicable to facilitate the understanding of mucoadhesion [49].

The occurrence of mucoadhesion, as in general adhesion, can basically be broken down into two steps: the contact stage and the consolidation stage [18]. Within the contact stage, an intimate contact between the mucosal surface and the mucoadhesive is established and in the subsequent consolidation stage different physicochemical processes consolidate the adhesive bond [18]. With regard to the physicochemical causes of adhesion, different explanatory approaches can be explored.

The *electronic theory* implies that an exchange of electrons between the two adhesive faces in intimate contact leads to the creation of an electric double layer, which facilitates consolidation of the bond due to attractivity between opposing charges [18].

A theory that is more applicable for liquid mucoadhesives, the *wetting theory*, assumes that surface as well as interfacial energies correlate with their ability to spread on the mucosal surface, thus interpreting the ability to spread as higher mucoadhesiveness [18].

The formation of molecular bonds, such as hydrogen and van der Waals' bonds up to covalent bonds, between the adhesive surfaces is the foundation of the *adsorption theory* [18].

Within the frame of the *diffusion theory*, it is presumed that in case of polymeric mucoadhesives, polymer chains of mucus and mucoadhesive interpenetrate one another through diffusion along a concentration gradient, thus creating a consolidation of the adhesive bond [18].

The *mechanical theory* of adhesion implies that the penetration of an adhesive, which in this case may be the mucus, into irregularities and voids of a rough surface leads to a mechanical interlocking, which is further stabilized through enlarged surface contact area and resulting increase in "viscoelastic and plastic dissipation of energy during joint failure" [18,50].

While all the hitherto mentioned theories rely on the explanation of adhesion as processes occurring at the interfaces of two adhesive surfaces, the *fracture theory* relates the required detachment energy to the mechanical response of the individual adhesives, such as the formation of propagating cracks [18,51].

As earlier mentioned in section 1.2, the *mechanical theory* served as the theoretical framework to motivate the creation of designs of microcontainers with surface area increasing anchor structures for increased mucoadhesive properties. With respect to the knowledge available about mucus, it can be assumed that the mechanical effect in mucoadhesion can become very strong under the circumstance that time allows for a reformation of disulfide and low affinity bonds between mucin fibers, thus "locking" structural irregularities in place.

Because mucoadhesion is a factor that critically influences the aptitude of an ODD system, it is of high interest to measure mucoadhesiveness. Up to the present, various testing methods have been developed, which rely on different principles. The techniques can be broadly categorized as measurements of mechanical forces, analyses of molecular mucoadhesive interactions, determination of resistance to flow forces, methods based on the use of fluorescent probes and examination of rheological properties [52]. These categories can be further split up into observational and molecular testing methods [52]. Tensile detachment force measurements as well as flow retention measurements are frequently utilized observational methods and both have been employed within the frame of the work presented in Manuscript III and Manuscript IV. Therefore, these methods are further described in sections 4.10 and 4.10.2, respectively.

One general criticism about the use of observational methods, such as tensile stress and flow retention tests, is the common use of ex-vivo intestinal tissue specimens obtained from slaughterhouse or laboratory animals as it often leads to high variations in data recordings due to high biological variability [49]. Moreover, the representative quality of tissue obtained from slaughterhouses is debatable as intensive livestock farming is often associated with poor physiological conditions of the animals. To reduce variations, the development of artificial tissue substitutes has been demanded [49]. For the work presented in Manuscript III, the problem of biological variability was circumvented by choosing a *Latin square* experimental design with two blocking factors.

3.1.4 Drug Absorption and Bioavailability in Oral Drug Delivery

Under the assumption that a drug molecule is successfully delivered through stomach, intestine, mucus layer and glycocalyx and therefore present in direct proximity to the epithelial cell surface, it is still required to pass through the tightly arranged cell layer to reach the nutrient transporting blood capillaries and consequently portal circulation. The mechanisms by which a drug molecule can surpass the epithelial cell barrier resembles the ones available for nutrients and other solutes and can be broadly separated into two categories: transcellular and paracellular uptake (Figure 9) [53].

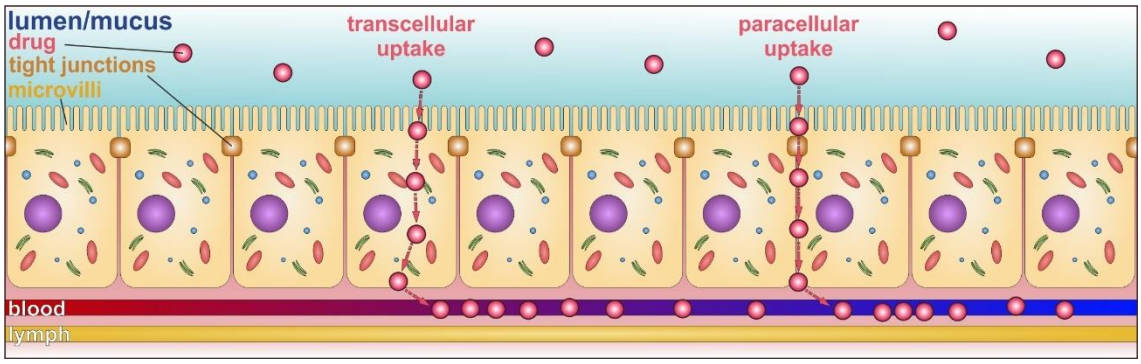

Figure 9 Pathways of intestinal drug absorption.

While transcellular uptake can be facilitated by different means, paracellular uptake is strictly based on passive diffusion but controlled by the arrangement of *tight junctions* between adjacent epithelial cells [53]. Moreover, it has to be noted that the available surface area for paracellular uptake in the intestine is low compared to transcellular uptake [54]. Transcellular uptake of nutrients or drugs can occur through passive diffusion, facilitated diffusion, counter transport, active transport and receptor mediated endocytosis [53]. Passive diffusion through the cellular membrane does not require additional energy and is governed by *Fick's law of diffusion*. However, due to the hydrophobic nature of the lipid cell membrane, only small amphiphilic molecules can readily diffuse through it [54]. Facilitated diffusion does not require additional energy and is promoted by channel-forming transmembrane proteins such as porins [53]. In this way, also polar and hydrophilic molecules can pass the membrane by diffusion. Counter transport relies on the principle of mediated carrier-transport in which two solutes are transported along the membrane simultaneously [53]. In this case, transport against a concentration gradient, which usually requires energy, is often coupled with transport along a concentration gradient (secondary-active transport). The creation of the initial concentration gradient is however often the result of active transport [55]. In active

transport, specialized carrier proteins facilitate the transport of a molecule past the cell membrane by undergoing a conformational change that requires energy [55]. Finally, in receptor mediated endocytosis, the interaction of a molecule with a specific cell membrane receptor results in the formation of a vesicle, which is then incorporated into the cytoplasm [53].

Although several possible pathways for drug absorption exist, it is an inherent fact in ODD that many drugs fail to be absorbed. One of the reasons for this is that for the mentioned uptake mechanisms the drugs have to be in solution. However, many drugs reveal poor solubility. Furthermore, even if drugs have a high solubility, they might still fail to be transported across the epithelial barrier, thus resulting in low permeability. To predict the absorption of drugs during drug screening in early drug discovery steps, the Biopharmaceutics Classification System (BCS) was developed by Amidon et al. and the U.S. Food and Drug Administration (FDA) [56,57]. The BCS evaluates the three factors dissolution, solubility and intestinal permeability and is based on the theoretical concept expressed in *Equation 1*, where J_{max} is the maximum flux of drug mass (M) per area (A) that is absorbed into the membrane per time (t), which in turn is equivalent to the local membrane permeability (P_{eff}) multiplied with the maximum concentration of solubilized drug (C_s) present at the membrane-luminal interface [56,58].

$$J_{max} = \left(\frac{1}{A}\right) \times \frac{dM}{dt} = P_{eff} \times C_s \qquad \textit{Equation 1}$$

The classification of drugs within the frame of the BCS is facilitated by employing a set of recommended *in vitro* evaluation methods, which according to the results allows the drugs to be placed within one of four classes: high solubility and high permeability, low solubility and high permeability, high solubility and low permeability and finally low solubility and low permeability (Figure 10) [57]. While the bioavailability of drugs falling into class 1 of the BCS is in principle not limited by absorption, it is for drugs falling into classes 2 to 4. In those cases, the causes for limitations in solubility or permeability of the drug need to be investigated and strategies for absorption enhancement may be applicable. In fact, it has been reported that an increasing number of marketed as well as developmental pipeline drugs fall into low-solubility classes 2 and 4 of the BCS [59]. As the developed drugs often show good performance from a pharmacological point of view, the further development of absorption enhancement strategies is of high interest [59].

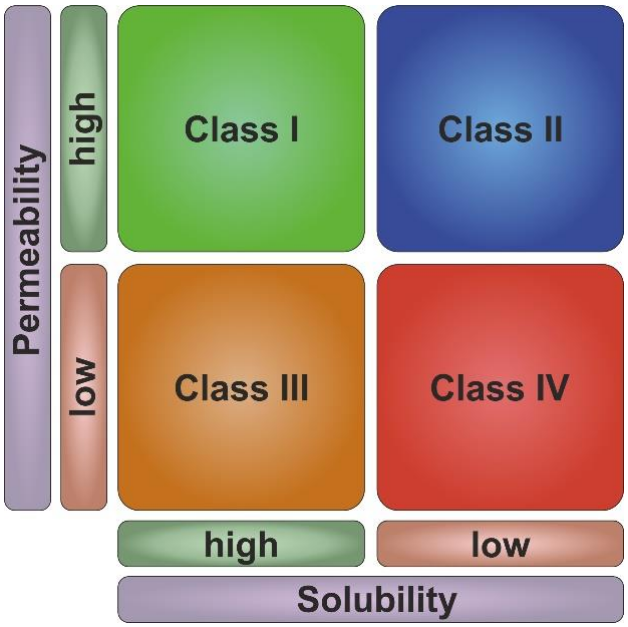

Figure 10 Biopharmaceutics Classification System (BCS) [56,57].

3.1.5 Oral Drug Delivery Systems for Increased Bioavailability

The former sections in this chapter have illustrated that the physiological environment of the GI tract leads to numerous challenges and limitations for ODD as it often causes low bioavailability of administered drugs. In order to cope with these challenges, many different strategies have been explored. It has to be emphasized that the variety of these strategies resembles the variety of present challenges, and that a combination of strategies aimed to solve different problems most probably yields higher success than considering them in isolation. For example, to increase the solubility of drugs, molecular modifications such as the use of co-solvents and the formation of prodrugs or salts may be feasible [60]. Also, the use and stabilization of the amorphous state, rather than the crystalline state, of drugs can increase absorption as it increases the solubility [60]. The oral delivery of drugs can be combined with the use of substances that facilitate the permeation of the epithelial barrier, e.g. by the opening of the *tight junctions*. These substances are called permeation enhancers and one commonly investigated substance for this purpose is the biopolymer chitosan [61]. For the delivery of proteins and peptides, protease inhibitors can be co-administered to decrease the effect of enzymatic protein digestion by native GI digestive enzymes [53]. A further approach is to employ particulate drug carrier platforms such as polymeric micro- and nanoparticles and liposomes [62]. These platforms can achieve multiple purposes: protection, targeting via functionalization, modified release, mucoadhesion and enhanced absorption [62].

In recent time, engineering approaches for the development of ODD systems gained popularity. Examples in this regard are the use of microneedle-equipped capsules for transmucosal injection, self-unfolding devices for prolonged gastric residence and sustained drug release as well as self-orienting devices with incorporated spring-loaded needles for transmucosal injection [63–65].

The work presented in this Ph.D. thesis addresses the development and characterization of a microfabricated universal carrier platform, of which the intended function is to protect the drug from external influences, i.e. prevent the drug from being degraded by gastric acid or digestive enzymes and facilitate the transport towards the intestinal mucosa. The focus is therefore not directed towards the improvement of absorption at the epithelial barrier. However, as the idea is to develop a universal carrier system, the use of other concepts employed for absorption enhancement will be compatible with this approach.

3.2 Microfabricated Oral Drug Delivery Systems

Microfabrication refers to the use of a collection of techniques that originated from and have been commonly used within the electronics industry for the fabrication of semiconductor devices and *integrated circuits* and later for the fabrication of *microelectromechanical systems* (MEMS) [66]. Microfabrication techniques usually encompass methods for the generation of thin films and patterns, e.g. by deposition, lithography or etching techniques [66,67]. Due to the suitability of silicon as a semiconductor material and the ease of forming silicon dioxide, which in turn has excellent insulator properties, thin polished slices of silicon crystal, namely silicon wafers, have been traditionally used as substrates in microfabrication [67]. Along with the trend of miniaturization and integration of devices, contamination of fabricated products with environmental contaminants, e.g. particles, increasingly led to loss of their functionality and thus threatened to dramatically reduce the yield of processes [67]. Therefore, it became standard that microfabrication is carried out in cleanroom environments. The need for elaborated cleanroom facilities as well as the use of silicon (50-300$ per kg depending on spot market) let microfabrication processes often to result in relatively high costs, so that cost-to-performance criteria need to be carefully considered in the early steps of product development [68,69]. The use of microfabrication technologies has evolved over time, meaning that it became more accessible and attractive for other branches in research and development [67]. The medical field is represented among those and one readily explored application has been the use of microfabrication technologies for the fabrication of microneedles for transdermal drug delivery [70].

The concept of top-down microfabricated devices for ODD was initiated by Ahmed et al. in 2001, who demonstrated the use of a combination of photolithography, dry etching and wet etching to produce square patch-like SiO_2 reservoir devices with a size of 50 µm and their subsequent surface functionalization with *tomato lectin* (TL) for enhanced bioadhesion [13]. The idea underlying this concept is that the reservoir may be filled with any drug and upon application, facilitated through surface functionalization, will closely associate with the intestinal mucosa, thus leading to a highly localized and unidirectional release of the drug [13]. The release of individual microdevices from the silicon wafer in order to be suitable for application was facilitated by use of a sacrificial release layer [13]. Studies in this initial work showed the clustering of TL-functionalized microdevices with *Caco-2* cells, an *in vitro* model cell line of the small intestine epithelium, thereby suggesting the desired effect of epithelial

cell binding [13]. However, in a following work, Ahmed et al. strengthened the idea behind the concept by demonstrating a potential drug loading mechanism using a microneedle and water as well as oil-based filling. Moreover, for effective delivery to the small intestine, the use of enteric coated (pH-sensitive) capsules, in which the microdevices should be loaded, was suggested and the bioadhesive potential of TL-functionalized microdevices to *Caco-2* cell monolayers was experimentally proven [14].

The pioneering work performed by Ahmed et al. was further expanded with numerous approaches to utilize different materials, fabrication protocols, surface modifications and drug loading techniques. SiO_2 as a material for fabrication of the microdevices was rapidly replaced by *poly(methyl methacrylate)* (PMMA), due to better properties in terms of biocompatibility and surface functionalization, which was subsequently demonstrated through binding of *tomato* and *peanut lectin* via surface aminolysis and adhesion to *Caco-2* cell monolayers [10]. According to Tao et al., the microdevice concept infers that the flat patch-like geometry of microdevices results in an increased contact area between device and intestinal mucosa as opposed to that in case of spherical microparticles. Additionally, the limitation of drug release to the reservoir opening of the devices, causing unidirectional release, is presumed to concentrate released drug at the interface of device and mucosa, so that an increase in epithelial drug absorption can be achieved. In contrast to that, spherical microparticles are thought to release the drug omnidirectionally, so that a fraction of the drug will be released into the intestinal lumen and hence will be prone to intestinal clearance [10]. The experimental comparison of spherical and square microdevices showed that spherical devices, probably due to less contact area, indeed bind less efficiently to *Caco-2* cell monolayers when modified with TL [71]. As the processing requirements of PMMA entailed a limitation of microdevice thickness, further materials such as epoxy-based *SU-8* negative photoresist as well as biodegradable and biocompatible *poly(lactic-co-glycolic acid)* (PLGA) and *gelatin* have been introduced [15,72].

Many of the subsequent studies focused on the exploration of further and more convenient fabrication approaches featuring improved versatility with respect to the use of a wider range of materials. In this regard, soft lithography in combination with the use of UV-curable liquid resin made of *poly(ethylene glycol methacrylate)* (PEGMA) and *poly(ethylene glycol di-methacrylate)* (PEGDMA) or PLGA was demonstrated [73]. Another rather sophisticated approach involved the fabrication of self-folding origami-based polymeric microdevices

consisting of *SU-8* elements and *polycaprolactone* (PCL) hinges [74]. The *Particle Replication In Non-wetting Templates* (PRINT)-method combines imprint lithography with the use of non-wetting surfaces and thereby broadens the range of available materials as well as the size range of fabricated particles, which can be at the micro- and nanoscale [75]. Consequently, this method has been considered to have great potential for the fabrication of microdevices for ODD [76]. A further method worth mentioning is the *StampEd Assembly of polymer Layers* (SEAL), in which layers of polymer are stacked on top of one another at high resolution and subsequently fused together in a thermal process, because it allows the fabrication of devices from any thermoplastic as it was demonstrated with the use of PLGA [77].

Aside from fabrication methods, a lot of progress on the drug loading of microfabricated devices for ODD has been shown. Initially, drug-loading was based on filling microdevices with drug-laden UV-photo-polymerizing hydrogels. *In vitro* release and permeation studies of BCS class 4 drug *camptothecin*-laden PEGDMA hydrogels in *SU-8* microdevices revealed promising results as it could be shown that the microdevices led to an increase of drug absorption inferred by an increased permeation through a *Caco-2* cell monolayer [78]. The increase in permeation, in this case, might have been a result of the localized high drug concentration at the device/cell layer interface as mentioned earlier [78]. These results could be further confirmed under relevant physiology-mimicking shear stress conditions employing displacement studies and a shear diffusion flow cell [11]. The increased *in vitro* permeation of released drug could also be facilitated by PMMA microdevices with multiple reservoirs, enabling the loading of multiple drugs and tailoring of release patterns by varying the degree of crosslinking of the different drug-laden hydrogels [16]. A milestone achievement in case of hydrogel-laden microdevices is represented by the experimental proof of increased *in vivo* murine intestinal retention due to TL surface functionalization and increased bioavailability of BCS class 3 drug *acyclovir* released from *monomethyl methacrylate* (MMA)-PEGDMA hydrogels in PMMA microdevices [12].

The loading of microdevices with hydrogels was usually achieved by spin coating a hydrogel precursor solution onto a wafer with microdevices and subsequent exposure to UV through a mask, thus restricting the photocuring reaction to the reservoirs of the devices [78]. While this procedure is very efficient in terms of throughput, it is unfortunately linked to excess wastage of drug [79]. Alternative methods for the loading of microdevices with minimized drug wastage comprise the utilization of passive diffusion as well as inkjet printing [80,81].

Loading based on diffusion was performed with the use of microdevices featuring a porous Al_2O_3 membrane with nanostraws, through which diffusion can take place, and was additionally shown to enhance mucoadhesion, probably due to increased surface roughness [80].

A similar approach to the hitherto mentioned microdevices for ODD is represented by cylindrical microcontainers. Although relying on the same concept, these microcontainers differ from the other microdevices, because of their higher aspect-ratio and vastly increased loading capacity [79]. The latter, in turn, allows for the loading of drug powder, which often is beneficial in terms of drug stability. Indeed, it has been shown that the compaction of drug powder within the cavity of the microcontainers can help to stabilize the amorphous form of BCS class 2 drug *indomethacin* [82]. Various methods have been proposed for the process of loading the drug powder into the reservoirs, including hot punching and powder embossing [83,84]. Experimental evaluations of the ODD performance of powder-loaded microcontainers yielded promising results. More specifically, it could be proven that microcontainers increased the absorption rate of BCS class 4 drug *furosemide* in *in situ* closed intestinal loop perfusion in rats, presumably due to enhanced mucoadhesion of the devices, and also led to an increase in oral bioavailability *in vivo* [19]. A further way to achieve an increased stability of the amorphous form of drugs is supercritical CO_2 impregnation of polymer matrices with drugs, hence forming solid dispersions [85]. Inkjet printing of a *polyvinylpyrrolidone* (PVP) matrix into the cavities of microcontainers and subsequent impregnation with BCS class 2 drug *ketoprofen,* dissolved in supercritical CO_2, has been demonstrated to be a feasible loading method [86–88]. An increase in oral bioavailability was likewise proven *in vivo* for microcontainers loaded via supercritical CO_2 impregnation with *ketoprofen* [89]. In both of the mentioned *in vivo* studies, microcontainers were individually coated with pH-sensitive lids and encapsulated in *gelatin* capsules for oral dosage, rather than encapsulating them in pH-sensitive capsules, as suggested by Ahmed et al. [14,19,89].

Apart from ODD, microcontainers and other microdevices have been suggested as useful tools for oral vaccine delivery [77,90,91].

Although microcontainers were successfully fabricated from biocompatible PCL using the scalable hot punching method, they have not been evaluated for their *in vivo* performance yet [92]. All other up to this point referenced studies relied on the use of microcontainers fabricated from *SU-8,* which is considered to be suitable for prototyping purposes [79].

The state-of-the-art protocol for the fabrication of *SU-8* microcontainers consists of six working steps (Figure 11) [87,89]. In the first step, a silicon wafer is spin coated with a release layer of *poly(acrylic acid)* (PAA). Then a layer of *SU-8* is applied via spin coating and soft-baked in order to remove solvents. In the third step, the bottom layers of the microcontainers are defined by use of UV-lithography and the corresponding mask. Thereafter, a second layer of *SU-8* is spin coated onto the wafer followed by a soft-bake. In a second lithography step, the reservoirs of the microcontainers are formed using UV-exposure and a second mask. Finally, the remaining uncured *SU-8* is removed during a developing step.

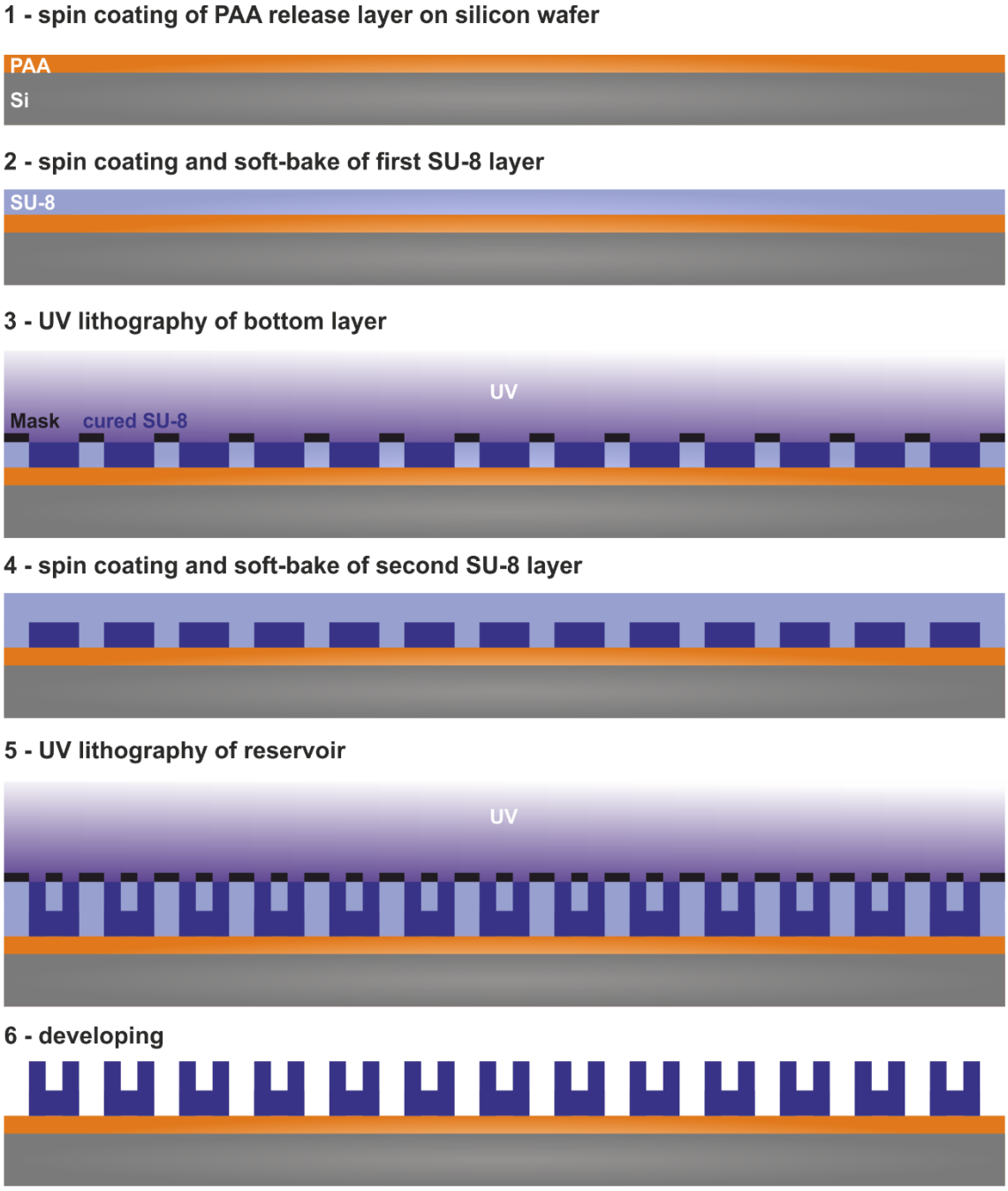

Figure 11 SU-8 photolithograhy of microcontainers for oral drug delivery [87,89].

The resulting product of this procedure is a 4-inch silicon wafer with 30 arrays of each 625 microcontainers on a water-soluble PAA sacrificial release layer (Figure 12a). For further batch-processing of microcontainers, the wafer is diced using either a large or a small dicing pattern, thus resulting in small chips containing 625 microcontainers or large chips containing 4 x 625 microcontainers (Figure 12b).

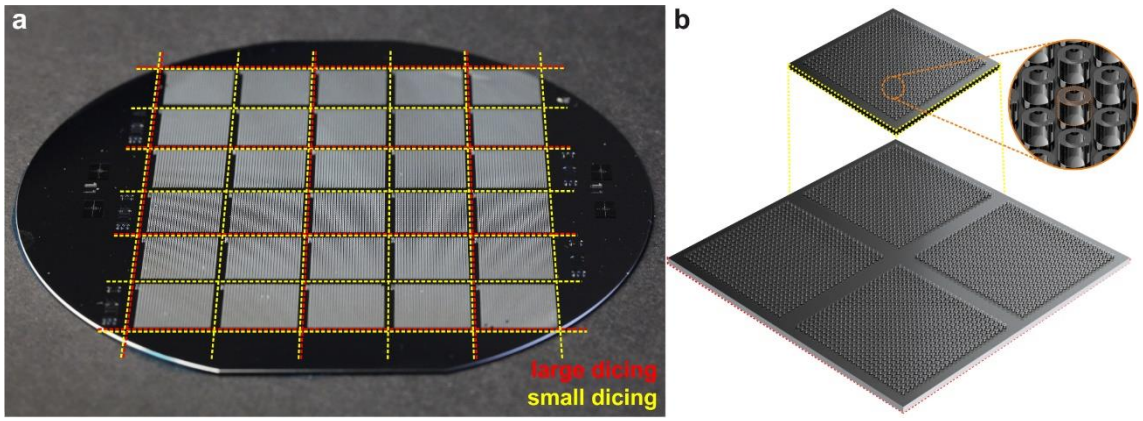

Figure 12 Batch processing of microcontainers. (a) Photograph of 4-inch wafer with arrays of microcontainers and illustrated big and small dicing patterns. (b) 3D renderings of silicon chips with arrays of microcontainers resulting from a small dicing pattern and a large dicing pattern.

The diced chips with microcontainers serve as substrates in other processing steps, such as drug loading via powder embossing or inkjet printing and lid sealing via spray coating (Figure 13) [19,84,86,89]. It has to be noted that the upright positioning of the microcontainers as well as the arrangement in form of a rectangular pattern are crucial for the conducted processing steps. While the powder embossing method employs a shadow mask specifically designed to fit the space in between this pattern, the inkjet printing and spray coating methods are computer-controlled and rely on the pattern coordinates.

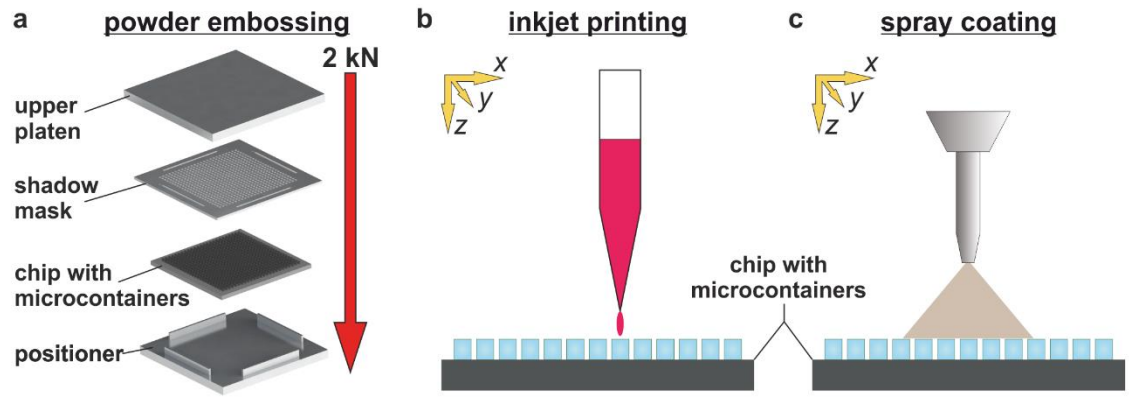

Figure 13 Microcontainer processing methods relying on rectangular patterns. Drug-loading via powder embossing and use of shadow mask [84]*. Reproduced from* [84] *with permission. (b) Drug-loading via inkjet-printing* [87]*. (c) Spray coating for sealing of microcontainers with a pH-sensitive lid* [19,89]*.*

Finally, after fabrication, loading and sealing of microcontainers is completed, the latter can be released from the silicon substrate by dissolving the sacrificial PAA release layer in water. After the microcontainers are harvested, they may be filled into a *gelatin* capsule for oral application as previously described (Figure 14) [19,89].

Figure 14 Microcontainers loaded into gelatin capsule for oral dosage.

In a recent review it has been stated that comparative studies with various designs of microcontainers/microdevices for ODD are lacking [79]. In this work, mainly as a part of Manuscript III, a comparative study with various designs, is shown, while exploring the possibility to utilize design features for increased functionality, i.e. increased mucoadhesion.

Additionally, the work presented in Manuscript I, for the first time demonstrates the use and applicability of micro additive manufacturing for the fabrication of microcontainers with different designs. Discovered issues, which were associated with the fabrication procedure, such as the lack of a release process as facilitated by a PAA sacrificial layer in *SU-8* lithography of microcontainers, were subsequently resolved as part of the work presented in Manuscript II.

Moreover, the work described in Manuscript II and Manuscript III suggest a new fabrication scheme for batch processing of microcontainers based on additive manufacturing technology.

3.3 Additive Manufacturing

3.3.1 Overview of Additive Manufacturing Technologies

Additive manufacturing (AM), also often referred to as 3D printing (3DP) or Rapid Prototyping (RP), is the term for a set of manufacturing technologies in which a three-dimensional object is formed through the sequential additive deposition and conjunction of material, usually in a layer-by-layer procedure [93]. It has to be noted that the term 3DP in principle describes a specific AM technology, but is often used interchangeably with AM, presumably due to its connection to digital manufacturing and ease of use comparable with that of normal desktop inkjet printers [93,94]. Since AM is technically the most correct term and recommended by *ASTM International*, it is mostly used in this thesis. However, in the attached manuscripts, the term 3DP is used as it is better known. Also, RP is a term frequently used as a synonym for AM, although RP in principal describes any technology capable of producing accurate parts from computer models within a short time frame [95]. Albeit, AM technologies comprise most of the methods which are considered as RP [95].

AM substantially differs from subtractive manufacturing (SM), which has been a conventional type of manufacturing for many years. SM is a material removal process, meaning that material is successively removed from a block of bulk material to form the desired shape of an object. SM comprises machining technologies such as milling, turning, grinding and drilling. Although SM still represents the gold standard for the manufacturing of functional end-products, AM has several advantages over SM and is regarded as a technology with great potential for the use in various industry branches and fields of research [96–98].

One of the main advantages of AM, from a technical point of view, is the possibility to fabricate parts with high complexity. The layer-by-layer nature of AM drastically increases the design flexibility, since it removes the need for complicated fixtures, various tooling steps and allows the implementation of design elements that would not be physically reachable for the tool during manufacturing, when using conventional machining [98]. The possibility to realize complex geometries in turn enables the utilization of topology optimization approaches for further improvement of functionality [98]. Therefore, AM is considered to be a promising tool in the area of automotive and aerospace engineering as it can be employed to produce components with the best trade-off between light weight and high stiffness [99,100]. Furthermore, AM allows the one-step manufacturing of multi-component products, that otherwise would require further assembly steps [98]. Such products may even include

moving parts, and a prominent example, which is commonly used to illustrate the capability of AM in this regard, is the manufacturing of planetary gear bearings (Figure 15).

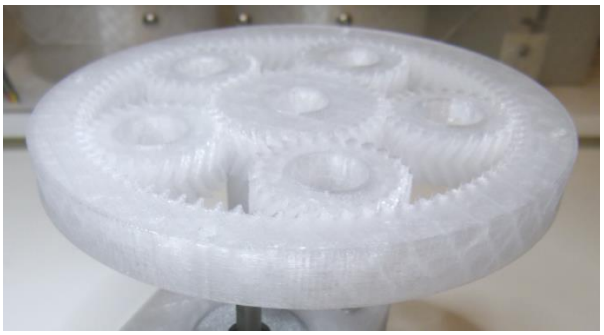

Figure 15 Additively manufactured functional planetary gear bearing. This part was fabricated as a single part and facilitated by the smaller gears, it is functioning as a rotating bearing. The part was used to construct a rotary autosampler as presented in Manuscript IV.

Although AM is far inferior to other conventional manufacturing techniques such as injection molding in terms of speed and throughput, its cost efficiency due to low-cost machinery and unnecessity of start-up tooling, makes it highly attractive for low volume production as it is often required in research and development and the production of spare parts [96,101]. Moreover, the cost efficiency and design flexibility renders AM an excellent choice for the manufacturing of mass-customized products as for example necessary in the medical sector. The hearing aid industry, in which the customization of shells is crucial for the performance of the product, has shifted exclusively to the use of AM and hence demonstrates that AM is the most economical solution for mass-customization [102]. Further examples include the manufacturing of dental appliances, implants and customized prosthetics [103,104].

In addition to its cost efficiency, the nature of AM, through reduced raw material usage, minimalizes waste and consequently increases environmental sustainability [96].

Another positive effect related to the emergence of AM technologies is an increased public accessibility due to the availability of low-cost machines [98]. Especially within the last decade many affordable machines entered the retail market and furthermore the *RepRap* project, which describes the development of a largely self-replicating AM machine, initiated in 2004, significantly boosted the maker movement [98,105,106]. Taken together, these effects empower people to realize engineering projects they would not have been able to realize before [106]. In a study, in which the implications of the *RepRap* project on private households is analyzed, it has been concluded that obtaining and maintaining a standard *RepRap* AM machine is already an “economically attractive investment” [107]. Therefore, the

emergence of AM is not only considered to have contributed to the democratization of technology but is also sometimes referred to as the "third industrial revolution" [96].

Apart from the industrial sectors already mentioned, AM is extensively employed in several areas of research, including electrochemistry, tissue engineering, microfluidics, medicine, drug delivery and customized labware [108].

The general process chain of AM can be broken down into four major steps. In the first step, a digital design of the object to be manufactured is composed using Computer Aided Design (CAD). The design is then converted into the *.STL* (STereo Lithograhy or Standard Tesselation Language)-file format, which is the standard file format for AM processes and contains geometric data in the form of triangulate meshes [97]. Using special processing software, the *.STL*-file is sliced into layers, i.e. the outer contour of the triangulate mesh is sequentially traced out in two dimensions along the vertical axis of the later deposited layers [98,109]. The sliced layers of the *.STL*-file in turn serve to create the machine code, which includes the information about specific actions that the machine will undertake in order to build the object [97]. Finally, the machine code is interpreted by the AM machine and the object is manufactured in a layer-by-layer process [110].

According to the standardization organization *ASTM International*, different AM technologies can be divided into seven categories [98,111]:

- Material extrusion

  e.g. *Fused Deposition Modelling* (FDM)
- Powder bed fusion

  e.g. *Selective Laser Sintering* (SLS), *Selective Laser Melting* (SLM)
- Vat photopolymerization

  Stereolithography (SL)
- Material jetting

  e.g. *Polyjet* and *Inkjet* printing techniques
- Binder jetting

  includes the technology referred to as *Three-Dimensional Printing* (3DP)
- Sheet lamination

  e.g. *Laminated Object Manufacturing* (LOM)
- Directed energy deposition

  e.g. *Electron Beam Welding* (EBW)

To review all of these categories would be beyond the scope of this work. Therefore, the next paragraphs will concentrate on technologies based on vat photopolymerization and material extrusion, which are both methods that were used in the process of the Ph.D. project.

SL represents the oldest AM technology and was developed and patented by Charles W. Hull, who then founded the company *3D Systems*, in 1986 [112]. SL is a direct laser writing technique in which a build platform, a motorized vertical stage (z-stage), a vat containing photo-reactive polymer, a *galvanometer mirror scanner* and a laser source are required (Figure 16) [97]. The laser beam, by the action of the galvanometer, is scanned at the interface between the build platform and the transparent bottom of the vat, thereby leading to a highly localized photocuring reaction of the photopolymer [113]. The incident laser beam promotes the reaction of photoinitiators with monomers that subsequentially polymerize and thus lead to a solidification of the material [113]. Depending on the type of photopolymer, the curing reaction is either based on free-radical photopolymerization (acrylate-based polymers) or on cationic photopolymerization (epoxy-based polymers) [113]. The scanning of the laser beam facilitates the creation of two-dimensional patterns of lines of solidified polymer. By vertically moving the build platform, a second layer of solidified polymer can be created. The movement basically corresponds to the thickness of the former solidified layer. The repetition of these procedures eventually leads to the incremental fabrication of a three-dimensional object, in a layer-by-layer fashion. The patterns created in each layer, thereby, reproduce the two-dimensional slices that were created during the *.STL*-file processing.

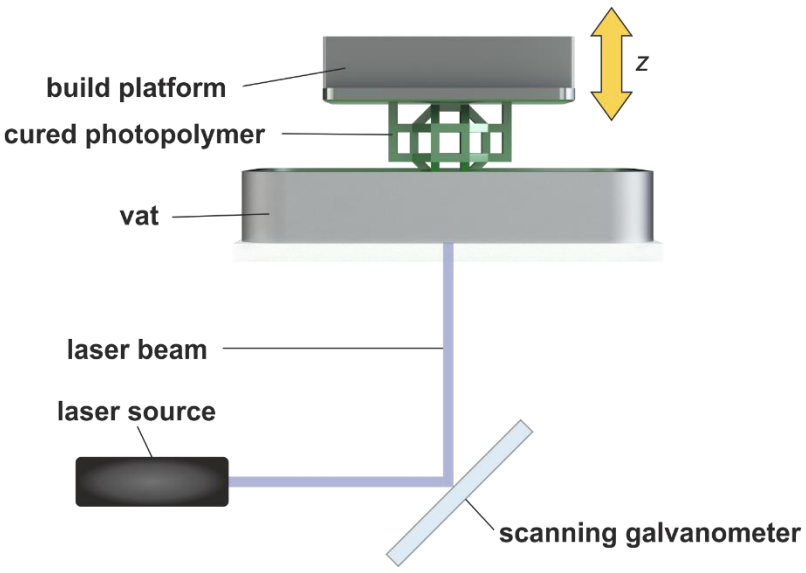

Figure 16 Working principle of Stereolithography (SL) Additive Manufacturing (AM).

A further vat photopolymerization-based AM technology is represented by *Digital Light Processing* (DLP)-SL, also referred to as *Mask Projection Stereolithography* (MPSL) [113]. The working principle of this technology is similar to that of SL, in the sense that a layer-by-layer photopolymerization procedure is used to create an object. However, in DLP-SL, a DLP projector serves to illuminate an entire image on the interface between build platform and transparent bottom of the vat, thereby replacing the laser beam (Figure 17). In this method, the solidified patterns of each layer are achieved with the use of a *digital micromirror device* (DMD), which is the core functional element of the DLP projector [114,115]. The DMD features an array of actuated and individually controllable micromirrors, which, when actuated, reflect the light coming from the light source [115]. The advantage of DLP-SL over traditional SL is mainly the manufacturing speed, as all patterns in a layer are cured simultaneously and not drawn out by a laser beam [97].

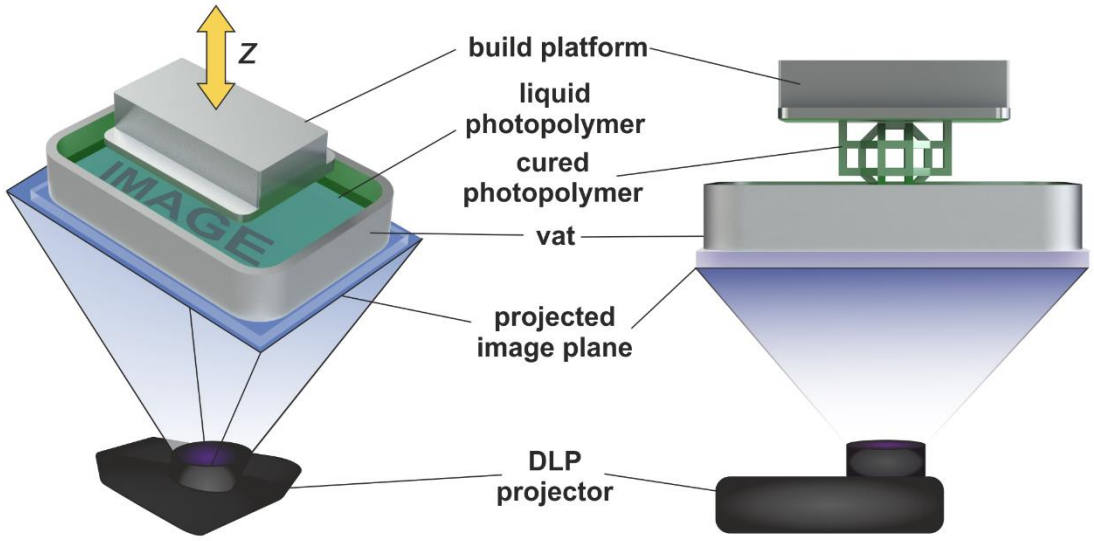

Figure 17 Working principle of Digital Light Processing (DLP)-Stereolithography (SL).

The lateral resolution of an SL system is defined by the position resolution of the scanning galvanometer and the laser spot size [93]. In case of DLP-SL systems, the lateral resolution is mainly depending on the pixel size or pixel density per area of the projected image (Figure 18) [115]. The vertical resolution, defined by the layer thickness, on the other hand, is restricted by the resolution of the linear stage system [93].

A special case of mask-based SL is *Continuous Liquid Interface Production* (CLIP)-SL, as it circumvents the traditional layer-by-layer approach through the formation of a *dead zone*, in which the photocuring reaction is inhibited [116]. The *dead zone* is achieved through the

creation of an oxygen gradient as a result of an oxygen-permeable bottom of the vat [116]. As a consequence, the production speed is only limited by the curing rate of the photopolymer and its viscosity, thus resulting in dramatically increased manufacturing speed [116].

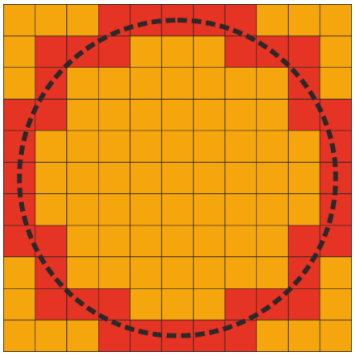

Figure 18 Resolution specification of DLP-SL. The resolution is dependent on the pixel size. When the designed feature meets the limit of the resolution capacity, the displayed image will deviate stronger from the feature as exemplified by a circle (dotted line) that becomes pixelated (red).

A further direct laser writing SL technique is *Two-Photon Polymerization* (2PP), which was first developed by Maruo and Kawata in 1998 [117]. In this technique, a femtosecond-pulsed laser beam is focused on a droplet of photopolymer (Figure 19a) [118]. For the photo-polymerization reaction via free-radical formation to take place, the photoinitiator requires the absorption of two photons at the same time [115]. The laser intensity and consequent photon density required to trigger this process is only high enough at the focal point of the beam, thus confining the polymerization to the focal point as well [118]. The technique is hence capable of achieving a spatial resolution below 100 nm and is apt of fabricating delicate structures at the microscale as exemplified by a micro-sized Eiffel Tower (Figure 19b) [118]. A further advantage of 2PP is the possibility to generate arbitrary geometries as the polymerization is not limited to a build surface [118].

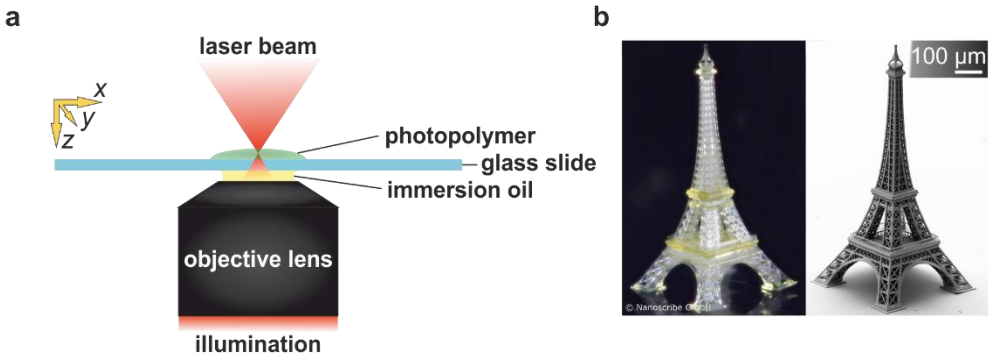

Figure 19 Two-photon-polymerization (2PP)-Stereolithography (SL). (a) Working principle of a 2PP SL instrument [118]*. (b) 2PP-SL fabricated Eiffel Tower. Reproduced with permission from Nanoscribe GmbH (© Nanoscribe GmbH).*

The most prominent AM technology within the material extrusion category is *Fused Deposition Modelling* (FDM), which is also often termed *Fused Filament Fabrication* (FFF). FDM was developed and patented by S. Scott Crump and the company *Stratasys* in 1992 [119]. Most of the commercially available AM machines are based on FDM and furthermore, due to their low cost, FDM is the most accessible AM technology for the general public. The beforementioned *RepRap* project is likewise focused on the development of FDM machines [105]. This technology has a fundamentally different working principle from the other hitherto mentioned AM methods and is based on the use of thermoplastic materials. In FDM, a thin filament, usually 1.75 or 3 mm in diameter, is inserted into an extruder unit, which is constituted of a feeding-mechanism and temperature control units (Figure 20) [97]. The feeding-mechanism usually consists of a tractor wheel assembly (*hobbed pulley* and *idler ball bearing*) [120]. The tractor wheel is mounted onto the shaft of a motor and through rotation of the tractor wheel as well as spatial restriction by the idler wheel, the filament is pushed into the temperature control unit, which in turn comprises a *cold end* and a *hot end* [121]. While the *hot end* is heated to the melting temperature of the polymeric filament, the *cold end* is constructed as a heat sink in order to confine the melting temperature to the *hot end* [121]. The pressure generated by the tractor wheel leads to the extrusion of molten plastic from a nozzle with a small orifice which is commonly in the size of 0.4 mm in diameter. Finally, the movement of the extruder unit relative to a build platform, facilitated by three linear stages, enables the layer-by-layer fabrication of a three-dimensional object.

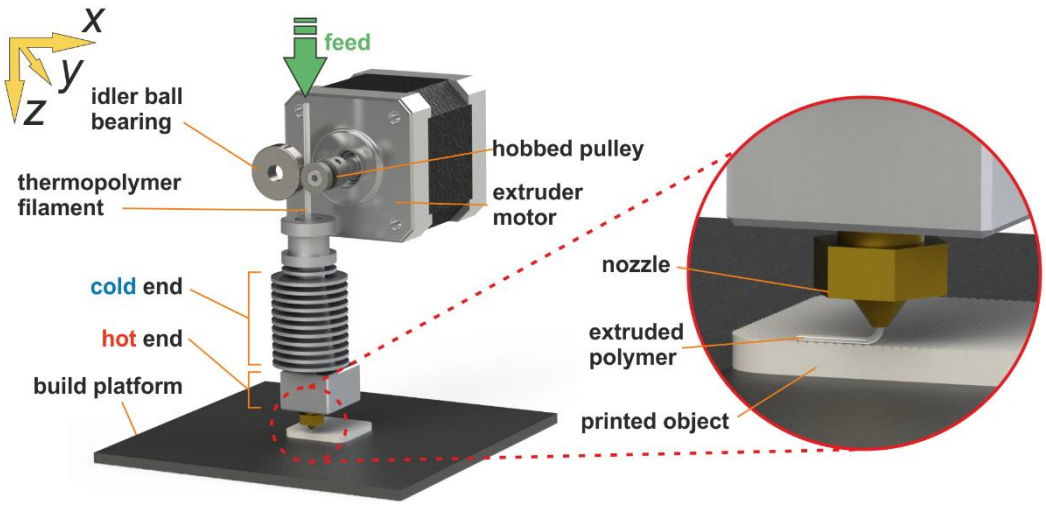

Figure 20 Working principle of Fused Deposition Modelling (FDM) Additive Manufacturing (AM).

As in case of SL and DLP-SL, the vertical resolution of FDM is basically limited by the resolution of the linear stage system. The lateral resolution of FDM is however limited by the size of the nozzle's orifice. As a consequence, the resolution properties of FDM is easily outcompeted by the resolution available in vat photopolymerization techniques.

Due to the high spatial resolution of 2PP, it represents the technology which is most promising for microfabrication purposes. However, 2PP bears certain drawbacks, which include the inability of fabricating larger objects (>1 mm) as well as the slow speed caused by the serial nature of direct laser writing [118]. As a compromise, DLP-SL was mainly chosen for microfabrication purposes within this work as it reveals a good trade-off between resolution and fabrication speed. While SL was tested and evaluated in the work presented in Manuscript I, DLP-SL was utilized for the work presented in Manuscript II and Manuscript III. FDM was used for the manufacturing of experimental setups and fixtures throughout the project, but mainly for the work described in Manuscript IV.

3.3.2 Additive Manufacturing in Oral Drug Delivery

The manufacturing flexibility and customization associated with AM drew attention not only in the areas of mechanical and manufacturing engineering, but also in the pharmaceutical sciences. AM enables the fabrication of solid oral dosage forms with alternative geometries, which cannot be produced by conventional powder compaction processes [122]. The tailoring of tablet geometry enables the creation of tablets with modified release kinetics. Goyanes et al. have shown that simply tuning the density of the *infill* patterns of FDM manufactured tablets can already yield products with different release kinetics [123]. They could further show that different three-dimensional geometries lead to different release patterns, probably due to a difference in surface area to volume ratio [124]. FDM enables the use of different materials, even at the same time. Using a dual-extrusion FDM setup, core-shell tablets from two different materials were fabricated, thus enabling gastric-resistant products with modified release kinetics based on varying shell thicknesses [125].

In addition, the customization suitability of AM has been suggested as a means to realize fully personalized dosage forms with tailored drug loading, including the loading of multiple drugs in one dosage form, which can be made widely accessible through on-site manufacturing and distribution [122].

While the low-cost availability of FDM systems is responsible for the fact that most experimentation on applications in ODD have been carried out with this technology, attempts have been made to utilize other techniques such as SL [122,126].

The design flexibility and RP capabilities of AM are well demonstrated in a recent work, in which FDM was employed in combination with other fabrication methods to construct a wirelessly communicating gastric-resident electronic device with drug-release modules [127]. Through the incorporation of sensor modules as well as drug-release modules into the ingestible device, automated feedback loops were enabled, thus leading to an increased potential for synchronicity between diagnostics and therapeutics [127].

In the work at hand, AM technology was explored as a potential tool to fabricate drug-carrying microdevices for ODD. The achievements of using AM for this purpose are presented in Manuscript I and Manuscript III.

3.4 Poly(vinyl alcohol)

Poly(vinyl alcohol) (PVA) was used as a sacrificial polymer substrate during vat photopolymerization-based AM in the context of the work presented in Manuscript II and Manuscript III. PVA is a polymeric compound that was first synthesized from *poly(vinyl esters)* by Herrmann and Haehnel in 1924 and published in 1927 [128,129]. It has the chemical formula $[CH_2CHOH-]_n$ and can exist with various degrees of polymerization and hydrolysis (Figure 21) [128].

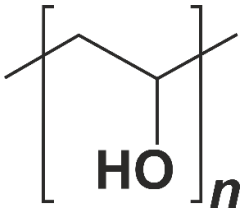

Figure 21 Structural formula of Poly(vinyl alcohol) (PVA) [128].

The primary motivation for using PVA for the presented work was due to its special properties. PVA is water-soluble but highly resistant to organic solvents and oil [128]. The solubility of PVA in water is highly dependent on the degree of polymerization and even more on the degree of hydrolysis as well as temperature [128]. PVA is a very robust material but can be easily processed owing to its water solubility and the fact that it behaves as a thermoplastic [128].

These properties have led to the early industrial exploitation of PVA as textile sizing starting from 1926 [128]. Industrial use was rapidly expanded e.g. within the production of paper and bank notes to improve smoothness, abrasion resistance, folding and bursting strength, as well as resistance against oil and solvents [128]. Due to strong adherence to cellulosic materials, such as paper and wood, PVA was utilized to produce adhesives [128]. Further applications of PVA include the production of packaging films due to good film-forming properties and low oxygen permeability. In optics, PVA is used for polarization, retardation, and filtration [128]. More recent applications encompass the application as sacrificial release layers in micromachining and the use as filament in FDM [130,131]. These applications are relying on the water-solubility of PVA. In FDM, PVA filament is commonly used to generate support structures for a simultaneously manufactured object, usually in a dual extrusion setup [131]. However, additively manufactured PVA constructs have also been utilized as sacrificial molding elements in the fabrication of microfluidic devices or cell scaffolds as well as biocompatible carrier material for customized oral dosage forms [122,132].

3.5 Surface Metrology

Surfaces are defined as the outermost layer of any object and therefore form the interface between the object and the outside. Surfaces can have a multitude of properties that influence the interaction with the outer world. Among those are physical interactions, which greatly depend on the three-dimensional surface texture, also known as surface finish. Surface metrology is the science of measuring the textures of surfaces. Surface properties are highly relevant in everyday life and industrial fabrication as they influence the aptitude of an object's desired functionality [133]. While this principle holds true irrespectively of scale, it has to be noted though that the importance of surface properties increases at smaller sizes due to a shift from inertial to elastic forces as dominating effects [133]. With respect to functionality, the surface structure of roads, for example, determines the friction and thus driving behavior of vehicles, and is finally also related to their fuel consumption [134,135]. On the other hand, the famous examples of lotus leaves and gecko feet demonstrate how micro- and nano-structuring can lead to functionalities of extreme hydrophobicity and adhesiveness, respectively [136,137].

The surface of an object may be tailored for a specific application. In this regard, it has been shown that for example surface roughening can positively affect the adhesive bond strength of cleavage joints [138]. Manuscript II describes the fabrication, characterization and use of PVA substrates as build surfaces in the application of vat photopolymerization-based AM. The surface of the PVA substrate interacts with the polymerization interface at the bottom of the vat as well as with the cured layers of photopolymer that are successively built on top of it. Consequently, the surface properties of the PVA substrate are crucial to the entire procedure. More specifically, the surface of the PVA substrate must be sufficiently flat to ensure uniform contact to the bottom of the vat and it must have a suitable texture for adherence of the cured photopolymer. To characterize the PVA substrates properly and to ensure repeatability of the procedure, relevant surface characteristics were studied.

The systematic definition of structural properties and parameters of surfaces and their measurement trace back to 1942 when Dr. Georg Schlesinger addressed the problem of lacking standardization of surface finishes and are meanwhile standardized by the *International Organization for Standardization* (ISO) in the standards catalogues for *geometrical product specification* (GPS) and *properties of surfaces* [139–141]. The following paragraphs give an overview and explanation of the relevant and used surface parameters.

Different techniques can be employed to measure surfaces. Among those are contact and non-contact methods, which are described more thoroughly in section 4.7. Data obtained from a measurement instrument can be two-dimensional (profile) or three-dimensional (areal), while the first can in turn be derived from the latter [142]. The untreated two-dimensional data is called a *primary profile*, whereas the untreated three-dimensional data in form of a digital surface representation is called an *extracted surface* [143,144]. For the characterization of PVA substrates, the *peak-to-valley flatness FLTt*, the *arithmetic mean height Sa* and the *developed interfacial area ratio* S_{dr} were determined. The meaning of these parameters can be clarified by considering a hypothetical *extracted surface* (Figure 22a).

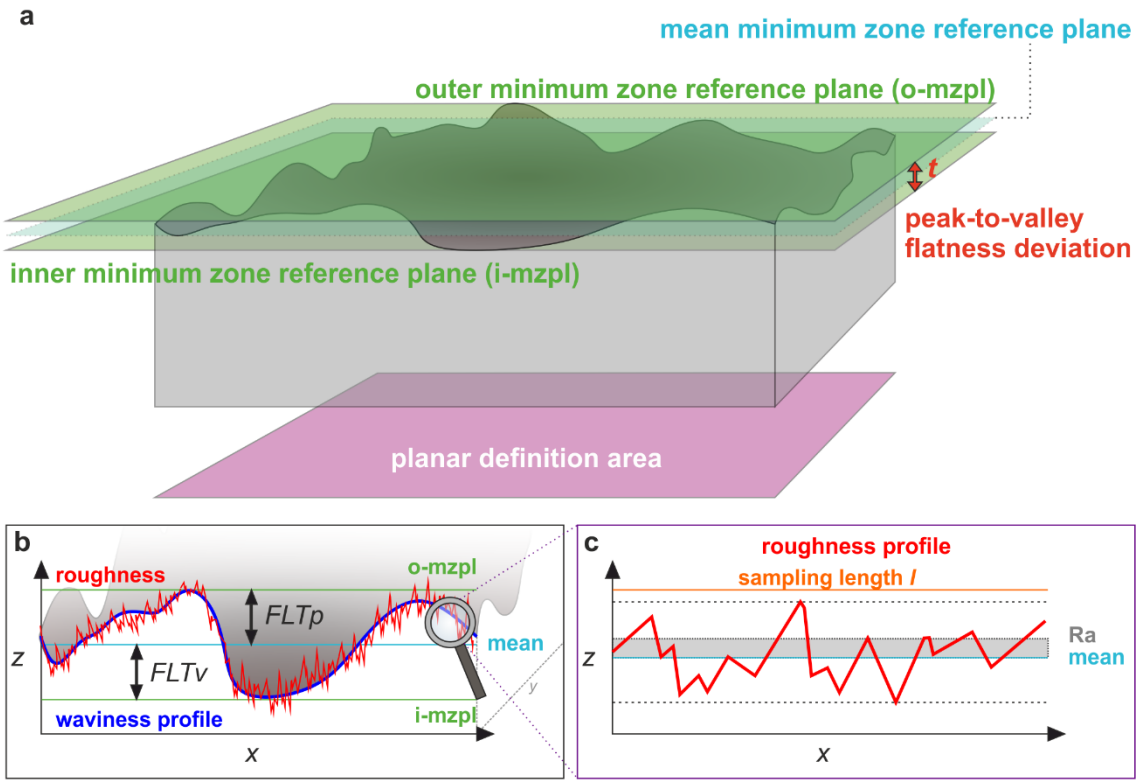

Figure 22 Properties of a surface. (a) 3D representation of extracted surface. (b) Close-up of 2D projection from extracted surface. (c) 2D roughness profile.

In contrast to a perfectly flat plane, the *extracted surface* is composed of peaks and valleys, which can be found at different scale-levels, i.e. the surface of a single peak is composed of smaller peaks and valleys. The ISO standard describes that for the analysis of flatness, reference planes are defined from which in turn the definition of the flatness parameter is derived. Two *minimum zone reference planes* (MZPLs) enclose the surface with the outer being coincident with the highest peak of the surface and the inner being coincident with the deepest valley. The *mean minimum zone reference plane* constitutes the arithmetic mean

plane of the MZPLs. *FLTt* is defined as the distance *t* between the two MZPLs or as the sum of the largest positive local flatness deviation *FLTp* and the absolute value of the largest negative local flatness deviation *FLTv* (Figure 22b, Equation 2) [144].

$$FLTt = FLTp + FLTv \qquad \textit{Equation 2}$$

When deriving a primary surface profile from a surface, the profile is composed of a combination of short- and long-wave deviations. Herein, the short-wave deviations represent the surface *roughness*, whereas the long-wave deviations represent *waviness* (Figure 22b) [145]. As recommended by ISO, these two properties are typically separated with use of a Gaussian profile filter that smoothens the profile by averaging the values of neighboring peaks within a specified filter cut-off length [143]. For the analysis and description of surface roughness, the profile parameter *Ra* is the most commonly used value [146]. *Ra* is defined as the arithmetic mean of the deviation of the absolute ordinate values *Z(x)* from the mean line for the roughness profile within a sampling length *l* (Figure 22, Equation 3) [143].

$$Ra = \frac{1}{l}\int_0^l |Z(x)|dx \qquad \textit{Equation 3}$$

The *Ra* value is a profile parameter, which means it is not applicable for areal surface data. The areal parameter *Sa* represents the adaption of the *Ra* value for areal surface roughness and extends the definition by implementation of the sampling area *A* (Equation 4) [147].

$$Sa = \frac{1}{A}\iint_A |Z(x,y)|dxdy \qquad \textit{Equation 4}$$

Due to the definition of *Sa*, surfaces with very different morphology and complexity can have similar *Sa* values [148]. One objective of measuring the surface roughness of PVA chips was to correlate the surface roughness with adhesive bond strength to additively manufactured objects. The S_{dr} value represents a measure of surface complexity and has been found to be a good indication of adhesive properties [149]. S_{dr} is defined as the ratio of the increment of the interfacial area of the surface within the planar definition area *A* over the planar definition area (Figure 22a, Equation 5) [147].

$$S_{dr} = \frac{1}{A}\left[\iint_A \left(\sqrt{\left[1 + \left(\frac{\partial z(x,y)}{\partial x}\right)^2 + \left(\frac{\partial z(x,y)}{\partial y}\right)^2\right]} - 1\right)dxdy\right] \qquad \textit{Equation 5}$$

3.6 Rapid Prototyping and Open Labware

The *Maker Movement* refers to a re-initiation of a technology-driven *do-it-yourself* (DIY) culture, which was promoted by the appearance of the magazine *Make* in 2005 and by subsequent *Maker Faires* taking place in different areas and countries [150]. The movement has led to the emergence of so-called *MakerSpaces*, alternatively *Hackerspaces* or *FabLabs*, in many places. *MakerSpaces* are laboratories/workshops that allow people to access working space and equipment that is often not easily accessible for individuals. The *Maker Movement* has been regarded for its potential positive impact on education and creativity. Hence, *MakerSpaces* can be frequently found in universities as well as companies [151]. The *Maker Movement* profited a lot from the emergence and development of *free and open-source software* (FOSS) and RP techniques as they allow for customized solutions, simple and cheap manufacturing of complex objects and the online-sharing of digital blueprints and codes [152]. RP is a collecting term for digital manufacturing technologies that enable fast iterations of digital design and direct fabrication of accurate parts before a significant investment in tooling processes is made [95]. The most abundant RP tools in *MakerSpaces* are FDM machines and CO_2 laser cutters [152]. The widespread use of FDM machines is probably due to increased and cheaper availability as a consequence of the *RepRap* project started by Adrian Bowyer in 2004 [105]. The *RepRap* project encompasses the development of various types of affordable FDM machines that are partly self-replicating as their construction includes the use of additively manufactured parts.

The *Maker Movement* did not only have impact on universities with regards to the provision of *MakerSpaces* but is also affecting the work in scientific research. The use of FOSS and RP technologies such as FDM, has given researchers the possibility to create customized scientific instrumentation and equipment at an extreme cost reduction [153,154]. RP has already enabled researchers to create several customized devices ranging from optical equipment to fluorescence microscopes and microsyringe autosamplers [155–157].

Manuscript IV describes the design and construction of a retention model setup for the evaluation of mucoadhesion. In accordance to the spirit of the *Maker Movement* as well as construction of open labware, the setup is fully replicable by use of FDM and CO_2 laser cutting. Furthermore, the control of the setup is based on the open-source microcontroller *Arduino* and all digital files for reproduction have been published online [158,159].

4 | Fabrication and Characterization Methods

4.1 Additive Manufacturing of Microcontainers

As mentioned in section 3.3.1, DLP-SL was mainly chosen as a manufacturing technology for the fabrication of microcontainers for ODD. The employed DLP-SL system had a lateral resolution of 30 µm and a vertical resolution of 25 µm. While several manufacturing constraints had to be considered, the resolution properties were one of them. Using *SU8*-photolithography, microcontainers with a size of 300 µm in diameter were fabricated. When taking the resolution properties of the employed DLP-SL system into account, it becomes apparent that this size range is at the very limit of the machine's capacity. This can be illustrated with use of Figure 18, in which the circle is corresponding to a diameter of 300 µm and the pixels to a size of 30 µm. With the DLP-SL system at hand, it was technically not feasible to fabricate microcontainers with a diameter of 300 µm. It was however possible to fabricate microcontainers with outer diameters starting from approximately 500 µm. Since no investigation of the effect of the size of microcontainers has been conducted up to this point, this constraint was largely considered to be irrelevant.

A further constraint was that the commercially obtained DLP-SL instrument did not offer the possibility of using exchangeable substrates and/or release layers. As the microcontainer concept and batch processing scheme rely on the formation of arrays of microcontainers, and the subsequent release of individual microcontainers intended for application, it was considered to be a necessity to resolve this constraint. As a solution, PVA sacrificial polymer substrates were used as a fabrication platform. In order to implement the use of PVA substrates into the fabrication procedure of the DLP-SL system, a customized holder was designed and manufactured. The next section provides further details about the latter.

In general, the fabrication of the microcontainers was conducted as it is generally the case in AM. Digital designs of microcontainers were exported as *.STL*-files, then positioned, sliced and converted into machine code with a proprietary processing software and finally loaded onto the machine, with which the fabrication procedure could be carried out. Afterwards, the uncured photopolymer was dissolved, and the fabricated structures exposed to UV light for post-curing.

Further information about the fabrication are given in Manuscript II and Manuscript III.

4.2 Design and Manufacturing of Customized Holder

Three different vacuum-actuated holders were designed and machined (Figure 23). The machining operations were mainly carried out by CNC milling. In case of the first design iteration (Figure 23a), the holder was designed to simultaneously hold three standard laboratory microscopy object slides as substrates. A channel connecting all cavities was connected to the laboratory vacuum line, while O-rings were used to seal the vacuum below the substrates, thus holding them in place. The holder was attached to a connecting piece belonging to the machine. This design iteration was abandoned in the process of the project, as it was designed for a different DLP-SL machine than the one that was finally used.

The second design iteration (Figure 23b) relies on the same ideas and in principle represents a functional holder for the employed DLP-SL machine. The substrate cavity was designed to fit substrates with dimensions corresponding to the large dicing pattern of silicon wafers in the batch processing of microcontainers (Figure 12). The design however had the drawback, that it required a leveling operation, which had to be carried out on the DLP-SL machine, thus limiting the use of build platforms on the machine to only this specific holder.

This issue was resolved with the design and manufacturing of the third holder iteration (Figure 23c). In this case, an integrated spring-leveling mechanism enabled the individual leveling of the holder to the bottom of the vat in the DLP-SL machine, thus allowing the holder to be used interchangeably with other build platforms. Another design improvement was that the substrate cavity was embedded in a detachable shim. Consequently, shims with different shapes and dimensions of cavities could be combined with the same holder.

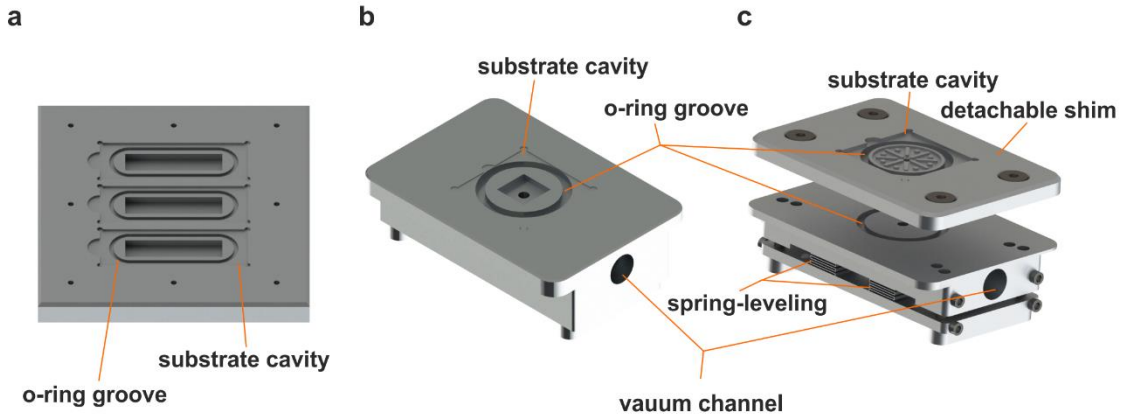

Figure 23 Design iterations of a customized vacuum-actuated substrate holder for a DLP-SL machine.

4.3 CNC Milling

In contrast to AM, subtractive manufacturing (SM) relies on the progressive removal of material to form the desired shape of an object. SM is one of the conventional ways of manufacturing and includes many different machining techniques, such as milling, turning or drilling. SM is suitable for a wide range of solid materials including metals, woods and polymers [160]. Milling refers to a technique in which a tool with sharp cutting edges is held in a spindle, which rotates at a defined frequency and moves into the work piece progressively to remove excessive material (Figure 24) [161,162]. The rotating tool is fed into the workpiece with the help of moving stages. In *computer numerical control* (CNC) milling, the path that a milling machine moves during operation is controlled by a computer that sends positioning commands to motors that are attached to the axes of the machine [163]. CNC milling machines typically have 3 axes but can also have 5 axes [160]. For CNC milling, typically a chain of three fundamental processes is required [160,163]. In the first step, a virtual design is created with *computer aided design* (CAD)-software. Then a *computer aided manufacturing* (CAM)-software serves to transform the virtual design into a sequence of commands (*G-code*) that encodes the movement of the milling machine. Finally, the *G-code* is interpreted by the CNC milling controller software and the object is machined.

In the work presented in Manuscript II, CNC milling was employed to machine different iterations of customized holders for build substrates in vat photopolymerization-based AM. It was further utilized to machine customized molds for compression molding.

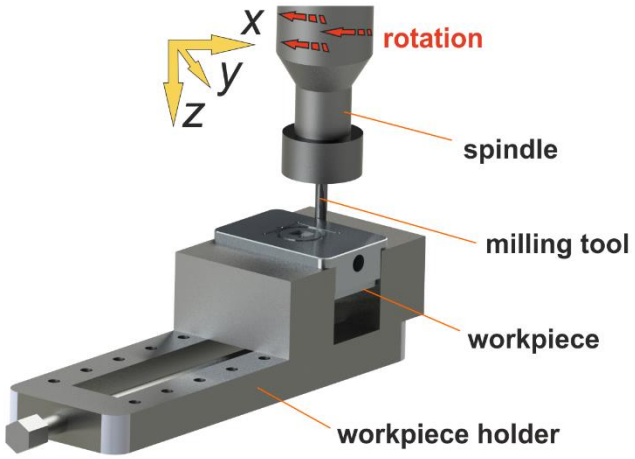

Figure 24 Working principle of Computer Numerical Control (CNC) milling.

4.4 CO_2 Laser Cutting

As mentioned in section 3.6, *CO_2* laser cutting is a rapid prototyping capable technology that is frequently utilized in *MakerSpaces*. In the work presented in Manuscript IV, *CO_2* laser cutting was used to fabricate parts for a fully replicable retention model setup.

CO_2 laser cutting is a method that can be used to cut or engrave various materials, which are usually in a sheet format. The working principle relies on the generation of a high intensity infrared laser that is focused on the workpiece through a lens, thereby creating a highly localized melt kerf in the material [164]. The molten material is forced out of the workpiece by a pressurized gas stream acting coaxially with the laser beam [164]. In a machine setup, the laser beam is guided by a sequence of mirrors to a head-unit, which is mounted on a movable stage system. By moving the laser beam across the workpiece via CNC, a cut geometry defined by the digital design is achieved (Figure 25).

Advantages of the *CO_2* laser cutting method include that it is a non-contact method (in contrast to e.g. machining), high resolution cuts (cutting kerfs within the micrometer range), digital manufacturing capability through CNC, high speed and highly localized melt induction, thus resulting in overall low thermal input to the workpiece [164].

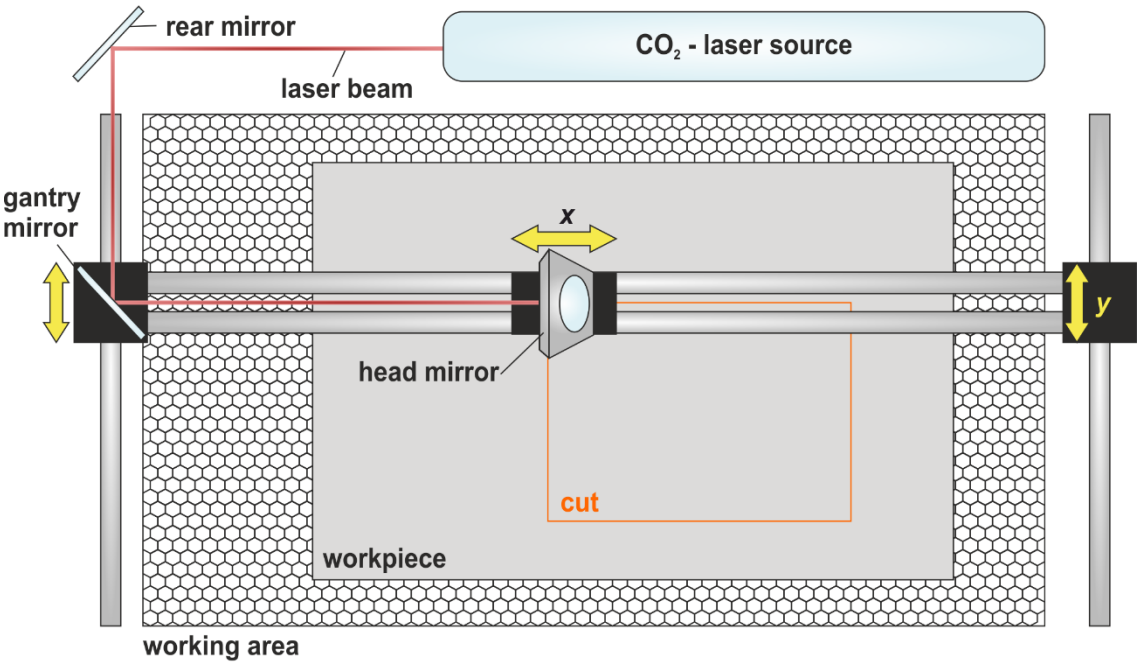

Figure 25 Working principle of CO_2 laser cutting.

4.5 Fabrication of Poly(vinyl alcohol) Sacrificial Release Substrates

The fabrication of PVA sacrificial release substrates, which were required for the work presented in Manuscript II and Manuscript III, was carried out by different means. The substrates mainly used for the studies were fabricated in a sequence of FDM and compression molding. First, a precursor substrate from PVA filament was manufactured by FDM. Employing a mold assembly, consisting of a mold, two thick aluminum foil sheets and two steel sheets, the precursor substrate was pressed flat and into its final dimensions with the use of a laboratory platen press (Figure 26). The mold was made by CNC milling and the dimensions of the substrate (cavity of the mold) were chosen according to the dimensions of the large dicing pattern of silicon wafers in the batch processing of microcontainers (Figure 12), in order to facilitate potentially required compatibility of AM-based fabrication of microcontainers with other processing methods as depicted in Figure 13. This method of PVA substrate fabrication is described in more detail in Manuscript II.

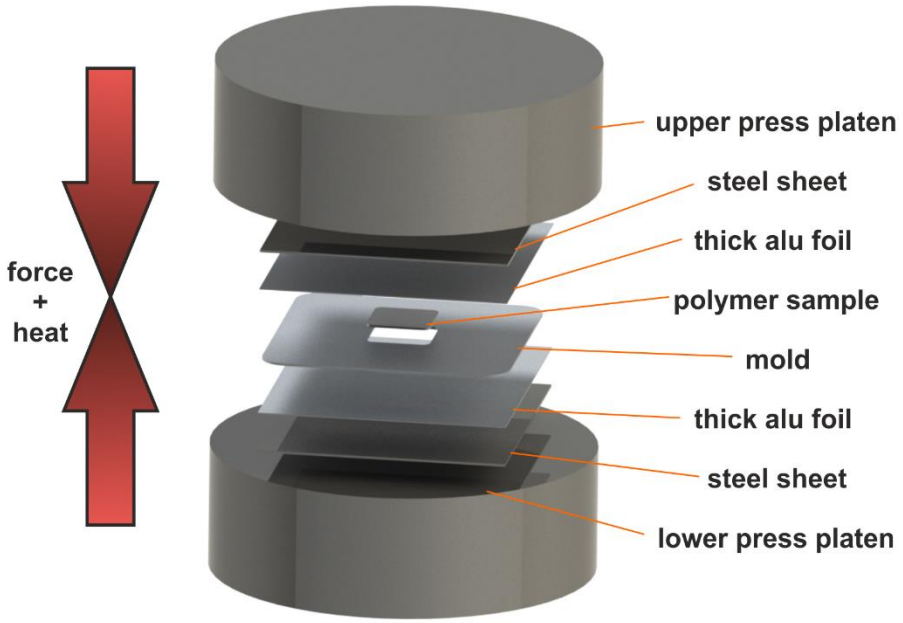

Figure 26 Compression molding of PVA substrates.

A further fabrication procedure that was explored for the production of PVA substrates was based on CO_2 laser cutting. Therein, a sheet of PVA was initially formed from PVA pellets in a compression step, similar to the one shown in Figure 26. Subsequently, a CO_2 laser cutter was employed to cut out the desired shape of the substrate. A drawback of this approach is the generation of toxic fumes due to thermal degradation of PVA during laser cutting [165].

In order to demonstrate the scalability of PVA substrate fabrication, injection molding was performed. Injection molding is the gold standard for high-throughput fabrication of thermoplastic components. There are several different types of injection molding technologies/machines, and the review of those is beyond the scope of this work. The conventional type of injection molding machines is the *reciprocating (single-stage) screw machine* (Figure 27) [166]. In this type of injection molding, the procedure can be briefly described as follows. Polymer pellets are filled into an *extruder barrel* through a *hopper*. The *extruder barrel* is heated to the melting temperature of the polymer, facilitated through the heating action of heater elements lining the outside of the *extruder barrel*. The screw, actuated by a *screw drive motor*, is rotating reciprocally, thus forcing molten polymer through a small channel (*sprue*) into the mold in a single stage (*shot*). Further, the tip of the screw is pushed towards the *sprue* to force plastic into the mold. As very high forces are required for the compaction procedure (*packing*), the *screw drive motor* often relies on hydraulic mechanisms. The mold consists of two pieces and one of them is mounted onto a movable platen (*clamping cylinder*), which during the molding procedure is tightly pressed against the other half. *Non-return valves* present at the mold-facing end of the *extruder barrel* prevent molten polymer from flowing back as a consequence of the high pressure. Finally, the linear retraction of the movable platen, which contains the second half of the mold, allows the ejection of the molded component. This procedure can be repeated many times on the order of minutes down to seconds, thus rendering injection molding unbeatable in terms of throughput [167].

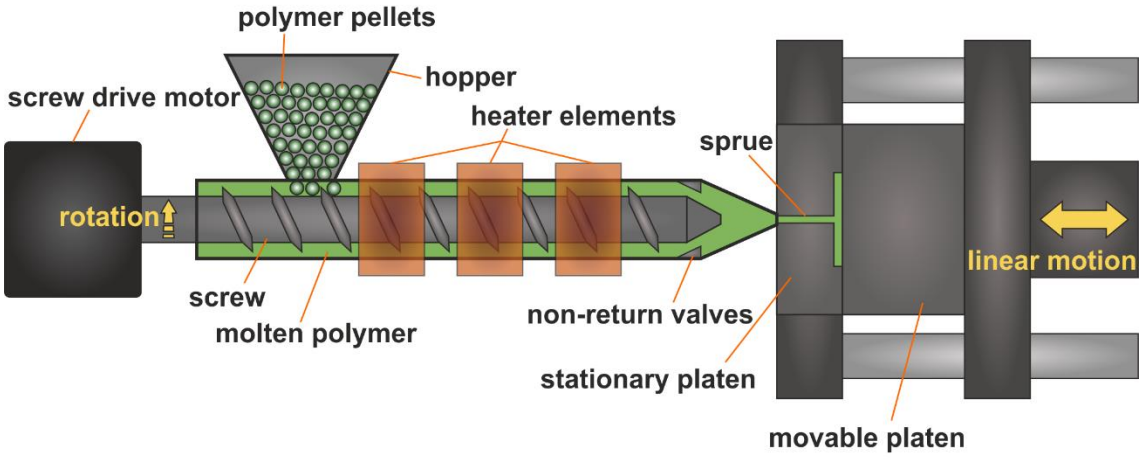

Figure 27 Working principle of injection molding.

4.6 Raman Spectroscopy

The *Raman effect* was independently discovered by Raman and Krishnan as well as Mandelstam and Landsberg in 1928 [168,169]. *Raman spectroscopy* in turn is based on the phenomenon of inelastic scattering of light (*Raman effect*) and is nowadays a standard laboratory procedure for the characterization of molecules. In Manuscript II, *Raman spectroscopy* was employed to determine so-called molecular fingerprints of different vat photopolymerization AM photopolymers in order to detect potential contamination with PVA. This served to evaluate the suitability of PVA as non-contaminating build substrate in DLP-SL.

Here, a brief overview about the working principle of *Raman spectroscopy* is provided (Figure 28a) [170,171]. In *Raman spectroscopy*, an incident light source, usually a laser, is used to illuminate a specimen. As a result, incident light particles (photons as per the wave-particle duality) can be scattered elastically or inelastically, meaning that their kinetic energy is either maintained or altered. The elastic scattering of photons, called *Rayleigh scattering*, accounts for the majority of scattered photons [170]. The *Raman effect* however relies on inelastically scattered photons that exist in two configurations: *Stokes*- and *anti-Stokes* scattering. For both configurations, the incident photons are energetically shifted as a consequence of interaction with the intermolecular vibrational modes present in the specimen. And this energetical shift of the scattered photon is associated with the energy of the intermolecular vibrational mode. In this way, the *Raman effect* provides molecule specific information (fingerprints) about the specimen through the study of vibrational modes [171]. Due to the superimposed *Rayleigh* scattering, *Raman* scattering is a weak effect that is very dependent on proper instrumentation. In current *Raman spectroscopes*, special *Rayleigh filters* (*notch filters*) are used to prevent *Rayleigh*-scattered light from entering the detector composed of spectrograph and *charge-coupled device* (CCD) [170].

The nature of the *Raman effect* can be further explained with a simplified *Jablonski diagram* (Figure 28b). Upon interaction of an incident photon with a molecule, the molecule is excited to a higher virtual energy state. In case of elastic *Rayleigh* scattering, the molecule returns to the ground energy state, and in *Stokes Raman* scattering the molecule returns to an excited vibrational state. In *anti-Stokes Raman* scattering, the molecule with an initial excited vibrational energy state undergoes relaxation from virtual state to its ground energy state [171].

Since Raman spectroscopy relies on the vibrational states of a molecule, it is highly specific and thus obtained *Raman* spectra can be utilized to derive molecular fingerprints [171]. Consequently, *Raman spectroscopy* was used in Manuscript II to determine a molecular fingerprint of a control specimen to which a potentially contaminated specimen was compared.

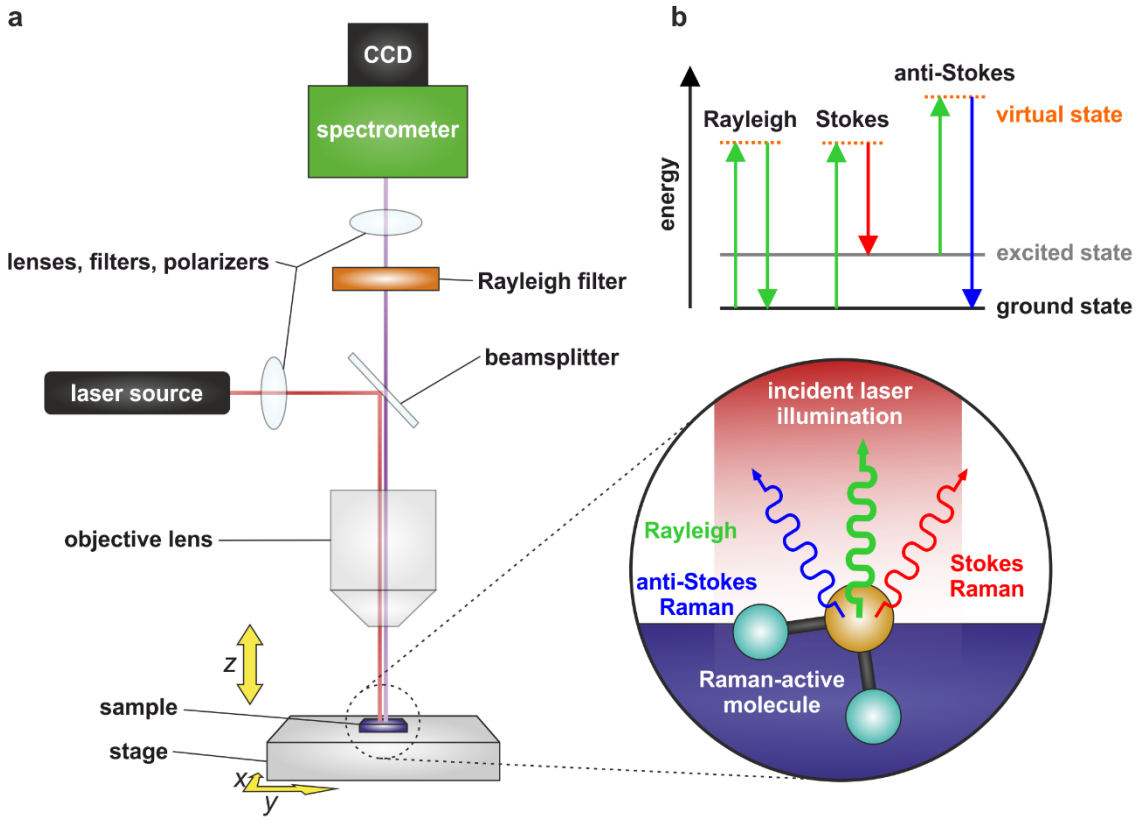

Figure 28 Working principle of Raman spectroscopy [170,171]. *(a) Typical setup of a Raman spectroscope and differentiation of scattered light. (b) Jablonski diagram of molecular energy states of elastically (Rayleigh) and inelastically (Stokes-Raman and anti-Stokes Raman) scattered light* [172].

4.7 Surface Profilometry

The measurement of surfaces is usually conducted with contact or non-contact techniques. The contact method is based on the use of stylus profilometer instruments and represents the traditional and commonly used technique (Figure 29a) [142]. A stylus profilometer consists of a drive unit with a stylus that has a diamond tip of specific shape and size, a base on which the specimen is mounted, a column on which the drive unit is mounted and moving stages [142]. During measurement, the diamond tip of the stylus is dragged along the specimen's surface and through a transducer the physical movement is converted into an electrical signal, which can be recorded and visualized.

In case of non-contact techniques, most often optical methods are used. For the surface characterization of PVA substrates in Manuscript II, two different optical profilometry techniques were used: confocal and (vertical scanning) interferometry-based profilometry (Figure 29b, c). Current optical techniques can be divided into two main categories, namely scanning optical techniques that include confocal profilometry and areal optical techniques that include interferometry [142]. Scanning optical profilometry is similar to stylus profilometry in the way that a beam of light is scanning the surface and thereby measuring the actual surface topography [142]. Areal optical profilometry, on the contrary, derives the surface topography from measuring the distribution of reflected light [142].

In confocal optical profilometry (Figure 29b), two special optical elements termed pinholes are used to filter light coming from the illumination source (usually a laser) and light entering the detector [142]. The pinhole causes a smaller field of view, thus enhancing lateral resolution of the system [173]. Furthermore, the pinhole restricts light that comes from out of the focal plane from entering the detector. Consequently, elements which are out of the focal plane have a low intensity [173]. Information on the texture of a surface is determined by performing vertical scans. This means that the focal plane moves vertically at the surface, thus leading to an intensity profile where the maximum intensity at a specific focal plane corresponds to the height of the surface [173]. Thereby, a surface texture representation is recorded in a layer-by-layer fashion.

In interferometry-based profilometry (Figure 29c), a reference light path is generated additionally to the light path going to and coming from the specimen [174]. A beam splitter serves to separate the incident light into a path going towards the specimen and a path going

towards a reference mirror at a specified distance. The reference mirror reflects the light, which is then led back to the beam splitter to be combined with the light reflected from the specimen. When the combination of both light paths then enters a camera sensor, an interference fringe pattern, which corresponds to areas of equal surface height, is recorded [175]. The sensor measures the light intensity pixel by pixel and thereby a difference between reference path length and specimen path length can be precisely determined [175]. Through further calculations a surface topography can be recreated from the measurements.

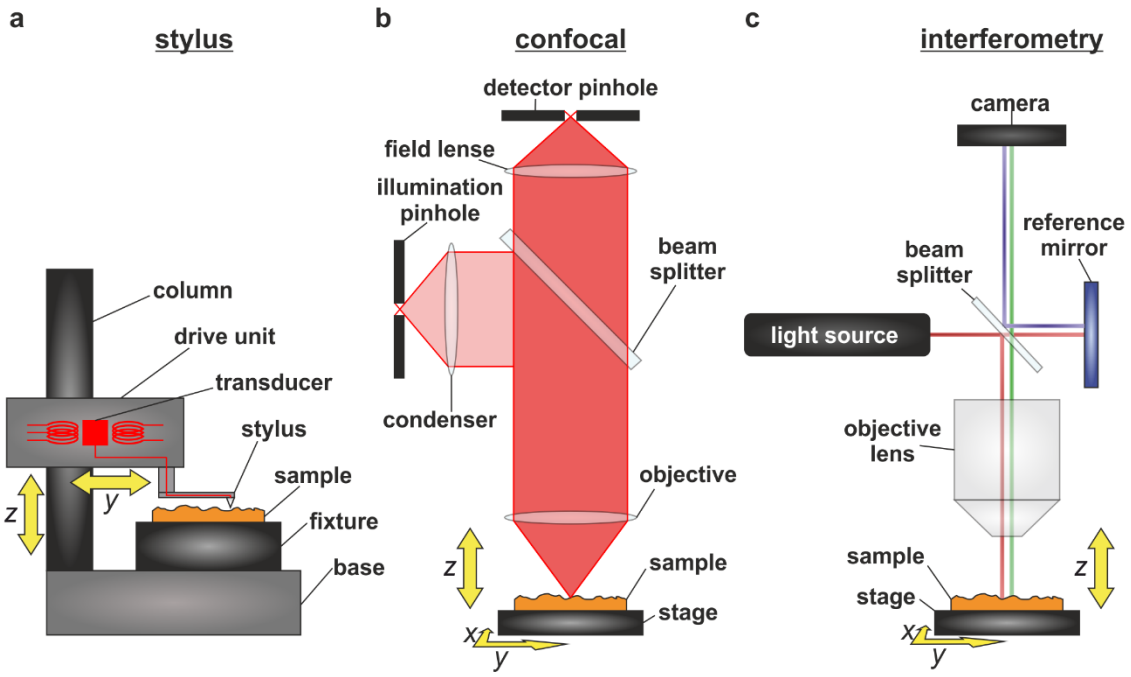

Figure 29 Working principles of different surface profilometry techniques. (a) Stylus profilometer [142]*, (b) confocal optical profilometer* [142]*, (c) interferometry optical profilometer* [174].

For the surface characterization of PVA substrates, as described in Manuscript II, optical profilometry was preferred over stylus profilometry as the stylus can damage the relatively soft polymeric surface of the PVA substrate during the measurement and thus lead to the recording of false data [142]. Other advantages of optical profilometry include increased vertical resolution and high scanning speed [142]. Among the optical profilometry techniques, different methods have different advantages and disadvantages. Phase-shifting interferometry for example has a vertical resolution within the nanometer range, however it is only suitable for smooth surfaces with an *Ra* or *Sa* value one tenth of the incident light wavelength [142]. Since the performed experiments included the surface characterization of substrates with varying degrees of surface roughness, both confocal and interferometry optical profilometry were used.

4.8 Scanning Electron Microscopy

SEM is a technique that, in contrast to a light source and optical lenses in optical microscopy, employs an electron beam and electromagnetic lenses for microscopy with high resolution beyond the *Abbe* diffraction limit of light [176]. In a SEM instrument, an arrangement of an *electron gun*, an *anode*, *condenser lenses*, an *objective lens*, *scanning deflector coils* and various detectors is used to produce an incident electron beam on a specimen and to detect various thereby produced signals (Figure 30) [176]. In the *electron gun*, an electron source, which can either be *tungsten hairpin*, *lanthanum hexaboride* or *field emission cathodes* (the latter is commonly used in modern instruments), is set under high voltage with reference to the *anode*, so that a beam of electrons towards the *anode* is generated [176]. The generated beam of electrons passes through the *anode*, and electromagnetic *condenser lenses* serve to converge, collimate and demagnify the electron beam, while an *objective lens* focusses the beam on the specimen and provides further demagnification [176,177]. *Scanning deflector coils* are used to scan the focused electron beam over an area of the specimen. The deflectors are computer-controlled and along with the employed detector fundamental for obtaining a scanned image.

As the incident electron beam impinges upon the specimen's surface, different signals are produced (Figure 30). Similar to the *Raman effect*, the incident source can interact with the atoms of the specimen, elastically or inelastically.

In the case of elastic interaction, the primary beam electrons collide with the nuclei of specimen atoms which causes them to bounce back, while retaining most of the energy [176]. These electrons are called *backscattered electrons* (BSE). BSEs have a certain escape depth, which is depending on the chemical composition of the specimen [176]. Therefore, the imaging of BSEs is mainly used to obtain information about the composition of a specimen.

In case of inelastic interaction, the primary beam electrons lead to a transfer of their energy to the specimen atoms and cause potential expulsion of one electron from the specimen's atom, thereby causing ionization [177]. The expelled electron has a low energy (below 50 eV) and is called a *secondary electron* (SE) [177]. Due to their low energy status, SEs have a low escape depth from the specimen. As a consequence, the imaging of SEs gives topographic information of the specimen with high resolution [176].

While BSEs and SEs are signals generally used to create an image of the specimen, further signals can be detected and interpreted for more detailed analysis of the chemical composition of the specimen. In the event of inelastic interaction between a primary beam electron and a specimen atom, similar as in the case of SEs, transfer of energy can lead to expulsion of an electron from an inner shell of the specimen's atom. If the vacancy created by the omitted electron is filled by an electron with higher energy level from an outer shell of the specimen's atom, the released energy results in the emission of an *X-ray characteristic* or an *Auger electron* [176,177]. While *Auger electrons* have low energy and an accordingly low escape depths, *X-ray characteristics* have higher energy as well as higher escape depths [176]. These phenomena are utilized in *Auger electron spectroscopy* and *energy-dispersive X-ray spectroscopy* to analyze the chemical composition of specimens.

For the analysis of additively manufactured specimens as presented in Manuscript I, Manuscript II and Manuscript III, information about the chemical composition was regarded as irrelevant as the study focused on the analysis of surface topography. Therefore, all the conducted SEM was performed using the SE detector.

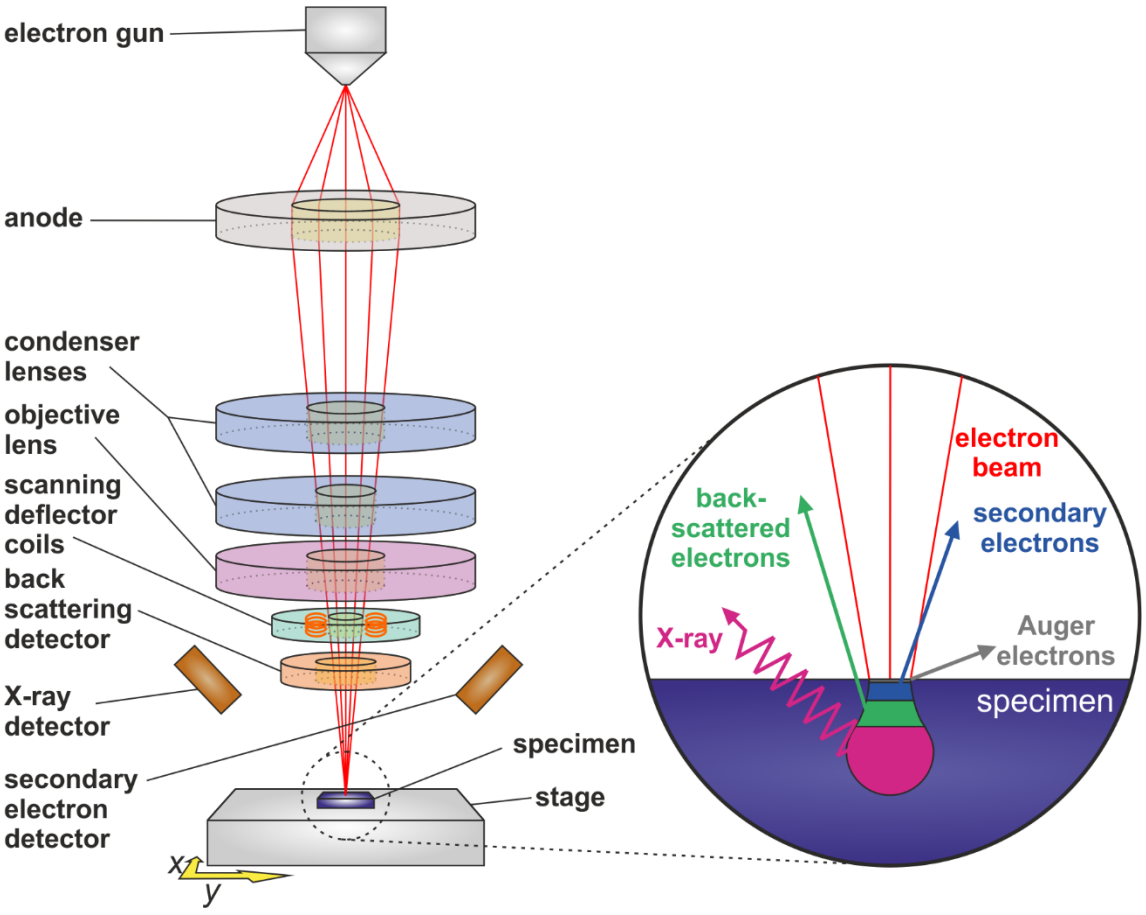

Figure 30 Working principle of scanning electron microscopy (SEM) [176].

4.9 Measurement of Detachment Forces

To measure the adhesive bond strength of small additively manufactured objects to PVA substrates (Manuscript II), a *Texture Analyzer* (TA) instrument was employed. In a TA instrument, a *probe holder* is connected to a force sensor, also called *load cell*, which in turn is placed inside a holding platform that can move vertically through the action of a motorized linear stage system (Figure 31a). To facilitate the measurements, a customized experimental setup was established. A manual two-axes horizontal micro-positioning system was mounted on the bottom of the TA instrument and a customized lab syringe holder was designed and additively manufactured with FDM technology. A standard 10 ml lab syringe equipped with a 600 µm injection needle was assembled to the holder and the assembly was, in turn, mounted to the TA probe holder. The tip of the needle was bent to a 90-degree angle so that it could be inserted into the cavity of the test objects using the positioner.

The measurement of the adhesive bond strengths was carried out indirectly via determination of the detachment forces, which were required to separate the adhesive bonds. Upon start of the experimental sequence, the probe holder was raised, and the applied force was measured and recorded in a force displacement graph, in which the force is plotted against the travel distance of the probe (Figure 31b). After breakage of the bond, the measured force dropped to zero and the probe holder was eventually moved back to its initial position. The two values extracted from the obtained graph was the *maximum peak force* as well as the *Work Of Adhesion* (WOA), which corresponds to the *Area Under the Curve* (AUC) of the graph.

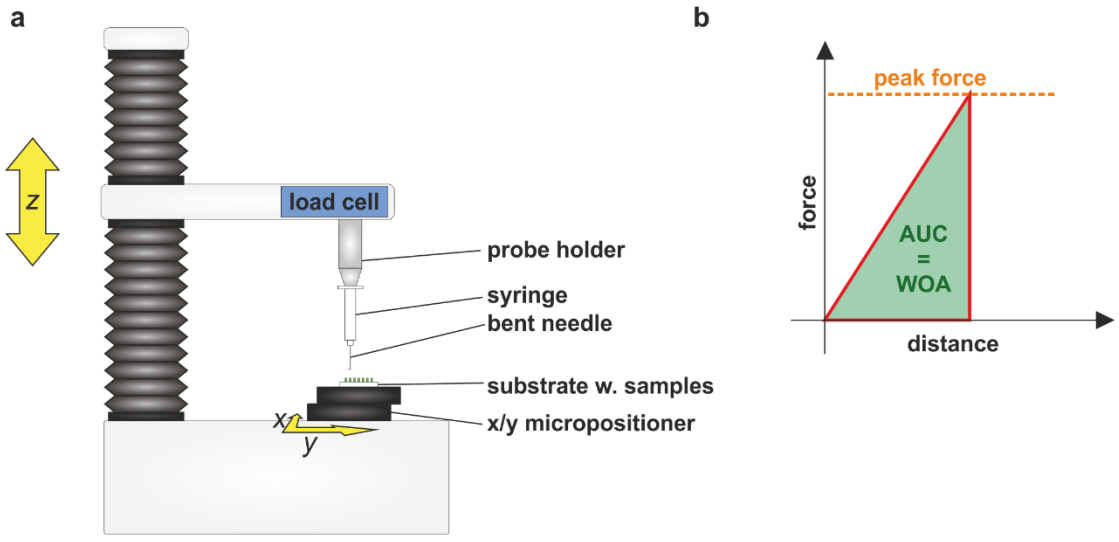

Figure 31 Detachment force determination using a Texture Analyzer (TA). (a) Customized TA setup, (b) Force displacement graph (AUC = area under the curve, WOA = work of adhesion).

4.10 Mucoadhesion Measurements

As part of the work presented in Manuscript III, two different mucoadhesion tests were conducted in order to evaluate the mucoadhesive potential of additively manufactured reservoir devices for ODD. The two methods are described within the next sections.

4.10.1 Tensile Mucoadhesion Measurements

The tensile mucoadhesion test method is usually conducted with the use of a TA instrument and is based on the measurement of detachment forces [49]. A TA is an instrument in which a *probe holder* is attached to a vertical linear stage system (Figure 32a). On the one end, the *probe holder* is connected to a *load cell*, which is embedded into a holding platform, and on the other end, the *probe holder* is connected to an exchangeable *probe*, to which in turn any kind of specimen may be attached. To measure the detachment force required to separate a mucoadhesive bond, a special *tissue holder*, fixing a piece of excised mucosal tissue, is placed below the probe and specimen and thereafter the specimen is lowered towards and moved into the tissue at a specific velocity (*pre-test speed*). When the specimen is touching the tissue, a pre-determined force (*contact force*) is applied for a specified amount of time (*contact time*), and then the probe with the specimen is lifted from the tissue in a certain velocity (*post-test speed*) and the force is being measured. In this kind of setup, the tissue may also be fixed to the probe and the specimen to the holder at the bottom [49].

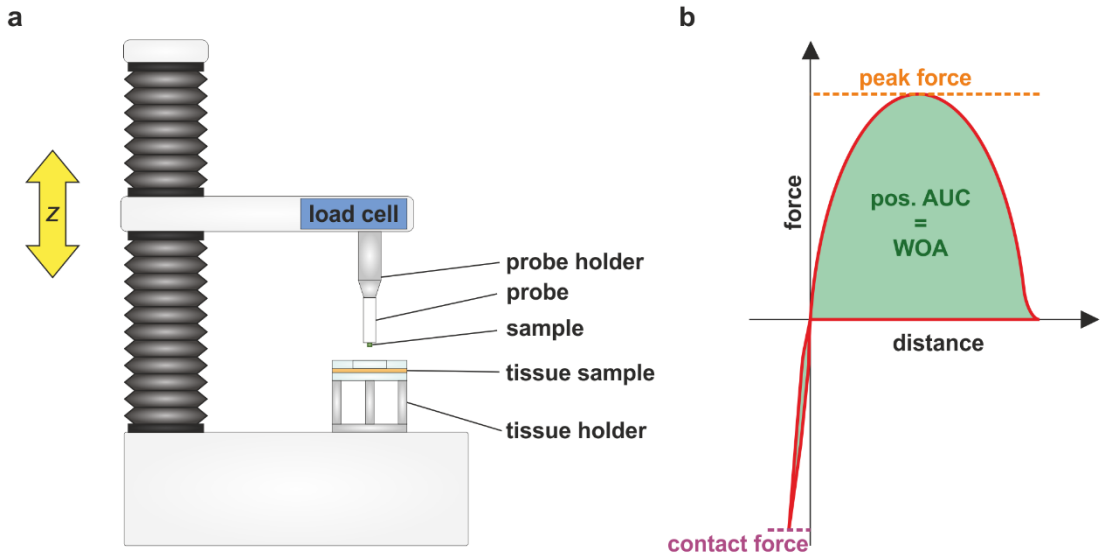

Figure 32 Determination of mucoadhesive forces using a Texture Analyzer (TA). (a) TA setup with mucoadhesion rig. (b) Force displacement graph of detachment (AUC = area under the curve and WOA = work of adhesion).

The recording of the force throughout the experiment yields a force displacement graph (Figure 32b). As the probe moves down to press the specimen against the mucosal tissue, the applied force as well as the displacement (measured as distance) become negative values. When the probe lifts the specimen, the force and displacement first return to zero, but then become positive values. As soon as the adhesive bond is broken, the measured force will drop to zero and after reaching a specified distance, the probe will return to the initial position. From the force displacement graph usually two values are obtained, the *maximum peak force* and the WOA, which is defined as the positive AUC.

Tensile mucoadhesion measurements are a suitable method to compare the relative mucoadhesion of specimens, although tensile detachments are thought to be of little physiological relevance [178]. Tensile forces might however act in the physiological environment of the GI tract, presumably due to the occurrence of circular contractions. In order to mimic these phenomena, contact forces equivalent to reported values of intestinal circular contraction forces (10 g) were used in the experiments [179].

In some reported experimental approaches, the entire tissue is immersed in a buffer solution, in others it is not [180,181]. In this work, the objective was to measure the mucoadhesion of additively manufactured reservoir devices with surface area-increasing structures. The main interaction between the specimens and the mucus was therefore expected to be in accordance with the *mechanical theory* of mucoadhesion [18]. Since the viscosity of mucus is highly dependent on its water content, it was assumed that immersing the tissue in a buffer solution will lead to full hydration of the mucus and subsequently the lowest viscosity [37]. As a result, the adhesion between the specimen and the mucus might be decreased. Moreover, full hydration of the mucus might not represent the physiological status as mucus hydration is believed to be highly regulated [37]. For this reason, the experiments were performed with tissue as it was obtained from the sacrificed animals and without immersing the mucosal tissue in buffer solution. Finally, the experiments were performed in a *Latin square* experimental design, in which the sequence of tested specimens was chosen as a blocking factor, thus potentially counteracting any influence caused by mucus dehydration.

4.10.2 Flow Retention Method for Evaluation of Mucoadhesion

In addition to tensile mucoadhesion measurements, the flow retention method was employed to evaluate the mucoadhesiveness of different designs of additively manufactured reservoir devices for ODD. The method was developed by Rao and Buri in 1989 and is based on the action of shear forces induced by a flow of liquid, thus realistically mimicking the physiological conditions of several mucosal tissues, including the intestinal mucosa [20,49]. In a typical flow retention measurement, specimens (e.g. microparticles [20]) are applied to the surface of a segment of excised mucosal tissue, which is placed on a specific holder that in turn is held in an inclined position. The specimens are then subjected to a flow of buffer solution at a specific flowrate and for a specific amount of time and finally the remaining specimens on the tissue are quantified [20]. Since specimens that are more mucoadhesive will require higher shear forces to be flushed away, the quantity of remaining specimens is interpreted as an indicator for mucoadhesiveness.

In order to perform this type of experiment, a setup needed to be constructed. Several parts were designed and additively manufactured with FDM and subsequently combined with an optical breadboard, a square aluminum tube, a peristaltic pump tubing and a peristaltic pump to form the required setup (Figure 33). The constructed setup had the advantage that it was portable, that all pieces fit precisely together, and that an angle scale was implemented in the design of the *slide* and the *slide holder*, thus enabling a reproducible as well as precise inclination of the *slide*. A detailed description of how the experiment was performed is provided in Manuscript III.

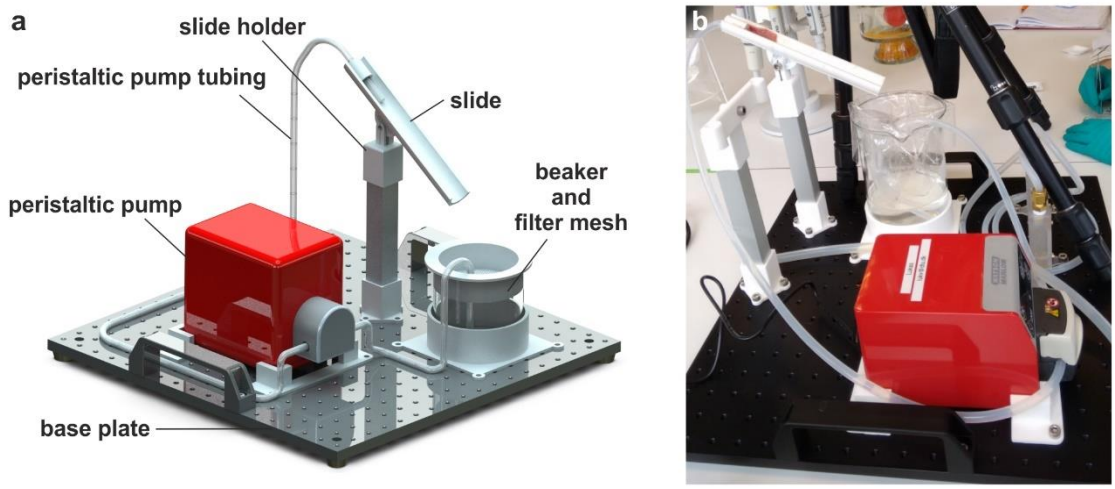

Figure 33 First design iteration of retention model setup with FDM-fabricated parts. (a) CAD model, (b) photograph of constructed experimental setup.

Although not utilized for the characterization of reservoir devices for ODD, an improved second version of the experimental flow retention setup was designed and constructed (Figure 34). The setup was, in principle, based on the same core elements as the first version, however it incorporated several beneficial features. Using aluminum extrusions and acrylic sheets, a chamber was constructed around the *slide*, in which an infrared ceramic heat lamp as well as a custom-designed humidifier and several ventilation fans were placed. The humidifier, the heat lamp and the fans were connected to an *Arduino Uno* microcontroller, which by execution of a custom-developed program, served to maintain a feedback-loop for temperature and humidity control. The regulation of external factors, such as temperature and humidity, is considered to be of high importance for increasing the reproducibility and physiological relevance of the flow retention method [49]. A further addition to the setup was a custom-designed and FDM fabricated manual, but remotely controlled, rotational sampler. The rotational motion of the sampler was actuated through a manually-driven syringe pump and a hydraulic translated *slider-crank mechanism*. The motivation for adding the sampler was to create the possibility to take samples of perfusate coming from the mucosal tissue, without the necessity of opening the climate-controlled chamber as it would lead to a disturbance in temperature and humidity continuity. The collection of perfusate samples is especially of interest when the mucoadhesive specimens on the tissue contain components of which the concentration can be measured, e.g. drugs, dies or polymers. Using spectroscopy or chromatography-based methods, the quantity of lost components can be determined [49].

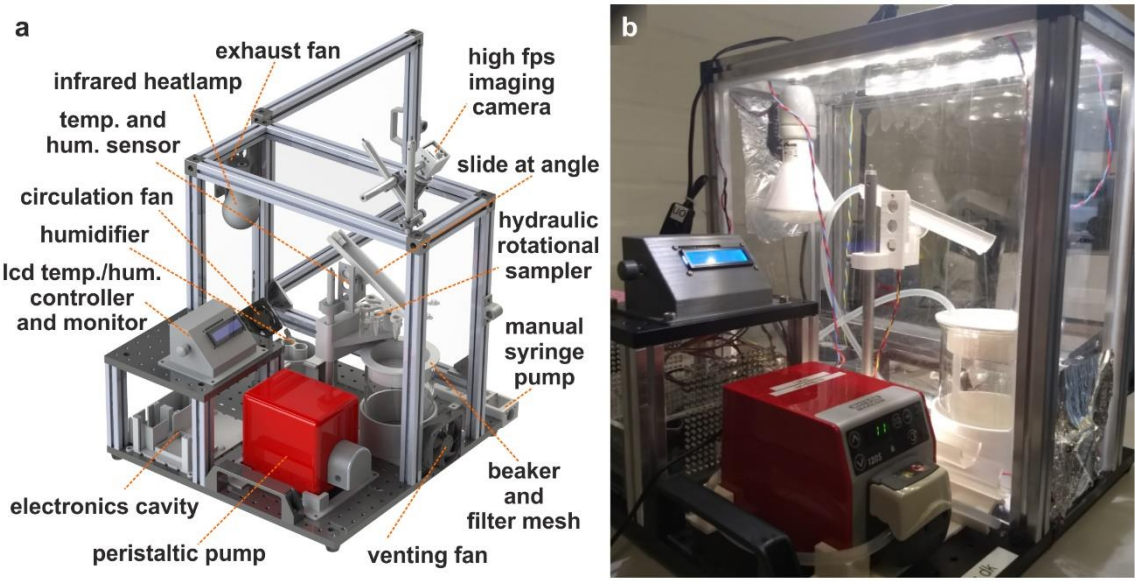

Figure 34 Second design iteration of retention model setup with FDM-fabricated parts, temperature and humidity-controlled chamber and manually controlled rotational sampler. (a) CAD model, (b) photograph of constructed setup.

Outgoing from the experiences made during the design and construction process of the two versions of flow retention model setups, it became apparent that the construction of such setups is usually not explicitly documented, and that replication of the efforts made by other researchers is often impossible as they often include parts, which are not easy to source, and improvised solutions. Both presented versions, up to this point, can, in principle, be completely replicated as they consist of FDM-fabricated parts, standard optical hardware and a limited amount of other easy to source parts. However, they are not very cost-efficient due to the high cost of optical hardware and the second version is, additionally to that, also rather heavy, thus impeding the idea of a versatile setup.

Inspired by the idea of open labware, which is introduced in section 3.6, the idea was to design and construct a third version of the flow retention model setup, which would be easy to replicate as most of the parts are made by RP technologies, is light in weight, and which is very versatile as it includes further useful functionalities (Figure 35). These functionalities are based on a fully automated control circuit with integrated peristaltic pump and motorized rotational autosampler.

Manuscript IV describes the work in detail and includes complete build instructions, so that other researchers will be enabled to fully replicate this flow retention model setup and build upon it. To facilitate this process, all required design files and codes are published online [159].

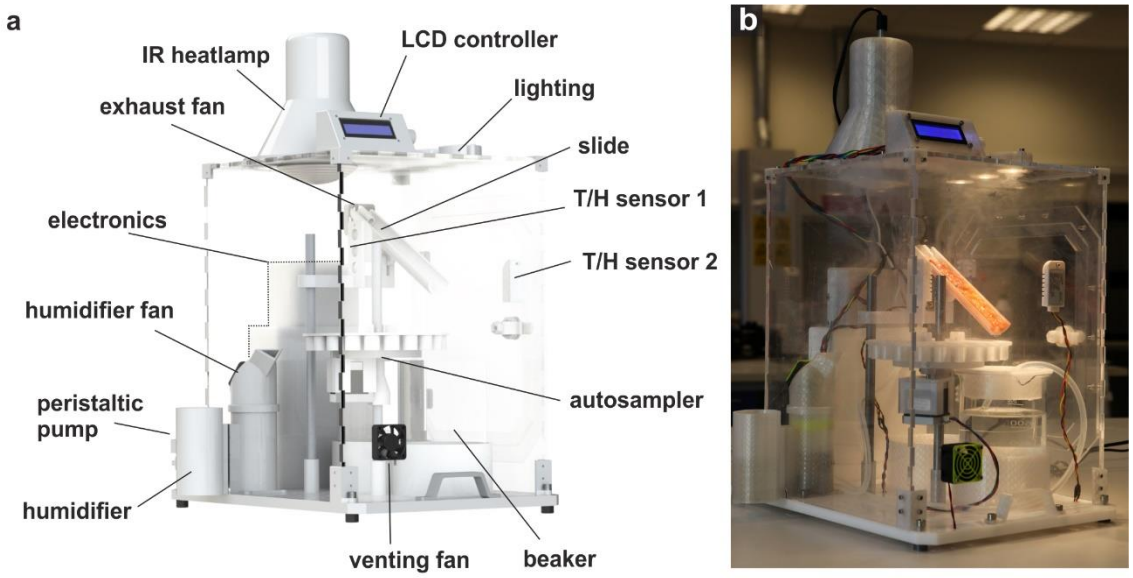

Figure 35 Third design iteration of retention model setup with FDM-fabricated and laser-cut parts, temperature and humidity-controlled chamber, integrated peristaltic pump and rotational autosampler. (a) CAD model, (b) photograph of constructed setup.

5 | Conclusions and Outlook

The objectives of the Ph.D. project were to employ AM technology to fabricate mini-devices for ODD and to characterize different designs with respect to their aptitude as ODD carrier platforms. In this regard, particular attention was paid to the design of specific surface structures that might increase the mucoadhesiveness of mini-devices.

The results of this work demonstrate that AM technology, particularly DLP-SL, is indeed a suitable technology for the fabrication of mini-devices and micro-devices/microcontainers. As part of this project, a potential batch-processing scheme based on AM has been enabled through the implementation of water-soluble sacrificial substrates into the fabrication procedure of DLP-SL (Manuscript II and Manuscript III). Moreover, the applicability of direct laser writing SL for the manufacturing of the same mini-devices was thoroughly examined (Manuscript I).

The prototyping potential of AM with respect to the realization of various designs of mini-devices was demonstrated. Using an established method for the characterization of mucoadhesiveness, it became apparent that, only by tailoring the design of mini-devices, the desired property of increased mucoadhesiveness could be achieved (Manuscript III). It has to be emphasized that the increased mucoadhesiveness was selectively achieved for the reservoir-containing side of the devices, thus increasing the probability of correctly oriented attachment to the intestinal mucosa and consequent mucosa-directed drug release.

A logical continuation of the research on these devices would be to subject them to the same processing steps as *SU-8* microcontainers, namely drug-loading and lid sealing, in order to obtain a completed ODD product. Subsequently, further *in vitro* evaluation methods, such as drug release and permeation under physiologically relevant shear conditions (similar to the study presented by Ainslie et al. [11]), could be utilized to confirm the benefit of increased mucoadhesive properties for ODD applicability. Furthermore, *in vivo* evaluation will be essential to prove the implications of design alterations on ODD performance and hence oral bioavailability.

From a technical point of view, the presented research would highly benefit from the availability of AM technologies with increased resolution, speed and build area. A higher resolution would enable the downscaling of fabricated structures and therefore facilitate the

use of smaller animal models in potential *in vivo* studies, such as rats, for which the fabricated mini-devices were too large. Within this project, a DLP-SL instrument with a spatial resolution of 30 µm was employed. Meanwhile, alternative DLP-SL instruments with higher resolutions were reported in the literature. Gong et al. for example reported the construction of a custom DLP-SL system with a lateral resolution below 10 µm [182]. This shows that the resolution constraint could be reduced, already at this time.

For the case that microfabricated devices for ODD would become industrially relevant, AM could in fact be a potent method for their fabrication. However, an increased fabrication speed as well as build area would be required to catch up with the demands of industrial serial production. The CLIP-method represents an attractive technology in this case, as the fabrication speed is solely dependent on the height of manufactured objects and the curing rate as well as viscosity of the photopolymer [116]. Therefore, the fabrication time for an entire batch of mini-devices/microcontainers will presumably amount to only a couple of minutes.

In this project, mini-devices/microcontainers were fabricated from prototyping materials, which are unsuitable for pharmaceutical applications due to potential toxicity, thus rendering any attempts of commercialization pointlessly. Albeit, research on biocompatible resin materials for vat photopolymerization-based AM techniques is intensive and promising alternatives exist even now. Urrios et al. for instance showed that additively manufactured objects from PEGDA revealed promising results in terms of cytocompatibility [183].

The implementation of pre-fabricated sacrificial substrates into the fabrication procedure of vat photopolymerization-based AM (Manuscript II) is a byproduct of this Ph.D. project, which has the potential to develop impact on its own. The combination of serving as a rapidly exchangeable build surface, a common processing substrate (similar as the wafer in microfabrication) and a sacrificial release layer, introduces many possibilities and resolves issues hitherto inherent to AM-based micromanufacturing.

Lastly, the development of a fully and easily replicable flow retention model setup alongside a detailed documentation, might not only provide other researchers with the necessary input to construct their own but might as well contribute to a certain standardization and increased reproducibility of this particular experiment. Moreover, the increased range of functions through integration of features might spur the performance of new kinds of experiments.

6 | References

1. Anselmo, A.C., and Mitragotri, S. (2014). An overview of clinical and commercial impact of drug delivery systems. J. Control. Release *190*, 15–28.
2. Anselmo, A.C., Gokarn, Y., and Mitragotri, S. (2018). Non-invasive delivery strategies for biologics. Nat. Rev. Drug Discov. *18*, 19–40.
3. Vela Ramirez, J.E., Sharpe, L.A., and Peppas, N.A. (2017). Current state and challenges in developing oral vaccines. Adv. Drug Deliv. Rev. *114*, 116–131.
4. Sultatos, L. (2007). Routes of Drug Administration. In xPharm: The Comprehensive Pharmacology Reference, S. J. Enna and D. B. Bylund, eds. (New York: Elsevier), pp. 1–3.
5. Lautenschläger, C., Schmidt, C., Fischer, D., and Stallmach, A. (2014). Drug delivery strategies in the therapy of inflammatory bowel disease. Adv. Drug Deliv. Rev. *71*, 58–76.
6. Gandhi, R., Lal Kaul, C., and Panchagnula, R. (1999). Extrusion and spheronization in the development of oral controlled-release dosage forms. Pharm. Sci. Technolo. Today *2*, 160–170.
7. Flynn, E. (2007). Drug Bioavailability. In xPharm: The Comprehensive Pharmacology Reference, S. J. Enna and D. B. Bylund, eds. (New York: Elsevier), pp. 1–2.
8. Peer, D., Karp, J.M., Hong, S., Farokhzad, O.C., Margalit, R., and Langer, R. (2007). Nanocarriers as an emerging platform for cancer therapy. 751–760.
9. Sonia, T.A., and Sharma, C.P. (2012). An overview of natural polymers for oral insulin delivery. Drug Discov. Today *17*, 784–792.
10. Tao, S.L., Lubeley, M.W., and Desai, T.A. (2003). Bioadhesive poly(methyl methacrylate) microdevices for controlled drug delivery. J. Control. Release *88*, 215–228.
11. Ainslie, K.M., Lowe, R.D., Beaudette, T.T., Petty, L., Bachelder, E.M., and Desai, T.A. (2009). Microfabricated devices for enhanced bioadhesive drug delivery: Attachment to and small-molecule release through a cell monolayer under flow. Small *5*, 2857–2863.
12. Chirra, H.D., Shao, L., Ciaccio, N., Fox, C.B., Wade, J.M., Ma, A., and Desai, T.A. (2014). Planar Microdevices for Enhanced In Vivo Retention and Oral Bioavailability of Poorly Permeable Drugs. Adv. Healthc. Mater. *3*, 1648–1654.
13. Ahmed, A., Bonner, C., and Desai, T.A. (2001). Bioadhesive microdevices for drug delivery: A feasibility study. Biomed. Microdevices *3*, 89–96.
14. Ahmed, A., Bonner, C., and Desai, T.A. (2002). Bioadhesive microdevices with multiple reservoirs: A new platform for oral drug delivery. J. Control. Release *81*, 291–306.
15. Tao, S.L., Popat, K., and Desai, T.A. (2007). Off-wafer fabrication and surface modification of asymmetric 3D SU-8 microparticles. Nat. Protoc. *1*, 3153–3158.
16. Chirra, H.D., and Desai, T.A. (2012). Multi-reservoir bioadhesive microdevices for

independent rate-controlled delivery of multiple drugs. Small *8*, 3839–3846.

17. Vert, M., Doi, Y., Hellwich, K.H., Hess, M., Hodge, P., Kubisa, P., Rinaudo, M., S.F. (2012). Terminology for biorelated polymers and applications (IUPAC Recommendations 2012). Pure Appl. Chem. *84*, 377–408.

18. Smart, J.D. (2005). The basics and underlying mechanisms of mucoadhesion. Adv. Drug Deliv. Rev. *57*, 1556–1568.

19. Nielsen, L.H., Melero, A., Keller, S.S., Jacobsen, J., Garrigues, T., Rades, T., Müllertz, A., and Boisen, A. (2016). Polymeric microcontainers improve oral bioavailability of furosemide. Int. J. Pharm. *504*, 98–109.

20. Rao, K.V.R., and Buri, P. (1989). A novel in situ method to test polymers and coated microparticles for bioadhesion. Int. J. Pharm. *52*, 265–270.

21. Farid, R.M., El-Salamouni, N.S., El-Kamel, A.H., and El-Gamal, S.S. (2017). Chapter 16 - Lipid-based nanocarriers for ocular drug delivery. In Nanostructures for Drug Delivery Micro and Nano Technologies., E. Andronescu and A. M. Grumezescu, eds. (Elsevier), pp. 495–522.

22. Jin, J., Sklar, G.E., Min Sen Oh, V., and Chuen Li, S. (2008). Factors affecting therapeutic compliance: A review from the patient's perspective. Ther. Clin. Risk Manag. *4*, 269–286.

23. Nelson, A.G., Zhang, X., Ganapathi, U., Szekely, Z., Flexner, C.W., Owen, A., and Sinko, P.J. (2015). Drug delivery strategies and systems for HIV/AIDS pre-exposure prophylaxis and treatment. J. Control. Release *219*, 669–680.

24. Sultatos, L. (2007). Drug Absorption from the Gastrointestinal Tract. In xPharm: The Comprehensive Pharmacology Reference, S. J. Enna and D. B. Bylund, eds. (New York: Elsevier), pp. 1–2.

25. Chen, M., Sonaje, K., Chen, K., and Sung, H. (2011). A review of the prospects for polymeric nanoparticle platforms in oral insulin delivery. Biomaterials *32*, 9826–9838.

26. Jain, K.K. (2008). Drug Delivery Systems - An Overview. In Drug Delivery Systems, K. K. Jain, ed. (Totowa, NJ: Humana Press), pp. 1–50.

27. Silverthorn, D.U. (2016). The Digestive System. In Human Physiology: An Integrated Approach (London: Pearson), pp. 654–692.

28. Evans, D.F., Pye, G., Bramley, R., Clark, A.G., Dyson, T.J., and Hardcastle, J.D. (1988). Measurement of gastrointestinal pH profiles in normal ambulant human subjects. Gut *29*, 1035–1041.

29. Helander, H.F., Fändriks, L., Helander, H.F., and Fändriks, L. (2014). Surface area of the digestive tract – revisited Surface area of the digestive tract – revisited. *5521*.

30. Fanucci, A., Cerro, P., and Fanucci, E. (1988). Normal Small-Bowel Measurements by Enteroclysis. Scand. J. Gastroenterol. *23*, 574–576.

31. Greenwood-Van Meerveld, B., Johnson, A.C., and Grundy, D. (2017). Gastrointestinal Physiology and Function. In Gastrointestinal Pharmacology, B. Greenwood-Van Meerveld, ed. (Cham: Springer International Publishing), pp. 1–16.

32. Madara, J.L. (1998). Regulation of the movement of solutes across tight junctions. Annu. Rev. Physiol. *60*, 143–159.

33. Vitale, S., Picascia, S., and Gianfrani, C. (2016). The cross-talk between enterocytes and intraepithelial lymphocytes. Mol. Cell. Pediatr., 0–3.

34. Mcconnell, E.L., Fadda, H.M., and Basit, A.W. (2008). Gut instincts : Explorations in intestinal physiology and drug delivery. *364*, 213–226.

35. Dew, M.J., Hughes, P.J., Lee, M.G., Evans, B.K., and Rhodes, J. (1982). An oral preparation to release drugs in the human colon. Br. J. Clin. Pharmacol. *14*, 405–408.

36. Porter, C.J.H., Trevaskis, N.L., and Charman, W.N. (2007). Lipids and lipid-based formulations: optimizing the oral delivery of lipophilic drugs. Nat. Rev. Drug Discov. *6*, 231.

37. Cone, R.A. (2009). Barrier properties of mucus. Adv. Drug Deliv. Rev. *61*, 75–85.

38. Lehr, C.-M., Poelma, F.G.J., Junginger, H.E., and Tukker, J.J. (1991). An estimate of turnover time of intestinal mucus gel layer in the rat in situ loop. Int. J. Pharm. *70*, 235–240.

39. Schuhl, J.F. (1995). Nasal mucociliary clearance in perennial rhinitis. J. Investig. Allergol. Clin. Immunol. *5*, 333—336.

40. Atuma, C., Strugala, V., Allen, A., and Holm, L. (2001). The adherent gastrointestinal mucus gel layer: thickness and physical state in vivo. Am. J. Physiol. Liver Physiol. *280*, G922–G929.

41. Allen, A., Cunliffe, W.J., Pearson, J.P., and Venables, C.W. (1990). The adherent gastric mucus gel barrier in man and changes in peptic ulceration. J. Intern. Med. *228*, 83–90.

42. Perez-Vilar, J., and Hill, R.L. (1999). The Structure and Assembly of Secreted Mucins. J. Biol. Chem. *274*, 31751–31754.

43. Martínez-Sáez, N., Peregrina, J.M., and Corzana, F. (2017). Principles of mucin structure: implications for the rational design of cancer vaccines derived from MUC1-glycopeptides. Chem. Soc. Rev. *46*, 7154–7175.

44. Lai, S.K., Wang, Y.-Y., Wirtz, D., and Hanes, J. (2009). Micro- and macrorheology of mucus. Adv. Drug Deliv. Rev. *61*, 86–100.

45. Matsui, H., Verghese, M.W., Kesimer, M., Schwab, U.E., Randell, S.H., Sheehan, J.K., Grubb, B.R., and Boucher, R.C. (2005). Reduced Three-Dimensional Motility in Dehydrated Airway Mucus Prevents Neutrophil Capture and Killing Bacteria on Airway Epithelial Surfaces. J. Immunol. *175*, 1090–1099.

46. Khanvilkar, K., Donovan, M.D., and Flanagan, D.R. (2001). Drug transfer through mucus. Adv. Drug Deliv. Rev. *48*, 173–193.

47. Ahuja, A., Khar, R.K., and Ali, J. (1997). Mucoadhesive Drug Delivery Systems. Drug Dev. Ind. Pharm. *23*, 489–515.

48. Netsomboon, K., and Bernkop-Schnürch, A. (2016). Mucoadhesive vs. mucopenetrating particulate drug delivery. Eur. J. Pharm. Biopharm. *98*, 76–89.

49. Khutoryanskiy, V. V. (2011). Advances in Mucoadhesion and Mucoadhesive Polymers. Macromol. Biosci. *11*, 748–764.

50. Peppas, N.A., and Sahlin, J.J. (1996). Hydrogels as mucoadhesive and bioadhesive materials: a review. Biomaterials *17*, 1553–1561.

51. Kammer, H.W. (1983). Adhesion between polymers. Review. Acta Polym. *34*, 112–118.

52. Mackie, A.R., Goycoolea, F.M., Menchicchi, B., Caramella, C.M., Saporito, F., Lee, S., Stephansen, K., Chronakis, I.S., Hiorth, M., Adamczak, M., Waldner, M., Nielsen, H.M., and Marcelloni, L. (2017). Innovative Methods and Applications in Mucoadhesion Research. Macromol. Biosci. *17*, 1–32.

53. Wagner, A.M., Gran, M.P., and Peppas, N.A. (2018). Designing the new generation of intelligent biocompatible carriers for protein and peptide delivery. Acta Pharm. Sin. B *8*, 147–164.

54. Daugherty, A.L., and Mrsny, R.J. (1999). Transcellular uptake mechanisms of the intestinal epithelial barrier Part one. Pharm. Sci. Technolo. Today *2*, 144–151.

55. Karp, G., Iwasa, J., and Marshall, W. (2005). The Structure and Function of the Plasma Membrane. In Cell and Molecular Biology: Concepts and Experiments (Hoboken: John Wiley & Sons).

56. Amidon, G.L., Lennernäs, H., Shah, V.P., and Crison, J.R. (1995). A Theoretical Basis for a Biopharmaceutic Drug Classification: The Correlation of in Vitro Drug Product Dissolution and in Vivo Bioavailability. Pharm. Res. An Off. J. Am. Assoc. Pharm. Sci. *12*, 413–420.

57. CDER/FDA (2000). U.S. Department of Health and Human Services Food and Drug Administration Center for Evaluation and Research (CDER). In Guidances for industry: waiver of in vivo bioavailability and bioequivalence studies for immediate-release solid oral dosage forms based on a Biopharmaceutics Classification System.

58. Shah, V.P., and Amidon, G.L. (2014). G.L. Amidon, H. Lennernas, V.P. Shah, and J.R. Crison. A theoretical basis for a biopharmaceutic drug classification: the correlation of in vitro drug product dissolution and in vivo bioavailability, Pharm Res 12, 413-420, 1995--backstory of BCS. AAPS J. *16*, 894–898.

59. Padrela, L., Rodrigues, M.A., Duarte, A., Dias, A.M.A., Braga, M.E.M., and de Sousa, H.C. (2018). Supercritical carbon dioxide-based technologies for the production of drug nanoparticles/nanocrystals – A comprehensive review. Adv. Drug Deliv. Rev. *131*, 22–78.

60. Perrie, Y., and Rades, T. (2012). Immediate-release drug delivery systems I: increasing the solubility and dissolution rate of drugs. In Pharmaceutics : Drug Delivery and Targeting (London: Pharmaceutical Press), pp. 25–58.

61. Thanou, M., Verhoef, J.C., and Junginger, H.E. (2001). Oral drug absorption enhancement by chitosan and its derivatives. Adv. Drug Deliv. Rev. *52*, 117–126.

62. Chen, H., and Langer, R. (1998). Oral particulate delivery: status and future trends. Adv. Drug Deliv. Rev. *34*, 339–350.

63. Traverso, G., Schoellhammer, C.M., Schroeder, A., Maa, R., Lauwers, G.Y., Polat, B.E., Anderson, D.G., Blankschtein, D., and Langer, R. (2015). Microneedles for Drug Delivery via the Gastrointestinal Tract. J. Pharm. Sci. *104*, 362–367.

64. Bellinger, A.M., Jafari, M., Grant, T.M., Zhang, S., Slater, H.C., Wenger, E.A., Mo, S., Lee, Y.-A.L., Mazdiyasni, H., Kogan, L., Barman, R., Cleveland, C., Booth, L., Bensel, T., Minahan, D., Hurowitz, H.M., Tai, T., Daily, J., Nikolic, B., Wood, L., Eckhoff, P.A.,

Langer, R., and Traverso, G. (2016). Oral, ultra–long-lasting drug delivery: Application toward malaria elimination goals. Sci. Transl. Med. *8*, 365ra157-365ra157.

65. Abramson, A., Caffarel-Salvador, E., Khang, M., Dellal, D., Silverstein, D., Gao, Y., Frederiksen, M.R., Vegge, A., Hubálek, F., Water, J.J., Friderichsen, A. V, Fels, J., Kirk, R.K., Cleveland, C., Collins, J., Tamang, S., Hayward, A., Landh, T., Buckley, S.T., Roxhed, N., Rahbek, U., Langer, R., and Traverso, G. (2019). An ingestible self-orienting system for oral delivery of macromolecules. Science (80-.). *363*, 611–615.

66. Pimpin, A., and Srituravanich, W. (2012). Reviews on micro- and nanolithography techniques and their applications. Eng. J. *16*, 37–55.

67. Franssila, S. (2010). Introduction. In Introduction to Microfabrication Wiley Online Books. (Hoboken: John Wiley & Sons), pp. 1–13.

68. Franssila, S. (2010). Economics of Microfabrication. In Introduction to Microfabrication Wiley Online Books. (Hoboken: John Wiley & Sons), pp. 457–468.

69. Luttge, R. (2011). Chapter 1 - Introduction. In Micro and Nano Technologies, R. B. T.-M. for I. A. Luttge, ed. (Boston: William Andrew Publishing), pp. 1–11.

70. Luttge, R. (2011). Chapter 8 - Microfabrication for Novel Products in Drug Delivery: An Example. In Micro and Nano Technologies, R. B. T.-M. for I. A. Luttge, ed. (Boston: William Andrew Publishing), pp. 235–272.

71. Tao, S.L., and Desai, T.A. (2005). Micromachined devices: The impact of controlled geometry from cell-targeting to bioavailability. J. Control. Release *109*, 127–138.

72. Tao, S.L., and Desai, T.A. (2005). Microfabrication of multilayer, asymmetric, polymeric devices for drug delivery. Adv. Mater. *17*, 1625–1630.

73. Guan, J., He, H., Lee, L.J., and Hansford, D.J. (2007). Fabrication of Particulate Reservoir-Containing, Capsulelike, and Self-Folding Polymer Microstructures for Drug Delivery. Small *3*, 412–418.

74. Azam, A., Laflin, K.E., Jamal, M., Fernandes, R., and Gracias, D.H. (2011). Self-folding micropatterned polymeric containers. Biomed. Microdevices *13*, 51–58.

75. Rolland, J.P., Maynor, B.W., Euliss, L.E., Exner, A.E., Denison, G.M., and DeSimone, J.M. (2005). Direct Fabrication and Harvesting of Monodisperse, Shape-Specific Nanobiomaterials. J. Am. Chem. Soc. *127*, 10096–10100.

76. Canelas, D.A., Herlihy, K.P., and DeSimone, J.M. (2009). Top-down particle fabrication: control of size and shape for diagnostic imaging and drug delivery. Wiley Interdiscip. Rev. Nanomedicine Nanobiotechnology *1*, 391–404.

77. McHugh, K.J., Nguyen, T.D., Linehan, A.R., Yang, D., Behrens, A.M., Rose, S., Tochka, Z.L., Tzeng, S.Y., Norman, J.J., Anselmo, A.C., Xu, X., Tomasic, S., Taylor, M.A., Lu, J., Guarecuco, R., Langer, R., and Jaklenec, A. (2017). Fabrication of fillable microparticles and other complex 3D microstructures. Mater. Sci. *1142*, 1138–1142.

78. Ainslie, K.M., Kraning, C.M., and Desai, T.A. (2008). Microfabrication of an asymmetric, multi-layered microdevice for controlled release of orally delivered therapeutics. Lab Chip *8*, 1042–1047.

79. Nielsen, L.H., Keller, S.S., and Boisen, A. (2018). Microfabricated devices for oral drug delivery. Lab Chip *18*, 2348–2358.

80. Fox, C.B., Cao, Y., Nemeth, C.L., Chirra, H.D., Chevalier, R.W., Xu, A.M., Melosh, N.A., and Desai, T.A. (2016). Fabrication of Sealed Nanostraw Microdevices for Oral Drug Delivery. ACS Nano *10*, 5873–5881.

81. Fox, C.B., Nemeth, C.L., Chevalier, R.W., Cantlon, J., Bogdanoff, D.B., Hsiao, J.C., and Desai, T.A. (2017). Picoliter-volume inkjet printing into planar microdevice reservoirs for low-waste, high-capacity drug loading. Bioeng. Transl. Med. *2*, 9–16.

82. Nielsen, L.H., Keller, S.S., Gordon, K.C., Boisen, A., Rades, T., and Müllertz, A. (2012). Spatial confinement can lead to increased stability of amorphous indomethacin. Eur. J. Pharm. Biopharm. *81*, 418–425.

83. Petersen, R.S., Keller, S.S., and Boisen, A. (2017). Loading of Drug-Polymer Matrices in Microreservoirs for Oral Drug Delivery. Macromol. Mater. Eng. *302*, 1–6.

84. Abid, Z., Gundlach, C., Durucan, O., von Halling Laier, C., Nielsen, L.H., Boisen, A., and Keller, S.S. (2017). Powder embossing method for selective loading of polymeric microcontainers with drug formulation. Microelectron. Eng. *171*, 20–24.

85. Vasconcelos, T., Sarmento, B., and Costa, P. (2007). Solid dispersions as strategy to improve oral bioavailability of poor water soluble drugs. Drug Discov. Today *12*, 1068–1075.

86. Marizza, P., Keller, S.S., and Boisen, A. (2013). Inkjet printing as a technique for filling of micro-wells with biocompatible polymers. Microelectron. Eng. *111*, 391–395.

87. Marizza, P., Keller, S.S., Müllertz, A., and Boisen, A. (2014). Polymer-filled microcontainers for oral delivery loaded using supercritical impregnation. J. Control. Release *173*, 1–9.

88. Marizza, P., Pontoni, L., Rindzevicius, T., Alopaeus, J.F., Su, K., Zeitler, J.A., Keller, S.S., Kikic, I., Moneghini, M., De Zordi, N., Solinas, D., Cortesi, A., and Boisen, A. (2016). Supercritical impregnation of polymer matrices spatially confined in microcontainers for oral drug delivery: Effect of temperature, pressure and time. J. Supercrit. Fluids *107*, 145–152.

89. Mazzoni, C., Tentor, F., Strindberg, S.A., Nielsen, L.H., Keller, S.S., Alstrøm, T.S., Gundlach, C., Müllertz, A., Marizza, P., and Boisen, A. (2017). From concept to in vivo testing: Microcontainers for oral drug delivery. J. Control. Release *268*, 343–351.

90. Nielsen, L.H., Rades, T., Boyd, B., and Boisen, A. (2017). Microcontainers as an oral delivery system for spray dried cubosomes containing ovalbumin. Eur. J. Pharm. Biopharm. *118*, 13–20.

91. von Halling Laier, C., Gibson, B., Moreno, J.A.S., Rades, T., Hook, S., Nielsen, L.H., and Boisen, A. (2019). Microcontainers for protection of oral vaccines, in vitro and in vivo evaluation. J. Control. Release *294*, 91–101.

92. Petersen, R.S., Keller, S.S., and Boisen, A. (2015). Hot punching of high-aspect-ratio 3D polymeric microstructures for drug delivery. Lab Chip *15*, 2576–2579.

93. Gibson, I., Rosen, D.W., and Stucker, B. (2010). Introduction and Basic Principles BT - Additive Manufacturing Technologies: Rapid Prototyping to Direct Digital Manufacturing. In, I. Gibson, D. W. Rosen, and B. Stucker, eds. (Boston, MA: Springer US), pp. 20–35.

94. Sachs, E., Cima, M., and Cornie, J. (1990). Three-Dimensional Printing: Rapid Tooling

and Prototypes Directly from a CAD Model. CIRP Ann. *39*, 201–204.

95. Pham, D.T., and Gault, R.S. (1998). A comparison of rapid prototyping technologies. Int. J. Mach. Tools Manuf. *38*, 1257–1287.

96. Huang, S.H., Liu, P., Mokasdar, A., and Hou, L. (2013). Additive manufacturing and its societal impact: a literature review. Int. J. Adv. Manuf. Technol. *67*, 1191–1203.

97. Gross, B.C., Erkal, J.L., Lockwood, S.Y., Chen, C., and Spence, D.M. (2014). Evaluation of 3D printing and its potential impact on biotechnology and the chemical sciences. Anal. Chem. *86*, 3240–3253.

98. Gao, W., Zhang, Y., Ramanujan, D., Ramani, K., Chen, Y., Williams, C.B., Wang, C.C.L., Shin, Y.C., Zhang, S., and Zavattieri, P.D. (2015). The status, challenges, and future of additive manufacturing in engineering. Comput. Des. *69*, 65–89.

99. Moon, S.K., Tan, Y.E., Hwang, J., and Yoon, Y.-J. (2014). Application of 3D printing technology for designing light-weight unmanned aerial vehicle wing structures. Int. J. Precis. Eng. Manuf. Technol. *1*, 223–228.

100. Lim, C.W.J., Le, K.Q., Lu, Q., and Wong, C.H. (2016). An Overview of 3-D Printing in Manufacturing, Aerospace, and Automotive Industries. IEEE Potentials *35*, 18–22.

101. Quinlan, H.E., Hasan, T., Jaddou, J., and Hart, A.J. (2017). Industrial and Consumer Uses of Additive Manufacturing: A Discussion of Capabilities, Trajectories, and Challenges. J. Ind. Ecol. *21*, S15–S20.

102. Sandström, C.G. (2016). The non-disruptive emergence of an ecosystem for 3D Printing - Insights from the hearing aid industry's transition 1989-2008. Technol. Forecast. Soc. Change *102*, 160–168.

103. Gibson, I., Rosen, D.W., and Stucker, B. (2010). Medical Applications for Additive Manufacture BT - Additive Manufacturing Technologies: Rapid Prototyping to Direct Digital Manufacturing. In, I. Gibson, D. W. Rosen, and B. Stucker, eds. (Boston, MA: Springer US), pp. 400–414.

104. Harris, R., and Savalani, M. (2006). Medical Applications. In Rapid Manufacturing (John Wiley & Sons, Ltd), pp. 175–194.

105. Jones, R., Haufe, P., Sells, E., Iravani, P., Olliver, V., Palmer, C., and Bowyer, A. (2011). Reprap - The replicating rapid prototyper. Robotica *29*, 177–191.

106. Tanenbaum, J.G., Williams, A.M., Desjardins, A., and Tanenbaum, K. (2013). Democratizing Technology: Pleasure, Utility and Expressiveness in DIY and Maker Practice. In Proceedings of the SIGCHI Conference on Human Factors in Computing Systems CHI '13. (New York, NY, USA: ACM), pp. 2603–2612.

107. Wittbrodt, B.T., Glover, A.G., Laureto, J., Anzalone, G.C., Oppliger, D., Irwin, J.L., and Pearce, J.M. (2013). Life-cycle economic analysis of distributed manufacturing with open-source 3-D printers. Mechatronics *23*, 713–726.

108. Gross, B., Lockwood, S.Y., and Spence, D.M. (2017). Recent advances in analytical chemistry by 3D printing. Anal. Chem. *89*, 57–70.

109. Gibson, I., Rosen, D.W., and Stucker, B. (2010). Software Issues for Additive Manufacturing BT - Additive Manufacturing Technologies: Rapid Prototyping to Direct Digital Manufacturing. In, I. Gibson, D. W. Rosen, and B. Stucker, eds. (Boston, MA: Springer US), pp. 357–377.

110. Gibson, I., Rosen, D.W., and Stucker, B. (2010). Generalized Additive Manufacturing Process Chain BT - Additive Manufacturing Technologies: Rapid Prototyping to Direct Digital Manufacturing. In, I. Gibson, D. W. Rosen, and B. Stucker, eds. (Boston, MA: Springer US), pp. 59–77.

111. ISO / ASTM52900-15 (2015). Standard Terminology for Additive Manufacturing – General Principles – Terminology. In ASTM International (West Conshohocken, PA).

112. Hull (UVP Inc.), C.W. (1986). Apparatus for production of three-dimensional objects by stereolithography. US 4575330.

113. Gibson, I., Rosen, D.W., and Stucker, B. (2010). Photopolymerization Processes BT - Additive Manufacturing Technologies: Rapid Prototyping to Direct Digital Manufacturing. In, I. Gibson, D. W. Rosen, and B. Stucker, eds. (Boston, MA: Springer US), pp. 78–119.

114. Beluze, L., Bertsch, A., and Renaud, P. (1999). Microstereolithography: a new process to build complex 3D objects. In Proc.SPIE.

115. Vaezi, M., Seitz, H., and Yang, S. (2013). A review on 3D micro-additive manufacturing technologies. Int. J. Adv. Manuf. Technol. *67*, 1721–1754.

116. Tumbleston, J.R., Shirvanyants, D., Ermoshkin, N., Janusziewicz, R., Johnson, A.R., Kelly, D., Chen, K., Pinschmidt, R., Rolland, J.P., Ermoshkin, A., Samulski, E.T., and DeSimone, J.M. (2015). Continuous liquid interface production of 3D objects. Science (80-.). *347*, 1349–1352.

117. Maruo, S., and Kawata, S. (1998). Two-photon-absorbed near-infrared photopolymerization for three-dimensional microfabrication. J. Microelectromechanical Syst. *7*, 411–415.

118. Mao, M., He, J., Li, X., Zhang, B., Lei, Q., Liu, Y., and Li, D. (2017). The Emerging Frontiers and Applications of High-Resolution 3D Printing. Micromachines *8*.

119. Crump (Stratasys Inc.), S.S. (1992). Apparatus and method for creating three-dimensional objects. US 5121329.

120. Gibson, I., Rosen, D.W., and Stucker, B. (2010). Extrusion-Based Systems BT - Additive Manufacturing Technologies: Rapid Prototyping to Direct Digital Manufacturing. In, I. Gibson, D. W. Rosen, and B. Stucker, eds. (Boston, MA: Springer US), pp. 160–186.

121. RepRap.org (2015). Category:Extruders. Available at: https://reprap.org/wiki/Category:Extruders.

122. Lim, S.H., Kathuria, H., Tan, J.J.Y., and Kang, L. (2018). 3D printed drug delivery and testing systems — a passing fad or the future? Adv. Drug Deliv. Rev. *132*, 139–168.

123. Goyanes, A., Buanz, A.B.M., Hatton, G.B., Gaisford, S., and Basit, A.W. (2015). 3D printing of modified-release aminosalicylate (4-ASA and 5-ASA) tablets. Eur. J. Pharm. Biopharm. *89*, 157–162.

124. Goyanes, A., Robles Martinez, P., Buanz, A., Basit, A.W., and Gaisford, S. (2015). Effect of geometry on drug release from 3D printed tablets. Int. J. Pharm. *494*, 657–663.

125. Okwuosa, T.C., Pereira, B.C., Arafat, B., Cieszynska, M., Isreb, A., and Alhnan, M.A. (2017). Fabricating a Shell-Core Delayed Release Tablet Using Dual FDM 3D Printing for Patient-Centred Therapy. Pharm. Res. *34*, 427–437.

126. Wang, J., Goyanes, A., Gaisford, S., and Basit, A.W. (2016). Stereolithographic (SLA) 3D printing of oral modified-release dosage forms. Int. J. Pharm. *503*, 207–212.

127. Kong, Y.L., Zou, X., McCandler, C.A., Kirtane, A.R., Ning, S., Zhou, J., Abid, A., Jafari, M., Rogner, J., Minahan, D., Collins, J.E., McDonnell, S., Cleveland, C., Bensel, T., Tamang, S., Arrick, G., Gimbel, A., Hua, T., Ghosh, U., Soares, V., Wang, N., Wahane, A., Hayward, A., Zhang, S., Smith, B.R., Langer, R., and Traverso, G. (2018). 3D-Printed Gastric Resident Electronics. Adv. Mater. Technol. *0*, 1800490.

128. Finch, C.A. (1973). Polyvinyl alcohol, Properties and Uses (Wiley, Hoboken, NJ, USA).

129. Herrmann, W.O., and Haehnel, W. (1927). Über den Polyvinylalkohol. Berichte der Dtsch. Chem. Gesellschaft *60*, 1658–1663.

130. Schaper, C.D., and Miahnahri, A. (2004). Polyvinyl alcohol templates for low cost, high resolution, complex printing. J. Vac. Sci. Technol. B Microelectron. Nanom. Struct. Process. Meas. Phenom. *22*, 3323–3326.

131. Duran, C., Subbian, V., Giovanetti, M.T., Simkins, J.R., and Jr, F.R.B. (2015). Experimental desktop 3D printing using dual extrusion and water-soluble polyvinyl alcohol. Rapid Prototyp. J. *21*, 528–534.

132. Pimentel C., R., Ko, S.K., Caviglia, C., Wolff, A., Emnéus, J., Keller, S.S., and Dufva, M. (2018). Three-dimensional fabrication of thick and densely populated soft constructs with complex and actively perfused channel network. Acta Biomater. *65*, 174–184.

133. Whitehouse, D. (2002). 1 - Introduction. In Surfaces and Their Measurement, D. Whitehouse, ed. (Oxford: Kogan Page Science), pp. 1–15.

134. Persson, B.N.J., Albohr, O., Tartaglino, U., Volokitin, A.I., and Tosatti, E. (2005). On the nature of surface roughness with application to contact mechanics, sealing, rubber friction and adhesion. J. Phys. Condens. Matter *17*.

135. Svenson, G., and Fjeld, D. (2016). The impact of road geometry and surface roughness on fuel consumption of logging trucks. Scand. J. For. Res. *31*, 526–536.

136. Barthlott, W., and Neinhuis, C. (1997). Purity of the sacred lotus, or escape from contamination in biological surfaces. Planta *202*, 1–8.

137. Autumn, K., Sitti, M., Liang, Y.A., Peattie, A.M., Hansen, W.R., Sponberg, S., Kenny, T.W., Fearing, R., Israelachvili, J.N., and Full, R.J. (2002). Evidence for van der Waals adhesion in gecko setae. Proc. Natl. Acad. Sci. U. S. A. *99*, 12252–6.

138. Shahid, M., and Hashim, S.A. (2002). Effect of surface roughness on the strength of cleavage joints. Int. J. Adhes. Adhes. *22*, 235–244.

139. Schlesinger, G. (1942). Research on surface finish. J. Inst. Prod. Eng. *XXI*.

140. Standards catalogue 17.040.40 - Geometrical Product Specification (GPS) (International Organization for Standardization, Vernier, Geneva, Switzerland).

141. Standards catalogue 17.040.20 - Properties of surfaces (International Organization for Standardization, Vernier, Geneva, Switzerland).

142. Leach, R. (2014). Chapter 6 - Surface Topography Measurement Instrumentation. In Fundamental Principles of Engineering Nanometrology (Second Edition) Micro and Nano Technologies., R. Leach, ed. (Oxford: William Andrew Publishing), pp. 133–204.

143. ISO 4287:1997 Geometrical product specifications (GPS) -- Surface texture: Profile method -- Terms, definitions and surface texture parameters (1997). (International Organization for Standardization, Vernier, Geneva, Switzerland).

144. ISO 12781-1:2011 - Geometrical product specifications (GPS) -- Flatness -- Part 1: Vocabulary and parameters of flatness (2011). (International Organization for Standardization, Vernier, Geneva, Switzerland).

145. Whitehouse, D. (2002). 2 - Identification and separation of surface features. In Surfaces and Their Measurement, D. Whitehouse, ed. (Oxford: Kogan Page Science), pp. 16–47.

146. Whitehouse, D. (2002). 3 - Profile and areal (3D) parameter characterization. In Surfaces and Their Measurement, D. Whitehouse, ed. (Oxford: Kogan Page Science), pp. 48–95.

147. ISO 25178-2:2012 - Geometrical product specifications (GPS) -- Surface texture: Areal -- Part 2: Terms, definitions and surface texture parameters (2012). (International Organization for Standardization, Vernier, Geneva, Switzerland).

148. Bhushan, B. (2001). Surface Roughness Analysis and Measurement Techniques. In Modern Tribology Handbook, Two Volume Set (Boca Raton: CRC Press), pp. 49–119.

149. Leach, R. (2013). Characterisation of Areal Surface Texture (Springer-Verlag GmbH, Heidelberg, Germany).

150. Dougherty, D. (2012). The maker movement. Innov. Technol. Governance, Glob. *7*, 11–14.

151. Barrett, T., Pizzico, M., Levy, B.D., Nagel, R.L., Linsey, J.S., Talley, K.G., Forest, C.R., and Newstetter, W.C. (2015). A review of university maker spaces. In 122nd ASEE Annual Conference & Exposition (Seattle, WA).

152. Martin, L. (2015). The promise of the maker movement for education. J. Pre-College Eng. Educ. Res. *5*, 4.

153. Pearce, J.M. (2012). Building Research Equipment with Free, Open-Source Hardware. Science (80-.). *337*, 1303–1304.

154. Baden, T., Chagas, A.M., Gage, G.J., Marzullo, T.C., Prieto-Godino, L.L., and Euler, T. (2015). Open Labware: 3-D Printing Your Own Lab Equipment. PLoS Biol. *13*, 1–12.

155. Zhang, C., Anzalone, N.C., Faria, R.P., and Pearce, J.M. (2013). Open-Source 3D-Printable Optics Equipment. PLoS One *8*, e59840.

156. Chagas, A.M., Prieto-godino, L.L., Arrenberg, A.B., and Baden, T. (2017). The € 100 lab : A 3D-printable open-source platform for fluorescence microscopy , optogenetics , and accurate temperature control during behaviour of zebrafish , Drosophila , and Caenorhabditis elegans. 1–21.

157. Carvalho, M.C., and Murray, R.H. (2018). Osmar, the open-source microsyringe autosampler. HardwareX *3*, 10–38.

158. Arduino LLC (2019). Arduino. Available at: https://www.arduino.cc/ [Accessed February 6, 2019].

159. Vaut, L., and Scarano, E. (2019). Fully replicable and automated retention measurement setup for characterization of bio-adhesion. Mendeley Data *v1*.

160. 3DHubs (2019). CNC machining: The Complete Engineering Guide. Available at:

https://www.3dhubs.com/guides/cnc-machining/ [Accessed February 7, 2019].

161. Groover, M.P. (2010). Theory of metal machining. In Fundamentals of modern manufacturing: materials processes, and systems (Hoboken: John Wiley & Sons), pp. 483–506.

162. Groover, M.P. (2010). Machining operations and machine tools. In Fundamentals of modern manufacturing: materials processes, and systems (Hoboken: John Wiley & Sons), pp. 507–551.

163. Groover, M.P. (2010). Automation Technologies for manufacturing systems. In Fundamentals of modern manufacturing: materials processes, and systems (Hoboken: John Wiley & Sons), pp. 886–917.

164. Powell, J. (1993). The Basic Principles. In CO2 Laser Cutting (London: Springer London), pp. 1–22.

165. ILO, and WHO (2004). ICSC 1489 Polyvinyl alcohol. Available at: https://www.ilo.org/dyn/icsc/showcard.display?p_lang=en&p_card_id=1489&p_version=2 [Accessed September 3, 2018].

166. Rosato, D. V, Rosato, D. V, and Rosato, M.G. (2000). Injection Molding Machines BT - Injection Molding Handbook. In, D. V Rosato, D. V Rosato, and M. G. Rosato, eds. (Boston, MA: Springer US), pp. 28–150.

167. Rosato, D. V, Rosato, D. V, and Rosato, M.G. (2000). The Complete Injection Molding Process BT - Injection Molding Handbook. In, D. V Rosato, D. V Rosato, and M. G. Rosato, eds. (Boston, MA: Springer US), pp. 1–27.

168. Raman, C.V., and Krishnan, K.S. (1928). A new type of secondary radiation. Nature *121*, 501.

169. Landsberg, G., and Mandelstam, L. (1928). A novel effect of light scattering in crystals. Naturwissenschaften *16*, 5.

170. Jimenez, J., and Tomm, J.W. (2016). Raman Spectroscopy. In Spectroscopic Analysis of Optoelectronic Semiconductors (Cham: Springer International Publishing), pp. 77–142.

171. Prochazka, M. (2016). Basics of Raman Scattering (RS) Spectroscopy. In Surface-Enhanced Raman Spectroscopy: Bioanalytical, Biomolecular and Medical Applications (Cham: Springer International Publishing), pp. 7–19.

172. Ember, K.J.I., Hoeve, M.A., McAughtrie, S.L., Bergholt, M.S., Dwyer, B.J., Stevens, M.M., Faulds, K., Forbes, S.J., and Campbell, C.J. (2017). Raman spectroscopy and regenerative medicine: a review. npj Regen. Med. *2*, 12.

173. Artigas, R. (2011). Imaging Confocal Microscopy. In Optical Measurement of Surface Topography, R. Leach, ed. (Berlin, Heidelberg: Springer Berlin Heidelberg), pp. 237–286.

174. Whitehouse, D. (2002). 8 - Optical methods. In Surfaces and Their Measurement, D. Whitehouse, ed. (Oxford: Kogan Page Science), pp. 185–201.

175. de Groot, P. (2011). Phase Shifting Interferometry. In Optical Measurement of Surface Topography, R. Leach, ed. (Berlin, Heidelberg: Springer Berlin Heidelberg), pp. 167–186.

176. Zhou, W., Apkarian, R., Wang, Z.L., and Joy, D. (2007). Fundamentals of Scanning Electron Microscopy (SEM). In Scanning Microscopy for Nanotechnology: Techniques and Applications, W. Zhou and Z. L. Wang, eds. (New York, NY: Springer New York), pp. 1–40.

177. Hafner, B. (2007). Scanning electron microscopy primer. Charact. Facil. Univ. Minnesota-Twin Cities, 1–29.

178. Edsman, K., and Hägerström, H. (2005). Pharmaceutical applications of mucoadhesion for the non-oral routes. J. Pharm. Pharmacol. *57*, 3–22.

179. Ahluwalia, N.K., Thompson, D.G., Barlow, J., and Heggie, L. (1994). Human small intestinal contractions and aboral traction forces during fasting and after feeding. Gut *35*, 625–630.

180. Thirawong, N., Nunthanid, J., Puttipipatkhachorn, S., and Sriamornsak, P. (2007). Mucoadhesive properties of various pectins on gastrointestinal mucosa: An in vitro evaluation using texture analyzer. Eur. J. Pharm. Biopharm. *67*, 132–140.

181. Lee, Y.A.L., Zhang, S., Lin, J., Langer, R., and Traverso, G. (2016). A Janus Mucoadhesive and Omniphobic Device for Gastrointestinal Retention. Adv. Healthc. Mater. *5*, 1141–1146.

182. Gong, H., Bickham, B.P., Woolley, A.T., and Nordin, G.P. (2017). Custom 3D printer and resin for 18 μm × 20 μm microfluidic flow channels. Lab Chip *17*, 2899–2909.

183. Urrios, A., Parra-Cabrera, C., Bhattacharjee, N., Gonzalez-Suarez, A.M., Rigat-Brugarolas, L.G., Nallapatti, U., Samitier, J., DeForest, C.A., Posas, F., Garcia-Cordero, J.L., and Folch, A. (2016). 3D-printing of transparent bio-microfluidic devices in PEG-DA. Lab Chip *16*, 2287–2294.

7 | Appendix

7.1 Manuscript I

Additive Manufacturing of Microreservoir Devices for Oral Drug Delivery using an Acculas BA-30 Micro-Stereolithography Instrument: A feasibility study

L. Vaut, K. E. Jensen, G. Tosello, A. Khosla, H. Furukawa, A. Boisen

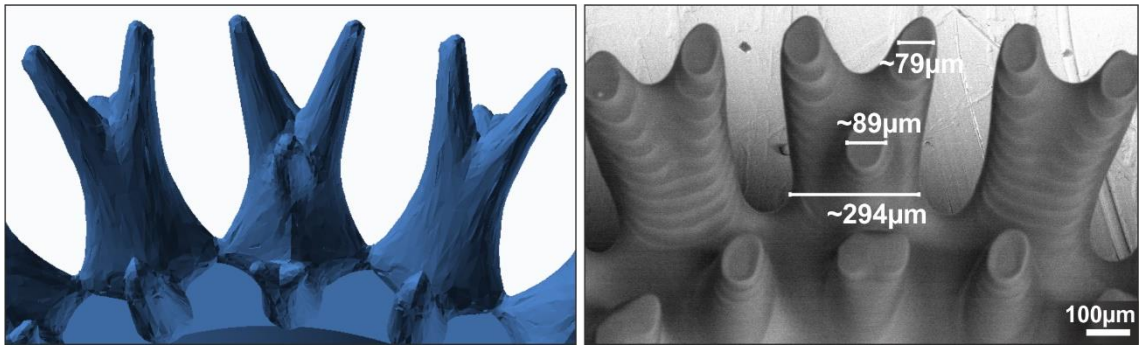

Additive Manufacturing of Microreservoir Devices for Oral Drug Delivery using an Acculas BA-30 Micro-Stereolithography Instrument: A feasibility study

Author Names: Lukas Vaut[1z], Kristian E. Jensen[1], Guido Tosello[2], Ajit Khosla[3], Hidemitsu Furukawa[3], Anja Boisen[1]

[1]The Danish National Research Foundation and Villum Foundation's Center for Intelligent Drug Delivery and Sensing Using Microcontainers and Nanomechanics (IDUN), Department of Health Technology, Technical University of Denmark, Kgs. Lyngby, 2800, Denmark

[2]Department of Mechanical Engineering, Technical University of Denmark, Kgs. Lyngby, 2800, Denmark

[3]Department of Mechanical Systems Engineering, Graduate School of Science and Engineering, Yamagata University, Jonan 4-3-16, Yonezawa, Yamagata, 992-8510, Japan

[z]lukv@dtu.dk

Within the research and the development of protective carrier platforms intended for oral drug delivery, polymeric microreservoir devices with sizes around 300 µm have been proposed as a delivery system capable of unidirectional drug release. So far, microreservoir devices have been fabricated with simple shapes by means of high-throughput fabrication methods. In this feasibility study, state-of-the-art micro-stereolithography 3D printing is used for the fabrication of various microreservoir geometries. Scanning electron microscopy characterization and conducted resolution tests demonstrated the capability of the used technology and unveils challenges and opportunities associated with the proposed fabrication process.

Introduction

When administered orally, many important drugs, such as insulin, reveal poor absorption efficiencies. This problem has triggered a lot of interest within the pharmaceutical and related sciences in developing mechanisms that could help to overcome the barriers that restrict efficient oral delivery. The necessity to realize the oral administration in those cases is mainly driven by the fact that the oral route exhibits several advantages, including increased patient compliance and in general its less invasive nature, compared to alternative drug delivery methods which comprise the parenteral, nasal, transdermal, pulmonary, rectal and vaginal routes. In case of inefficient oral drug delivery, the restrictions are set by the nature of the gastrointestinal system. The presence of hydrochloric acid associated with a harsh decline in pH down to 1.5, proteolytic and other digestive enzymes and finally a tightly arranged mucus-secreting epithelial cell layer prove to be very efficient barriers against the delivery and absorption of functional molecules.

Within the research areas of nano- and microtechnology, different platforms, e.g. nanoparticles, microparticles and liposomes, but also engineered microfabricated reservoir devices have been developed and tested with promising results as bioavailability-enhancing carrier systems.[1,2] A carrier system ideally provides resistance against enzymes and pH-

gradients, a stable and biocompatible environment, a permeability enhancing effect, a prolonged release pattern and a non-toxic/biosafe profile.[3] In contrast to particulate systems, in which the drug loading efficiency also depends on the molecular interactions between the drug and encapsulating molecules, microfabricated reservoir devices represent universal carrier platforms, that can be loaded with different drugs.

Besides oral drug delivery, additive manufacturing also represents a heavily debated topic in recent time, and it is steadily gaining more popularity largely in the areas of mechanical and manufacturing engineering as well as rapid prototyping of solid three-dimensional macro parts made of various materials. However, additive manufacturing meanwhile also draws increasing interest for the fabrication of three-dimensional structures at the micro- and nanoscale.[4] In this respect, additive manufacturing becomes a promising tool to be used in micro- and nanotechnology.

Microfabricated reservoir devices, intended for the oral delivery of drugs, have the advantage of an asymmetric design, which in turn allows for a unidirectional release of the loaded drug, potentially promoting increased release towards the intestinal mucosa.[2]

Previously, polymeric microreservoir devices, termed microcontainers, have been fabricated by lithography- or hot-embossing-based procedures, which allow for a high throughput, but which are also limited in terms of geometric freedom for container-shape.[5,6] The presented work investigates the feasibility of employing additive manufacturing/3D printing technology for the microfabrication of polymeric microcontainers with various geometrical shapes.

Results and Discussion

In the course of this work, the applicability of micro-stereolithography (μSLA) 3D printing for the fabrication of microcontainers for oral drug delivery was investigated. In this way, the technology was confronted with designs of varying complexity and also with different design dimensions in order to push the technology to its limit and to determine at which dimensions the smallest features can be obtained with the highest level of detail. The first section in this paragraph describes the fabrication of a complex microcontainer geometry which resulted after employing a topology-optimization algorithm.

Fabrication of complex three-dimensional micro-structures

A microcontainer design with everting micro-pillars from which even smaller pillars are branching out was created using a topology-optimization algorithm which solved a heat conduction problem subject to a volume constraint (Figure 1a, b, g, i). This design represented the ideal and ultimately desired geometry in this work and apart from technical limitations it should be fabricated within a size range of 300 to 500 μm in diameter. However, in this size range the smallest feature size would be around 6 μm. However, due to the laser spot size of the employed μSLA system, the possible theoretical resolution of the machine is limited to 30 μm. As a consequence, the design was scaled up to an outer container diameter of 2200 μm and the smallest feature size to approximately 30 μm as it can be noted in Figure 1i.

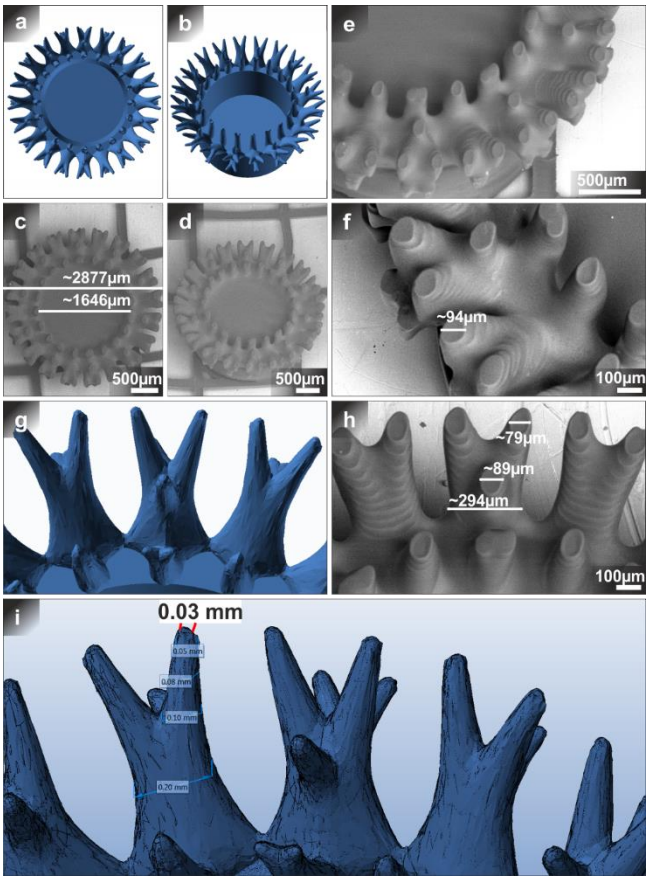

Figure 1 *3D printing of complex topology-optimized microcontainers. SEM images of 3D printed (micro-stereolithography) microcontainers (c, d, e, f, h) and STL-file (a, b, g, i) images of the corresponding complex microcontainer design with everting micro-pillars which were generated using a topology optimization algorithm. The outer diameter of the container design excluding the pillars (a, b) was 2200 µm, including the pillars 2980 µm. The inner diameter was 1800 µm and the height 1000 µm. Observed sizes are depicted in the SEM images and theoretical measurements of the micro-pillars in the STL-file are illustrated in (i). Images (d, e, f, h) were recorded at a tilted angle of 35°.*

When comparing the overall appearance and dimensions of the scanning electron microscopy (SEM) images (Figure 1c, d, e, f, h) of the resulting 3D printed object, it can be recognized that the object was not fully defined and that the dimensions were deviating from the specifications given by the design. The outer diameter of the whole object was 3.5% and the inner diameter 8.6% smaller. Upon inspection of the pillars it became noticeable that single lithographic layers (Z-direction) were visible and that the pillars were not entirely printed in the object, which means that the basic structure was laid out in any case, but the smallest features were missing. This leads to the conclusion that the fabrication of the pillars stopped at some point because a threshold to what was technically possible was reached. The measurements of the tips of the pillars in comparison to the theoretical measurements in the design suggest that approximately only 80% of the pillars, up to a diameter of approximately 80 µm, were fabricated. Since in the design the pillars are directed outwards from the object, the unfinished pillars could also be an explanation for the smaller outer diameter of the object.

Finally, another remarkable finding is that the reservoir of the container is not clearly recognizable and seems to be filled. This circumstance could have resulted from improper removal of excess uncured resin residue.

Fabrication of simple three-dimensional micro-structures

Since the complex microcontainer design presented in the previous section could not be 3D printed with a satisfactorily outcome, a new design with a much lower level of complexity was introduced and additively manufactured (Figure 2). In contrast to the previous design, the minimum feature size was increased to 80 µm whereas the overall size was reduced to 500 µm. Contradictory to the expectation that a simpler design and an increased minimum feature size would lead to an improved print outcome, the microcontainer depicted in Figure 3b and c exhibited a rather bulky appearance with a measured minimum feature size which was about 42.5% larger as specified by the design. In contrast to the complex microcontainer, no single lithographic layers could be observed. The gained findings suggest that the dimensions used in this design, especially the minimum feature sizes were too small to obtain acceptable results with the used instrument.

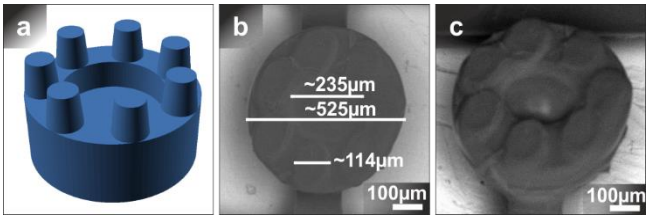

Figure 2 *3D printed simple microcontainers at small scale. SEM images of 3D printed microcontainers (b, c) and STL-file (a) images of the corresponding microcontainer design made with OpenSCAD software. The outer diameter of the container design (a) was 500 µm, the inner diameter 300 µm. The micro-pillars had a bottom diameter of 100 µm, a top diameter of 80 µm, a height of 100 µm and a pitch of 80 µm. The image (c) was taken from a 35° tilted angle.*

Influence of laser power on print quality

In the previous sections the 3D printing of complex and simple microcontainer designs have been described, respectively. As the printing outcome was neither satisfying in case of the complex model nor in the case of the simple model, a short test on the influence of laser power on the print quality was performed. The 3D printing instrument uses two different laser parameters. One laser power value for the outline of the printed structure and one laser power value for the infill of the printed structure. In the first test (Figure 3a, b), the laser power was decreased about 66% for the outline and about 20% for the infill when compared to the previous laser settings. The exemplary SEM-image reveals that the structures were not fully printed as the bottoms of the microcontainers were missing and no micro-pillars were visible. Additionally, the print obviously shifted in horizontal direction which means that the cylindrical shape of the microcontainer was distorted. In the second test (Figure 3c, d), the laser power was increased about 33% for the outline and about 60% for the infill. In this case,

the obtained microcontainers exhibited correct cylindrical shape, however, the structures had a rather bulky appearance. The reservoir of the microcontainer was not visible and shapes of micro-pillars could only be detected in a very rudimentary way.

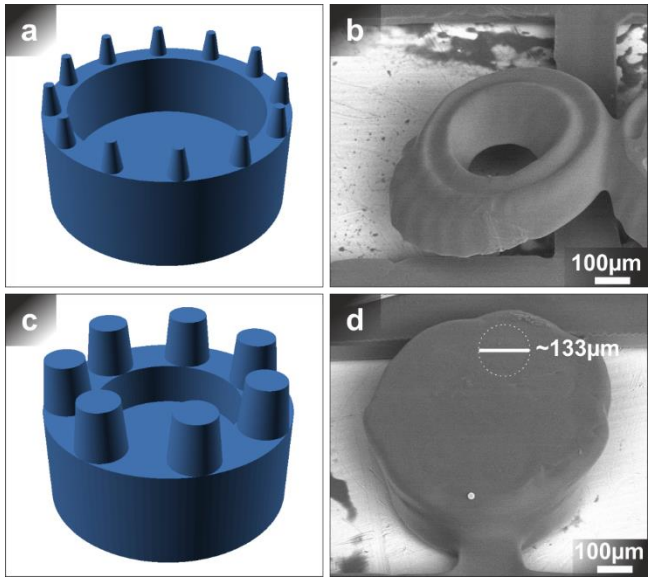

Figure 3 *Simple microcontainers 3D printed with differing laser parameters. 3D representations of design-files in STL format (a, c) and SEM images (b, d) of 3D printed microcontainers, where structure (b) is corresponding to model (a) and (d) to (c), respectively. The STL-files featured dimensions of 500 µm in total diameter and pillar dimensions of 20 µm top-diameter and 40 µm base-diameter (a), as well as 80 µm top-diameter and 100 µm base-diameter (c). The height of the micro-pillars was set as 60 µm in (a) and 100 µm in (c). Structure (b) was printed using a decreased laser power about 66% for the outline of the object and about 20% for the infill of the object when compared to the laser power settings for the earlier specimens. Contrary, the structure displayed in (d) was printed with an increase in laser power of about 33% for the outline and about 60% for the infill. The SEM-images were recorded from a 35° tilted angle.*

In conclusion, these results suggest that in the first test the laser power was too low. As a consequence of this fact, the print resin was not fully cured and ultimately the structures of the object did not emerge. Contrary to this, in the second test the laser power was obviously too high so that more resin was cured than it was supposed to and then the reservoir as well as the interspace between the micro-pillars was closed. Since the 3D printer was considered to be appropriately calibrated before these tests, it was decided to use the previous laser parameters and not to focus on optimizing laser power any further. Also, in this case, no lithographic layers were visible.

Fabrication of simple but larger three-dimensional micro-structures

As described before, the 3D printing of microcontainers with highly detailed and small features could not be successfully accomplished. In order to improve the print quality, the dimensions of the design were increased, and an overhang was added so as to enlarge the available space for the placement of micro-pillars (Figure 4). In contrast to previous designs, the new design exhibited a container diameter of 1000 µm excluding and 1300 µm including the overhang, respectively, and a microcontainer height of 300 µm, which means that the size was doubled in the XY-plane. Samples denoted as (a) and (b) were manufactured. They only differed in the height of their micro-pillars which was 150 µm for (a) and 200 µm for (b), respectively.

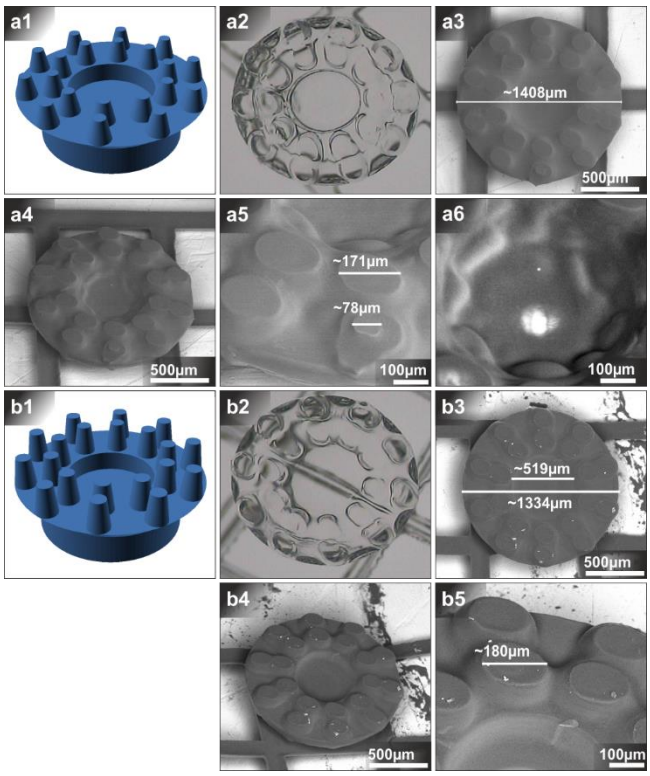

Figure 4 *3D printed micro-containers with overhang and micro-pillars. STL-file representations (a1, b1), optical microscope images (a2, b2) and SEM images of microcontainers. Images (a2) - (a6) are corresponding to model (a1) and (b2) - (b5) to model (b1). (a1) featured an overall diameter of 1000 µm in the bottom and 1300 µm including the overhang. The height of the microcontainers is 300 µm. The featured micro-pillars had a bottom diameter of 150 µm, a top diameter of 80 µm and a height of 150 µm. Model (b1) contained the same dimension parameters, only the height of the micro-pillars was increased to 200 µm. Images (a4) - (a6), (b4) and (b5) were recorded from a 35° tilted angle.*

In conformity with the previous results, it can be noted that the obtained small features were larger than it was specified in the CAD model. For (a) samples, the outer diameter including the overhang was 8.3% larger than specified in the design, whereas the top diameter of the micro-pillars was 114% larger. Interestingly, a structure with a size of 78 µm could be found

on one of the pillars. If this was the tip of the micro-pillar, it would fit the 80 µm given by the design very closely. However, the fact that this structure could only be found on one of the micro-pillars makes it more likely that it was a print artifact. Additionally, it can be noted that the bottom diameter of the pillars was drastically larger than the 150 µm specified by the design in any case. Other remarkable findings were related to the fact that the distance between the inner micro-pillars and the outer micro-pillars placed on the overhang was not homogenous, since some pillars seem to be connected while others seem to be clearly separated. Also, the cavity was undefined and bumpy and only showed a clear outline in the light microscopy image.

As far as the (b) samples were concerned, the outer diameter including the overhang was 2.6% larger and the top diameter of the micro-pillars was 125% larger than defined by the CAD model. The appearance of samples (b) was similar to that of (a) and the change in the micro-pillars' height showed no noticeable effect. In contrast to (a), only the outline of the cavity was more defined for (b) samples. For both types of samples, no single lithographic layers could be detected as it was the case with the two previously presented experiments.

In summary, the described samples showed that the dimensions of small features, micro-pillars in this case, highly deviated from the specifications that were given by the design parameters, while larger features (e.g. outer diameter of container) deviated less.

Resolution assays

Proceeding from the previous experiments, more systematic resolution testing was conducted. A microcontainer base structure with fixed dimensions was defined and then arrays of microcontainers with differently sized micro-pillars were additively manufactured (Figure 5). It has to be stressed that these experiments were mainly focused on the print outcome of the micro-pillars as an indication for print resolution. The basic structure consisted of a microcontainer with an outer diameter of 1300 µm including and 1000 µm excluding overhang, an inner diameter of 600 µm, a height of 500 µm and a micro-pillar height of 200 µm. The micro-pillar diameters varied from (a) to (f), starting with a top diameter of 30 µm and a bottom diameter of 80 µm for (a) and changing to values of 60/100, 80/130, 100-170,120/200, 90/200 µm for the other iterations.

The SEM images of printed microcontainers showed structures that appear to be very different than the CAD models. The cavities of the microcontainers seemed to be at least partly filled and the pillars were not clearly separated. In this way, the print outcome of the first experiment reveals a very poor efficiency of the post-print cleaning process, since all containers and especially all micro-pillars and cavities were obviously covered with leftover of uncured resin material. Despite the blurry and undefined appearance, some indications on the shape of the micro-pillars could be observed. When taking these indications into account and comparing the dimensions of the probable pillar diameters with the dimensions from the CAD model, it becomes apparent that, in accordance with all previous experiments, there is a strong deviation between these dimensions, because the printed pillars were larger in all cases. Though, the extent of size deviation was dependent on the pillar size, as from smaller to larger pillars, the print outcome was 6.3 (a), 3.4 (b), 2.6 (c), 2.4 (d), 2.2 (e) and 2.1 (f) times

larger. When comparing the CAD drawings with the SEM images of the printed samples it also becomes apparent that there was much less space in between the pillars and that the different samples generally looked much more similar than the CAD-drawings did. Additionally, some samples (a, e and f) show flat structures protruding out of the container base, suggesting that the print shifted in the XY-plane during the print, causing a print defect. In accordance with the previously described experiments, no single lithographic layers were visible.

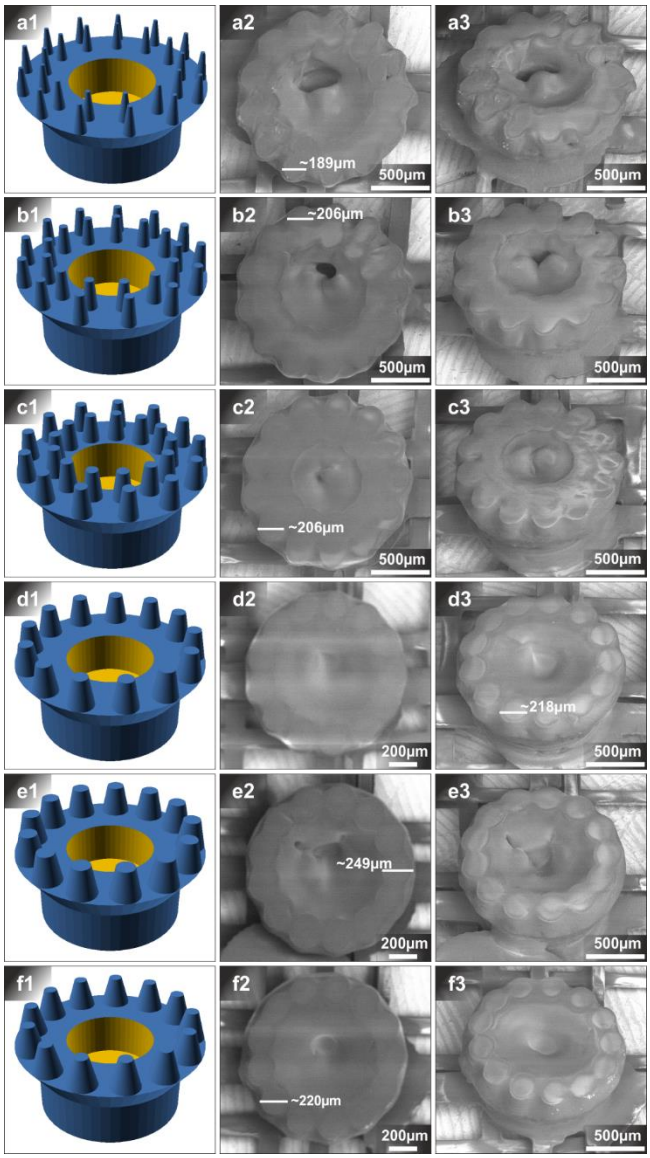

Figure 5 *Resolution assay 1: effect of micro-pillar dimensions on print outcome. STL-file models (a1-f1) and SEM images (a2-f2, a3-f3) of microcontainers with differently sized micro-pillars placed on overhang. All STL-models featured an overall diameter of 1000 µm in the bottom and 1300 µm including overhang. Excluding the pillars, all microcontainers had a height of 500 µm. The dimensions of the micro-pillar top- and bottom diameters were as follows: (a1) 30 µm-80 µm, (b1) 60 µm-100 µm, (c1) 80 µm-130 µm, (d1) 100 µm-170 µm, (e1) 120 µm-200 µm and (f1) 90 µm-200 µm. The height of the micro-pillars was set to be 200 µm. SEM images (a3-f3) were recorded from a 35° tilted angle.*

In the following experiments, the influence of other single parameters on the print outcome was investigated. At first, the pillar height was increased from 200 µm to 300 µm (Figure 6). Also, in this case, the pillars and container cavities were covered with leftover resin. The overall morphologies were similar to those of the previous experiment and no effect of the increased pillar height could be noticed. The size deviation of the pillars followed the same trend as reported before, since the pillars were 6.7 (a), 3.5 (b), 2.9 (c), 2.4 (d), 2.3 (e) and 1.9 (f) times larger than the dimensions given in the CAD-model.

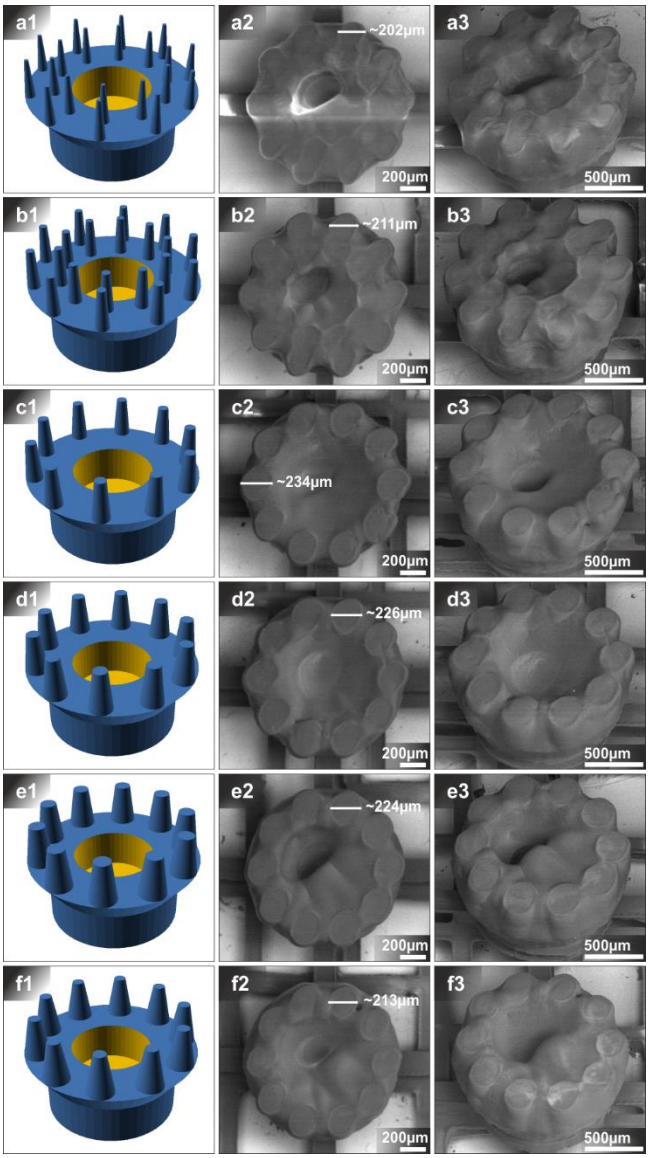

Figure 6 *Resolution assay 2: effect on micro-pillar height on print outcome. STL-file models (a1-f1) and SEM images (a2-f2, a3-f3) of microcontainers with differently sized micro-pillars placed on overhang. All STL-models featured an overall diameter of 1000 µm in the bottom and 1300 µm including overhang. Excluding the pillars, all microcontainers had a height of 500 µm. The dimensions of the micro-pillar top- and bottom diameters were as follows: (a1) 30 µm-80 µm, (b1) 60 µm-100 µm, (c1) 80 µm-130 µm, (d1) 100 µm-170 µm, (e1) 120 µm-200 µm and (f1) 90 µm-200 µm. The height of the micro-pillars was set to be 300 µm. SEM images (a3-f3) were recorded from a 35° tilted angle.*

In the next step, the overall container diameter was decreased from 1300 to 1000 µm including and from 1000 to 700 µm excluding overhang (Figure 7). As a consequence, the computer algorithm to generate the CAD models placed fewer micro-pillars on top of the containers and increased the space between those.

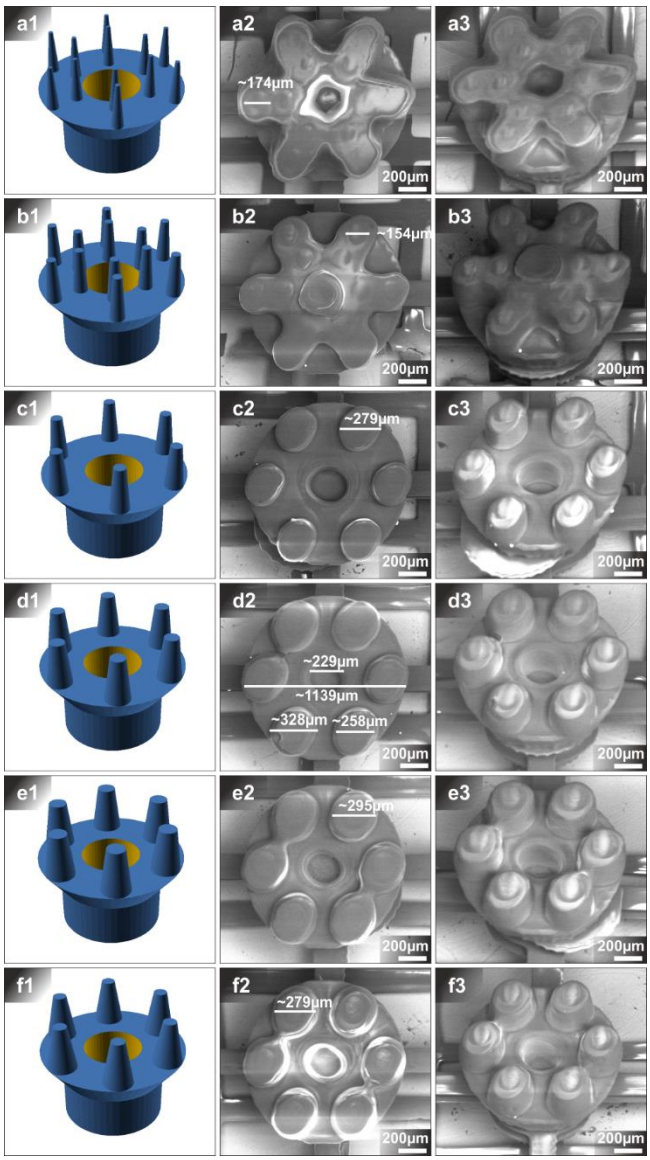

Figure 7 *Resolution assay 3: decreasing microcontainer size. STL-file models (a1-f1) and SEM (a2-f2, a3-f3) of microcontainers with differently sized micro-pillars placed on overhang. In contrast to the other figures, all STL-models featured an overall diameter of 700 µm in the bottom and 1000 µm including overhang. Excluding the pillars, all microcontainers had a height of 500 µm. The dimensions of the micro-pillar top- and bottom diameters were: (a1) 30 µm-80 µm, (b1) 60 µm-100 µm, (c1) 80 µm-130 µm, (d1) 100 µm-170 µm, (e1) 120 µm-200 µm and (f1) 90 µm-200 µm. The height of the micro-pillars was set to be 300 µm. SEM images (a3-f3) were recorded from a 35° tilted angle.*

The samples illustrated in (a) and (b) were covered with leftover of uncured resin as it was the case in the previous described experiments. However, in contrast to prior observations, samples (a) and (b) seemed to be covered with less resin, as the uncured material was only connecting the pillars forming a star shape and leaving surface of the microcontainer exposed. In case of the other samples (c-f) even less leftover resin could be observed. Despite the presence of leftover resin on the pillars, the shape of the top diameter could be seen as the pillars displayed a rather shiny surface in the center as compared to the edges. This could be observed best when considering the SEM images taken from an angled perspective. In accordance with prior experiments, the size deviation of the pillars followed the trend of deviating stronger at smaller dimensions, since the pillars were 5.8 (a), 2.6 (b), 3.5 (c), 3.1 (d), 2.6 (e) and 2.5 (f) times larger than given in the CAD drawing. Single lithographic layers were not detected as well. In comparison with the CAD drawings, the cavities were smaller. In case of the sample displayed in (d), the cavity was measured to be 229 µm wide while the CAD-model specified a width of 400 µm. The samples shown in (c) and (e) showed similar print defects as described earlier.

In summary, it can be concluded that the change of container overall size did not deteriorate the general print outcome. In contrast, the placement of fewer pillars on top of the microcontainers facilitated a better separation of the pillars and as a consequence the post-print cleaning process probably removed more resin residue than in the other cases.

In the next experiment, the general container height was decreased from 500 to 350 µm and the height of the pillars was decreased down to 200 µm, because the change of pillar height did not show a noticeable effect in prior experiments (Figure 8). The printed microcontainers displayed similar morphologies to those of the previous experiment. In (a) and (b), the leftover resin connected the micro-pillars to form a star shape. However, in these cases the cavities of the containers did not seem to be filled with resin residue while they were still smaller as defined in the CAD models. For example, in (a) the cavity was measured to be 257 µm wide instead of 400 µm as given in the design. The morphologies were not similar with respect to the varying shine of the pillar surfaces that was mentioned earlier. For the samples at hand, no differences were visible. Therefore, close inspection revealed that single lithographic layers were visible at the sides of the micro-pillars in the case of samples (c) to (f). This can be seen best from a tilted angle. With increasing size, the pillars were 6.4 (a), 3.3 (b), 2.9 (c), 2.6 (d), 2.6 (e) and 2.3 (f) times larger than the dimensions given by the design. The differences in morphology, when comparing with previously described results, could not be considered to be associated with the reduction in container and pillar height, since they were probably related to variations in the presence of resin residue.

As a last experiment, the overall diameter of the microcontainers was increased from 1000 µm including and 700 µm excluding overhang to 2000 µm including and 1500 µm excluding overhang (Figure 9). As a consequence of this change, more pillars could be arranged on top of the microcontainer surfaces.

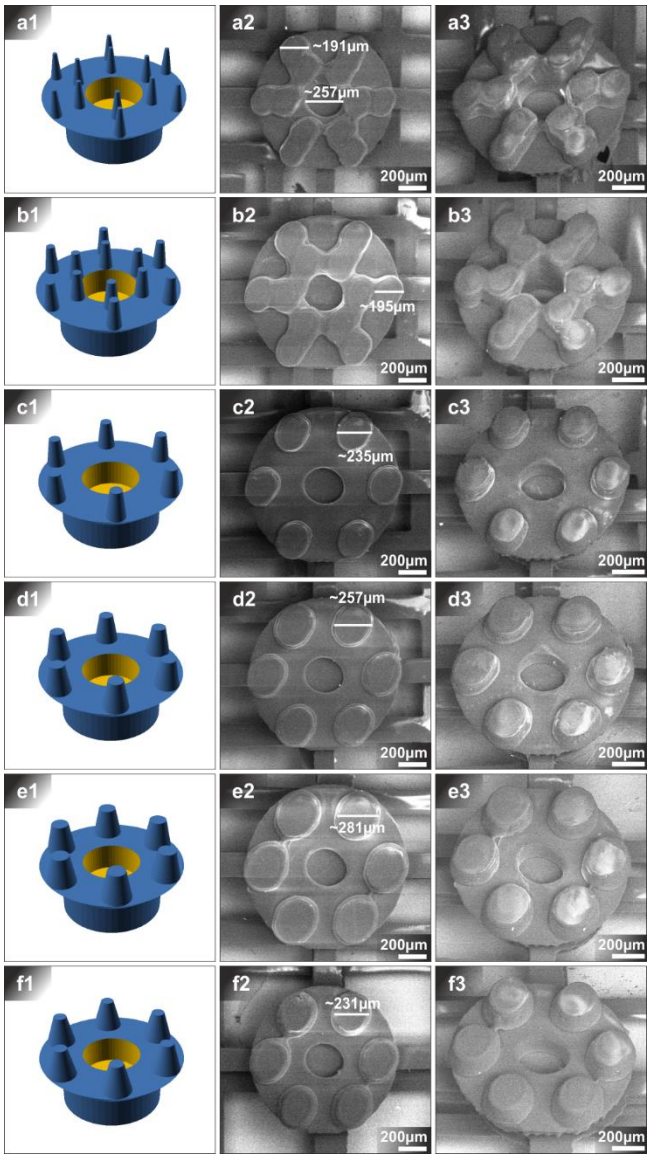

Figure 8 *Resolution assay 4: effect of microcontainer height on print outcome. STL-file models (a1-f1) and SEM images (a2-f2, a3-f3) of microcontainers with differently sized micro-pillars placed on overhang. All STL-models featured an overall diameter of 700 µm in the bottom and 1000 µm including overhang. The dimensions of the micro-pillar top- and bottom diameters were: (a1) 30 µm-80 µm, (b1) 60 µm-100 µm, (c1) 80 µm-130 µm, (d1) 100 µm-170 µm, (e1) 120 µm-200 µm and (f1) 90 µm-200 µm. The height of the microcontainers excluding micro-pillars (height = 200 µm) was set to be 350 µm. SEM images (a3-f3) were recorded from a 35° tilted angle.*

The micro-pillars of the samples that are depicted in (a) to (d) were not separated and shared a uniform surface. However, patterns that indicated the shape of the top diameter of the pillars could be found in all cases. Apart from that, the pillars could be recognized when considering the images taken from an angle. These findings suggest that in coherence with the other results, resin residue was covering the pillar structures of the microcontainers. Upon further inspection from the tilted perspective, single lithographic layers could be recognized, not only for the pillars, but also for the container structure. Except from the pillar surfaces which were

covered with resin residue, the surfaces of the microcontainers were smooth and the cavities were sharply defined. The measured dimensions of the pillar diameters which are displayed in the SEM images deviated from the dimensions that were defined in the CAD drawings. Beginning from small pillars to large pillars, they were 7.8 (a), 3.9 (b), 3.2 (c), 2.9 (d), 2.6 (e) and 2.1 (f) times larger than specified nominal dimensions. Although the size deviation of the micro-pillars could not be considered to differ a lot from the previous results, the overall print quality of the microcontainers as a whole was improved in this experiment. Additionally, less resin residue could be found.

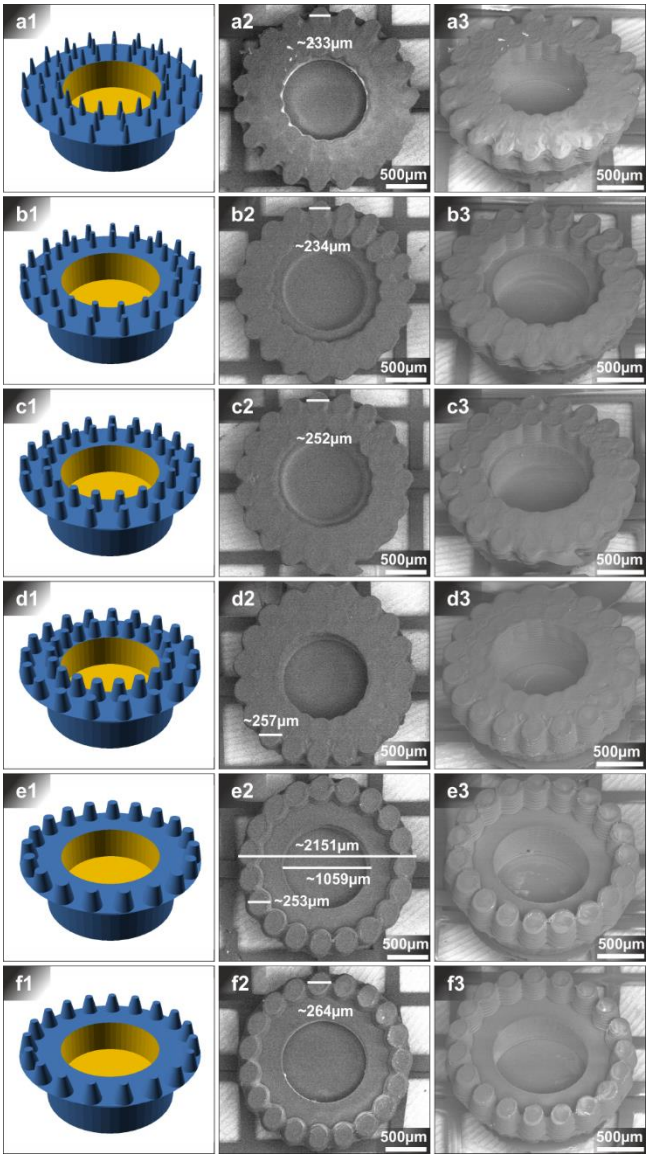

Figure 9 *Resolution assay 5: increasing microcontainer overall size. STL-file models (a1-f1) and SEM images (a2-f2, a3-f3) of microcontainers with differently sized micro-pillars placed on overhang. In contrast to the other figures, all STL-models featured an overall diameter of 1500 µm in the bottom and 2000 µm including overhang. Excluding the pillars, all microcontainers had a height of 600 µm. The dimensions of the micro-pillar top- and bottom diameters were: (a1) 30 µm-80 µm, (b1) 60 µm-100 µm, (c1) 80 µm-130 µm, (d1) 100 µm-170 µm, (e1) 120 µm-200 µm and (f1) 90 µm-200 µm. The height of the micro-pillars was set to be 200 µm. SEM images (A-F3) were recorded from a 35° tilted angle.*

Conclusions

In this work challenges and opportunities of using μSLA 3D printing for the manufacturing of various microcontainer geometries were investigated. The reported results showed an obvious deviation between dimensions of the printed structures and the ones given by the CAD models. In general, it could be observed that structures with smaller dimensions deviated more from the defined target values than structures with larger dimensions, thus showing the technical limitations of the employed 3D printing system.

Moreover, it was noticeable that in all experiments, the outcome of the 3D printing was substantially affected by the presence of leftover uncured print resin. The resin filled the reservoirs of the microcontainers and the interspaces between the micro-pillars placed on the edges. While the problem of 3D printing "cups" in stereolithography is a known issue, the post processing of 3D printed structures should accommodate for the removal of excess uncured print resin.[8] Under the premise that the post-treatment/cleaning protocol will necessarily need to be the subject of a thorough optimization work, this research demonstrates the feasibility of using μSLA 3D printing to fabricate microcontainers for oral drug delivery since millimeter-sized devices could be realized with this micro manufacturing technology.

From an application point of view a further problem remains. All microcontainers were additively manufactured on a likewise 3D printed grid which irreversibly connected them. Nevertheless, the working principle of microcontainers for oral drug delivery relies on individually acting containers that attach to the intestinal mucosa. With the current 3D printing method, the release of individual microcontainers is not possible. Therefore, the implementation of 3D printing on a sacrificial release layer as done in micromachining is suggested.[9]

Experimental

Generation of Microcontainer Designs: The topology optimized design was created by solving a heat conduction problem subject to a volume constraint as presented previously.[7]
All other designs were programmed in OpenSCAD open-source software.

3D Printing of Microcontainers: 3D printing files were prepared with Magics software (Materialise NV, Belgium). All 3D prints were conducted using a D-MEC Acculas BA-30 micro-stereolithography system (D-MEC LTD., Japan). After completing the 3D printing procedure, printed structures were immersed in isopropanol for 5 min using a spray bottle and dried with pressurized air.

Scanning Electron Microscopy of Samples: All microscopy was performed using a JSM-6510 Series scanning electron microscope (JEOL Ltd., Japan).

Conflict of Interest

The authors declare no conflict of interest.

Acknowledgements

The authors acknowledge the Center for Intelligent Drug Delivery and Sensing Using Microcontainers and Nanomechanics (IDUN) whose research is funded by the Danish National Research Foundation (DNRF122) and Villum Fonden (Grant No. 9301).

This study was partly supported by the Grant-in-Aid for Scientific Research (Category A, Project no. 17H01224) from the Japan Society for the Promotion of Science (JSPS), the Centre Of Innovation (COI) program from the Japan Science and Technology Agency (JST), the Strategic Innovation Creation Project (SIP) from the New Energy and Industrial Technology Development Organization (NEDO) of Japan, and the Program on Open Innovation Platform with Enterprises, Research Institute and Academia (OPERA) from the JST.

The authors would also like to thank Kyuuichiro Takamatsu for operating the 3D printer and Masato Wada for operating the scanning electron microscope.

References

1. A. Ahmed, C. Bonner, and T. A. Desai, *Biomed. Microdevices*, **3**, 89–96 (2001).

2. H. D. Chirra, L. Shao, N. Ciaccio, C. B. Fox, J. M. Wade, A. Ma, and T. A. Desai, *Adv. Healthc. Mater.*, **3**, 1648–1654 (2014).

3. T. A. Sonia and C. P. Sharma, *Drug Discov. Today*, **17**, 784–792 (2012).

4. P. E. Petrochenko, J. Torgersen, P. Gruber, L. A. Hicks, J. Zheng, G. Kumar, R. J. Narayan, P. L. Goering, R. Liska, J. Stampfl, and A. Ovsianikov, *Adv. Healthc. Mater.*, **4**, 739–747 (2015).

5. P. Marizza, S. S. Keller, A. Müllertz, and A. Boisen, *J. Control. Release*, **173**, 1–9 (2014).

6. R. S. Petersen, S. S. Keller, and A. Boisen, *Lab Chip*, **15**, 2576–2579 (2015).

7. K. E. Jensen, in *Advances in Structural and Multidisciplinary Optimization*,, p. 1224–1238, Springer International Publishing, Cham (2018).

8. Formlabs Inc., (2018) https://support.formlabs.com/s/article/Model-Orientation?language=en.

9. V. Linder, B. D. Gates, D. Ryan, B. A. Parviz, and G. M. Whitesides, *Small*, **1**, 730–736 (2005).

7.2 Manuscript II

Sacrificial Polymer Substrates in Photopolymerization-based Micro 3D Printing for Fabrication and Release of Complex Micro Components

L. Vaut, G. Zeng, G. Tosello, A. Boisen

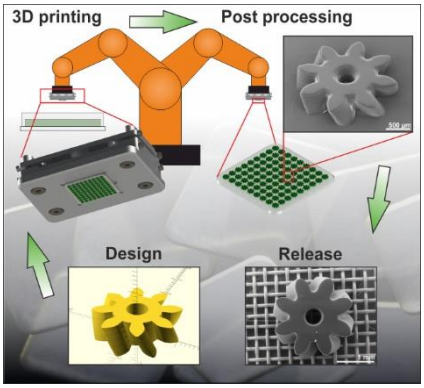

3D printing on top of sacrificial substrates is demonstrated. The used 3D printing workflow enables the 3D printing on quickly exchangeable substrates, further array-based processing of 3D printed products and easy manipulation, as well as integration into industrial production lines. 3D printed products can be mildly released from the substrates upon dissolution of sacrificial material and harvested.

Sacrificial Polymer Substrates in Photopolymerization-based Micro 3D Printing for Fabrication and Release of Complex Micro Components

Lukas Vaut[1], Guanghong Zeng, Guido Tosello and Anja Boisen*[2]*

L.Vaut, Prof. A. Boisen, The Danish National Research Foundation and Villum Foundation's Center for Intelligent Drug Delivery and Sensing Using Microcontainers and Nanomechanics (IDUN), Department of Health Technology, Technical University of Denmark, Kgs. Lyngby, 2800, Denmark

Dr. G. Zeng, DFM A/S (Danish Fundamental Metrology), Hørsholm, 2970, Denmark

Prof. G. Tosello, Department of Mechanical Engineering, Technical University of Denmark, Kgs. Lyngby, 2800, Denmark

E-mail: [1] lukv@dtu.dk, [2] aboi@dtu.dk

Keywords: micro additive manufacturing, sacrificial release layers, 3D microfabrication, micro stereolithography, medical device manufacturing

3D printing technology is widely employed in various scientific disciplines as well as industrial applications such as hearing aid manufacturing. While technological advances and increasing resolution are making 3D printing accessible for microfabrication purposes, one question remains: how can small and delicate components like micro gears, lattices or micro medical devices be released from the build surface of the 3D printer without manual intervention? Herein, a method for 3D printing on top of water-soluble sacrificial substrates made from polyvinyl alcohol (PVA) is presented. Pre-fabricated sacrificial PVA substrates can be mounted onto a customized holder and serve as build surface during the 3D printing operation. The substrates do not only facilitate a mild release of 3D printed objects after dissolution of the sacrificial material, they also potentially allow for a convenient manipulation, automation, further array-based processing steps and consequently full integration into production lines. The fabrication of PVA substrates is thoroughly characterized and the 3D printing of various exemplary structures on sacrificial substrates is demonstrated. Finally, the release of 3D printed objects from PVA substrates is shown.

3D printing has attracted interest since the release of the core inventions of stereolithography (SL) in 1986 and fused deposition modeling (FDM) in 1992, and continues to be a hot topic.[1,2] The use of 3D printing spans a broad range of applications in different areas such as architecture, automotive industry and medicine. It is used to rapidly produce prototypes as well as functional end-products. Especially in the medical field, 3D printing holds great potential due to the possibility to fabricate customized components with high complexity. Examples of already successful implementations of 3D printing in industrial fabrication of medical products comprise for example dental appliances and hearing aids.[3,4] Medical and biomedical applications often require miniaturization of products.[5] Due to advances in resolution and material availability, 3D printing has become a viable alternative to other microfabrication methods in many areas, including biomedical research.[6] Research efforts in this area cover a broad variety of 3D printed products, ranging from micro medical

components such as bioresorbable vascular stents to microscale 3D scaffolds for tissue engineering, oral modified-release dosage forms as well as to propulsion-capable artificial microfish intended for toxin-neutralization applications.[7–10]

As pointed out by Quinlan et al., 3D printing has a low overall build rate when compared to other manufacturing processes, e.g. injection molding, and is therefore less attractive for mass production in general. However, the start-up as well as maintenance costs related to conventional manufacturing processes like injection molding and machining can be very high, especially when the complexity of the product increases.[11] The low capital costs of 3D printing thus makes it attractive for small to medium scale production in research and development. When compared to other lithography- or micromachining-based fabrication techniques, micro 3D printing is advantageous as the other techniques are limited with respect to three-dimensional complexity, ease of operation and production of assemblies with moving parts.[12] One major drawback of 3D printing, however, is the low resolution compared to e.g. photolithography (minimum feature size of 2-3 μm) and electron beam lithography (down to 5 nm).[13] It must be noted though, that 3D printing resolution is a subject of development and progress is shown on a frequent basis (e.g. custom built 3D printer by Gong et al. with a resolution of 7.6 μm).[14] Using common digital light processing (DLP)-based SL as well as conventional SL 3D printing, voxel sizes down to 30 μm can easily be achieved.

Current micro 3D printing requires manual removal of the printed objects from the build surface by human intervention. This presents an obstacle towards automation and serial production as any component pattern enabling further computer numerical control (CNC) or other array-based processing is corrupted. Additionally, small prints are easily damaged during the manual print removal process. The release of single structures from a common substrate by means of a sacrificial release layer, e.g. a water soluble release layer, is a common procedure in micromachining and microfabrication.[15] In FDM 3D printing, Polyvinyl alcohol (PVA) and high impact polystyrene (HIPS) are used as built-in sacrificial support structures.

Here, we use a sacrificial material substrate as the build surface in vat photopolymerization-based 3D printing. The substrate enables further processing steps in an automated production line, and it allows for a mild release by dissolution of the sacrificial material. We developed a simple workflow to fabricate substrates from PVA (**Scheme 1**a), which can be placed into a vacuum actuated holder (Scheme 1b). This assembly can be inserted into a desktop DLP-SL 3D printer, in which the PVA substrate serves as the build surface (Scheme 1c). Later, the substrate can be utilized for easy manipulation of the 3D printed structures as well as for further processing steps. The PVA substrate can finally be dissolved in water to release the individual 3D printed structures. Advantages of PVA, in this case, include water solubility and chemical resistance against many solvents.[16]

To ensure that the substrate material does not interfere with the photopolymer or the photocuring reaction, Raman spectroscopy was performed on three different 3D printing photopolymers mixed with three different PVAs (Figure S 1, Supporting Information).

Comparing the spectra of non-contaminated photopolymer as control and photopolymer/PVA mixture, no changes could be observed and the PVA did not dissolve in the photopolymer or affect it otherwise. Consequently, we conclude that PVA does not alter the chemical status of the photopolymer, does not interfere with the 3D printing process and thus is a suitable substrate material.

The substrates used in this work for vat photopolymerization 3D printing were fabricated by FDM 3D printing of a precursor substrate and subsequent compression molding as described in Scheme 1a. To demonstrate the possibility for cheap and scalable substrate production we also performed laser cutting of a sheet of PVA as well as direct injection molding of PVA-polymer substrates (Figure S 2, Supporting Information).

For 3D printing, the fabricated PVA substrates must be produced with suitable surface characteristics as well as uniform thickness.

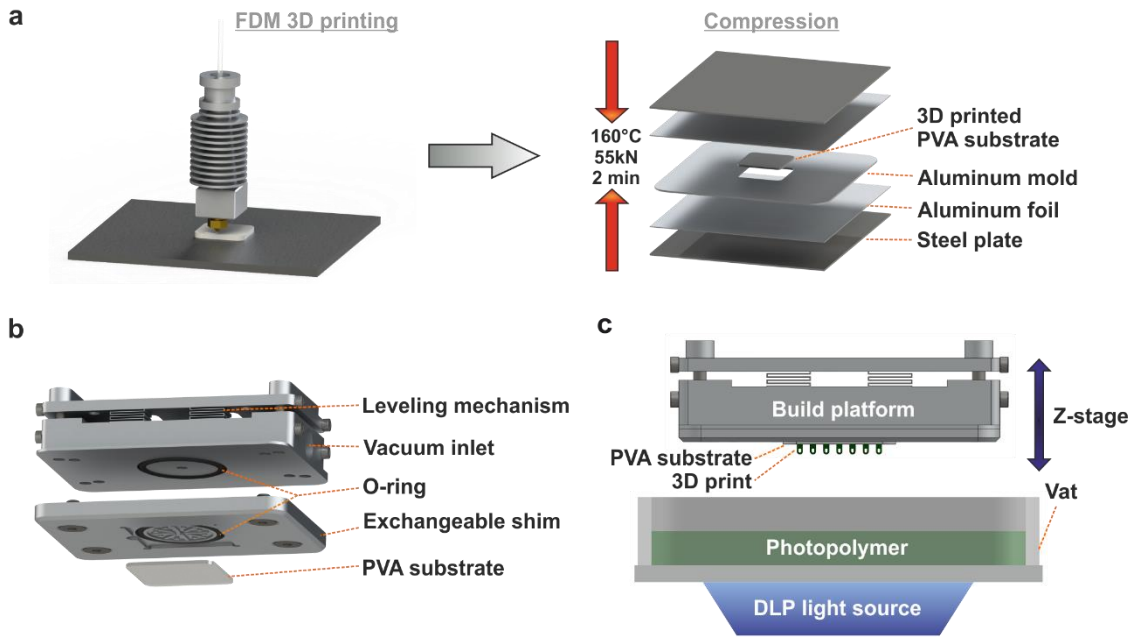

Scheme 1. *Illustration of workflow for the realization of DLP-SL 3D printing on sacrificial substrates. a) Two step fabrication sequence of PVA substrates. FDM 3D printing of PVA precursor substrates and subsequent compression molding using a simple mold assembly. b) Design of customized vacuum-actuated substrate holder for the use in a desktop DLP-SL 3D printer. c) Working principle of using pre-fabricated PVA substrates in a DLP-SL 3D printer. The PVA substrate is used as the build surface and held in place by the vacuum-actuated holder (build platform) which moves in Z direction. In an industrial production line setting, the holder could be operated by a robotic arm which also carries out further processing steps.*

It is required that the substrates have sufficient surface flatness to ensure good contact between the substrate and the polymerization interface during the printing procedure, especially when the first layers of the objects are created. The peak-to-valley flatness parameter (FLTt; ISO 12781) was locally probed in areas of 1.27 x 0.96 mm using optical

profilometry with digital interferometry (DI) and confocal (CF) observation conditions and analyzed after applying a robust gaussian filter (cut-off: 25 µm; ISO 16610) to eliminate noise, outliers and short-wave details (**Figure 1**a).[17,18] Different substrates were analyzed: compression molded (CM), hand-roughened (CM-S) and injection molded (IM) PVA substrates. A commercial anodized aluminum 3D printer build platform (BP), plain aluminum substrates (Al) and a silicon wafer (Si) were included as reference substrates. BP and Al substrates served to compare the fabricated PVA substrates to frequently used 3D printing surfaces, Si exclusively served as a quality reference. The analysis of the flatness measurements (**Figure 2**a) shows that, except for CM and Al samples, which exhibit similar flatness (FLTt ≈ 2.4 µm; DI), samples have significantly different FLTt values with large effect sizes (Table S 1, Supporting Information). During the compression molding, the polymer surface adapts the negative of the molds' surface texture. Thus, CM and Al samples have similar flatness as CM substrates were molded with the use of flat aluminum sheets. While BP has the lowest flatness (FLTt ≈ 12.11 (DI) and 15.55 µm (CF)), Si has the highest flatness with an FLTt value (0.18 µm; DI) up to two orders of magnitude lower than the ones of the other samples. In comparison with CM samples (FLTt ≈ 3.37 µm; CF), CM-S samples show a reduced flatness (FLTt ≈ 5.46 µm; CF), which can be explained by the hand-roughening treatment as sanding marks can be observed (Figure 1a). IM samples also show lower flatness (5.78 µm; DI) when compared to CM. In the case of IM samples, the surface texture is determined by the manufacturing of the molding tool.

The roughness of the surface can affect adhesion and has been found to be proportional with bond strength of adhesives.[19,20] During the 3D printing procedure, it is fundamental that the first layer of cured photopolymer adheres well to the build surface since the 3D printed objects are subject to tensile stress due to continuous movement of the Z-axis and subsequent separation from the polymerization interface. The local surface roughness, more specifically the arithmetical mean height (Sa), was determined using digital interferometry-based optical profilometry (Figure 1b).[21] The evaluation of conducted Sa measurements (Figure 2b) show significant differences with large effect sizes between the different samples, except for CM-S (Sa ≈ 573 nm) and IM samples (Sa ≈ 623 nm) (Table S 2, Supporting Information). Si has the lowest roughness (Sa ≈ 2nm), which matches the specifications of the manufacturer, while BP appears to have the roughest surface (Sa ≈ 1.79 µm). When compared to BP, CM has a significantly lower roughness (Sa ≈ 134 nm). The hand-roughening treatment is seen to greatly increase the roughness of CM-S substrates when compared with CM substrates, which can also be seen in the example of the very complex surface in Figure 1b. Even though CM-S and IM have similar Sa values, the surfaces exhibit very different surface morphologies. The Sa value does not give any indications of the surface morphology and therefore we calculated the developed interfacial area ratio (Sdr), which is a measure for surface complexity and also a better indication of adhesive properties.[22] The analysis of Sdr values shows significant differences between all samples (Table S 3, Supporting Information). The results mainly follow the trend that could be observed in Sa measurements, with better differentiated values for CM-S and IM. The Sdr-value for CM-S was two orders of magnitude higher than for CM.

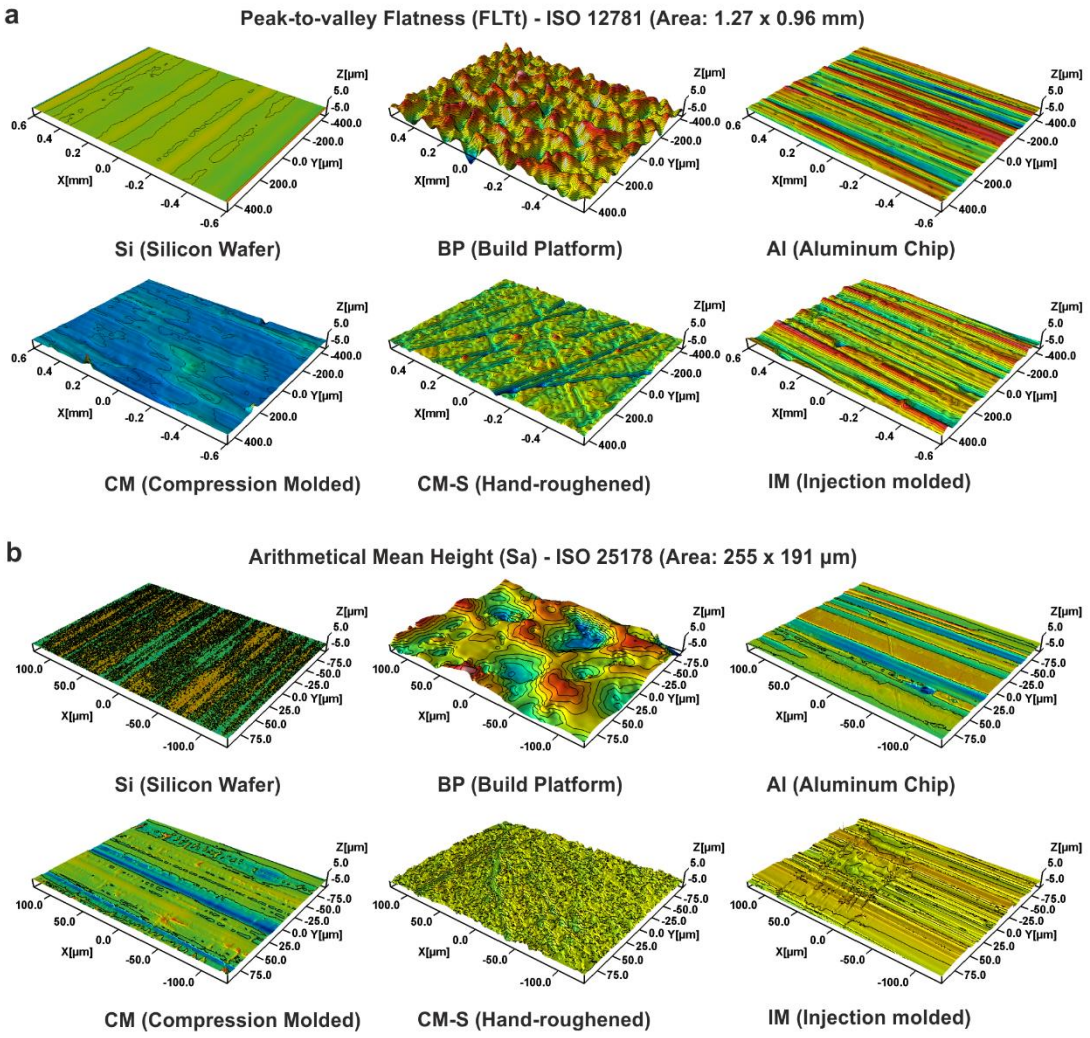

Figure 1. *Flatness and roughness measurements obtained by optical profilometry. a) Representative surface renderings of substrates used for flatness analysis. Computed from data acquired with a 20X confocal lens in stitching mode (BP, CM and CM-S) and a 10X interferometry lens (Si, Al and IM). b) Representative surface renderings of data used for roughness analysis (Sa and Sdr). Computed from acquisitions with a 50X interferometry lens.*

Thickness measurements of different PVA substrates were conducted (Figure 2d), and the measurements on deviation from target thickness show that values obtained for the compression molded PVA substrates (CM) lie in a range of ≈ 26 µm. In the case of hand-roughened compression molded samples (CM-S) and injection molded samples (IM), the measurements lie in a range of ≈ 43 µm and ≈ 23 µm, respectively. To ensure a successful printing without the need for recurring calibrations, the thickness deviation of the substrates should be smaller than the layer thickness of the individually exposed layers during the 3D printing procedure. As the layer height of the 3D printer in this case was 25 µm, a thickness deviation above 25 µm could call for recurring homing calibrations. The lack of precision in thickness repeatability for CM substrates can partially be explained by the deviation in material dispensing during FDM 3D printing of the precursor substrate. Here, an observed weight deviation with a range of 8.66 mg (N = 10) can translate into a 16-17 µm thickness

deviation when taking the final substrate dimensions into account and assuming a PVA density of 1.19-1.31 g/cm³.[23] Furthermore, the manual handling during the molding procedure leaves room for error. It is to be expected that the thickness deviation is higher for CM-S substrates than for CM substrates, since it is likely that the hand-roughening treatment unevenly affected the final thickness of the substrates. We note that the deviation for CM substrates is not much higher than for injection molded substrates. A further optimization of the CM fabrication processes can lead to a much higher precision in thickness repeatability, allowing for users without access to injection molding to fabricate their own high-quality substrates.

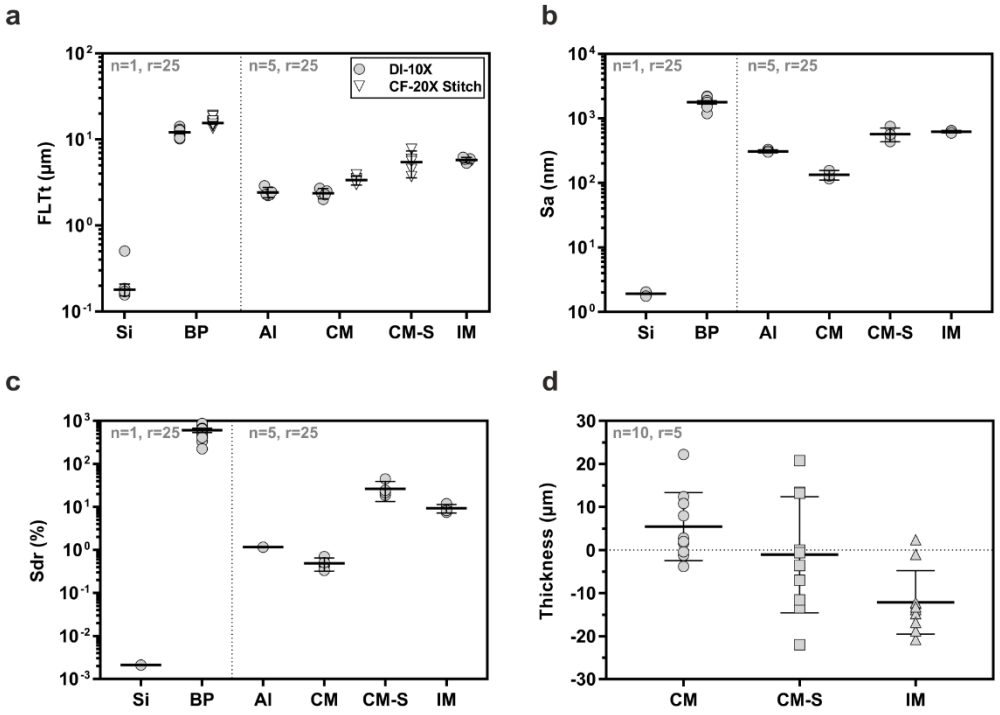

Figure 2. *Flatness, roughness and thickness characterization of different 3D printing substrates: Plain aluminum (Al), compression molded (CM), hand-roughened CM (CM-S) and injection molded (IM) PVA and reference substrates: Silicon wafer (Si) and commercial anodized 3D printer build platform (BP). Error bars represent 95% confidence interval in a, b and c and standard deviation in d. a) Peak-to-valley flatness deviation (FLTt) measurements from optical profilometry surface data obtained with digital interferometry (DI) and confocal (CF) observation conditions. For statistical comparison see Table S 1. b) Arithmetical mean height (Sa) measurements from optical profilometry surface data. For statistical comparison see Table S 2. c) Developed interfacial area ratio (Sdr) computed from optical profilometry surface data. d) Micrometer thickness measurements of PVA substrates adjusted to target values. Y = 0 represents target value of final substrate thickness. N = 10. Statistical comparison available in Table S 3. For a), b) and c) counts: N=5 with 5 different samples in case of Al, CM, CM-S and IM and N = 1 with 25 repeated measurements on the same sample in case of Si and BP.*

Since standard deviations were smaller than ± 25 µm in all cases, the study was continued based on the same CM fabrication process and without recurring homing calibrations.

Using a commercial DLP-SL 3D printer and a custom vacuum-actuated holder (see Scheme 1b), we were able to 3D print various exemplary structures on CM PVA substrates (**Figure 3**). The workflow allowed us to 3D print arrays of defined geometrical objects on top of PVA substrates and to remove the entire substrate from the holder after finished 3D printing. 3D printed example structures include those, e.g. helical micro-gear and micro-truss lattice, which are nearly impossible to fabricate by other conventional manufacturing techniques, such as injection molding or micromachining.

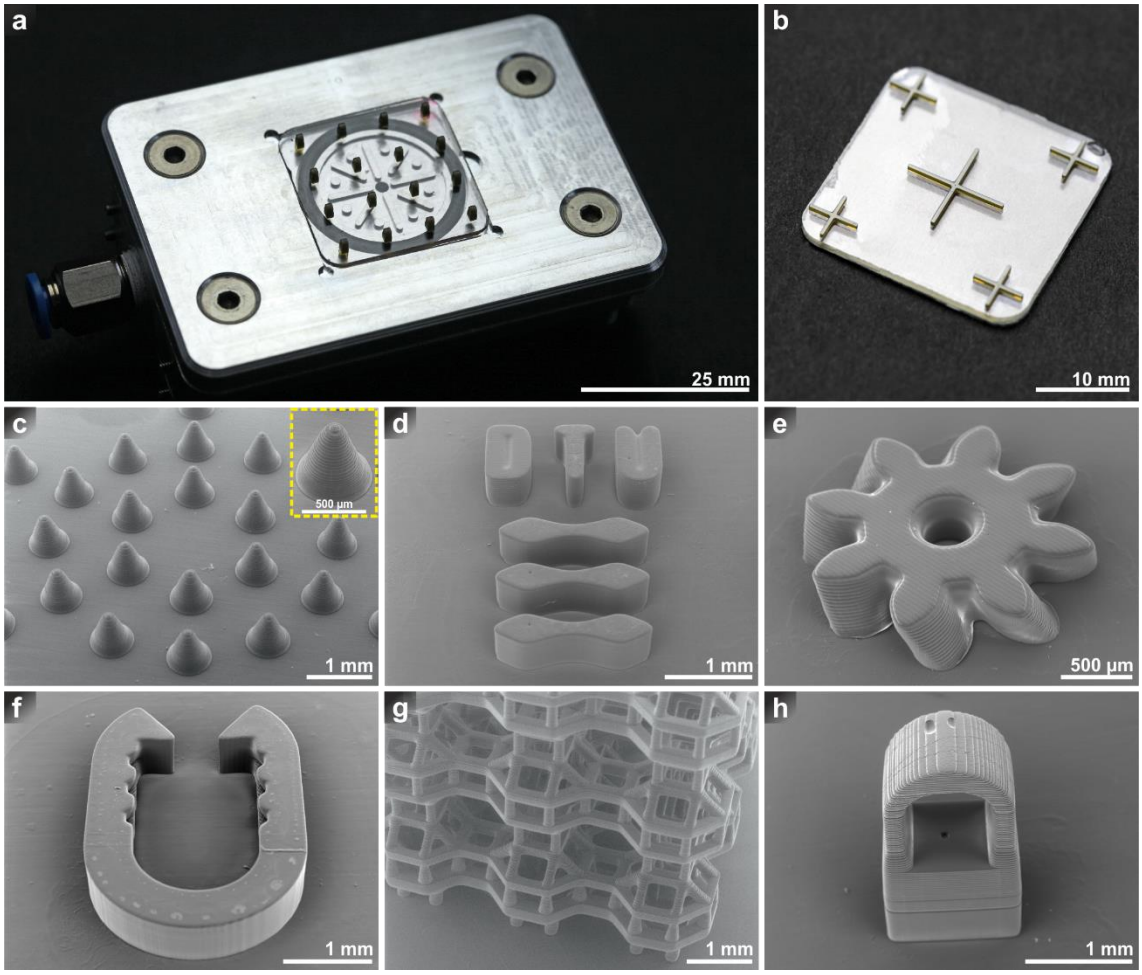

Figure 3. *Photographs and SEM micrographs of 3D printed structures on compression molded PVA substrates (CM). a) Array of printed structures on PVA substrate inserted in vacuum-actuated holder (see schematics in Scheme 1b and c). b) 3D printed crosshairs, facilitating evaluation of alignment of PVA substrate and printed structures. c) Circular array of micro-cones. d) DTU logo assembly from separate 3D printed parts. e) Helical micro-gear with a twist of 25°. f) Surgical staple. g) Complex lattice made from micro-sized trusses.*[24] *h) Small structure used for evaluation of bond strength of 3D print to PVA substrate.*

Using a specifically for this purpose designed and 3D printed test object (Figure 3h) and a texture analyzer, we determined the detachment force to study the relationship between surface characteristics of the build surface and bond strength of the 3D print. The footprint of the test object matches the dimensions of areas probed for the flatness characterization. Arrays of the test object were 3D printed on BP, Al, CM and CM-S substrates and detachment force as well as work of adhesion (area under curve of detachment graph) were determined (Figure S 3, Supporting Information). The evaluation of the detachment force shows statistically significant differences with large effect sizes between all samples (Table S 4). Hand-roughening of PVA substrates significantly affected the bond strength between the test objects and CM-S substrates, thus revealing a much higher detachment force when compared to CM substrates. Despite having a rougher surface, Al and BP have lower detachment forces while Al has the lowest. An explanation for this might be the occurrence of polymer-polymer (photopolymer-PVA) interactions between the PVA substrates and the 3D printed objects, hence leading to a higher bond strength. The evaluation of the work of adhesion follows a similar trend, except for the fact that no difference between BP and Al can be found (Table S 5).

An array of helical micro-gears (Figure 3e) 3D printed on CM PVA substrates was released from the substrate within 150 min. (Figure S 4, Movie S 1, Supporting Information). Scanning electron microscopy of the harvested individual micro-gears shows that the gears are intact and free of substrate material (**Figure 4**). The dissolution rate of PVA is highly dependent on the type of PVA and also on the temperature.[16] Furthermore, the time needed for the dissolution depends on the amount of material to be dissolved. To illustrate that the release time can be reduced, composite CM PVA substrates with a non-dissolving polylactic acid (PLA) core were fabricated. The PLA core was fully encapsulated by the surrounding PVA and reduced the total amount of PVA by 50%. Using this substrate, the same array of micro-gears could be released within 90 min. (Figure S 5, Movie S 2, Supporting Information).

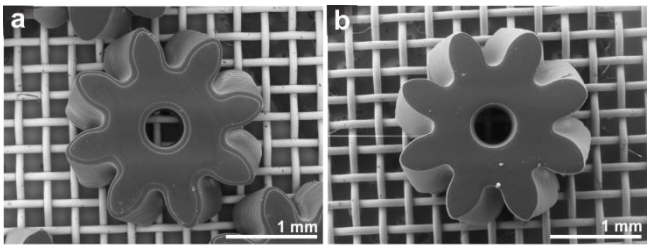

Figure 4. *SEM micrographs of 3D printed helical micro-gears (see Figure 3e) on stainless steel filtering mesh after dissolution of compression molded PVA substrates (CM) and subsequent release. a) front side. b) backside.*

In summary, we have demonstrated the use of water-soluble PVA sacrificial substrates in vat photopolymerization-based 3D printing. The fabrication of substrates with suitable flatness, roughness and thickness characteristics was accomplished at lab scale, and their specifications are compatible with industrial fabrication. The substrates were chemically compatible with different 3D printing photopolymers and exhibited good bond strengths to the 3D printed

objects. Using a custom-made vacuum-actuated holder, PVA substrates could be quickly exchanged and taken from the 3D printer, thereby enabling further array-based processing and potential integration into production lines. We showed that advanced 3D printed objects can be released through dissolution of the substrate, thereby eliminating the need for manual intervention.

Experimental Section

Materials: All chemicals and reagents were used as received. For the fabrication of PVA substrates different kinds of PVA material were used: RS Pro PVA 3D printing filament (RS Components A/S, Denmark), MOWIFLEX™ C17 and MOWIFLEX™ C600 (Kuraray Nordic Ab Oy, Finland). HTM 140M V2 3D printing photopolymer (EnvisionTEC GmbH, Germany) was used to 3D print onto PVA substrates. Further photopolymers were used for a compatibility study: PIC100 (EnvisionTEC GmbH, Germany) and Form Clear resin (Formlabs GmbH, Germany). 2-propanol (Sigma-Aldrich Denmark A/S, Denmark) was used for the post-treatment of 3D printed structures.

Characterization of PVA and reference substrates: The thickness of the fabricated substrates was measured in the center and in the four corners of each substrate using an RS Pro micrometer screw with an error of 0.001 mm (RS Components, Denmark). A PLu neox optical 3D profiler (Sensofar Metrology, Spain) served to conduct surface topology measurements, using confocal and interferometric microscopy. To analyze the flatness property of the various specimen, 10X interferometry and 20X confocal lenses were used for data acquisition. To compensate the loss in field of view when using the 20X confocal lens, stitching was used to combine four images to one bigger area image. A 50X interferometry lens was used to acquire data for the analysis of the surface roughness. In case of all specimens, a sampling procedure based on a 20 x 20 mm grid was performed to obtain surface measurements in a total of 25 spots in always the same relative positions. A 3" silicon wafer (No. 16013, Ted Pella inc., USA) with a specified roughness and total thickness variation of 2 nm and <20 μm, respectively, as well as the supplied build platform of an EnvisionTec Micro Plus High-Res DLP 3D printer were used as reference surfaces. Treatment and analysis of surface metrology data was done in SPIP 6.7.4 (Image Metrology A/S, Denmark) analytical software.

Computer aided design (CAD): All design tasks were carried out using SolidWorks 2015 (Dassault Systèmes SolidWorks Corporation, USA) and OpenSCAD open source software.

Machining of customized 3D printer build platform: A customized 3D printing build platform featuring a four-point spring leveling mechanism and a vacuum-actuated holding cavity for a print substrate was made to retrofit a Micro Plus High-Res digital light processing (DLP) 3D printer (EnvisionTec GmbH, Germany). The platform was machined by an external machining shop using a combination of CNC milling and electrical discharge machining.

3D printing on PVA substrates: The 3D printing on PVA substrates was conducted with an EnvisionTec Micro Plus High-Res DLP 3D printer with a XY resolution of 30 μm pixel size and a Z resolution of 25 μm. The 3D printer was retrofitted with a customized build platform to enable a flush leveling of the platform to the polymerization interface of the printer. Perfactory RP software (EnvisionTEC GmbH, Germany) served to create print files from the

prepared CAD models. After the printing procedure, the PVA substrate with printed structures on top was first cleaned from excess printing material in a beaker with 2-propanol placed in an ultrasound bath for 5 min and subsequently post-cured in an UV oven for 10 min (EnvisionTEC GmbH, Germany).

Scanning electron microscopy: All scanning electron microscopy was performed using a TM3030Plus tabletop scanning electron microscope (Hitachi High Technologies Europe GmbH, Germany). A 208HR high resolution sputter coater (Cressington Scientific Instruments, UK) equipped with a gold target was used to coat the specimens with a thin layer of gold (≈ 20 nm) prior to observation.

Statistics: All presented statistics were computed using R programming language and RStudio software (RStudio Inc., USA) as well as Microsoft Excel (Microsoft Corporation, USA). As in case of reference samples Si and BP only one specimen was available each, t-test results comparing those with Alu, CM, CM-S and IM samples are based on the assumption that the measured reference samples constitute ideal and representative samples of their kind. The results obtained in these cases can serve as an indication only, because resulting p-values might be distorted. Consequently, the reported effect sizes (Hedges' g) are more reliable.

Acknowledgements

The authors would like to acknowledge the Center for Intelligent Drug Delivery and Sensing Using Microcontainers and Nanomechanics (IDUN) whose research is funded by the Danish National Research Foundation (DNRF122) and Villum Fonden (Grant No. 9301).

Dr. Guanghong Zeng acknowledges funds from the Danish Agency for Institutions and Educational Grants, metrology for additively manufactured medical implants (short name: MetAMMI, project number: 15HLT09) from the EMPIR program. The EMPIR program is co-financed by the participating states and the European Union's Horizon 2020 research and innovation program.

The authors would also like to thank Dr. Kristian E. Jensen and Dr. Tommy Sonne Alstrøm for help with the manuscript preparation, Francesco Regi for performing injection molding and Jesper Scheel for photography. Furthermore, the authors would like to thank Ann-Britt Aspholm-van der Brugge and Kuraray Nordic Ab Oy for straightforward communication, great service and provision of free polymer samples.

Conflict of Interest

The authors declare no conflict of interest.

References

[1] C. W. Hull (UVP Inc.), *US 4575330,* 1986.

[2] S. S. Crump (Stratasys Inc.), *US 5121329,* 1992.

[3] N. Hopkinson, R. J. M. Hague, P. M. Dickens, *An Industrial Revolution for the Digital Age*, Wiley, Hoboken, NJ, USA, 2006.

[4] C. G. Sandström, *Technol. Forecast. Soc. Change* 2016, *102*, 160.

[5] L. Alting, F. Kimura, H. N. Hansen, G. Bissacco, *CIRP Ann.* 2003, *52*, 635.

[6] B. Gross, S. Y. Lockwood, D. M. Spence, *Anal. Chem.* 2017, *89*, 57.

[7] R. van Lith, E. Baker, H. Ware, J. Yang, A. C. Farsheed, C. Sun, G. Ameer, *Adv. Mater. Technol.* 2016, *1*, 1.

[8] N. A. Chartrain, C. B. Williams, A. R. Whittington, *Acta Biomater.* 2018, *74*, 90.

[9] J. Wang, A. Goyanes, S. Gaisford, A. W. Basit, *Int. J. Pharm.* 2016, *503*, 207.

[10] W. Zhu, J. Li, Y. J. Leong, I. Rozen, X. Qu, R. Dong, Z. Wu, W. Gao, P. H. Chung, J. Wang, S. Chen, *Adv. Mater.* 2015, *27*, 4411.

[11] H. E. Quinlan, T. Hasan, J. Jaddou, A. J. Hart, *J. Ind. Ecol.* 2017, *21*, S15.

[12] M. Vaezi, H. Seitz, S. Yang, *Int. J. Adv. Manuf. Technol.* 2013, *67*, 1721.

[13] A. Pimpin, W. Srituravanich, *Eng. J.* 2012, *16*, 37.

[14] H. Gong, B. P. Bickham, A. T. Woolley, G. P. Nordin, *Lab Chip* 2017, *17*, 2899.

[15] V. Linder, B. D. Gates, D. Ryan, B. A. Parviz, G. M. Whitesides, *Small* 2005, *1*, 730.

[16] C. A. Finch, *Polyvinyl Alcohol, Properties and Uses*, Wiley, Hoboken, NJ, USA, 1973.

[17] *ISO 12781-1:2011 - Geometrical Product Specifications (GPS) -- Flatness -- Part 1: Vocabulary and Parameters of Flatness*, International Organization For Standardization, Vernier, Geneva, Switzerland, 2011.

[18] *ISO 16610-71:2014 - Geometrical Product Specifications (GPS) -- Filtration -- Part 71: Robust Areal Filters: Gaussian Regression Filters*, International Organization For Standardization, Vernier, Geneva, Switzerland, 2014.

[19] M. Shahid, S. A. Hashim, *Int. J. Adhes. Adhes.* 2002, *22*, 235.

[20] P. Molitor, V. Barron, T. Young, *Int. J. Adhes. Adhes.* 2001, *21*, 129.

[21] *ISO 25178-2:2012 - Geometrical Product Specifications (GPS) -- Surface Texture: Areal -- Part 2: Terms, Definitions and Surface Texture Parameters*, International Organization For Standardization, Vernier, Geneva, Switzerland, 2012.

[22] R. Leach, *Characterisation of Areal Surface Texture*, Springer-Verlag GmbH, Heidelberg, Germany, 2013.

[23] ILO, WHO, “ICSC 1489 Polyvinyl alcohol,” https://www.ilo.org/dyn/icsc/showcard.display?p_lang=en&p_card_id=1489&p_version=2, accessed: 09, 2018.

[24] L. Rose, “Internal Structures for SLA, DLP, or SLS style printing,” https://www.thingiverse.com/thing:1394337/files, accessed: 03, 2018.

Supporting Information

Sacrificial Polymer Substrates in Photopolymerization-based Micro 3D Printing for Fabrication and Release of Complex Micro Components

Lukas Vaut[*1], *Guanghong Zeng, Guido Tosello and Anja Boisen*[*2]

E-mail: [1] *lukv@dtu.dk*, [2] *aboi@dtu.dk*

Experimental Section

Compatibility study using Raman spectroscopy: A compatibility assay was performed by incubating 200 mg of solid polyvinyl alcohol (PVA) material in 1 ml of liquid 3D printing photopolymer and analyzing a sample of the liquid after successive timepoints (1 h, 3 h, 1 d, 5 d) by Raman spectroscopy. When considering the use of one PVA substrate with a weight of 805 mg in the supplied vat of the 3D printer, which is filled with 150 ml of 3D printing polymer, the concentration amounts to 5.37 mg ml-1. The ratio of PVA to 3D printing polymer in the compatibility study was chosen to be multiple times higher. 3D printing polymer which was not in contact with PVA served as control. Raman spectroscopy was employed to determine molecular fingerprints of the samples.

Raman spectra were acquired with an in-house-built Raman spectroscopy system with improved sensitivity for Raman scattering registration in case of liquid samples. The system is based on a high power (500 mW) multimode laser with a wavelength of 785 nm. The laser had an intensity of 20 mW μm-2 and was focused on the sample through a liquid container with a CaF2 bottom plate. Measurements were carried out with a spectral resolution of 1.8 cm-1 in the range from 350 to 2100 cm-1 and collected using a CCD sensor. Wavelength and spectral sensitivity calibration of the instrument was performed according to ASTM 1840 and ASTM E2911 international guidelines.

Fabrication of PVA substrates: Whereas the FDM-3D printing step did not serve to produce the final substrate, but rather as a material dispensing step to fabricate a precursor substrate of a certain size, the compression molding process acted to transform the precursor into a flat substrate of desired shape by using a mold assembly. For the fabrication of the substrate precursor, a commercially available Original Prusa i3 MK2S desktop 3D printer was used (Prusa Research, Czech Republic) to print with likewise commercially acquired RS Pro PVA filament with a 100% infill, a hotend temperature of 210 °C and a print bed temperature of 85 °C (first layer) and 60 °C (following layers). The volume of the substrate precursor was calculated to equal the volume of the mold cavity which is used in the compression molding step. While the FDM 3D printing method can be quite accurate, it is – due to the nature of this technology – not precise enough to exactly dispense the correct volume of material as the layer-by-layer and line-by-line fabrication leads to the creation of small gaps within the print even though the infill ratio is set to 100%. In order to compensate for this phenomenon, the volume of the substrate precursor was increased by 3%, which was found to be an acceptable value to obtain a good substrate after compression molding. After FDM 3D printing of the precursor substrates, the substrates had an average weight of 804.96 mg (N = 10), ranging from 800.09 to 808.75 mg with a standard deviation of 2.93 mg.

The mold assembly for the compression molding consisted of a 1 mm thick aluminum mold, 90 µm aluminum foil and 1 mm stainless steel sheets. The compression molding procedure was carried out with a pressure of 55 kN and a temperature of 160 °C using a PW-H HKP300 laboratory press (Paul-Otto Weber GmbH, Germany).

For some of the resulting substrates, the surface was modified by sanding one side with 600 grit sanding paper.

Composite compression molded substrates consisting of PVA and polylactic acid (PLA) were as well fabricated using an FDM 3D printing and a compression molding step. PLA inserts were 3D printed with smaller dimensions, constituting 50 % of the final substrate. PVA substrates were designed to have a cavity and the 3D printing procedure was paused as soon as the cavity was completed. Then the PLA insert was inserted into the cavity and the 3D printing procedure was continued. The cavity was closed with the remaining layers of PVA, thereby fully engulfing the PLA in its' core. The compression molding step transformed the precursor composite substrates into smooth PLA-PVA core-shell substrates of 1 mm thickness using the same conditions as with plain PVA substrates.

In a different approach, a Press 300 SV laboratory platen press (Dr. Collin GmbH, Germany) served to transform 15 g of MOWIFLEX™ C17 PVA polymer pellets into a compressed sheet using a pressure of 50 bar and a temperature of 150 °C for a duration of 1000 s and subsequently cooling it down to 30 °C within 500 s. Substrates of desired shape were cut from the sheet with an Epilog Mini 18 laser cutter (Epilog Laser BV, The Netherlands) which was equipped with a 30 W CO_2 laser. This procedure needed to be performed with the necessary safety precautions as toxic fumes can be release during the procedure.[1]

Injection molding of PVA substrates was performed using an Arburg Allrounder 370A injection molding machine (Arburg GmbH & Co KG, Germany) equipped with an 18mm screw and MOWIFLEX™ C600 PVA polymer. Injection molding parameters were adjusted to 70 bar back pressure, 180 °C melt temperature, 40 °C mold temperature, 50 mm/s injection velocity, 500 bar packing pressure, 10 s packing time and 40 s cooling time.

Release of micro 3D prints from PVA substrates: 3D printed structures were released from the PVA substrate by retaining the substrate in a small box with a bottom of fine stainless-steel mesh and placing it in a de-ionized water-filled beaker, which in turn was placed into an ultrasound bath at a temperature of 55 °C. The samples were kept in the ultrasound bath until all PVA was dissolved. A waterproof USB endoscopic camera and Video Velocity Free software (Candy Labs Media, Canada) were used to record time-lapse photos during the release procedure. The samples were ultimately taken out of the water and left to dry in an oven at 37 °C.

Determination of bond strength: A TA.XT plus Texture Analyzer (Stable Micro Systems, UK) equipped with a 10 kg load cell and a customized probe was used to measure detachment forces needed to separate a printed sample from different 3D printing substrates. Detachment forces and work of adhesion were computed with a customized python program.

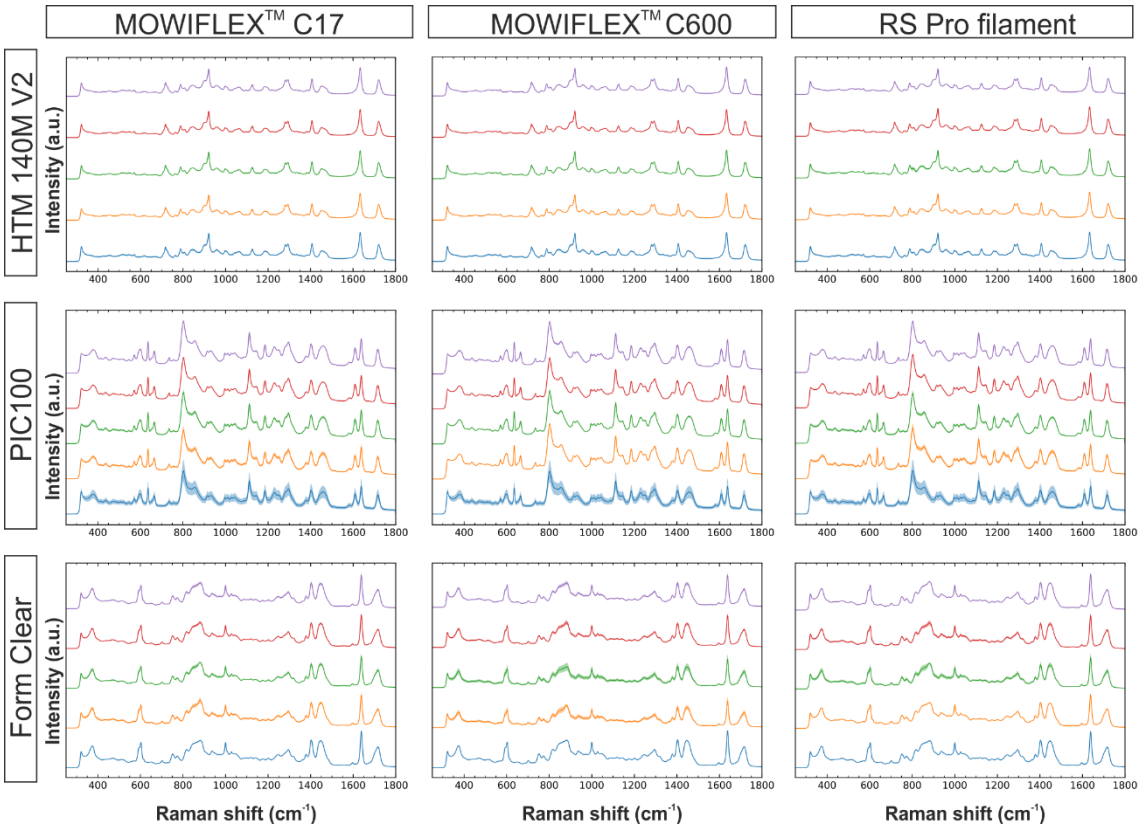

Figure S 1 *Compatibility study of different 3D printing photopolymers with different PVAs using Raman spectroscopy. Molecular fingerprints represented by Raman spectra measured after successive timepoints upon potential contamination of 3D printing photopolymer with PVA. Lighter shades below the lines represent the standard deviation. N = 3.*

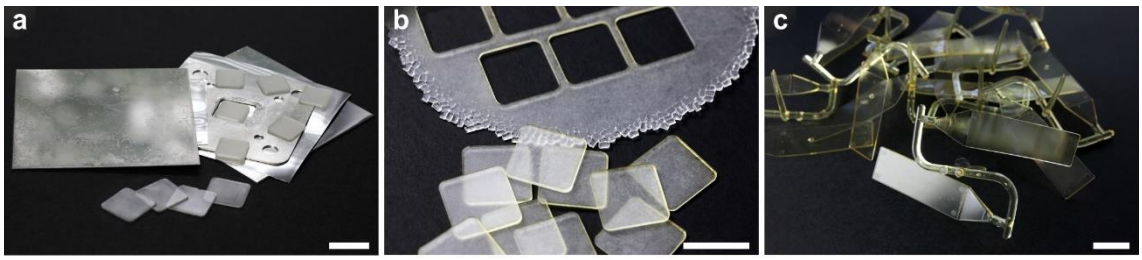

Figure S 2 *Photographs of differently fabricated PVA substrates. a) FDM 3D printed precursor substrates (substrates placed on mold assembly) and compression molded substrates (front). b) Laser-cut substrates from compressed PVA sheet. c) Injection molded PVA substrates in standard object slide format. Scale bars are equal to 25 mm.*

Table S 1 *Statistical evaluation of the peak-to-valley flatness parameter (FLTt) compared between different kinds of 3D printing substrates and reference substrates using a Welch's t-test (p-value; $p > 0.05 \triangleq$ ns, $p \leq 0.05 \triangleq$ *, $p \leq 0.01 \triangleq$ **, $p \leq 0.001 \triangleq$ ***, $p \leq 0.0001 \triangleq$ ****) and effect size determination (Hedges' g; $g = 0.2 \triangleq$ small effect, $g = 0.5 \triangleq$ medium effect, $g = 0.8 \triangleq$ large effect). In case of reference samples Si and BP N = 1 with 25 repeated measurements on only one sample each and in case of all other samples N = 5 with 5 different samples. Measurements obtained with a different acquisition setup (DI-10X and CF-20X Stitch) were not compared among each other except if they were done on the same type of substrate.*

	Si (DI-10X)	BP (DI-10X)	BP (CF-20X Stitch)	Alu (DI-10X)	CM (DI-10X)	CM (CF-20X Stitch)	CM-S (CF-20X Stitch)
Si (DI-10X)							
BP (DI-10X)	**** g = 17.2						
BP (CF-20X Stitch)		**** g = 2.9					
Alu (DI-10X)	**** g = 18.7	**** g = 10.6					
CM (DI-10X)	**** g = 18.8	**** g = 10.7		ns g = 0.2			
CM (CF-20X Stitch)			**** g = 9.6		** g = 3.3		
CM-S (CF-20X Stitch)			**** g = 7.3			* g = 1.9	
IM (DI-10X)	**** g = 38.6	**** g = 6.9		**** g = 10.8	**** g = 11.1		

Table S 2 *Statistical evaluation of the arithmetical mean height (Sa) compared between different 3D printing substrates and reference substrates using a Welch's t-test (p-value; p > 0.05 ≙ ns, p ≤ 0.05 ≙ *, p ≤ 0.01 ≙ **, p ≤ 0.001 ≙ ***, p ≤ 0.0001 ≙ ****) and effect size determination (Hedges' g; g = 0.2 ≙ small effect, g = 0.5 ≙ medium effect, g = 0.8 ≙ large effect). In case of reference samples Si and BP N = 1 with 25 repeated measurements on only one sample each and in case of all other samples N = 5 with 5 different samples.*

	Si	BP	Alu	CM	CM-S
Si					
BP	**** g = 10.0				
Alu	**** g = 59.1	**** g = 6.3			
CM	**** g = 19.2	**** g = 7.1	**** g = 10.9		
CM-S	*** g = 13.5	**** g = 5.1	** g = 3.3	*** g = 5.5	
IM	**** g = 69.4	**** g = 5.0	**** g = 16.1	**** g = 23.2	ns g = 0.6

Table S 3 *Statistical evaluation of the developed interfacial area ratio (Sdr), a measure for surface complexity, compared between different 3D printing substrates and reference substrates using a Welch's t-test (p-value; $p > 0.05$ ≙ ns, $p \leq 0.05$ ≙ *, $p \leq 0.01$ ≙ **, $p \leq 0.001$ ≙ ***, $p \leq 0.0001$ ≙ ****) and effect size determination (Hedges' g; $g = 0.2$ ≙ small effect, $g = 0.5$ ≙ medium effect, $g = 0.8$ ≙ large effect). In case of reference samples Si and BP N = 1 with 25 repeated measurements on only one sample each and in case of all other samples N = 5 with 5 different samples.*

	Si	BP	Alu	CM	CM-S
Si					
BP	**** g = 5.0				
Alu	**** g = 126.8	**** g = 3.8			
CM	** g = 9.5	**** g = 3.8	*** g = 7.0		
CM-S	** g = 6.7	**** g = 3.7	** g = 3.4	** g = 3.5	
IM	*** g = 14.7	**** g = 3.8	*** g = 6.9	*** g = 7.4	* g = 2.3

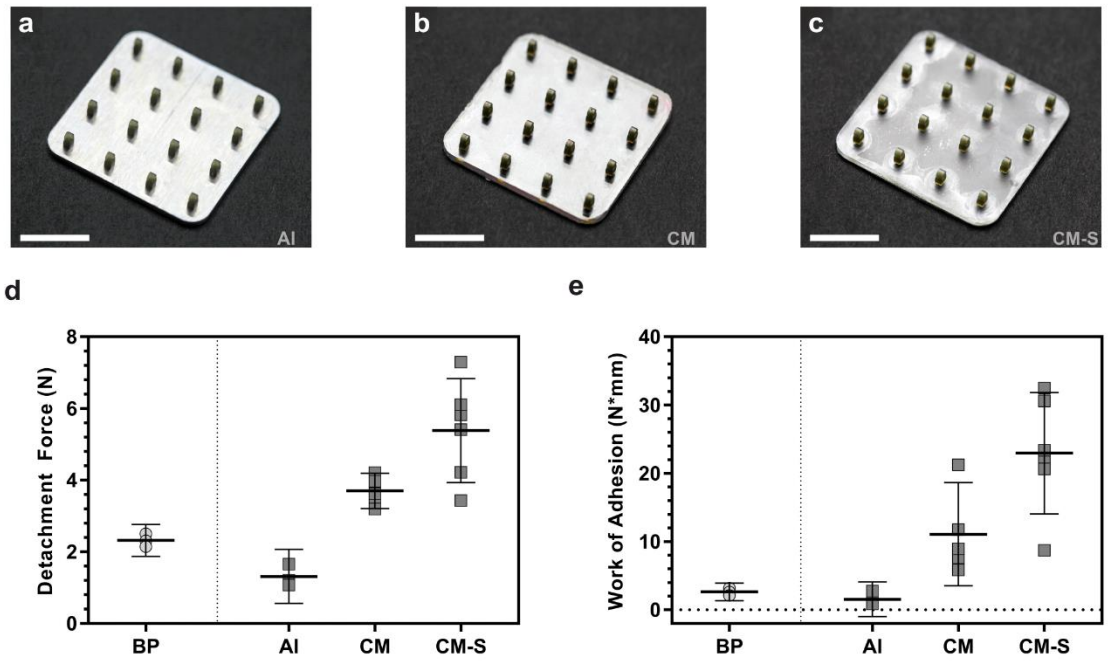

Figure S 3 *Photographs of manufactured samples for determination of bond strength of 3D printed structures to substrate and evaluation of experimentally determined bond strength. Scale bars are equal to 10 mm. a) Test structures 3D printed on plain aluminum substrates (Al). b) Test structures 3D printed on compression molded PVA substrates (CM) and c) hand-roughened CM PVA substrates (CM-S). d) Evaluation of detachment forces. e) Determined work of adhesion. Additional to the manufactured samples, a commercial 3D printer build platform (BP) also served as reference substrate. N = 3-6. Error bars represent 95% confidence interval. Statistical evaluation available in Table S 4 and Table S 5.*

Table S 4 *Statistical evaluation of detachment forces (bond strength) compared between different kinds of 3D printing substrates and reference substrates using a Welch's t-test (p-value; p > 0.05 ≙ ns, p ≤ 0.05 ≙ *, p ≤ 0.01 ≙ **, p ≤ 0.001 ≙ ***, p ≤ 0.0001 ≙ ****) and effect size determination (Hedges' g; g = 0.2 ≙ small effect, g = 0.5 ≙ medium effect, g = 0.8 ≙ large effect). N = 3-6.*

	BP	Alu	CM	CM-S
BP				
Alu	* g = 4.0			
CM	*** g = 4.1	*** g = 7.0		
CM-S	** g = 2.6	*** g = 3.5	* g = 1.4	

Table S 5 *Statistical evaluation of the determined work of adhesion compared between different kinds of 3D printing substrates and reference substrates using a Welch's t-test (p-value; p > 0.05 ≙ ns, p ≤ 0.05 ≙ *, p ≤ 0.01 ≙ **, p ≤ 0.001 ≙ ***, p ≤ 0.0001 ≙ ****) and effect size determination (Hedges' g; g = 0.2 ≙ small effect, g = 0.5 ≙ medium effect, g = 0.8 ≙ large effect). N = 3-6.*

	BP	Alu	CM	CM-S
BP				
Alu	ns g = 1.3			
CM	* g = 1.7	* g = 1.9		
CM-S	** g = 2.8	** g = 3.0	* g = 1.7	

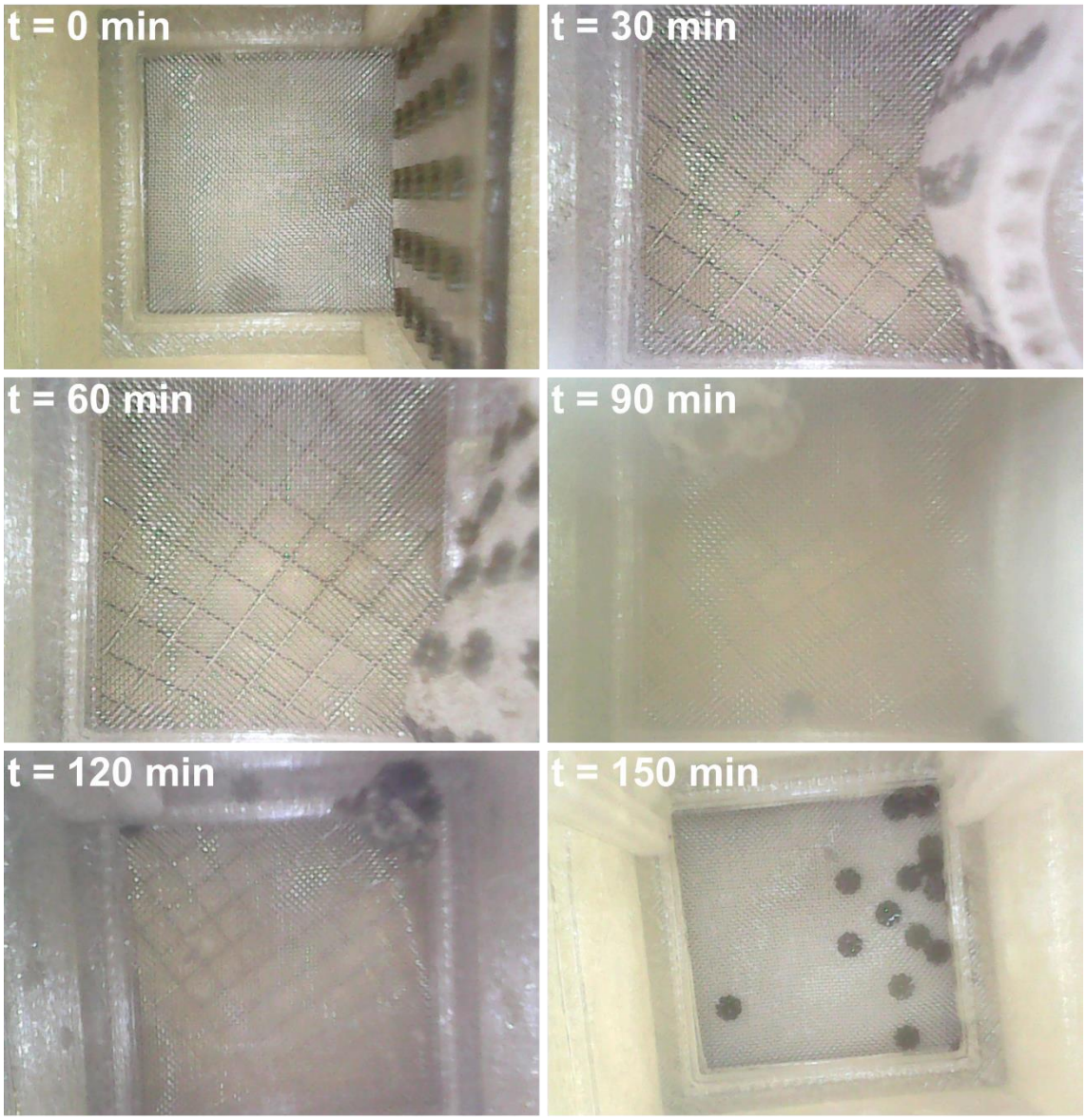

Figure S 4 *Time-lapse photos taken with a water-resistant endoscopic camera during the release procedure of 3D printed micro-gears from compression molded PVA substrates (CM). Release procedure was carried out in a customized release-chamber/substrate-holder combination at 55 °C in an ultrasound bath.*

Movie S 1 *Time-lapse recording of compression molded PVA substrate (CM) with array of helical micro-gears 3D printed on its' surface dissolving in water, thus releasing the individual 3D printed objects. The recording has an interval of 1 photo every 20 sec. Observation was aggravated by the formation of air bubbles on the lens of the endoscopic camera. The entire procedure was carried out in an ultrasound bath at 55 °C.*

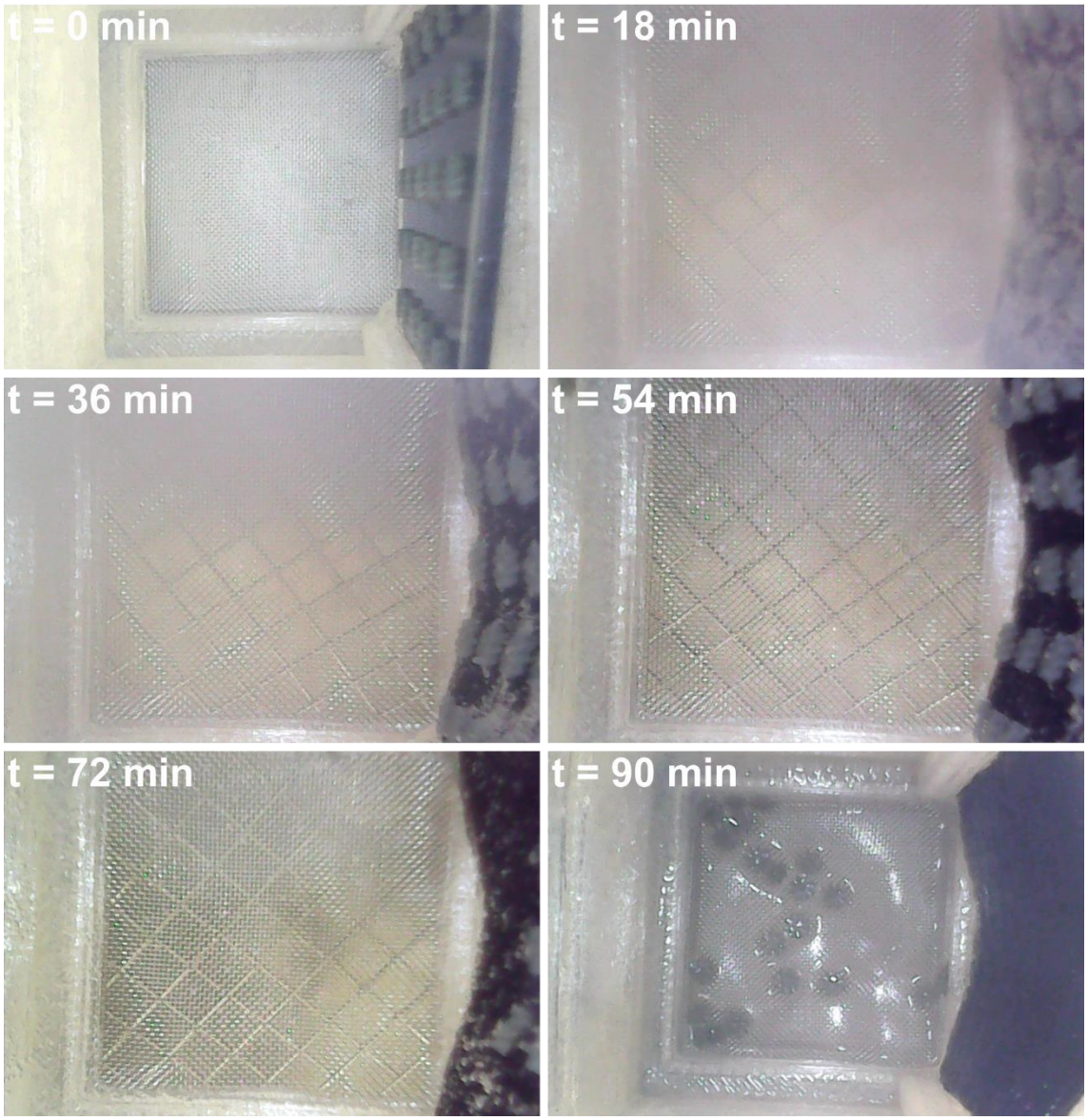

Figure S 5 *Time-lapse photos taken with a water-resistant endoscopic camera during the release procedure of 3D printed micro-gears from compression molded PLA (black)-PVA (transparent) core-shell-composite substrates. Release procedure was carried out in a customized release-chamber/substrate-holder combination at 55 °C in an ultrasound bath.*

Movie S 2 *Time-lapse recording of releasing individual helical micro-gears from composite compression molded PLA/PVA substrate with array of helical micro-gears 3D printed on its' surface through dissolution of the PVA in water. The recording has an interval of 1 photo every 20 sec. Observation was aggravated by the formation of air bubbles on the lens of the endoscopic camera. The entire procedure was carried out in an ultrasound bath at 55 °C.*

References

[1] ILO, WHO, ICSC 1489 Polyvinyl alcohol, https://www.ilo.org/dyn/icsc/showcard.display?p_lang=en&p_card_id=1489&p_version=2, accessed: 09, 2018.

7.3 Manuscript III

3D Printing of Reservoir Devices for Oral Drug Delivery and Enhanced Mucoadhesion

Lukas Vaut, Julia Joanna Juszczyk, Khorshid Kamguyan, Kristian Ejlebjærg Jensen, Guido Tosello and Anja Boisen

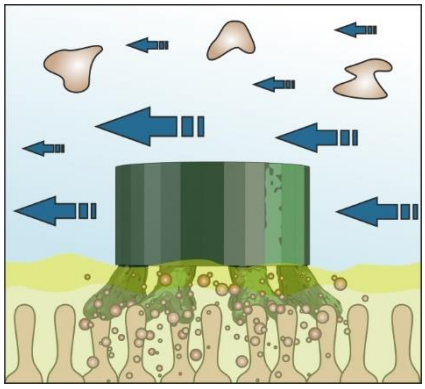

3D printing has great potential for research and development in oral drug delivery and can be used for the fabrication of fillable microreservoirs with unidirectional release. The prototyping abilities of 3D printing are utilized to design and print reservoir devices with anchor-like surface structures for increased mucoadhesion and mucosa-oriented drug release.

3D Printing of Reservoir Devices for Oral Drug Delivery and Enhanced Mucoadhesion

Lukas Vaut[1], Julia Joanna Juszczyk, Khorshid Kamguyan, Kristian Ejlebjærg Jensen, Guido Tosello and Anja Boisen*[2]*

L.Vaut, J. J. Juszczyk, K. Kamguyan, Dr. K. E. Jensen, Prof. A. Boisen, The Danish National Research Foundation and Villum Foundation's Center for Intelligent Drug Delivery and Sensing Using Microcontainers and Nanomechanics (IDUN), Department of Health Technology, Technical University of Denmark, Kgs. Lyngby, 2800, Denmark

Prof. G. Tosello, Department of Mechanical Engineering, Technical University of Denmark, Kgs. Lyngby, 2800, Denmark

Keywords: micro additive manufacturing, oral drug delivery, microdevices, microcontainers, mucoadhesion

E-mail: [1] lukv@dtu.dk , [2] aboi@dtu.dk

So far, microdevices for oral drug delivery have been fabricated as square or cylindrical reservoir structures with a localized and unidirectional release. The fabrication is usually carried out using sophisticated and costly microfabrication techniques. Here, 3D printing of various microreservoirs on sacrificial substrates is presented. This approach allows the devices to be accurately arranged in pre-determined patterns, enabling implementation into batch production schemes in which the fabrication of the devices is linked to processing steps such as automated drug loading and sealing. Moreover, design and 3D printing of alternative geometries of minireservoirs featuring anchor-like surface structures for optimized mucoadhesion and intestinal retention is demonstrated. Surface texturing of minireservoirs increases mucoadhesion of the devices up to a twofold compared to a non-structured control. The structuring also leads to a strong bias in mucoadhesion in different orientations, which can facilitate a correct orientation of the devices and thus lead to unidirectional release of drugs towards the intestinal mucosa for increased drug uptake.

Engineered microfabricated oral drug delivery (ODD) devices have emerged as an alternative strategy for increasing bioavailability.[1,2]

Since oral delivery is the preferred route of drug administration, much research effort has gone into the translation of parenteral administered dosage forms to orally administered dosage forms of drugs.[3] This translation often faces difficulties, because many drugs exhibit poor bioavailability when administered orally, as the complex physiological environment of the gastro-intestinal tract causes degradation (gastric acid, digestive enzymes), prevention of absorption (mucus layer, epithelial barrier) and rapid clearance (mucus secretion, gastro-intestinal transit).

To protect and transport drugs as well as to retain drugs close to their target site and promote absorption, various drug delivery technologies have been developed and investigated. Next to specialized coatings are particulate drug delivery systems relying on self-assembly of

molecules and polymers, such as liposomes, nano-/microparticles, etc. While microfabricated devices, due to the involved top-down engineering process, hold great potential for producing uniform devices with distinct morphologies, 3D printing offers much flexibility and sufficient throughput for fabrication of such ODD devices, enabling research and development of optimal shape and function.

Initially, Ahmed and co-workers designed and fabricated microdevices for ODD as square, flat and patch-like structures with a reservoir into which a drug can be filled. In contrast to particulate systems, microfabricated devices represent universal delivery platforms with the potential for a localized unidirectional release of the drug from the reservoir towards the target site.[1] Furthermore, this effect can be promoted by specific chemical surface modification of the devices.[1]

Based on this concept, different fabrication protocols and materials have been demonstrated and the suitability of the devices for ODD was highlighted, e.g. through the fabrication and drug-filling of multi-layered poly(methyl methacrylate), epoxy-based SU8 and biodegradable poly(DL-lactide-co-glycolide) microdevices.[4] With respect to fabrication, the concept was further expanded by the fabrication of biodegradable cylindrical microcontainers using hot punching, cylindrical SU8 microcontainers with pH-sensitive lids made with photolithography and capped microreservoir devices made by StampEd Assembly of polymer Layers (SEAL).[5–7] In-vitro as well as in-vivo release studies have shown promising results on the drug delivery performance of microfabricated devices.[6,8,9]

Although Ahmed et al. and Chirra et al. demonstrated an increased association of lectin-functionalized microdevices with epithelial cells and enhanced intestinal retention in mice, respectively, the unidirectional release of the drug towards the target site was not facilitated or proven in the hitherto referred cases.[10,11]

Furthermore, the employed fabrication techniques require elaborated lab conditions (e.g. clean room facilities) and are costly. 3D printing, on the contrary, is cheaper and generally considered to be a good tool for rapid prototyping, owing to a tool free workflow and few design constraints. The production of prototypes with conventional technologies used for large scale production, is often unfeasible as it is too expensive.[12] 3D printing enables the customization of products as exemplified with the use of fused-deposition modeling (FDM) for personalized 3D printed dosage forms in the context of point-of-care medication.[13,14] While print resolution limits FDM fabrication capabilities to the macroscale, vat photopolymerization-based 3D printing techniques, such as stereolithography (SL) or digital light processing (DLP) techniques, rely on operation principles which are very similar to those of photolithography.[15] These techniques can thus produce mesoscale down to microscale components, making them suitable for prototyping of microdevices for ODD.

In this work, we demonstrate the usage of a desktop DLP 3D printing system with a spatial resolution (i.e. voxel size) of 30 µm to 3D print microreservoir devices for ODD in dimensions close to SU8 microcontainers fabricated previously.[9] Moreover, the utilization of a recently developed 3D printing method enables full integration into production schemes that combine device fabrication with further processing steps, such as drug-loading and sealing.[16] To

showcase the prototyping potential of 3D printing for ODD devices, we present the 3D printing and characterization of miniaturized reservoir structures (minireservoirs) with different geometries designed to promote unidirectional release with controlled orientation and intestinal retention.

Bulk fabrication on a substrate (e.g. silicon wafer) is a common attribute of microdevices for ODD. Upon production completion, the individual devices are released by means of a sacrificial layer (e.g. water-soluble polyacrylic acid release layer) and harvested.[9] Moreover, in microfabrication, the wafer connects multiple processing steps by preserving the patterning of structures throughout the entire process. In vat photopolymerization-based 3D printing, the structures are printed on a machine-specific build platform, which is precisely leveled to the polymerization interface of the vat. After the printing procedure has finished, the printed structures are usually removed manually from the platform, which is often facilitated with the use of hand tools such as pliers, scrapers or razor blades. Finally, residual photopolymer is removed with a solvent. This process is, in principle, suitable for the fabrication of microdevices for ODD, however it prevents the utilization of subsequent processing steps in which the geometrical patterning of the devices is required. Previously, several techniques relying on geometrical patterning for the processing of microdevices for ODD were reported. For example the use of inkjet printing for drug loading, the application of micromachined shadow masks for drug loading and lid sealing via spray coating.[6,17–20] 3D printing microdevices with a likewise 3D printed base layer, thereby preserving the geometrical pattern, is not a suitable option, because it irreversibly connects all devices to a whole and hence removes the possibility to release them individually.

The use of pre-fabricated water-soluble polyvinyl alcohol (PVA) substrates has recently been shown to enable the release of disconnected microstructures. The substrates can be inserted into a customized holder of a vat photopolymerization-based 3D printer and therein used as a 3D printing substrate.[16] Translating this method to the 3D printing of microreservoir devices means that, similar to a wafer in microfabrication, the PVA substrates preserve the geometrical patterning of microreservoirs and thereby enable the connection of the fabrication method to further processing steps (**Scheme 1,** Figure S 1) such as drug loading and sealing. Finally, after completion of all processing steps, the substrate can be dissolved in water to release the individual microreservoirs, which can then be filled into a capsule for oral dosage. Using the aforementioned 3D printing technique, defined arrays of microreservoirs with different sizes and aspect-ratios have been 3D printed on sacrificial PVA substrates and later released (**Figure 1**). The printed microreservoirs have diameters of 570 and 650 µm with aspect-ratios of 1:1.16 and 1:0.54 (diameter:height), respectively. The 3D printed microreservoirs have characteristics similar to those of SU8 microcontainers and remained intact after release from the sacrificial substrate.

One of the hypotheses related to the microfabricated devices for ODD is the unidirectional release of the drug from the reservoir towards the target site, which in oral delivery most commonly is the intestinal mucosa. Unless the devices are self-propelling, their movement in the intestine and their orientation is entirely dependent on external forces, that in the

intestinal environment are most likely due to intestinal motility and peristaltic flow of intestinal contents. In this case, the orientation of microdevices is presumably random if no bias is applied to their faces. Chirra et al. aimed at promoting unidirectional release towards the intestinal mucosa by designing microdevices with flat aspect-ratio for decreased susceptibility to peristaltic shear stress and by functionalizing the reservoir side of the devices with lectins.[11] The latter are a group of proteins that among others bind to carbohydrate chains present at the epithelial cell surface.[21]

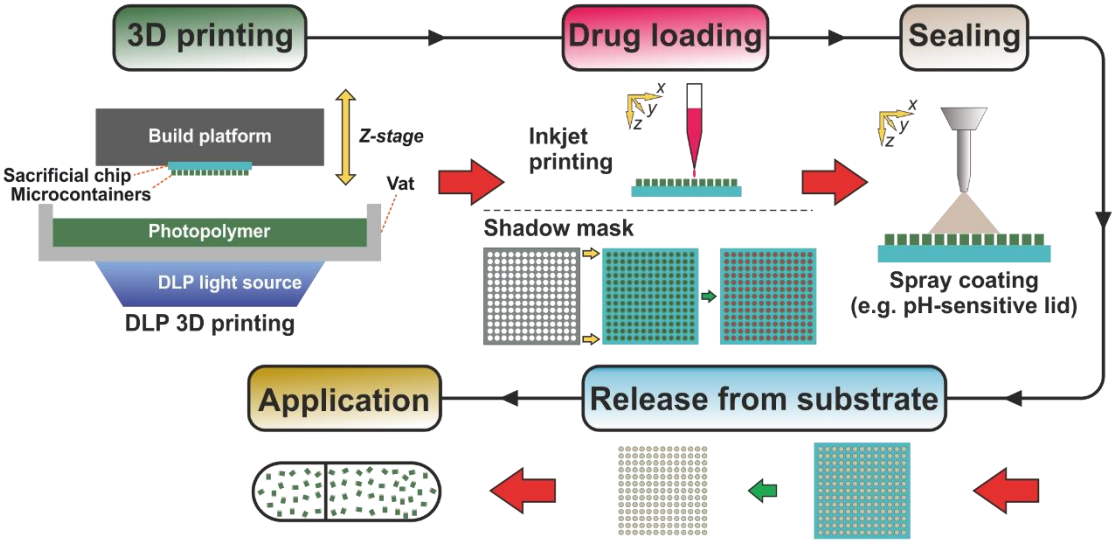

Scheme 1 *Workflow implementation of 3D printing into the fabrication of drug-loaded polymeric microreservoirs. 3D printing of arrays of micoreservoirs on a sacrificial polymer substrate using a specific 3D printing method enables the connection to further array-based processing steps that were previously demonstrated.[16] For example drug loading via inkjet printing or shadow mask, subsequent sealing with e.g. a pH-sensitive lid via spray coating and finally release of single microreservoirs from sacrificial substrate and their harvesting for application.[1,6,9,17–19]*

In contrast to such a chemistry-based approach, we present devices featuring a strong contrast between top and bottom geometry by means of specific surface texturing on the reservoir side (**Figure 2**a-e). According to the mechanical theory of mucoadhesion, the increase in surface area, and thereby increased surface interaction, enhances the "viscoelastic dissipation of energy during joint failure" and hence can increase adhesion to mucosal surfaces.[22] The generated surface structures are intended to ease the penetration of the devices into the mucus layer by increasing the local applied tension. Further, the increased friction forces between the mucus gel and the surface of the devices leads to enhanced detachment forces and thus stronger adhesion. The increased adhesiveness of the reservoir side compared to the bottom side of the devices has the potential to result in an orientation bias.

Next to a plain reservoir device ("Control"), two designs with different degrees of increased surface area ("TO1" and "TO2") were generated employing a topology optimization approach to solve a free form optimization problem.[23] The topology optimization is not aimed at optimizing adhesion, but generates branching structures with large surface areas.

Additionally, two more designs were manually created. The design named “Manual” features an overhang at the reservoir side (top side) as well as cone-shaped spikes for reduced fabrication complexity. This design is inspired by the overall shape of “TO1” and TO2. The bio-inspired “Phage” -design features an increased number of spikes, a rounded bottom side and side extensions along the lines of the morphology of T4 bacteriophages. The latter is known to infect bacteria by attaching to the cell surface through a sequential binding of the hexagonally arranged tail fibers, resulting in a stable upright position.[24] It must be emphasized that all designs are exterior modifications to the same reservoir design with a fixed height and outer diameter.

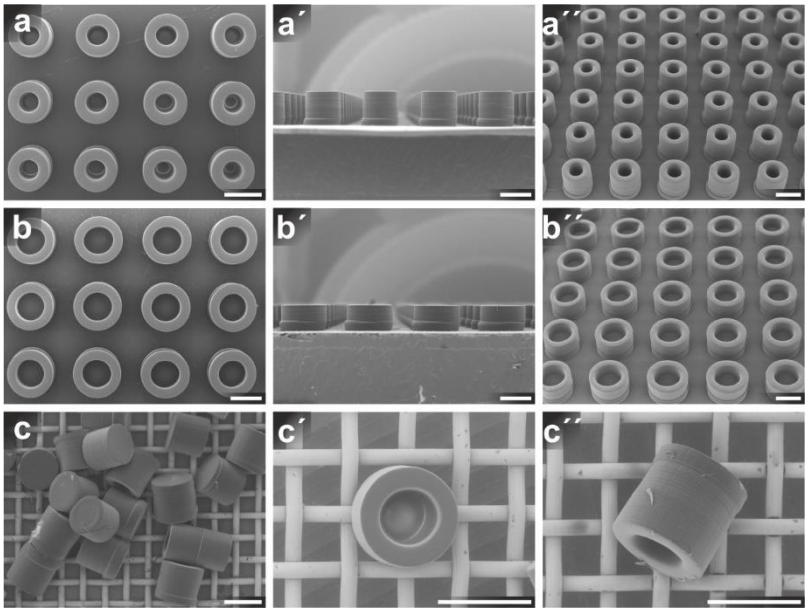

Figure 1 *Scanning electron microscopy images of differently sized 3D printed microreservoirs. Scale bars are equivalent to 500 µm. a) Microreservoirs with dimensions of 570 x 660 µm (diam. x height) and a wall thickness of 150 µm. b) Microreservoirs with dimensions of 650 x 350 µm and a wall thickness of 130 µm. Top view, side view (´) and 45° tilted view (´´). c) Microreservoirs after release from sacrificial substrate on steel filter mesh. Top view of several specimens, top view of single specimen (´) and side view of single specimen (´´).*

The presented designs were fabricated by 3D printing and characterized with scanning electron microscopy (Figure 2f-j). However, due to resolution limitations of the available 3D printing system, the size of the reservoirs was scaled up according to the minimum feature size of the designs. Resolution arrays for the different designs (Figure S 2, Figure S 3, Figure S 4, Figure S 5) were 3D printed to determine an achievable scale of the objects. In this aspect, “Manual” was not regarded, because it features the same dimensions as “Phage”. Also, the spikes were disregarded as they were scaled individually. “TO2”, with the smallest design elements, represents the size limiting factor. Consequently, a size with an outer reservoir diameter of 2.6 mm was chosen due to good repeatability. Using the same 3D printing method, also larger reservoir devices could be fabricated on sacrificial PVA substrates (Figure S 6).

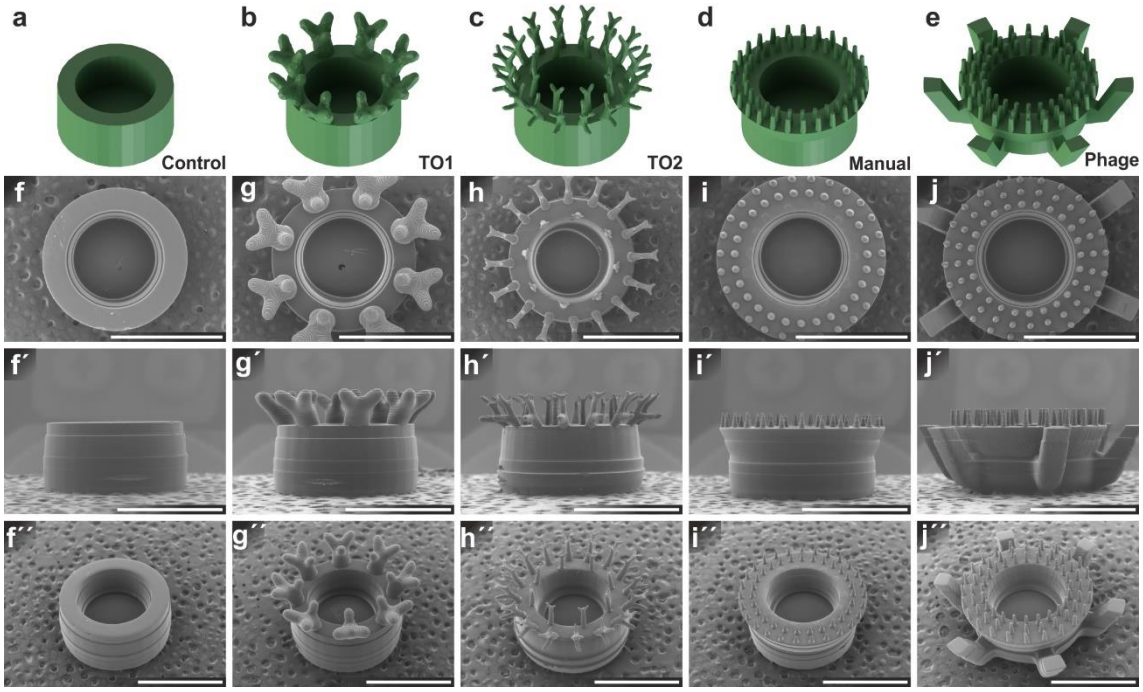

Figure 2 *Design and fabrication of alternative reservoir geometries. a, f) Plain reservoir structure as control specimen ("Control"). b, g) Design with large branching edge anchors ("TO1"). c, h) Design with small branching edge anchors ("TO2"). d, i) Design featuring overhang and straight anchor spikes ("Manual"). e, j) Bio-inspired phage-style design with straight anchor spikes, rounded bottom side and legs ("Phage"). a) – e) 3D design representations. f) – j) Scanning electron microscope images of 3D printed structures. Scale bars correspond to 2 mm. Top view, side view (´) and 45° tilted view (´ ´).*

Initially, the mucoadhesive effect of the surface texturing was tested with a tensile mucoadhesion setup and porcine intestinal tissue (Figure S 7), thus simulating the effect of intestinal contraction events. The experiment was carried out in a replicated Latin square design with tissue as well as sequence of tested structures as blocking factors. This prevented the testing sequence and the variability of the tissue from affecting the analysis of the measurements. The comparison of work of adhesion (area under curve of detachment graph; **Figure 3**a) shows that samples "TO1" and "TO2" have significantly lower mucoadhesion with respect to "Control", whereas "TO1" has the lowest with also significantly lower values than "Manual" and "Phage". Analysis of maximum peak forces (Figure S 7c) shows the same overall trend with the exception that "TO2" instead of "TO1" has the lowest values. In both cases, "Manual" and "Phage" are not significantly different from the control. While on one hand it is expected that increased surface area in case of "TO1" and "TO2" leads to increased contact area, it can on the other hand be presumed that the branching surface structures result in a reduction of required penetration force and thus better penetration into the mucus. Due to the relatively high stiffness of the 3D printed structures, the vertical force applied from the tensile instrument, through the branching structures, probably induces higher shear stress to the mucus when compared to less penetrating structures. Since mucus is a shear-thinning gel, the consequent reduction in viscosity can lead to a decrease in detachment force.[25] In this case, this method is not regarded as being suitable to evaluate the mucoadhesive potential of

different designs with surface structures. Additionally, it has been pointed out that the occasions of tensile detachments are probably rare events from a physiological point of view.[26]

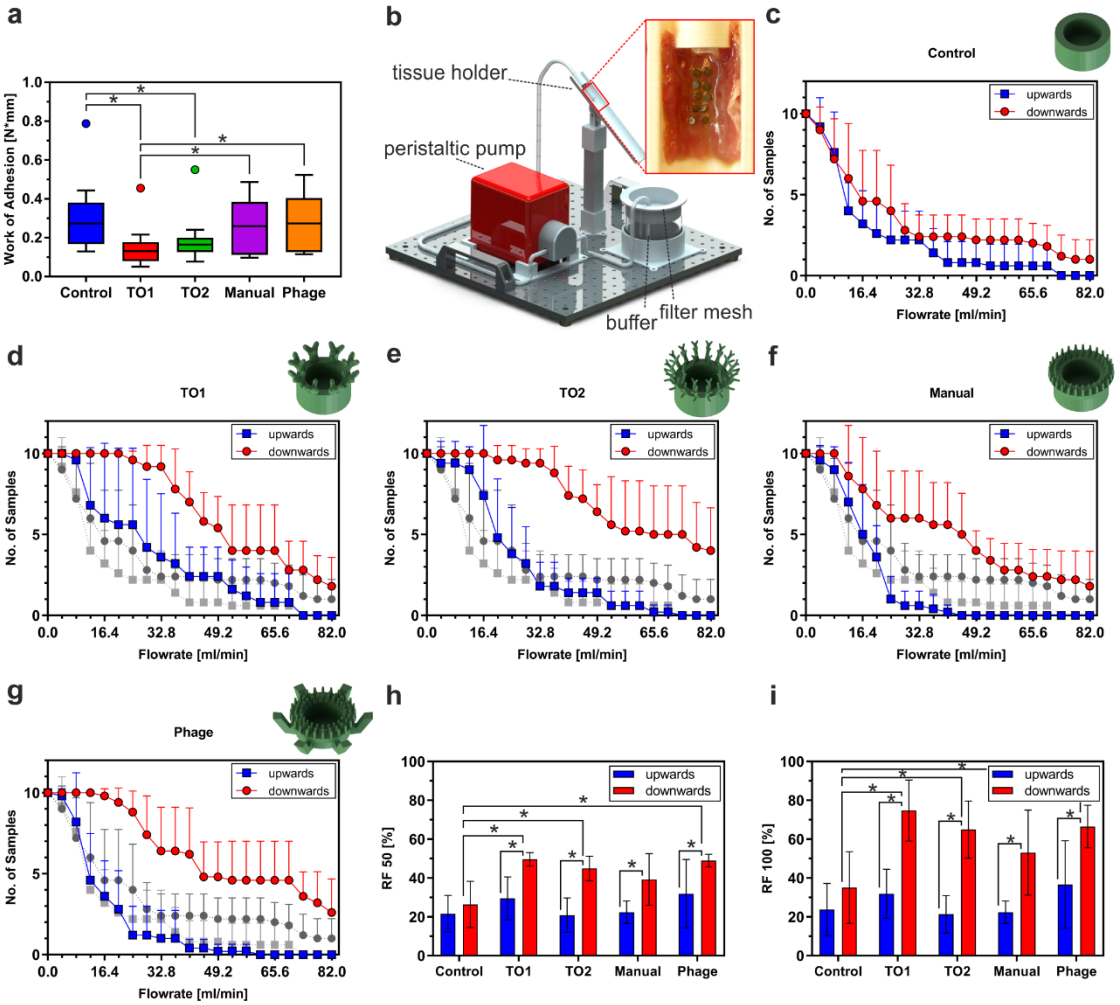

Figure 3 *Characterization of mucoadhesion. a) Analysis (Tukey boxplots) of mucoadhesion of alternative reservoir geometries with the tensile method. Work of adhesion (WOA) is defined as the area under the curve of the detachment graph where force is plotted against displacement. N = 10. b) Schematic of experimental setup for evaluation of mucoadhesion with the flow retention method adapted from Rao and Buri.[27] Retention graphs and comparison between downwards and upwards orientation relative to mucosal surface for c) "Control", d) "TO1", e) "TO2", f) "Manual" and g) "Phage" specimens. Values from c grayed out in d – g. Each flowrate lasted for 2 min. N = 5. h) Comparison of RF 50 value between different designs and different orientations based on retention graphs. RF 50 is defined as the relative cumulative amount of retained specimens at 50 % of the maximally applied flowrate. i) RF 100 values of different designs and orientations. RF 100 is defined like RF 50, but at 100% of the maximum applied flowrate. Error bars represent 95% confidence intervals (h, i). Stars indicate statistical significance with $p < 0.05$ according to Least Significant Difference test (a) and Welch´s t-test (h, i).*

Therefore, the same minireservoirs were characterized for mucoadhesion using a flow retention setup (Figure 3b).[27] Also here, to prevent the influence of tissue variability and mucus integrity, the experiments were performed in a Latin square design with tissue and sequence of tested structures as blocking factors. In addition to comparing different designs, the initial orientation of the minireservoirs was included. Although the overall average flowrate in the human small intestine is reported to be up to 3 ml min^{-1}, the retention experiment was performed over a range of different flowrates (4.1 – 81.9 ml min^{-1}), which might mimic the increased local shear stress induced by intestinal motility.[28] Plotting the number of retained minireservoirs against different flow rates shows very different retention profiles for different designs and different orientations (Figure 3c-g).

For comparison of the different designs, the relative cumulative number of retained devices up to a flowrate corresponding to 50% of the used maximum flowrate (RF50) and up to the maximum used flowrate (RF100) were calculated and analyzed for statistical significance (Figure 3h, i). The results remarkably show that in both cases there is no significant difference between all samples when placed with the reservoir side up (upwards). However, when placed downwards on the surface of the intestinal tissue, all samples with surface structures show significantly higher values when compared to the control. Furthermore, all samples with surface structures, but not the control, show a significant effect of orientation. This suggests that the minireservoirs with surface structures are more likely to adhere to the intestinal mucosa in the correct orientation and thus realize unidirectional drug release towards it. During the performance of the experiments it was observed that when placing the devices downwards, the surface structures rapidly penetrated the mucus. In contrast to tensile mucoadhesion tests that apply vertical stress, the flow retention test induces shear forces acting laterally on the devices. The surface structures, by penetrating the mucus, presumably increase the contact area and lead to a mechanical interlocking that increases resistance against lateral shear stress. Additionally, penetration reduces the effective surface area subjected to the flow, compared to placing the minireservoirs upwards.

Computer simulations relying on a simplified understanding of intestinal flow, in which the surface structures are likewise penetrating the mucus (in this case the wall of a cylinder), show a difference in drag force for downwards and upwards orientation, when the devices are subjected to a laminar flow over the same range of flow rates (**Figure 4**). The resulting asymmetry (orientation bias) in drag force versus flow rate for the different designs shows similarities to the asymmetry in the experimentally determined retention profiles of the devices. A comparison of orientation biases as quotients of values obtained for downwards and upwards orientation between experimentally determined values for retention and simulated values for drag force, show a similar trend (Figure S 8a). Consequently, increased retention of minireservoirs may be due to a combination of mechanical mucoadhesion and reduced shear stress/drag.

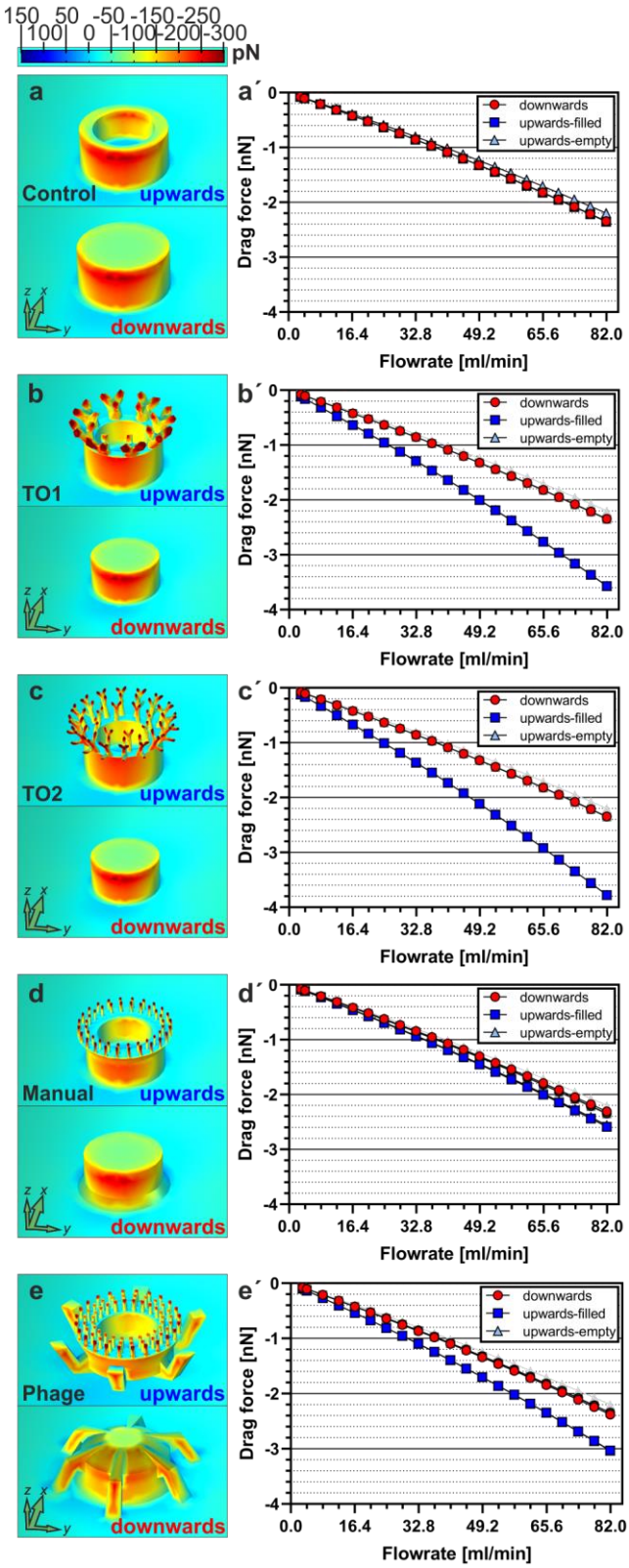

Figure 4 *Simulation of drag on different reservoir geometries in different orientations under laminar flow (x-direction) conditions in a tube (5x10 cm). When headed downwards, surface structures are simulated to enter the wall to mimic penetration of mucus. a) - e) Surface plots of drag in x direction for different designs and a´) - e´) computed drag force plotted against different flowrates. Values from a´ grayed out in b´ to e´.*

As of yet, reservoir devices for ODD were fabricated in sizes ranging from 50 to 300 µm.[1,9] By presenting reservoir devices with diameters from 400 to 3600 µm, this work drastically expands the size range of fabricated devices and calls for the question whether there is a specific size range for optimal functionality. In this context it should be noted that larger devices are subjected to higher shear stress and drag than smaller ones. This would be an important design constraint for reservoir devices that are designed to have an orientation bias based on a difference in shear stress/drag. However, computer simulations of drag force acting on reservoir devices with different sizes show only a marginal effect of size on orientation bias (Figure S 8b). Another important parameter to be considered is the drug loading efficiency of reservoir devices. A reduction of fabrication limitations at elevated dimensions can lead to a higher loading efficiency, e.g. through decreased relative wall-thicknesses (Figure S 9).

In summary, we have demonstrated the implementation of 3D printing into potential workflows for ODD microdevice fabrication by 3D printing microreservois with different shapes and sizes on sacrificial release substrates. To highlight the prototyping potential of 3D printing in this regard, we showed the design and fabrication of minireservoirs featuring anchor-like features for geometry-based mucoadhesion. Increased mucoadhesion as well as implications for unidirectional release with controlled orientation towards the intestinal mucosa have been presented experimentally and theoretically.

Experimental Section

Materials: All chemicals and reagents were used as received. For the fabrication of sacrificial substrates from polyvinyl alcohol (PVA), RS Pro PVA 3D printing filament (RS Components A/S, Denmark) was used. HTM 140M V2 3D printing photopolymer (EnvisionTEC GmbH, Germany) was used to 3D print reservoir structures. 2-propanol (Sigma-Aldrich Denmark A/S, Denmark) was used for the post-treatment of 3D printed structures and Dulbecco's phosphate buffered saline (Sigma-Aldrich Denmark A/S, Denmark) was used in the flow retention mucoadhesion tests.

Computer aided design (CAD): All design tasks were carried out using OpenSCAD open source software and SolidWorks 2015 (Dassault Systèmes SolidWorks Corporation, USA).
Fabrication of sacrificial PVA substrates: The fabrication of PVA substrates was performed as previously described.[16]

3D printing of reservoir structures on sacrificial PVA substrates: Reservoir structures were 3D printed on top of PVA substrates as previously reported.[16] After completion of the printing procedure, the substrate along with printed structures was sonicated in 2-propanol for 5 min to remove excess print material. After evaporation of the solvent, UV-post-curing was performed for 10 min.

Release of 3D prints from PVA substrates: The PVA substrate along with printed structures was placed in a cage made from stainless steel filter mesh and inserted into a Milli-Q water-filled beaker at a temperature of 55 °C with magnetic stirring for a mild release of the structures.

Scanning electron microscopy: All scanning electron microscopy was performed using a TM3030Plus tabletop scanning electron microscope (Hitachi High Technologies Europe GmbH, Germany). A 208HR high resolution sputter coater (Cressington Scientific Instruments, UK) equipped with a gold target was used to coat the specimens with a thin layer of gold (≈ 20 nm) prior to observation.

Tensile mucoadhesion tests: Experiments were performed using a TA.XTplus texture analyzer (Stable Micro Systems Ltd, UK) equipped with a 500 g loadcell. The samples were fastened to the probe holder with use of 3D printed probes and double-sided adhesive facing downwards and in the course of the experiment pressed down into a segment of porcine intestinal tissue, which was placed onto a holder platform with the mucosal side facing upwards. After a contact time of 60 s and a contact force of 10 g, according to intestinal contraction forces, the probe was moved upwards at a speed of 0.01 mm s^{-1}.[29] The experiments were performed in a replicated Latin square design with 5 different locations on two different tissues and the sequence of tested samples as blocking factors.

Flow retention mucoadhesion tests: A flow retention setup was constructed from 3D printed parts according to Figure 3b. A segment of porcine intestinal tissue was placed on the slide with the mucosal side facing upwards. The slide was held at an angle of 30° relative to the horizontal plane and connected to the tubing of a 120S/DV peristaltic pump (Watson-Marlow Flexicon A/S, Denmark). To remove loose mucus, the tissue was initially flushed with Dulbecco's phosphate buffered saline (PBS) at a flow rate of 40.9 ml min^{-1} for 5 min. 10 samples were placed on the tissue either facing upwards or downwards without applying force and incubated on the tissue for 1 min. Flow of PBS was started at a flow rate of 4.1 ml min^{-1} and increased with an interval of 2 min by 4.1 ml min^{-1}. After each flowrate, the retained devices were counted. The experiment was performed in a Latin square design with 5 different tissue segments and sequence of tested devices as blocking factors for each orientation.

Simulations: Simulations were conducted using COMSOL Multiphysics 5.4 (COMSOL AB, Sweden). 3D designs of minireservoirs were imported and placed at the center of the wall inside a cylinder with a diameter of 50 mm (according to average human intestinal diameter) and a length of 100 mm.[30] Laminar flow conditions and physical properties of water were used for the simulations. The sizing of mesh elements was selectively chosen to be coarser for the tube and finer for the minidevices.

Statistics: All presented statistics were computed using R programming language and RStudio software (RStudio Inc., USA) as well as GraphPad Prism 7 (GraphPad Software, USA).

Acknowledgements

The authors would like to acknowledge the Center for Intelligent Drug Delivery and Sensing Using Microcontainers and Nanomechanics (IDUN) whose research is funded by the Danish National Research Foundation (DNRF122) and Villum Fonden (Grant No. 9301).

The authors would also like to thank Tommy Sonne Alstrøm and Kinga Zór for help with preparation of the manuscript as well as Jesper Scheel for photography.

References

[1] A. Ahmed, C. Bonner, T. A. Desai, *Biomed. Microdevices* **2001**, *3*, 89.

[2] L. H. Nielsen, S. S. Keller, A. Boisen, *Lab Chip* **2018**, *18*, 2348.

[3] A. C. Anselmo, Y. Gokarn, S. Mitragotri, *Nat. Rev. Drug Discov.* **2018**, *18*, 19.

[4] S. L. Tao, T. A. Desai, *Adv. Mater.* **2005**, *17*, 1625.

[5] R. S. Petersen, S. S. Keller, A. Boisen, *Lab Chip* **2015**, *15*, 2576.

[6] L. H. Nielsen, A. Melero, S. S. Keller, J. Jacobsen, T. Garrigues, T. Rades, A. Müllertz, A. Boisen, *Int. J. Pharm.* **2016**, *504*, 98.

[7] K. J. McHugh, T. D. Nguyen, A. R. Linehan, D. Yang, A. M. Behrens, S. Rose, Z. L. Tochka, S. Y. Tzeng, J. J. Norman, A. C. Anselmo, X. Xu, S. Tomasic, M. A. Taylor, J. Lu, R. Guarecuco, R. Langer, A. Jaklenec, *Mater. Sci.* **2017**, *1142*, 1138.

[8] K. M. Ainslie, C. M. Kraning, T. A. Desai, *Lab Chip* **2008**, *8*, 1042.

[9] C. Mazzoni, F. Tentor, S. A. Strindberg, L. H. Nielsen, S. S. Keller, T. S. Alstrøm, C. Gundlach, A. Müllertz, P. Marizza, A. Boisen, *J. Control. Release* **2017**, *268*, 343.

[10] A. Ahmed, C. Bonner, T. A. Desai, *J. Control. Release* **2002**, *81*, 291.

[11] H. D. Chirra, L. Shao, N. Ciaccio, C. B. Fox, J. M. Wade, A. Ma, T. A. Desai, *Adv. Healthc. Mater.* **2014**, *3*, 1648.

[12] H. E. Quinlan, T. Hasan, J. Jaddou, A. J. Hart, *J. Ind. Ecol.* **2017**, *21*, S15.

[13] T. C. Okwuosa, B. C. Pereira, B. Arafat, M. Cieszynska, A. Isreb, M. A. Alhnan, *Pharm. Res.* **2017**, *34*, 427.

[14] R. C. R. Beck, P. S. Chaves, A. Goyanes, B. Vukosavljevic, A. Buanz, M. Windbergs, A. W. Basit, S. Gaisford, *Int. J. Pharm.* **2017**, *528*, 268.

[15] M. Vaezi, H. Seitz, S. Yang, *Int. J. Adv. Manuf. Technol.* **2013**, *67*, 1721.

[16] L. Vaut, G. Zeng, G. Tosello, A. Boisen, Manuscript submitted for publication, **2019**.

[17] P. Marizza, S. S. Keller, A. Boisen, *Microelectron. Eng.* **2013**, *111*, 391.

[18] C. B. Fox, C. L. Nemeth, R. W. Chevalier, J. Cantlon, D. B. Bogdanoff, J. C. Hsiao, T. A. Desai, *Bioeng. Transl. Med.* **2017**, *2*, 9.

[19] Z. Abid, C. Gundlach, O. Durucan, C. von Halling Laier, L. H. Nielsen, A. Boisen, S. S. Keller, *Microelectron. Eng.* **2017**, *171*, 20.

[20] L. H. Nielsen, J. Nagstrup, S. Gordon, S. S. Keller, J. Østergaard, T. Rades, A. Müllertz, A. Boisen, *Biomed. Microdevices* **2015**, *17*, 1.

[21] B. Naisbett, J. Woodley, *Heart* **1995**, *173*, 223.

[22] J. D. Smart, *Adv. Drug Deliv. Rev.* **2005**, *57*, 1556.

[23] K. E. Jensen, in *Adv. Struct. Multidiscip. Optim.*, Springer International Publishing, Cham, **2018**, pp. 1224–1238.

[24] B. Hu, W. Margolin, I. J. Molineux, J. Liu, *Proc. Natl. Acad. Sci.* **2015**, *112*, E4919 LP.

[25] R. A. Cone, *Adv. Drug Deliv. Rev.* **2009**, *61*, 75.

[26] K. Edsman, H. Hägerström, *J. Pharm. Pharmacol.* **2005**, *57*, 3.

[27] K. V. R. Rao, P. Buri, *Int. J. Pharm.* **1989**, *52*, 265.

[28] P. Kerlin, A. Zinsmeister, S. Phillips, *Gastroenterology* **1982**, *82*, 701.

[29] N. K. Ahluwalia, D. G. Thompson, J. Barlow, L. Heggie, *Gut* **1994**, *35*, 625.

[30] D. M. Mudie, G. L. Amidon, G. E. Amidon, *Mol Pharm* **2010**, *7*, 1388.

Supporting Information

3D Printing of Reservoir Devices for Oral Drug Delivery and Enhanced Mucoadhesion

Lukas Vaut[*1], *Julia Joanna Juszczyk, Khorshid Kamguyan, Kristian Ejlebjærg Jensen, Guido Tosello and Anja Boisen*[*2]

E-mail: [1] lukv@dtu.dk , [2] aboi@dtu.dk

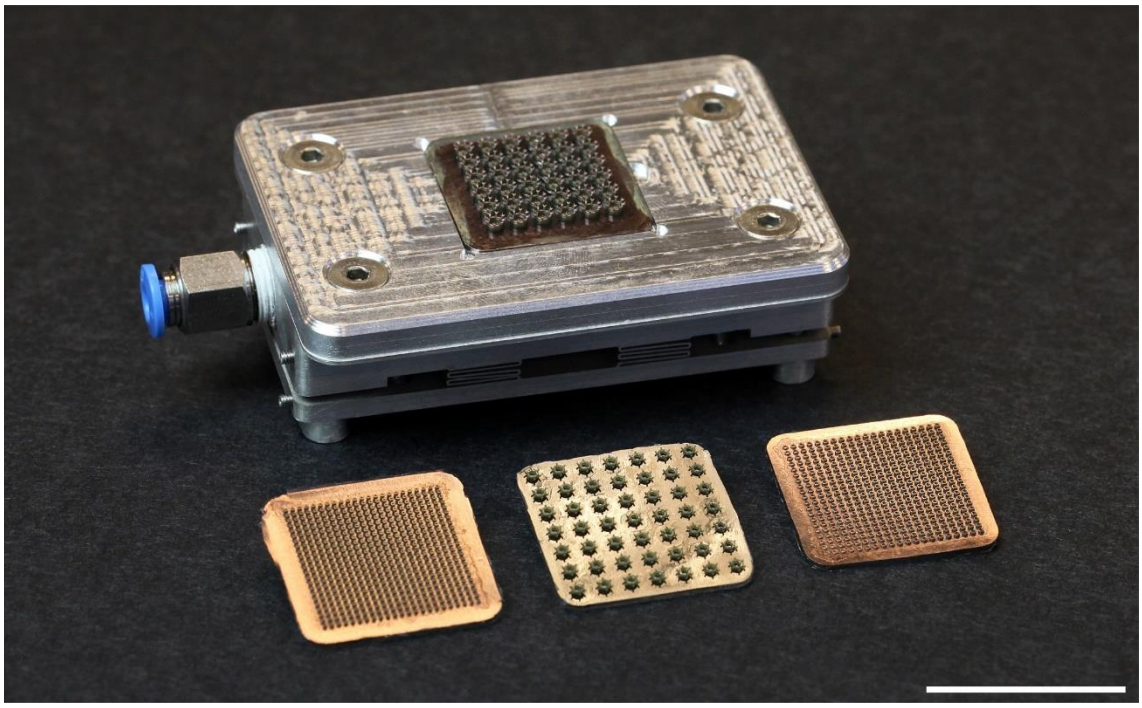

Figure S 1 *Photograph of different micro-/mini-reservoir devices on sacrificial polyvinyl alcohol substrates and customized holder for 3D printer. Scale bar is equal to 25 mm.*

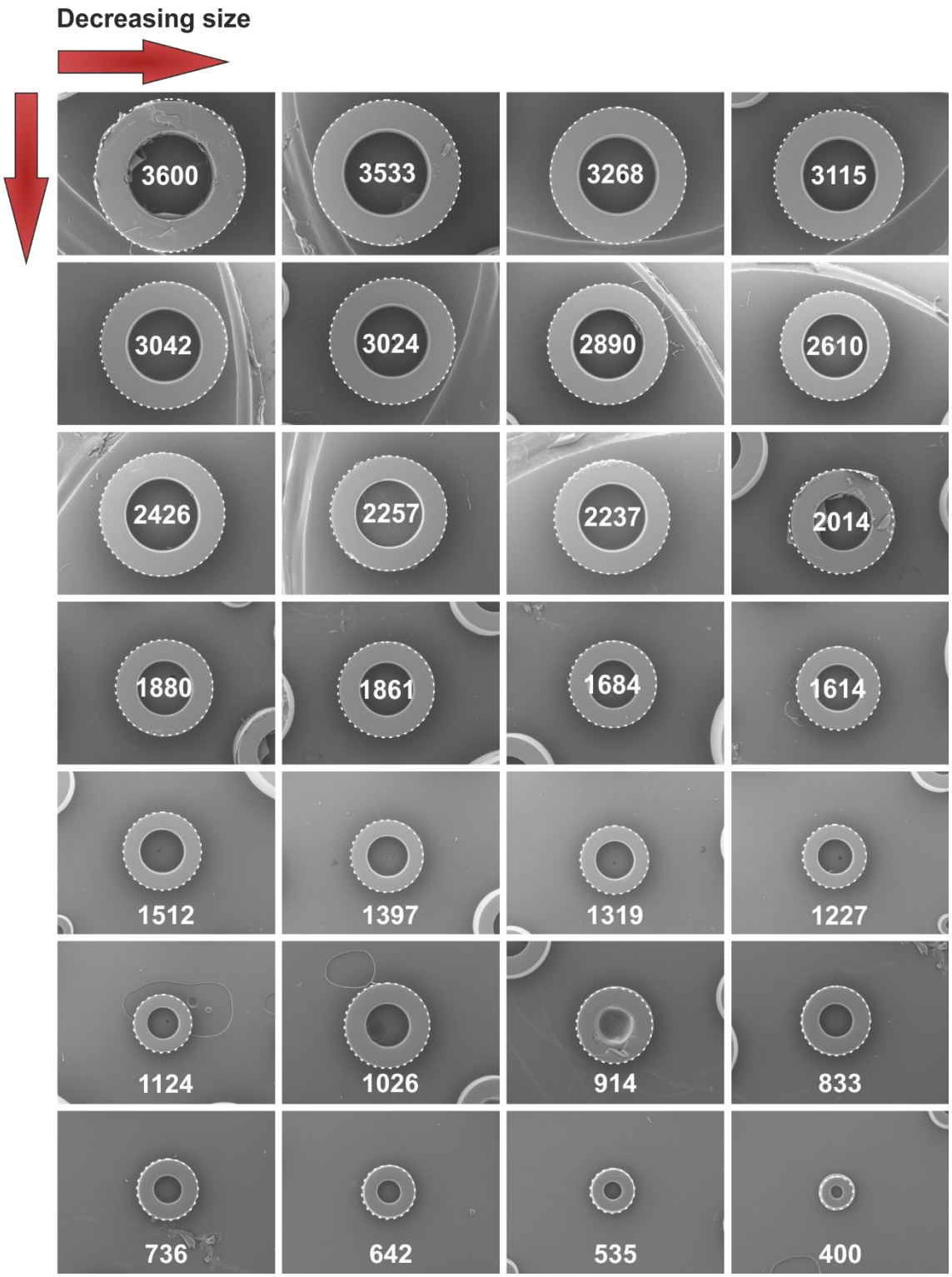

Figure S 2 *Scanning electron microscopy images of array of Control-design with different sizes. Numbers report the measured size of the outer reservoir diameter in micrometer. Dotted white lines illustrate the measurement.*

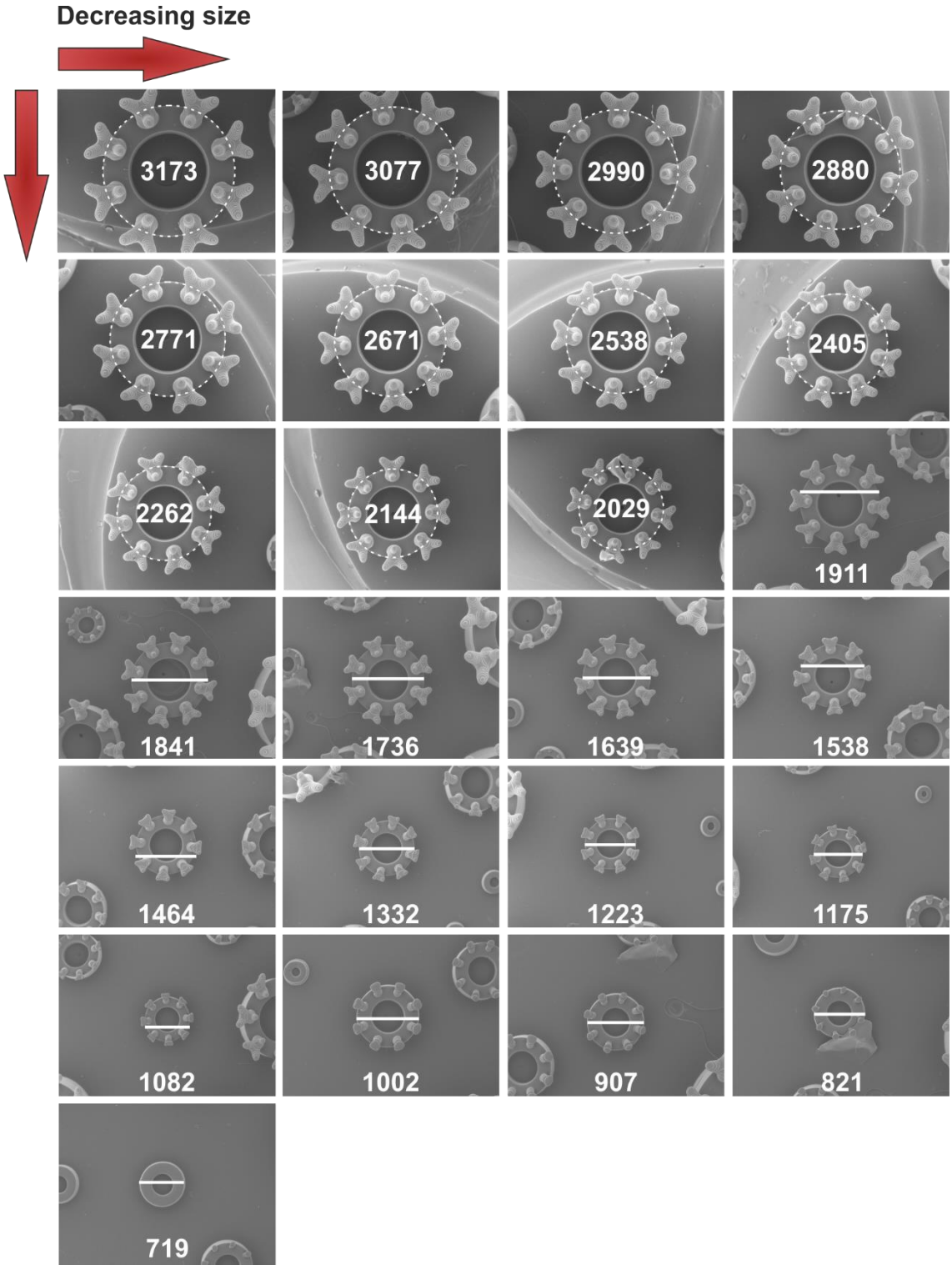

Figure S 3 *Scanning electron microscopy images of array of TO1-design with different sizes. Numbers report the measured size of the outer reservoir diameter in micrometer. Dotted white lines and white scale bars illustrate the measurement.*

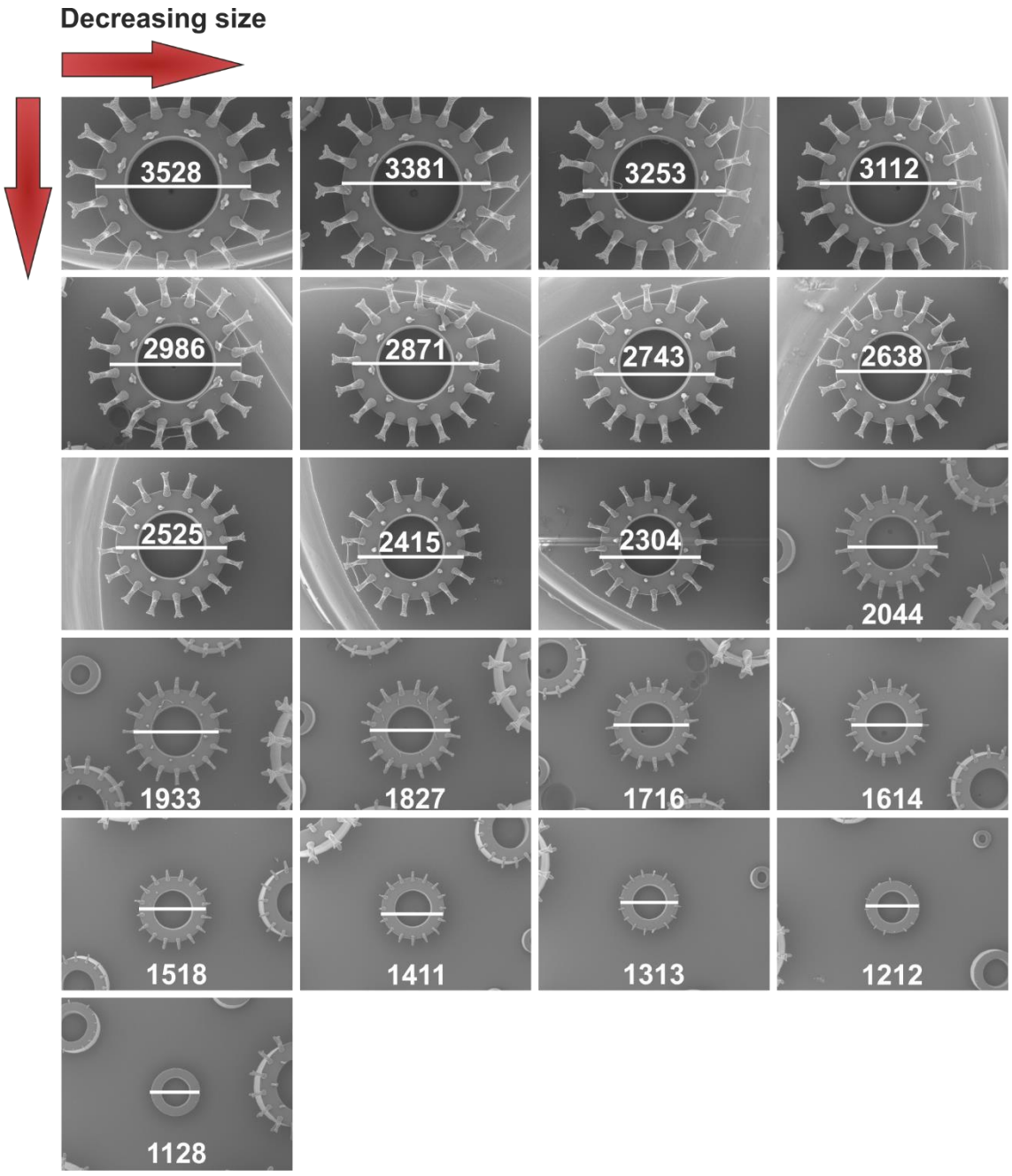

Figure S 4 *Scanning electron microscopy images of array of TO2-design with different sizes. Numbers report the measured size of the outer reservoir diameter in micrometer. White scale bars illustrate the measurement.*

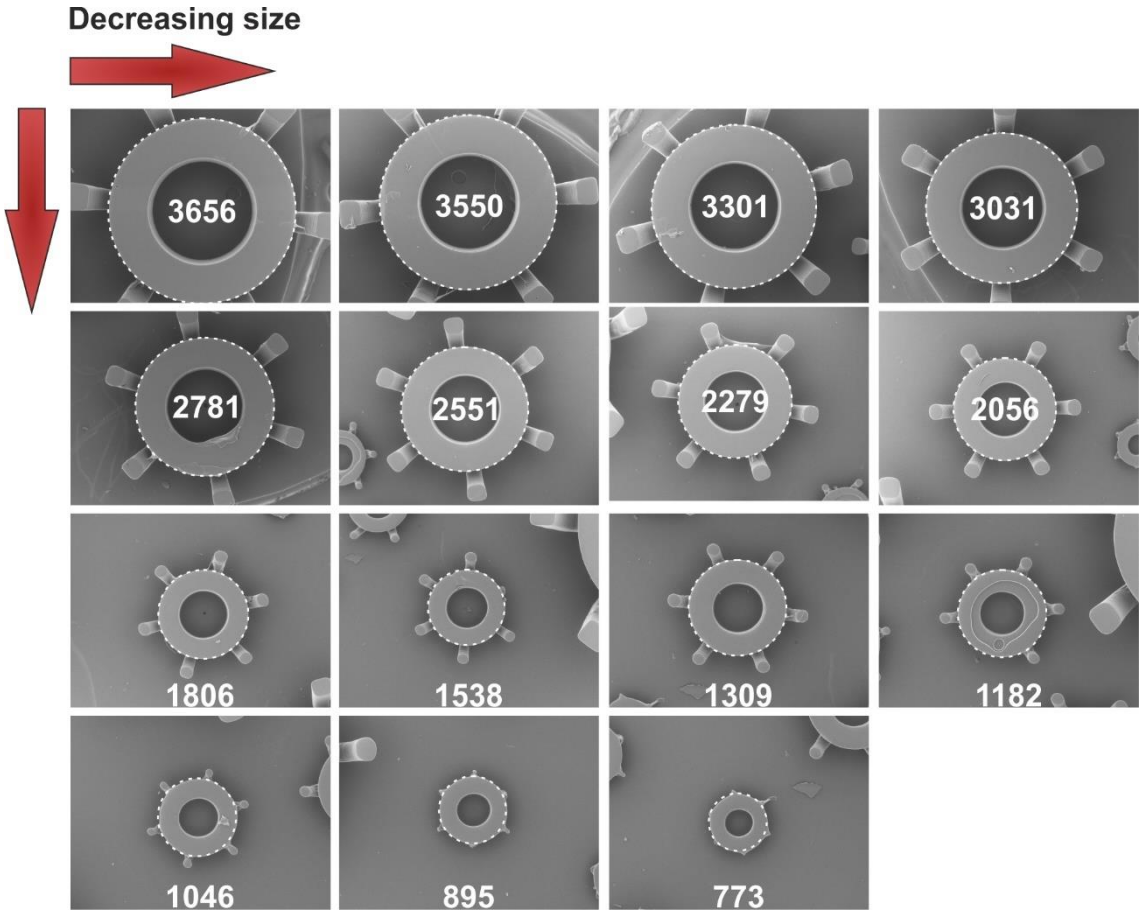

Figure S 5 *Scanning electron microscopy images of array of bio-inspired Phage-design (without spikes) with different sizes. Numbers report the measured size of the outer overhang diameter in micrometer. The diameter of the overhang is designed to be 1.2 times wider than the outer reservoir diameter. Dotted white lines illustrate the measurement.*

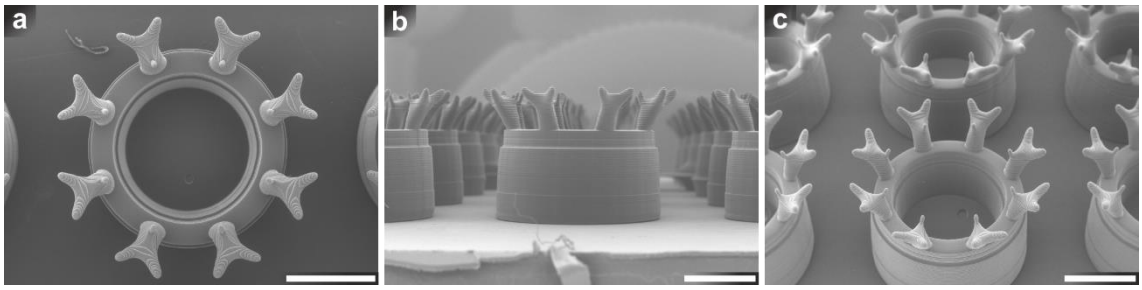

Figure S 6 *Scanning electron microscopy images of 3D printed array of miniaturized reservoir devices with edge anchors (TO1) on sacrificial polyvinyl alcohol substrates. Scale bar is equal to 1 mm. (a) top view, (b) side view and (c) 45° tilted view.*

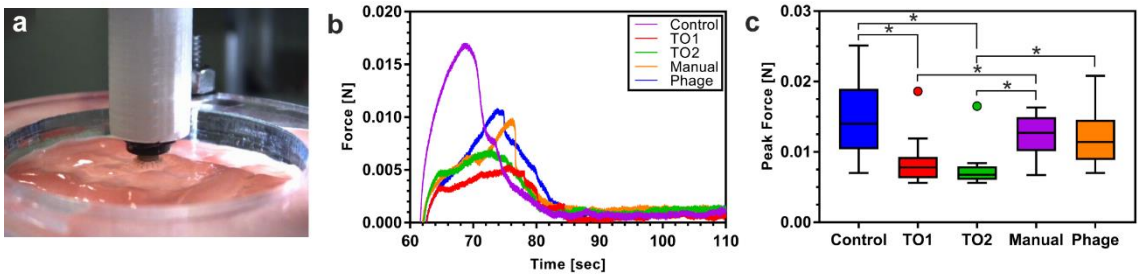

Figure S 7 *Tensile mucoadhesion measurement. (a) Measurement setup with porcine intestinal tissue and single reservoir device (TO2) at moment of peak force. (b) Exemplary force plot of different reservoir designs. (c) Comparison of peak force between different reservoir designs. N = 10. Stars indicate statistical significance with p < 0.05 according to Least Significant Difference test on a replicated latin square design.*

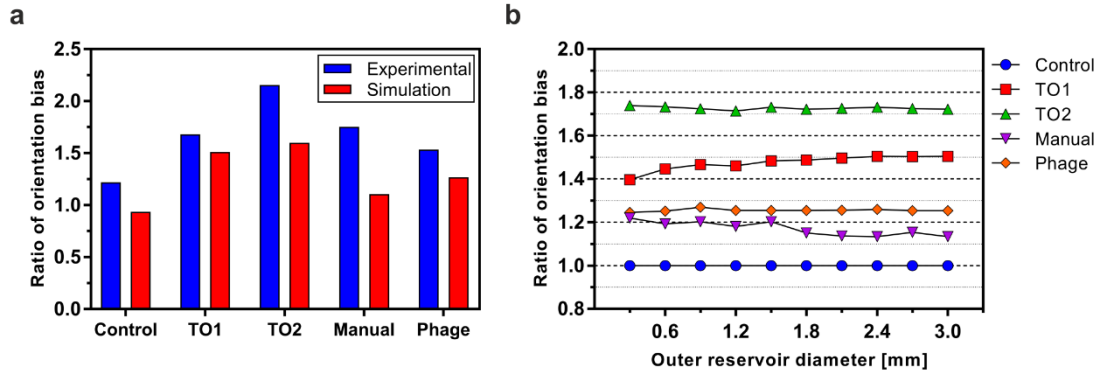

Figure S 8 *Comparison of orientation bias of different reservoir designs. (a) Orientation bias as quotient of retained devices oriented downwards and retained devices oriented upwards as experimentally observed at 40.9 ml min^{-1} (RF50) and quotient of simulated drag force on devices oriented downwards and upwards. (b) Orientation bias as quotient of simulated drag force on devices oriented downwards and devices oriented upwards over a range of outer reservoir diameters.*

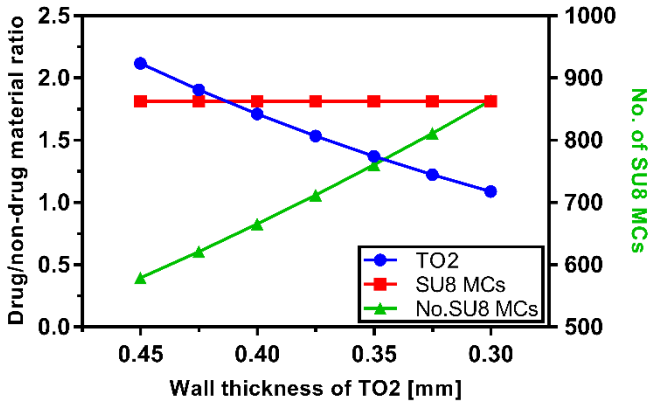

Figure S 9 *Drug to non-drug material ratio of one mini-reservoir and SU8 microcontainers. Calculated volume of device material divided by calculated volume of drug material (volume of reservoir). Comparison between one mini-reservoir (TO2 design) at a size of 3 mm (outer container diameter) and the adjusted number of required recently published SU8 microcontainers to match the volume of drug, over a span of different mini-reservoir wall thicknesses.* [1,2]

References

[1] L. H. Nielsen, A. Melero, S. S. Keller, J. Jacobsen, T. Garrigues, T. Rades, A. Müllertz, A. Boisen, *Int. J. Pharm.* **2016**, *504*, 98.

[2] C. Mazzoni, F. Tentor, S. A. Strindberg, L. H. Nielsen, S. S. Keller, T. S. Alstrøm, C. Gundlach, A. Müllertz, P. Marizza, A. Boisen, *J. Control. Release* **2017**, *268*, 343.

7.4 Manuscript IV

Fully replicable and automated retention measurement setup for characterization of bio-adhesion

Lukas Vaut, Ermes Scarano, Guido Tosello and Anja Boisen

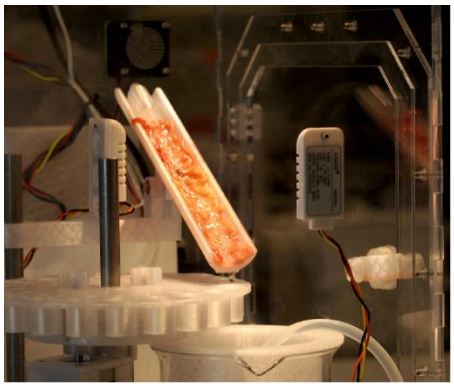

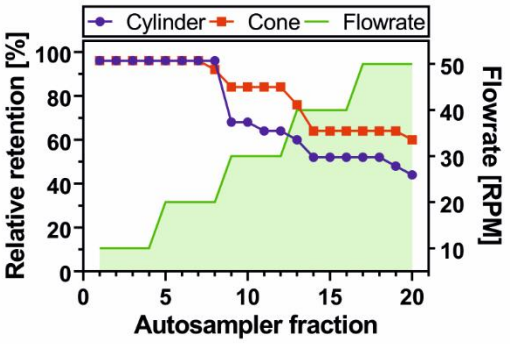

Fully replicable and automated retention measurement setup for characterization of bio-adhesion

Lukas Vaut, Ermes Scarano, Guido Tosello and Anja Boisen

L. Vaut, E. Scarano, Prof. A. Boisen, The Danish National Research Foundation and Villum Foundation's Center for Intelligent Drug Delivery and Sensing Using Microcontainers and Nanomechanics (IDUN), Department of Health Technology, Technical University of Denmark, Kgs. Lyngby, 2800, Denmark

Prof. G. Tosello, Department of Mechanical Engineering, Technical University of Denmark, Kgs. Lyngby, 2800, Denmark

Contact email: lukv@dtu.dk , aboi@dtu.dk

Keywords: open source hardware, open labware, retention model, ex vivo flow model, flow-through method, bioadhesion, mucoadhesion

The retention model by Rao and Buri is often used to characterize microparticles and other drug delivery systems for their bio-adhesive properties. Currently, these experiments are performed on customized setups, reducing reproducibility of results obtained in different labs. As a solution, we propose a fully replicable retention model, which can be constructed by parts mostly made by 3D printing and laser cutting as well as a limited amount of other easy to source commercially available parts. In addition of being fully replicable, the setup features integration of a climate-controlled chamber, a peristaltic pump and an autosampler, thereby enabling fully automated, but customized control of the experiments. Using the presented retention model setup and an automated experimental sequence, the setup has been proven capable of investigating mucoadhesion of differently shaped particles to porcine intestinal tissue.

Specifications table

Hardware name	*Integrated retention model setup*
Subject area	• Medical (e.g. Pharmaceutical Science)
Hardware type	• *Other [Evaluation of bio-adhesive properties of e.g. drug delivery devices, drug formulations, adhesive structures]*
Open Source License	CC BY 4.0, CC BY-NC-SA 4.0 and MIT license
Cost of Hardware	*400-500 USD*
Source File Repository	http://dx.doi.org/10.17632/v2rdbwpx7k.1

1 Hardware in context

The retention model, also referred to as ex-vivo flow model or flow-through method, was first introduced by Rao and Buri in 1989 and was developed as a method to assay the bio-adhesion of polymers and microparticles to rat gastro-intestinal tissue [1]. Since then it has proven to be a very versatile method, which is commonly used to investigate the mucoadhesive properties of various drug delivery formulations and therefore is regarded to be one of the main methods to measure mucoadhesion [2]. In this regard, the method has been applied to determine the mucoadhesiveness of e.g. thiomer microparticles to porcine intestinal tissue, metformin hydrochloride/chitosan microparticles to porcine buccal mucosal tissue or microfabricated janus devices to porcine intestinal tissue [3–5]. The precise control of experimental conditions, such as temperature, humidity, content of simulated biological fluids as well as the flow rate is considered to be very important as the lack of it can negatively affect reproducibility of the experiments [2].

The simplicity and versatility of the core elements of the experimental setup in general, a pump connected through a tube to a tissue holder, which holds a biological sample tissue at a specific angle, motivates researchers to construct their own customized setup. On the one hand, the construction of home-made setups provides a lot of flexibility and design freedom to researchers, but on the other hand it leads to a lack of reproducibility as well as comparability in the scientific community as there is no common standard with regards to the way setups are built and the experiments are performed. Furthermore, information about how these setups are constructed and/or used is often missing so that a replication of the same setup used for a published work is not possible. The commonly used experimental setups also exhibit various degrees of complexity. In contrast to the simplest system consisting of a pump, a tubing and a tissue holder, the system can get more sophisticated when temperature and humidity control of the ambient climate are included. Consequently, reproducing such a system can become more difficult.

The emergence of affordable 3D printing and other rapid prototyping techniques (e.g. laser cutting) has triggered the open sharing of design files for customized lab equipment, also called open labware [6,7]. Based on this principle, a retention model setup can be designed, 3D printed and therefore replicated everywhere where there is a 3D printer available (e.g. in Universities or public maker spaces). In this paper, we propose and share designs for a retention model setup that aims at balancing reproducibility with customizability and flexibility by being modular and upgradable. The setup can be fully and easily replicated by the use of 3D printed and laser cut parts as well as commonly available commercial components. As a free and open available development platform, the setup could in the future offer a standard for retention model experiments that researchers could refer to.

2 Hardware description

The retention model setup (**Figure 1**) was designed to fulfill certain requirements. Above all, it was considered important that 3D printing and laser cutting can be used to fabricate most of the parts, therefore making the replication process as simple as possible. All other parts that are needed should be cheap and easy to source. For this reason and to integrate several required functionalities in one control loop, we chose the Arduino Mega 2560 (microcontroller)/ RAMPS 1.4 (Arduino shield) combination, which is frequently used for the control of RepRap 3D printers. The RAMPS 1.4 shield possesses all required circuits and connectors to use it in combination with the Arduino for the control of temperature, humidity, pump flow and autosampler rotation. The simple control of temperature and humidity is accomplished with the use of relays, a ceramic infrared heat lamp, an ultrasonic mist fogger and three fans and two DHT22 temperature and humidity sensors. The basic design of the system is kept in a modular way by arranging all components on a breadboard-style base plate, therefore allowing further customization and upgradability. The integration of a peristaltic pump as well as a rotary autosampler adds versatility and precision to the setup as it enables the execution of customized and fully automated program sequences.
In summary, the presented retention model setup can offer:

- **Improved repeatability of flow retention experiments**
  (e.g. through climate-controlled environment and automation)
- **Improved reproducibility of flow retention experiments**
  (when different researchers use the same setup)
- **Expanded functional range**
  (by integration of peristaltic pump, auto-sampler and automation with Arduino microcontroller e.g. fully automated customized programs for experiments)

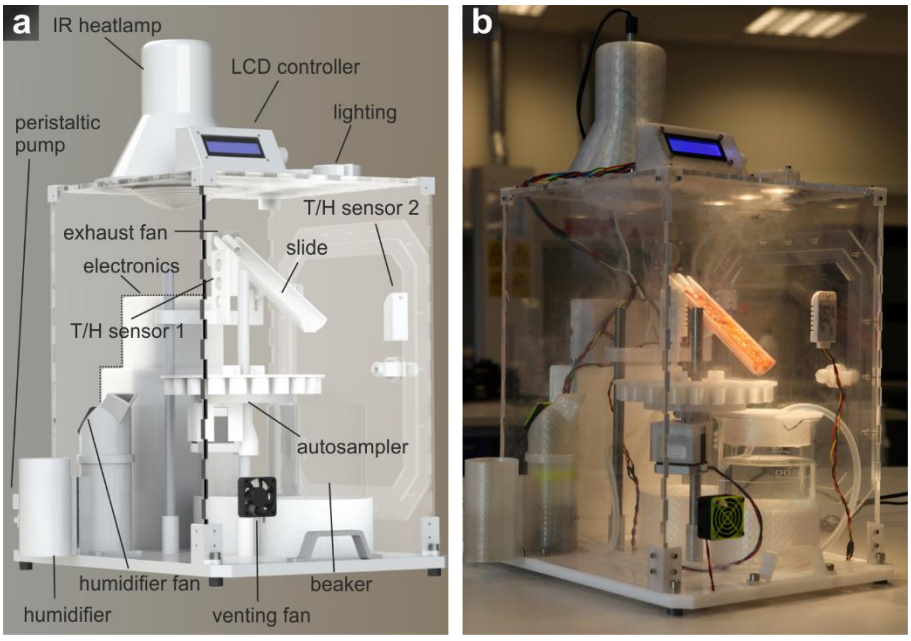

Figure 1 *3D rendering of technical drawing (a) and (b) photo of completed setup during use.*

3 Design files

3.1 Design Files Summary

All design files listed in this section are available for download from the Mendeley data repository. Most of the components were designed specifically for this project, however in some cases resources from other projects were used to obtain needed components. An online tool was used to generate the climate chamber box design with outside dimensions of 291 x 296.5 x 400 mm, a material thickness of 5 mm, finger slots with a tab length of 25 mm and a laser cut kerf of 0.1 mm, which then was modified according to the need of this project [8]. *lock_new-lever.SLDPRT* was designed as a modification to an online available lock design to fit the specifications given by the climate chamber design presented in this work [9]. *parametric_butt_hinge_3.5.2.scad* OpenSCAD library was used to generate a hinge design [10]. *Getriebe.scad* OpenSCAD library was used to generate the gear designs needed for the autosampler [11]. *pump_housing.SLDPRT* was designed as a modification to an open source precise peristaltic pump [12]. humidifier_2.0.SLDPRT and *humidifier_fan.SLDPRT* are a modified redesign of a mini desktop humidifier [13].

Design file name	Designator	File type	Open-source license	Location of the file
slide.SLDPRT	slide	CAD	CC BY 4.0	Click to download
height_adjustable_slide_holder.SLDPRT	slide	CAD	CC BY 4.0	Click to download
baseplate1.SLDPRT	baseplate +holders	CAD	CC BY 4.0	Click to download
baseplate2.SLDPRT	baseplate +holders	CAD	CC BY 4.0	Click to download
beaker_fix.SLDPRT	baseplate +holders	CAD	CC BY 4.0	Click to download
rod_holder.SLDPRT	baseplate +holders	CAD	CC BY 4.0	Click to download
handle.SLDPRT	baseplate +holders	CAD	CC BY 4.0	Click to download
foot.SLDPRT	baseplate +holders	CAD	CC BY 4.0	Click to download
outside_corner.SLDPRT	baseplate +holders	CAD	CC BY 4.0	Click to download
outside_corner_mirrored.SLDPRT	baseplate +holders	CAD	CC BY 4.0	Click to download

outside_corner_regular.SLDPRT	baseplate+holders	CAD	CC BY 4.0	Click to download
outside_corner_regular_mirrored.SLDPRT	baseplate+holders	CAD	CC BY 4.0	Click to download
box_back.SLDPRT	climate_chamber	CAD	CC BY 4.0	Click to download
box_front.SLDPRT	climate_chamber	CAD	CC BY 4.0	Click to download
box_top.SLDPRT	climate_chamber	CAD	CC BY 4.0	Click to download
box_side.SLDPRT	climate_chamber	CAD	CC BY 4.0	Click to download
box_doorside.SLDPRT	climate_chamber	CAD	CC BY 4.0	Click to download
box_doorframe.SLDPRT	climate_chamber	CAD	CC BY 4.0	Click to download
box_door.SLDPRT	climate_chamber	CAD	CC BY 4.0	Click to download
corner_top.SLDPRT	climate_chamber	CAD	CC BY 4.0	Click to download
lock_new-lever.SLDPRT	climate_chamber	CAD	CC BY 4.0	Click to download
hinges.scad	climate_chamber	CAD	CC BY 4.0	Click to download
parametric_butt_hinge_3.5.2.scad	climate_chamber	CAD	CC BY 4.0	Click to download
humidifier_2.0.SLDPRT	humidifier	CAD	CC BY 4.0	Click to download
humidifier_fan.SLDPRT	humidifier	CAD	CC BY 4.0	Click to download
humidifier_mesh.SLDPRT	humidifier	CAD	CC BY 4.0	Click to download
pump_housing.SLDPRT	peristaltic_pump	CAD	CC BY 4.0	Click to download
lamp_case.SLDPRT	electronics	CAD	CC BY 4.0	Click to download
controller_housing.SLDPRT	electronics	CAD	CC BY 4.0	Click to download

controller_knob.SLDPRT	electronics	CAD	CC BY 4.0	Click to download
plastic_washer.SLDPRT	electronics	CAD	CC BY 4.0	Click to download
electronics_housing.SLDPRT	electronics	CAD	CC BY 4.0	Click to download
ikea_led_housing.SLDPRT	electronics	CAD	CC BY 4.0	Click to download
ssr_housing.SLDPRT	electronics	CAD	CC BY 4.0	Click to download
warning_sign.SLDPRT	electronics	CAD	CC BY 4.0	Click to download
autosampler_gear_drive.scad	autosampler	CAD	CC BY 4.0	Click to download
Getriebe.scad	autosampler	CAD	CC BY-NC-SA 4.0	Click to download
gear_drive_cover.SLDPRT	autosampler	CAD	CC BY 4.0	Click to download
geardrive_motormount.SLDPRT	autosampler	CAD	CC BY 4.0	Click to download
thumbnut.SLDPRT	autosampler	CAD	CC BY 4.0	Click to download
eppiholder.SLDPRT	autosampler	CAD	CC BY 4.0	Click to download
eppiholder2.SLDPRT	autosampler	CAD	CC BY 4.0	Click to download
15ml_holder.SLDPRT	autosampler	CAD	CC BY 4.0	Click to download
50ml_holder.SLDPRT	autosampler	CAD	CC BY 4.0	Click to download
mesh_holder.SLDPRT	autosampler	CAD	CC BY 4.0	Click to download
small_mesh.SLDPRT	autosampler	CAD	CC BY 4.0	Click to download
mesh.SLDPRT	accessories	CAD	CC BY 4.0	Click to download

3.2 3D Printing Files

All 3D printing files are available in the STL file format for download from the linked Mendeley data repository. The table gives an overview of all files that have to be 3D printed in order to complete the project. Furthermore, the table gives information about how many replicates of the components are required, how they look and in which orientation they should be 3D printed (images were generated with 3D printing slicing software). For this project, usually all parts were 3D printed with a 0.4 mm nozzle, a layer height of 0.2 mm and 20% infill from PETG filament (2 spools of 1 kg each are sufficient). In some cases, the use of support material was necessary. The support material can be seen in the images as stacks of green lines. As the object humidifier_2.0 is supposed to contain water during the application, it should be printed with a higher infill density and increased amount of shells. In case water would still be leaking from the object, the authors recommend sealing the reservoir by impregnation with silicone or epoxy resin.
lock_hole-screw.stl, *lock_big-nut.stl*, *lock_key.stl* and *lock_small-nut.stl* were obtained from an open lock design and renamed [9]. *pump_case_bottom.stl*, *pump_case_top_120.stl*, *bearing_mount_top.stl* and *bearing_mount_bottom_01.stl* were obtained from an open source peristaltic pump design [12]. *40mm_Fan_grill_final.stl* was likewise obtained from external source as a publicly distributed design [14]. *thumbnut.stl* requires the insertion of an M3 nut during the 3D printing procedure.

Design file name	Designator	No. of required prints	Image	Open-source license	Location of the file
slide.stl	slide	1	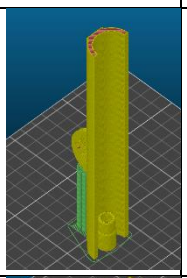	CC BY 4.0	Click to download
height_ adjustable_ slide_holder .stl	slide	1	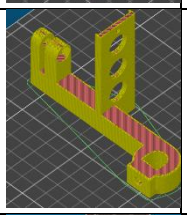	CC BY 4.0	Click to download
beaker_fix .stl	baseplate+ holders	1 (+ 1 optional)	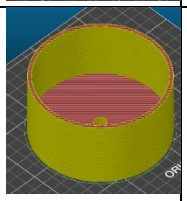	CC BY 4.0	Click to download
rod_holder .stl	baseplate+ holders	2	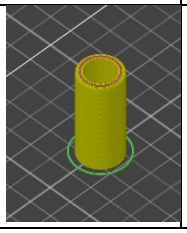	CC BY 4.0	Click to download

handle.stl	baseplate+ holders	2	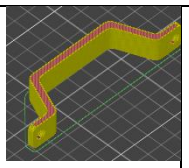	CC BY 4.0	Click to download
foot.stl	baseplate+ holders	5	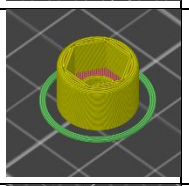	CC BY 4.0	Click to download
outside_ corner.stl	baseplate+ holders	1	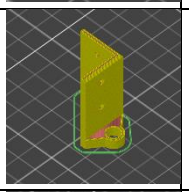	CC BY 4.0	Click to download
outside_corn er_mirrored .stl	baseplate+ holders	1	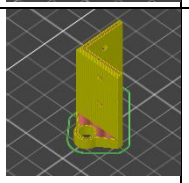	CC BY 4.0	Click to download
outside_corn er_regular .stl	baseplate+ holders	1	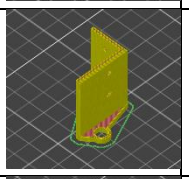	CC BY 4.0	Click to download
outside_corn er_regular_ mirrored.stl	baseplate+ holders	1	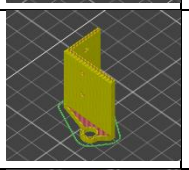	CC BY 4.0	Click to download
corner_top .stl	climate_ chamber	4	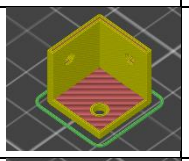	CC BY 4.0	Click to download
hinge.stl	climate_ chamber	2	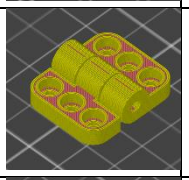	CC BY 4.0	Click to download
lock_hole- screw.stl	climate_ chamber	1	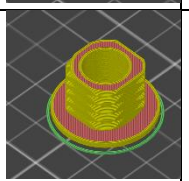	CC BY 4.0	Click to download
lock_big-nut .stl	climate_ chamber	1	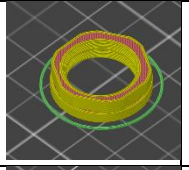	CC BY 4.0	Click to download
lock_key.stl	climate_ chamber	1	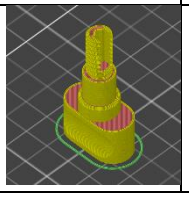	CC BY 4.0	Click to download

lock_small-nut.stl	climate_ chamber	2	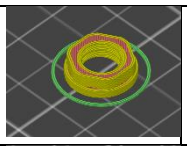	CC BY 4.0	Click to download
lock_new-lever.stl	climate_ chamber	1	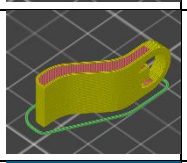	CC BY 4.0	Click to download
humidifier_ 2.0.stl	humidifier	1	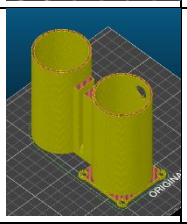	CC BY 4.0	Click to download
humidifier_f an.stl	humidifier	1	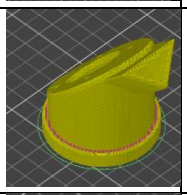	CC BY 4.0	Click to download
humidifier_ mesh.stl	humidifier	1	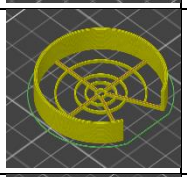	CC BY 4.0	Click to download
pump _housing.stl	peristaltic_ pump	1	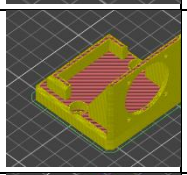	CC BY 4.0	Click to download
pump_case_ bottom.stl	peristaltic_ pump	1	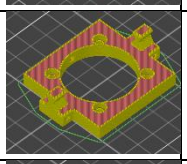	CC BY-NC-SA 4.0	Click to download
pump_case_ top_120.stl	peristaltic_ pump	1	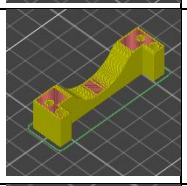	CC BY-NC-SA 4.0	Click to download
bearing _mount_top .stl	peristaltic_ pump	1	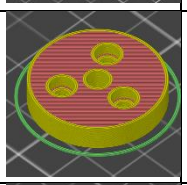	CC BY-NC-SA 4.0	Click to download
bearing_mo unt_bottom _01.stl	peristaltic_ pump	1	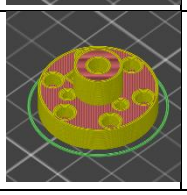	CC BY-NC-SA 4.0	Click to download

lamp_case .stl	electronics	1	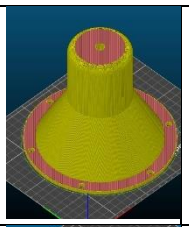	CC BY 4.0	Click to download
controller_ housing.stl	electronics	1	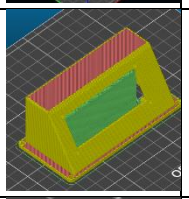	CC BY 4.0	Click to download
controller_ knob.stl	electronics	1	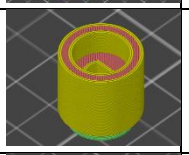	CC BY 4.0	Click to download
plastic _washer.stl	electronics	13	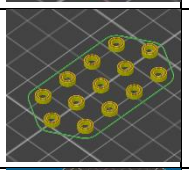	CC BY 4.0	Click to download
ssr_housing. stl	electronics	1	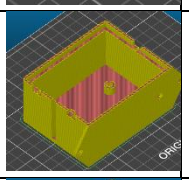	CC BY 4.0	Click to download
electronics_ housing.stl	electronics	1	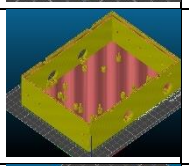	CC BY 4.0	Click to download
ikea_led_ housing.stl	electronics	1	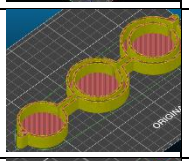	CC BY 4.0	Click to download
warning _sign.stl	electronics	1	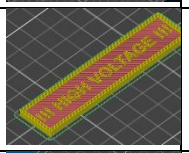	CC BY 4.0	Click to download
planetary _gear_drive .stl	autosampler	1	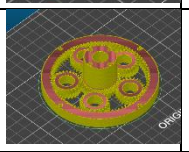	CC BY 4.0	Click to download
planetary _gear_drive_ shim.stl	autosampler	1	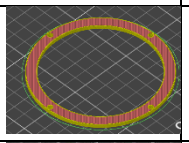	CC BY 4.0	Click to download
ring_gear.stl	autosampler	1	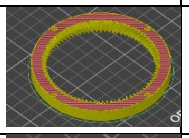	CC BY 4.0	Click to download
herringbone _gear.stl	autosampler	1	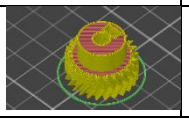	CC BY 4.0	Click to download

gear_drive_cover.stl	autosampler	1	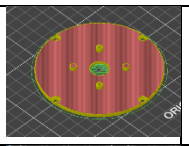	CC BY 4.0	Click to download
geardrive_motormount.stl	autosampler	1	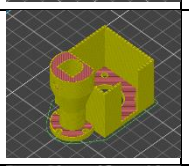	CC BY 4.0	Click to download
thumbnut.stl	autosampler	2	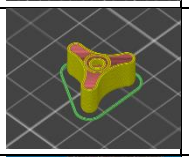	CC BY 4.0	Click to download
eppiholder.stl	autosampler	optional	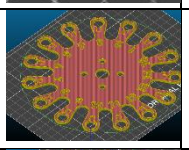	CC BY 4.0	Click to download
eppiholder2.stl	autosampler	optional	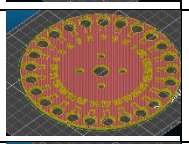	CC BY 4.0	Click to download
15ml_holder.stl	autosampler	optional		CC BY 4.0	Click to download
50ml_holder.stl	autosampler	optional	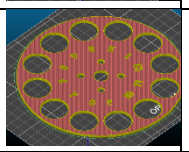	CC BY 4.0	Click to download
mesh_holder.stl	autosampler	optional	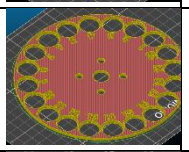	CC BY 4.0	Click to download
small_mesh.stl	autosampler	optional	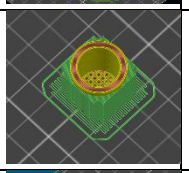	CC BY 4.0	Click to download
mesh.stl	accessories	1	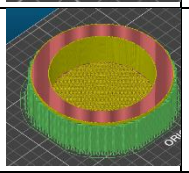	CC BY 4.0	Click to download
40mm_Fan_grill_final.stl	accessories	5	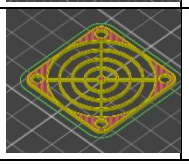	CC BY 4.0	Click to download

3.3 Laser Cutting Files

To complete the construction of the presented retention model setup, it is necessary to cut out several designs from sheets of polymer. All designs are available as DXF files for download from the Mendeley data repository. In this work, all designs were designed to fit in the A3 paper format and were cut from acrylic using a CO_2 laser cutter (Epilog Mini 18). The designs *baseplate1_labeled.dxf* and *baseplate2.dxf* were cut from 6 mm acrylic, while all other designs except for *woodplate_ssr.dxf* were cut from 5mm acrylic. *woodplate_ssr.dxf* was cut from 3 mm high density fiber board.

Due to the limited chemical resistance of acrylic, the authors recommend to not use solvents (e.g. ethanol) for cleaning of these boards. All sheets can also be cut from different materials and also by using different cutting methods (such as CNC routing).

Design file name	Designator	File type	Open source license	Location of the file
baseplate1_labeled.dxf	baseplate+holders	DXF	CC BY 4.0	Click to download
baseplate2.dxf	baseplate+holders	DXF	CC BY 4.0	Click to download
box_back.dxf	climate_chamber	DXF	CC BY 4.0	Click to download
box_doorside+electronics_cover.dxf	climate_chamber and electronics	DXF	CC BY 4.0	Click to download
box_front.dxf	climate_chamber	DXF	CC BY 4.0	Click to download
box_side.dxf	climate_chamber	DXF	CC BY 4.0	Click to download
box_top+SSR_cover.dxf	climate_chamber and electronics	DXF	CC BY 4.0	Click to download
door+frame.dxf	climate_chamber	DXF	CC BY 4.0	Click to download
woodplate_ssr.dxf	electronics	DXF	CC BY 4.0	Click to download

3.4 Software

An Arduino Mega 2560 microcontroller is used to control the feedback loop for the climate control as well as to control an autosampler and a peristaltic pump in combination with an Arduino Pro Mini. A rotary encoder and LCD display serve as a feedback and input interface to control the operation of the microcontrollers. The used Arduino sketches are available for download as ino files from the Mendeley data repository. In order to integrate the function of the DHT22 temperature and humidity sensor as well as an I2C LCD display, external libraries were employed. *Adafruit_Unified_Sensor* and *DHT-sensor-library-master* were obtained from Adafruit and *Newliquidcrystal_1.3.5* was obtained from an open source [15–17].

File name	File type	Open source license	Location of the file
main.ino	Arduino	CC BY 4.0	Click to download
mini_pump_control.ino	Arduino	CC BY 4.0	Click to download
Adafruit_Unified_Sensor	Arduino library	MIT license	Click to download
DHT-sensor-library-master	Arduino library	MIT license	Click to download
Newliquidcrystal_1.3.5	Arduino library	CC BY 4.0	Click to download

4 Bill of Materials

4.1 Bill of Materials

In addition to the 3D printed and laser cut components of the system, some parts must be obtained from external sources. The table gives an overview of which and how many items need to be purchased. While all listed components should be easy to source, the pricing of those can vary a lot. The displayed costs in the table are calculated based on the parts we have obtained or on the prices we could find at the given sources at time of publication.

Designator	Component	Number	Cost per unit - currency [USD]	Total cost - currency [USD]	Source of materials	Material type
baseplate+ holders	6mm acrylic sheet (297 x 420 mm)	2	15.00	30.00	Hardware store	Polymer
baseplate+ holders	5mm acrylic sheet (297 x 420 mm)	6	13.00	78.00	Hardware store	Polymer
baseplate+ holders	12 mm aluminum rod (300 mm)	2	1.60	3.20	Hardware store	Metal
humidifier	24 VDC Ultrasonic mist fogger	1	11.38	11.38	Amazon	Electronics
humidifier	12 VDC 40x10 mm fan	1	5.00	5.00	Mouser	Electronics
climate_ chamber	12 VDC 40x20 mm fan	2	5.00	10.00	Mouser	Electronics
electronics	12 VDC 40x20 mm fan	1	5.00	5.00	Mouser	Electronics
electronics	150W Ceramic infrared heat lamp for reptiles	1	28.50	28.50	Amazon	Electronics
electronics	Aluminum tape	1	7.30	7.30	RS Components	Tape

electronics	Ceramic heat lamp power socket	1	8.50	8.50	Amazon	Electronics
electronics	Kudom 10 A 280 VAC Solid State Relay Panel Mount	1	19.20	19.20	RS Components	Electronics
electronics	inline fuse holder	1	2.36	2.36	RS Components	Electronics
electronics	3A cartridge fuse	1	0.27	0.27	RS Components	Electronics
electronics	Arduino Mega 2560	1	9.00	9.00	Ebay	Electronics
electronics	RAMPS 1.4 Arduino Mega Shield	1	9.00	9.00	Ebay	Electronics
electronics	A4988 Stepper drivers	2	1.80	3.60	Ebay	Electronics
electronics	Arduino Pro mini	1	5.13	5.13	Ebay	Electronics
electronics	USB to serial converter for Arduino	1	2.50	2.50	Ebay	Electronics
electronics	Rotary Encoder	1	2.80	2.80	Ebay	Electronics
electronics	Ikea Ledberg spots (pack with 4)	1	13.00	13.00	Ikea	Electronics
electronics	DF Robot Gravity Digital 5A Relay Module	2	4.90	9.80	Mouser	Electronics
electronics	I2C 2x16 LCD	1	6.00	6.00	Ebay	Electronics
electronics	DHT22 Sensor	2	15.00	30.00	Mouser	Electronics
electronics	5A 250 VAC Toggle switch	1	2.85	2.85	RS Components	Electronics

electronics	LM2577 LED DC/DC boost converter	1	5.70	5.70	Ebay	Electronics
electronics	12V DC 7A LED power supply	1	11.40	11.40	Ebay	Electronics
electronics	colored wires 0.14 mm2 (+fem. pin headers)	1	10.00	10.00	Amazon	Electronics
autosampler	Nema 17 stepper motor	1	14.00	14.00	Ebay	Electronics
peristaltic_ pump	Nema 17 stepper motor	1	14.00	14.00	Ebay	Electronics
peristaltic_ pump	Needle bearing HK 0408	3	4.30	12.90	RS Components	Metal
peristaltic_ pump	4x14 mm pin	3	5.70	17.10	Amazon	Metal
peristaltic_ pump	ID 4mm 1.6mm wall thickness silicone tubing (1m)	1	6.61	6.61	Lab supplier	Polymer
General	PETG filament (2000g)	1	45.68	45.68	3D print supplier	Polymer
General	M6X25 hex head cap screws	10	0.28	2.76	Amazon or hardware store	Metal
General	M6X20 hex head cap screws	10	0.25	2.50	Amazon or hardware store	Metal
General	M6X16 hex head cap screws	10	0.56	5.59	Amazon or hardware store	Metal
General	M6X12 hex head cap screws	10	0.22	2.21	Amazon or hardware store	Metal

General	M6X10 hex head cap screws	10	0.22	2.21	Amazon or hardware store	Metal
General	M6 Nut	30	0.18	5.34	Amazon or hardware store	Metal
General	M4x10 Button head screws	20	0.20	3.95	Amazon or hardware store	Metal
General	M4x8 hex head cap screw	5	0.20	1.00	Amazon or hardware store	Metal
General	M3x30 hex head cap screws	20	0.21	2.13	Amazon or hardware store	Metal
General	M3x25 hex head cap screws	10	0.18	1.84	Amazon or hardware store	Metal
General	M3x20 hex head cap screws	10	0.17	1.72	Amazon or hardware store	Metal
General	M3x16 hex head cap screws	10	0.17	1.68	Amazon or hardware store	Metal
General	M3x10 hex head cap screws	50	0.10	4.85	Amazon or hardware store	Metal
General	M3x8 hex head cap screws	20	0.20	4.00	Amazon or hardware store	Metal
General	M3x6 hex head cap screws	10	0.16	1.62	Amazon or hardware store	Metal
General	M3x25 hex head countersunk screw	5	0.27	1.35	Amazon or hardware store	Metal
General	M3x6 hex head countersunk screw	5	0.25	1.24	Amazon or hardware store	Metal

General	M3x10 grub screw	10	0.23	2.34	Amazon or hardware store	Metal
General	M3x8 grub screw	10	0.23	2.34	Amazon or hardware store	Metal
General	M3 Nut	10	0.17	1.70	Amazon or hardware store	Metal

4.2 Required tools

For the fabrication and assembly process, access to the following tools is required:

- 3D printer
- Laser cutter
- M3, M4 and M6 thread cutting tool
- Soldering equipment
- Cable stripper
- Pliers
- Crimping tool for pin headers
- Adjustable spanner
- Allen keys:
    - 1.5 mm (M3 grub screws)
    - 2 mm (M3 hex head countersunk screws)
    - 2.5 mm (M3 hex head cap screws and M4 button head screws)
    - 3 mm (M4 hex head cap screws)
    - 5 mm (M6 hex head cap screws)

5 Build Instructions

5.1 Assembly of baseplate

To begin the construction of the retention model setup, we recommend starting with the assembly of the baseplate. To make the assembly process easier, numberings are included in the file *baseplate1_labeled.dxf*, which can be engraved into the sheet using the raster engraving function of the laser cutter. The single steps of the procedure are laid out in **Figure 2**.

1. Insert one M6 nut into the 5 feet (*foot.stl*) each (Figure 2a).
2. Stack baseplate1 (*baseplate1_labeled.dxf*) onto baseplate2 (*baseplate2.dxf*). Insert two M6x20 hex head cap screws from the top into slots B and D of baseplate1 and fasten them to the M6 nuts in two feet at the bottom of baseplate 2 (Figure 2b; green highlights).
3. Insert two M6x25 hex head cap screws into each of two of the climate chamber corners (*outside_corner.stl* and *outside_corner_mirrored.stl*) and then through baseplate1 in slots A and C (Figure 2b; purple highlights). Then fasten the bolts to the M6 nuts placed in two more feet. Now, the two baseplates should be attached to one another in the four corners A, B, C and D.
4. Insert two M6x15 hex head cap screws into the two left outside corners (*outside_corner_regular.stl* and *outside_corner_regular_mirrored.stl*) and fasten them to two M6 nuts placed on the bottom side of slots 14 and 184, so that the corners are directed inwards (Figure 2b; black highlights).
5. Attach the two handles (*handle.stl*) to the baseplate by fastening them with 4 M6x14 hex head cap screws and 4 M6 nuts in slots 52 and 120 as well as 68 and 136 (Figure 2b; blue highlights).
6. Next, attach the first aluminum rod holder (*rod_holder.stl*) to the baseplate by using an M6x25 hex head cap screw. Insert the screw into the holder and into slot 61 and fasten in from the bottom with the last foot in which an M6 nut was placed in step 1. Then attach the other rod holder to slot 74 using an M6x20 hex head cap screw and an M6 nut (Figure 2b; red highlights).
7. Attach the two beaker holders (*beaker_fix.stl*) to the baseplate in slots 124 and 129 with the use of two M6x10 hex head cap screws and two M6 nuts (Figure 2b; yellow highlights). Viewed from the top, the assembly should now look as in Figure 2b and viewed from the bottom, it should look like in Figure 2c.
8. Insert two 12x300 mm aluminum rods in the two rod holders (Figure 2d).
9. Insert the ultrasonic mist fogger into the humidifier base (*humidifier_2.0.stl*) and lead the cable through the hole in the side as depicted (Figure 2e).
10. Use two M6x15 hex head cap screws and two M6 nuts to attach the humidifier base to the baseplate in slots 11 and 47 (Figure 2f).

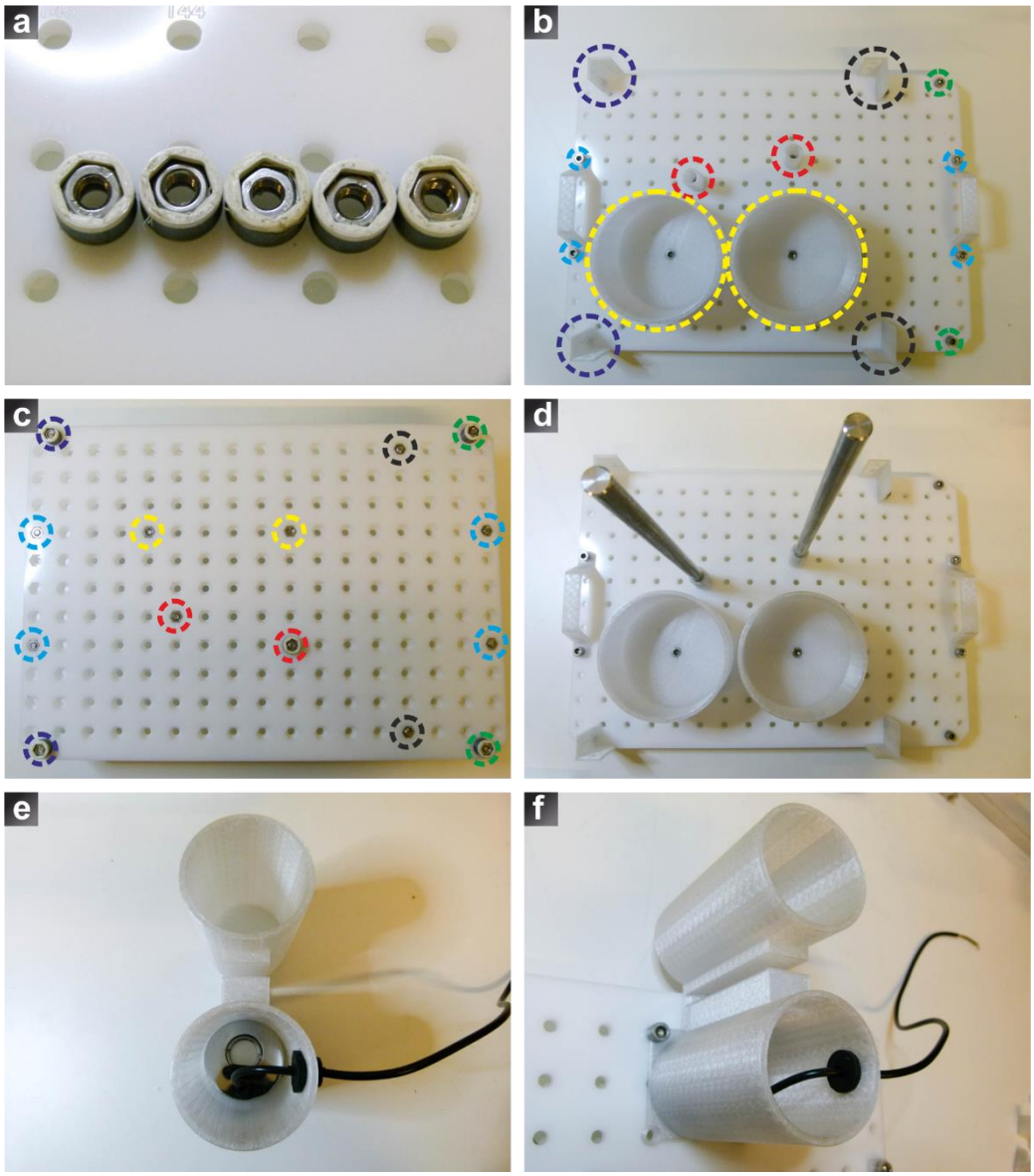

Figure 2 *Assembly of baseplate. (a) Insertion of M6 nuts into feet. (b) Arrangement of various holders on baseplate 1. (c) Arrangement of M6 nuts in baseplate 2. (d) Insertion of aluminum rods into rod holders. (e) Insertion of ultrasonic mist fogger in humidifier base. (f) Mounting of humidifier base on baseplate assembly.*

5.2 Assembly of climate chamber

After cutting the box components (*box_back.dxf*, *box_doorside+electronics_cover.dxf*, *box_front.dxf*, *box_side.dxf*, *box_top+SSR_cover.dxf* and *door+frame.dxf*) for the climate chamber from sheets of polymer, prepare them for assembly by cutting the threads into the relevant holes as shown in **Figure 3**.

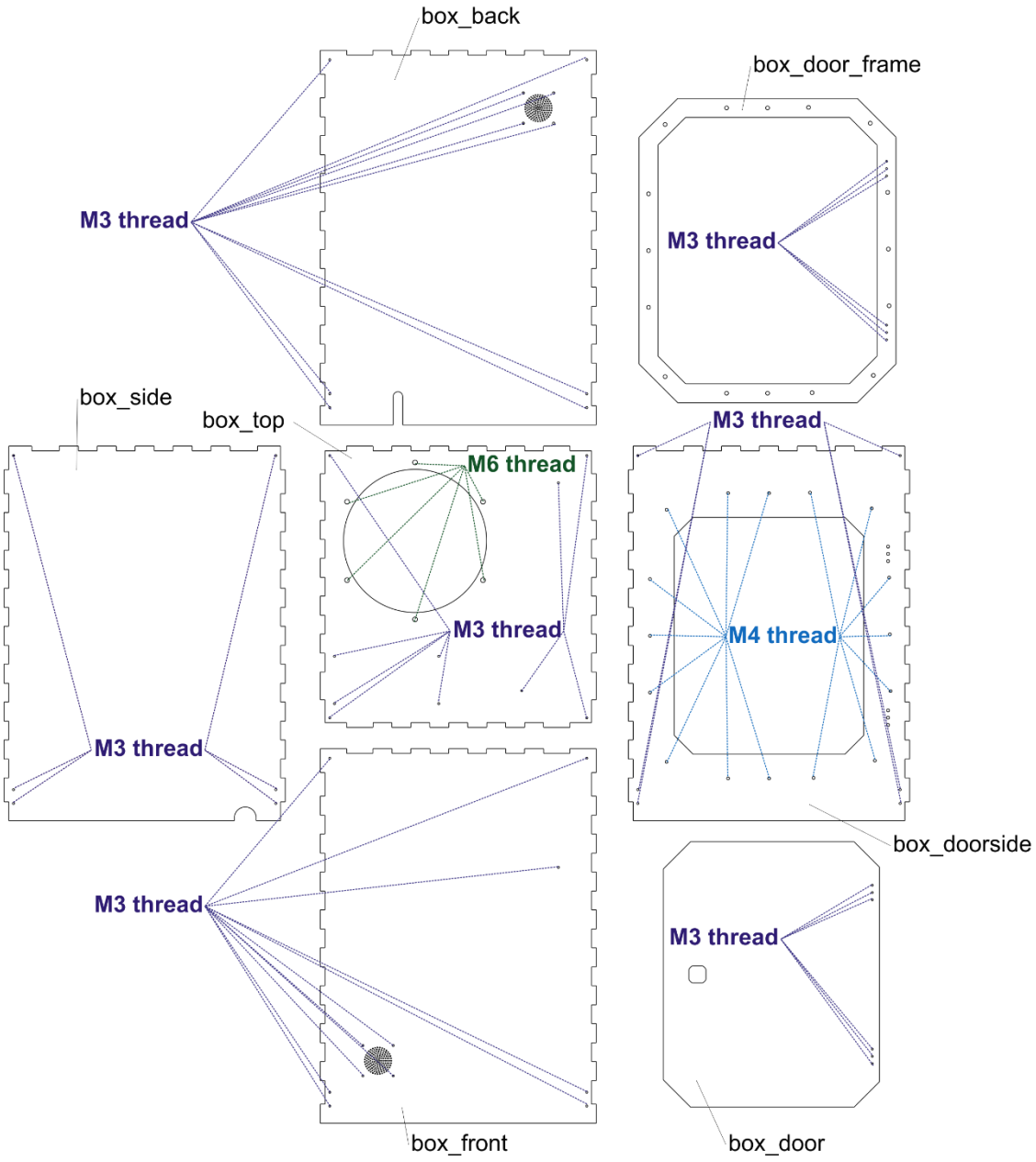

Figure 3 *Threading instructions for preparation of box elements for climate chamber.*

The climate chamber box is designed to be assembled with press-fits by using the finger joints at the edge of the single components. **Figure 4** gives an overview about how the box has to be assembled. If the cutting parameters of the laser cutter are suitable for the tolerance specified in the designs, the assembled box should stably hold together only due to the press-fit.

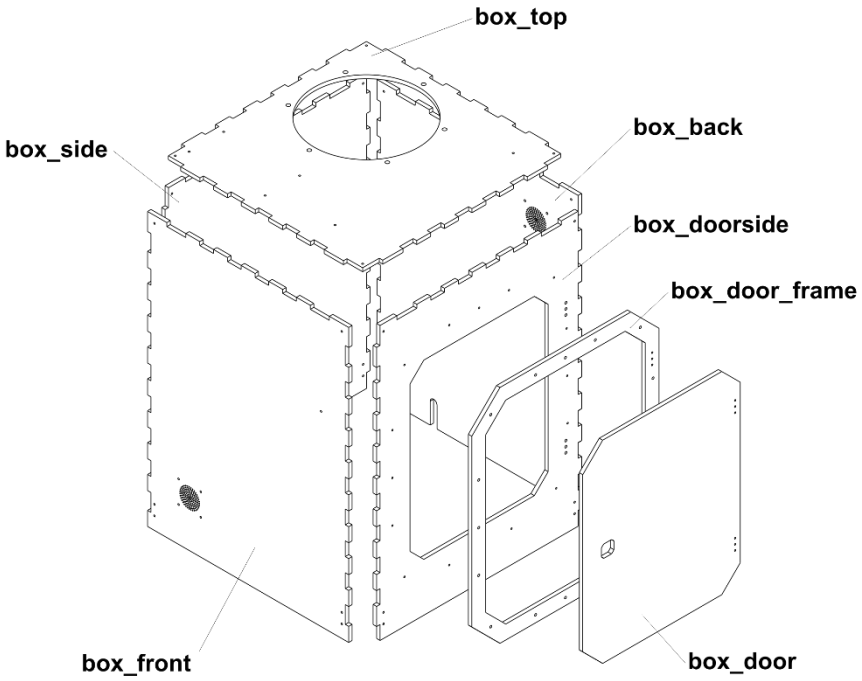

Figure 4 *Exploded view of climate chamber assembly.*

To complete the assembly of the climate chamber box, follow the next steps:

1. Once the press-fit assembly of the box is completed (**Figure 5**a), insert the box in between the box corners on top of the baseplate with the door cut-out of the box facing towards the direction of baseplate slots C and D. Then fasten the box to the box corners by using sixteen M3x10 hex head cap screws (Figure 5b).
2. For increased rigidity, attach the four top corners (*corner_top.stl*) to the upper corners of the box with twelve M3x10 hex head cap screws (Figure 5c).
3. Attach the laser-cut door frame to the door side of the box with sixteen M4x10 button head screws as shown in the picture (Figure 5d).
4. Mount the female leaves of the two door hinges to the door frame with six M3x10 hex head cap screws (Figure 5e). Then mount the male counterparts to the laser-cut door with six M3x6 hex head cap screws (Figure 5f).
5. To attach the door lock to the door of the box, insert the component lock_hole-screw (*lock_hole-screw.stl*) into the remaining hole of the door from the side of the attached hinges and fasten it with the component lock_big-nut (*lock_big-nut.stl*) from the other side (Figure 5g).
6. Assemble the lock with the missing components as shown in Figure 5h.
7. Attach the door to the box by connecting the male and female leaves of the hinges with the use of two M3x25 hex head cap screws (Figure 5i).

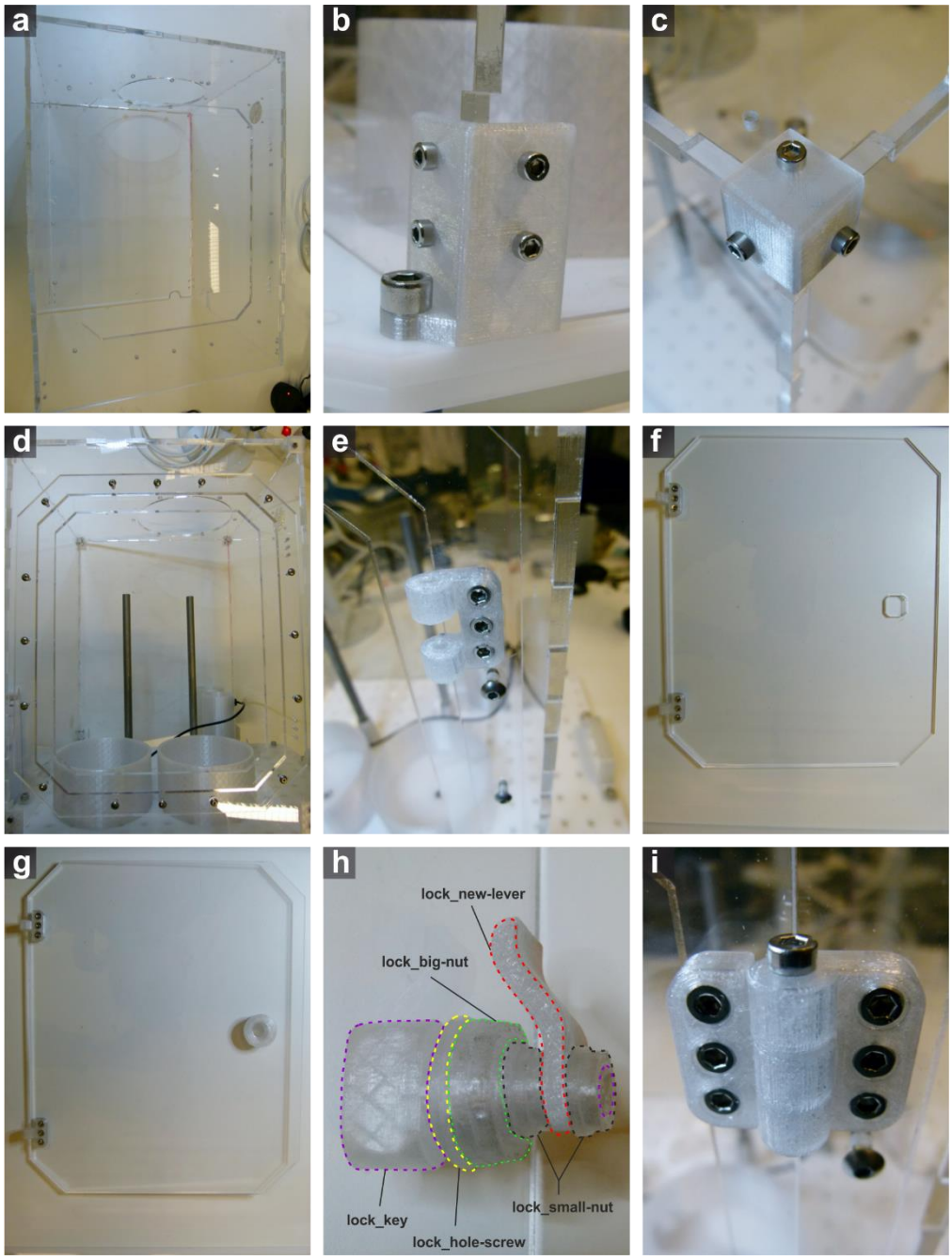

Figure 5 *Climate chamber assembly. (a) Finished press-fit assembly of acrylic box. (b) Fastening of acrylic box to 3D printed corners. (c) Mounting of box top corners. (d) Attachment of door frame to acrylic box. (e) Mounting of female hinge leaves on door frame. (f) Mounting of male hinge leaves on acrylic door. (g) Insertion of hole screw for door lock. (h) Assembly of door lock. (i) Assembly of door hinges with M3x25 screws.*

5.3 Assembly of peristaltic pump

To assemble the peristaltic pump, follow the next steps, which are illustrated in **Figure 6**:

1. Insert an M3 nut into the nut trap of the bottom part of the roller pump head (*bearing_mount_bottom_01.stl*) (Figure 6a). Then push three 4x14 mm straight pins into the cavities as shown (Figure 6b).
2. Insert an M3x10 grub screw from the side and screw it into the M3 nut (Figure 6c).
3. Mount three HK 0408 needle bearings on the straight pins (Figure 6d).
4. Attach the top part of the roller pump head (*bearing_mount_top.stl*) to the bottom part using three M3x20 hex head cap screws (Figure 6e).
5. Mount the Nema17 stepper motor to the housing (*pump_housing.stl*) by inserting four M3x10 hex head cap screws into the component pump_case_bottom (*pump_case_bottom.stl*) and fastening them through the holes in the housing into the threads of the stepper motor (Figure 6f). The small hole in pump_case_bottom has to face upwards.
6. Mount the roller pump head onto the shaft of the stepper motor and fasten it by inserting the correct Allen key through the hole in the top of the component pump_case_bottom (Figure 6g).
7. Insert two M3x25 hex head cap screws into the back of the component pump_case_top (*pump_case_top_120.stl*) and mount it onto pump_case_bottom. Then insert two M3x20 hex head cap screws into the remaining holes in the front (Figure 6h).
8. After the assembly of the peristaltic pump has been finalized, attach the housing of the pump to the baseplate in the slots 16 and 50 with the use of two M6x15 hex head cap screws and two M6 nuts. The roller pump head faces outward from the baseplate assembly (Figure 6i).

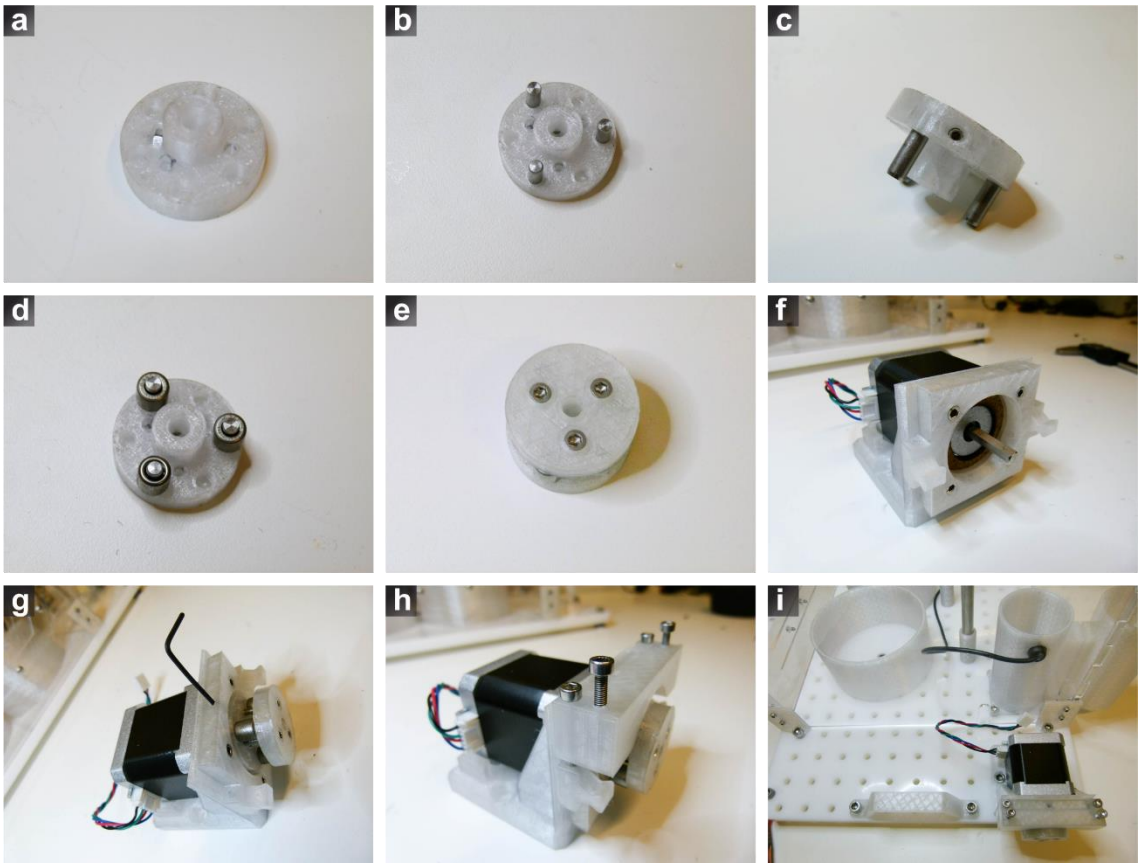

Figure 6 *Assembly of peristaltic pump. (a) Insertion of M3 nut into nut trap. (b) Insertion of 4x14 mm straight pins. (c) Installation of M3x10 grub screw into M3 nut. (d) Mounting of needle bearings. (e) Assembly of roller pump head. (f) Mounting of Nema17 stepper motor. (g) Installation of roller pump head. (h) Final assembly of pump. (i) Mounting peristaltic pump to baseplate.*

5.4 Assembly of heat lamp housing

To assemble the housing for the ceramic infrared heat lamp, refer to **Figure 7** and follow these steps:

1. Cover the entire inner surface of the lamp housing (*lamp_case.stl*) with aluminum tape (Figure 7a).
2. Install the ceramic power socket into the lamp housing (Figure 7b).
3. Mount the lamp housing on top of the climate chamber with the use of six M6x12 hex head cap screws (Figure 7c).

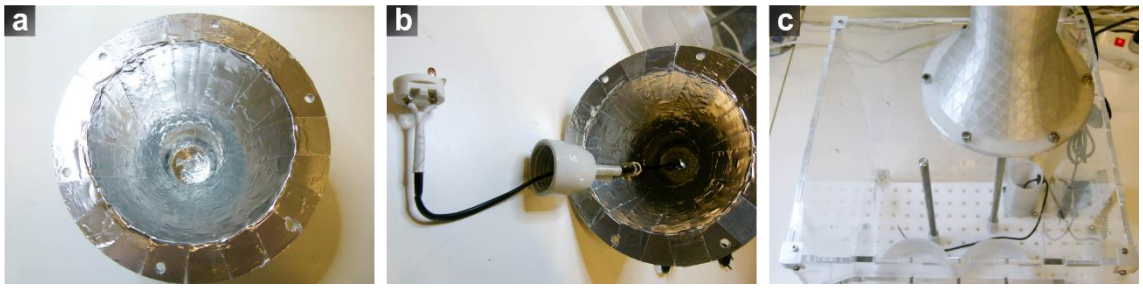

Figure 7 *Assembly of case and power socket for infrared heat lamp. (a) Covering of lamp housing with aluminum tape. (b) Installation of ceramic power socket. (c) Mounting of lamp housing on climate chamber with six M6x12 hex head cap screws.*

5.5 Assembly of display controller

The assembly of the display controller is illustrated in **Figure 8**.

1. Push the shaft of the rotary encoder from the inside of the controller housing (*controller_housing.stl*) through the hole in the side and fasten it with the supplied nut. Then press-fit the knob for the shaft (*controller_knob.stl*) onto the shaft (Figure 8a). Note that it is required that the rotary encoder possesses a 10kΩ pull-up resistor in the highlighted location.
2. Insert the I2C LCD into the cavity of the controller housing and fasten it with four M3x16 hex head cap screws and four M3 nuts. To not damage the printed circuit board (PCB), insert some plastic spacers. You can 3D print the plastic washers from the supplied design (*plastic_washers.stl*). Connect the cables to the rotary encoder and the LCD and feed them through the hole in the back. You can tie the cables together with a zip tie for strain relief (Figure 8b). The completed housing should look like depicted in Figure 8c.
3. Finally, attach the display controller to the climate chamber with the use of four M3x8 hex head cap screws (Figure 8d).

5.6 Lamp assembly

Three IKEA ledberg LED spots serve as a light source for the retention model setup. The assembly of the lamp is depicted in **Figure 9**. Follow these steps to complete the assembly:

1. Insert the three LED spots in the lamp housing (*ikea_led_housing.stl*) and feed the cables through the channels at the sides of the cavities (Figure 9a). You can use the supplied adhesive to hold the spots in the housing.
2. The LED spots are usually distributed in a pack of four, however for this purpose only three are required. The four LED spots are connected to power with a small PCB hub (Figure 9b). You can shorten the cables, de-solder the fourth LED spot and re-solder the rest of them. Finally, you can use one of the supplied adhesives to glue the hub on top of the climate chamber (Figure 9c).

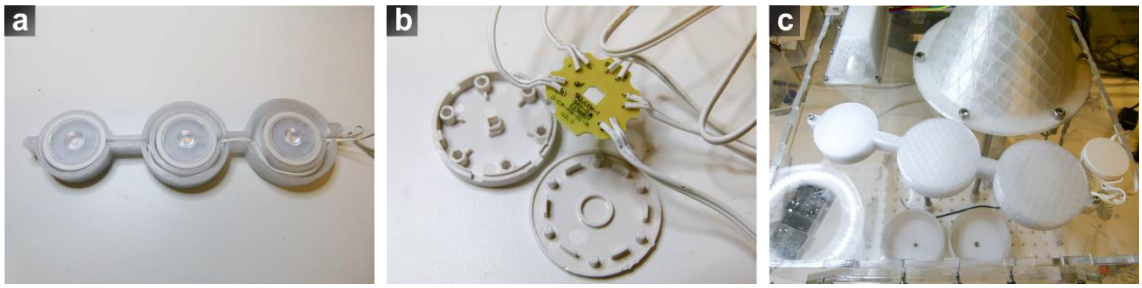

Figure 9 *Assembly of IKEA Ledberg LED lighting. (a) Insertion of LED spots into 3D printed housing. (b) PCB connector hub. (c) Mounting of lamp housing on top of climate chamber.*

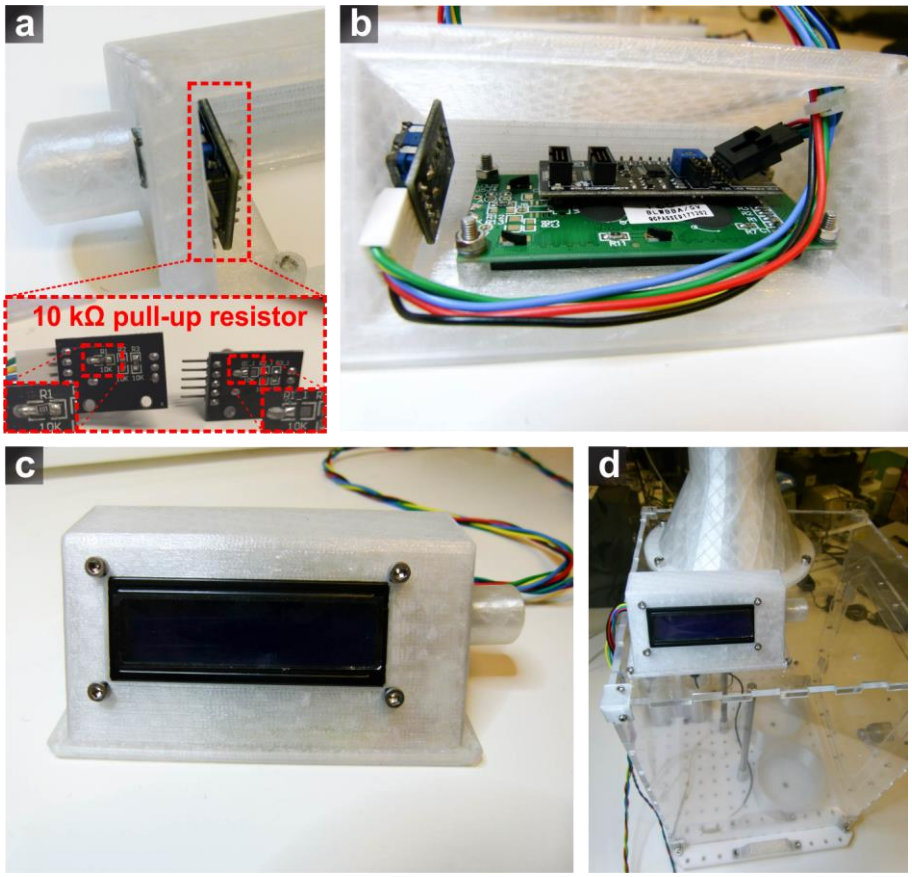

Figure 8 *Assembly of controller housing with rotary encoder and I2C LCD display. (a) Installation of rotary encoder and controller knob. Note that the rotary encoder needs to exhibit a 10 kΩ pull-up resistor in the labeled position. (b) Insertion and fastening of I2C LCD with four M3x16 hex head cap screws, four plastic washers and four M3 nuts to controller housing. (c) Front-view of assembled controller. (d) Mounting of controller on top of climate chamber with four M3x8 hex head cap screws.*

5.7 Mounting Sensors

The climate control (temperature and humidity) in the climate chamber uses input signals of two DHT22 temperature and humidity sensors. Each of them is placed differently in the chamber. While one of them measures the ambient temperature and humidity in the chamber, the other one measures local temperature and humidity at the slide holder, next to the slide where the tissue is placed. The instructions to mount the sensors are illustrated in **Figure 10** and are summarized in the next steps:

1. Insert an M6 nut and an M6x12 hex head cap screw into the slide holder (Figure 10a).
2. Mount the local sensor (T/H sensor 1) to the sensor holder on the slide holder with an M3x8 hex head cap screw (Figure 10b).
3. Mount the ambient sensor (T/H sensor 2) from the inside to the front of the climate chamber with an M3x8 hex head cap screw and mount the slide holder onto the aluminum rod, which is closer to the back of the climate chamber (Figure 10c).

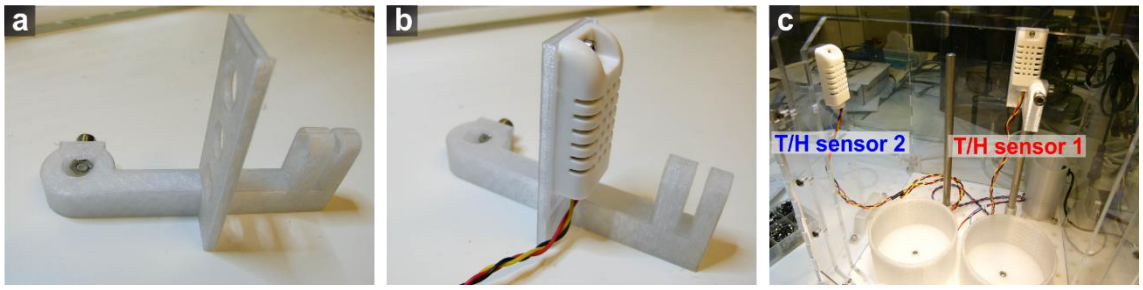

Figure 10 *Installation of DHT 22 temperature and humidity sensors. (a) Insertion of M6 nut and M6x12 hex head cap screw into slide holder. (b) Mounting of first DHT22 temperature and humidity sensor to slide holder with an M3x8 hex head cap screw. (c) Attachment of second DHT22 sensor to front of climate chamber.*

5.8 Installation of fans and cable routing

Temperature and humidity in the climate chamber are regulated, among others, with the use of three 12V DC fans. One fan acts as a venting fan that blows air from the outside into the chamber. A second fan acts as an exhaust fan, dragging air out of the chamber. The last fan is placed on the humidifier to distribute the steam, which is generated by the ultrasonic mist fogger. Refer to **Figure 11** for the installation of these fans.

1. The venting fan is mounted along with a fan grill (*40mm_Fan_grill_final.stl*) to the front of the climate chamber by using 4 M3x30 hex head cap screws (Figure 11a). Note that the direction of air flow should be towards the climate chamber. If the fan blades are too close to the fan grill, you can use the 3D printed plastic washers (*plastic_washers.stl*) to increase the spacing.
2. The exhaust fan is as well mounted together with a fan grill, but attached to the back of the climate chamber (Figure 11). Here, the direction of airflow should be away from the chamber.

3. You can route the cables of the venting fan and the two humidity sensors through the baseplate to the back of the climate chamber as it is depicted (Figure 11c). At this point, you can also already pre-install the cable for the motor of the autosampler.
4. Place a mesh (*humidifier_mesh.stl*) that hinders water splashes to hit the fan of the humidifier (*humidifier_2.0.stl*) into the humidifier cavity that holds the ultrasonic mist fogger (Figure 11d).
5. Install the humidifier fan (40x10 mm) in a "sandwich" with two fan grills to the cap of the humidifier (*humidifier_fan.stl*) by using four M3x30 hex head cap screws (Figure 11e) and then stack the cap onto the humidifier base (Figure 11f).

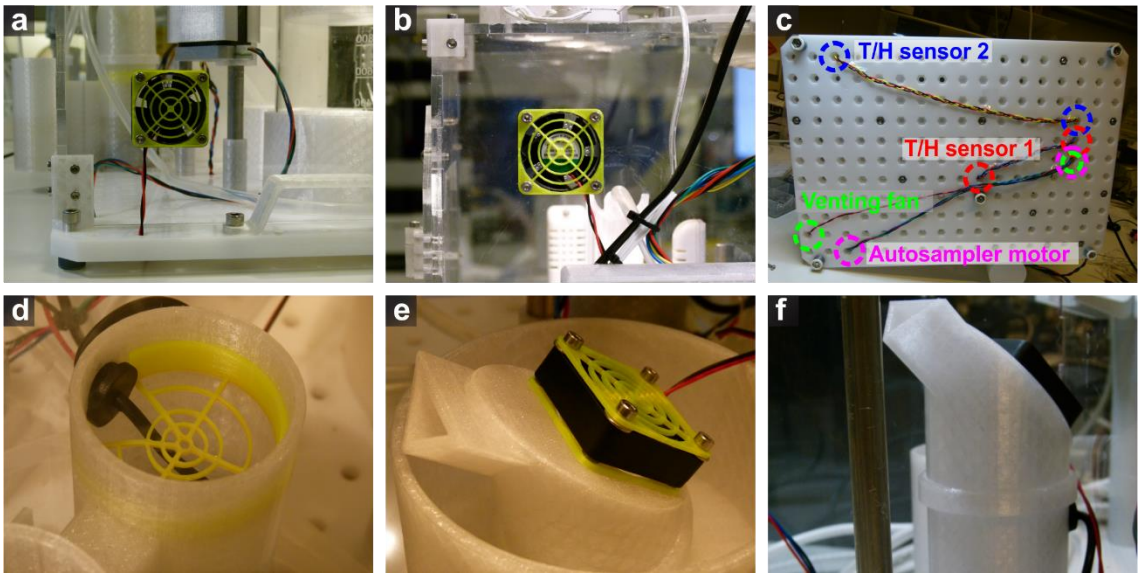

Figure 11 *Installation of fans with four M3x30 hex head cap screws. (a) Installation of venting fan and fan grill to the front of the climate chamber. (b) Mounting of exhaust fan in the same way to the back of the climate chamber. (c) Cable routing at the bottom of the baseplate. (d) Insertion of protection mesh into humidifier base. (e) Mounting of fan and two fan grills to the humidifier cap. (f) Installation of humidifier cap on humidifier.*

5.9 Autosampler assembly

For the facilitation of automated experiments and thereby increased reproducibility, the presented retention model setup features a fully 3D printed rotational autosampler. Execute the assembly of the autosampler as described (**Figure 12**).

1. Start the assembly by attaching the motor mount (*geardrive_motormount.stl*) to the planetary gear drive (*planetary_gear_drive.stl*) with one screw connection by using one M3x6 countersunk screw as highlighted (Figure 12a).
2. Insert the Nema17 stepper motor in to the cavity of the motor mount and fasten it with four M3x6 countersunk screws (Figure 12b). As the motor mount is attached to the planetary gear drive with only one screw, you can rotate the planetary gear drive to obtain access to all screws.
3. Insert an M3 nut into the nut trap of the small herringbone gear (*herringbone_gear.stl*) (Figure 12c).
4. Install the small herringbone gear onto the shaft of the stepper motor with one M3x10 hex head cap screw as highlighted (Figure 12d).
5. Fix the motor mount to the planetary gear drive with three more M3x10 hex head cap screws (Figure 12e).
6. Insert an M6 nut and M6x10 hex head cap screw into the motor mount as highlighted (Figure 12f).
7. Finalize the assembly by attaching the cover (*gear_drive_cover.stl*), the shim (*planetary_gear_drive_shim.stl*) and the ring gear (*ring_gear.stl*) to the planetary gear drive and each other with four M3x25 countersunk screws as shown in the picture (Figure 12g). Also, insert two M3x8 grub screws into the cover of the geardrive.
8. Mount the assembled autosampler on the aluminum rod in the front of the climate chamber (Figure 12h).
9. Mount a suitable sample holder onto the autosampler (in this case *mesh_holder.stl* and *small_mesh.stl*; several holder designs can be found in the Mendeley data repository) and secure it with 3D printed thumb nuts (*thumbnut.stl*) (Figure 12i). When 3D printing the thumbnuts, stop the print at the height of the end of the nut trap and insert an M3 nut, then continue the 3D print.

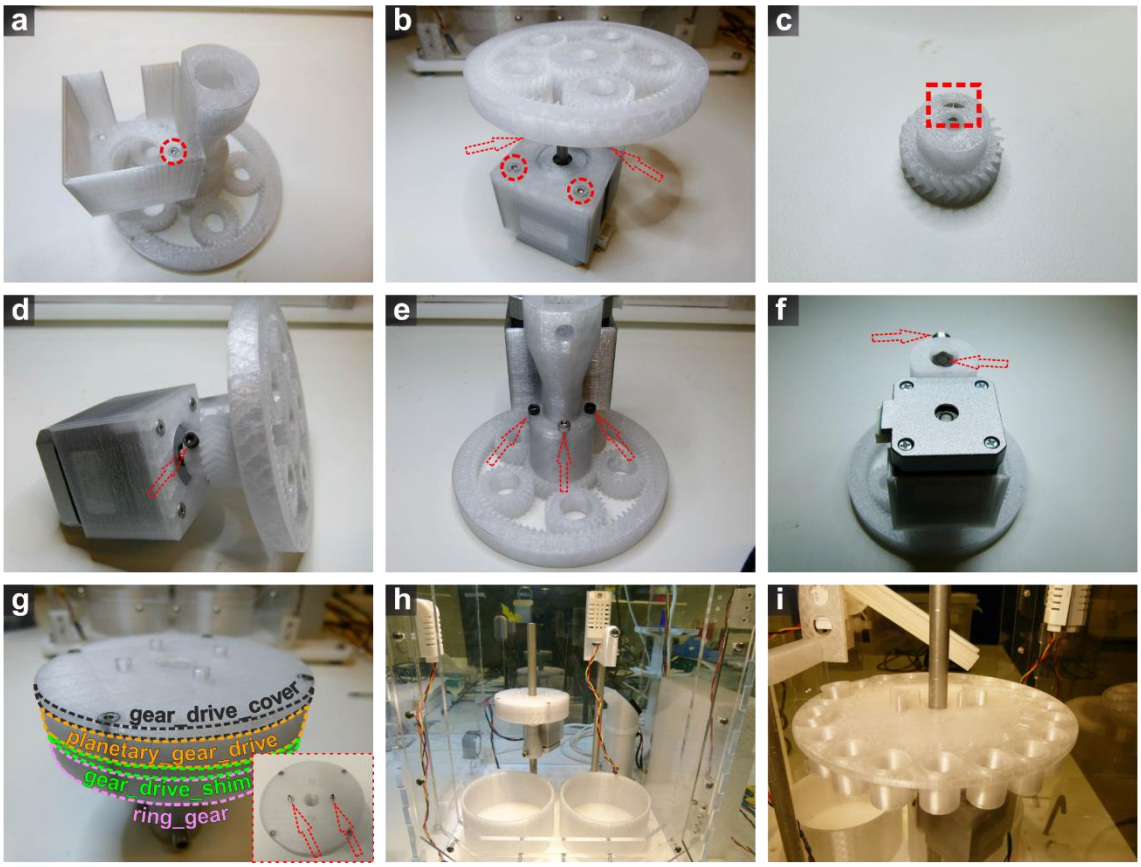

Figure 12 *Assembly of motorized rotary autosampler. (a) Connection of motor mount and planetary gear drive with one M3x6 countersunk screw. (b) Mounting of Nema17 stepper motor with four M3x6 countersunk screws. (c) Insertion of M3 nut into herringbone gear. (d) Mounting of herringbone gear on motor shaft with one M3x10 hex head cap screw. (e) Final fastening of motor mount to planetary gear drive with three M3x10 hex head cap screws. (f) Insertion of M6 nut and M6x10 hex head cap screw into motor mount. (g) Sandwich-style assembly of autosampler elements with four M3x25 countersunk screws. Inlet shows that two M3x8 grub screws are inserted into the top of the gear drive cover. (h) Installation of completed autosampler on aluminum rod in retention model setup. (i) Setup with sample holder and fastening with two thumb nuts.*

5.10 Assembly and wiring of solid-state relay

As the ceramic heat lamp for temperature-control needs to be connected to the power line with high voltage and to the Arduino through a solid-state relay, the solid-state relay is placed separated from all other components for safety reasons. Always refer to a professional to make sure that the connections are correct and safe. Additionally, a fuse is installed to prevent electrical accidents. To install and wire the solid state relay, refer to **Figure 13** and **Figure 14**, respectively.

1. Splice out one wire of the cable from the ceramic heat lamp power socket and connect it to the inline fuse holder and the load connectors of the solid-state relay (Figure 13a). Also, prepare two wires for the input signal of the relay. Finally, insert a 3A cartridge fuse into the fuse holder.
2. Insert the laser-cut wooden plate (*woodplate_ssr.dxf*) into the housing (*ssr_housing.stl*), so that the holes in the plate are aligned with the holes in the housing (Figure 13b).
3. Attach the solid-state relay to the housing by fastening it with two M4x8 hex head cap screws trough the wooden plate to the housing (Figure 13c). Feed the cable of the heat lamp power socket through the slot at the side and the wires for the input signal through the hole in the bottom. Place the fuse holder next to the relay and use zip ties for strain relief.
4. Finally, close the housing with an acrylic cover (from *box_top+SSR_cover.dxf*) by fastening it with three M3x10 hex head cap screws and apply the warning sign (*warning_sign.stl*) with adhesive tape (Figure 14d). You can print the warning sign with different colors to increase visibility.

5.11 Assembly of electronics and wiring

The installation and wiring of all electronic components inside the electronics housing (*electronics_housing.stl*) is illustrated in **Figure 15**, **Figure 16** and **Figure 17**.

1. Place the two required relay boards on the pins in the electronics housing (there are two expansion slots). Also, place the Arduino Mega 2560 and the DC/DC boost converter and fasten all components down with nine M3x8 hex head cap screws in the highlighted positions (Figure 15a). Furthermore, insert two M6x20 hex head cap screws in the bottom of the housing.
2. Solder two short wires for the Arduino Pro Mini to the RAMPS1.4 shield and stack it onto the Arduino afterwards (Figure 15b, Figure 16).
3. Fasten the electronics housing to the baseplate of the retention model setup with two M6 nuts in slots 83 and 151 and route the wires into the housing as depicted (Figure 15c). You can insert zip ties in special slots in the housing (highlighted) to tie the wires together. Feed the input signal wires from the solid-state relay through the hole in the top of the electronics housing and attach the with two M6x10 hex head cap screws.

4. Connect all wires and an Arduino Pro Mini (upload sketch *mini_pump_control.ino* beforehand) to the RAMPS1.4 shield according to the wiring schemes in Figure 16 and Figure 17 (Figure 15d). Connect and mount a power toggle switch as well (Figure 15e).
5. Finally, attach the last fan with fan grill to the acrylic cover (from *box_doorside +electronics_cover.dxf*) with four M3x30 hex head cap screws and flow direction towards the acrylic. Feed the fan wires through the hole in the acrylic and connect the fan (Figure 16, Fan4). Then screw the cover to the housing with use of four M3x10 hex head cap screws.

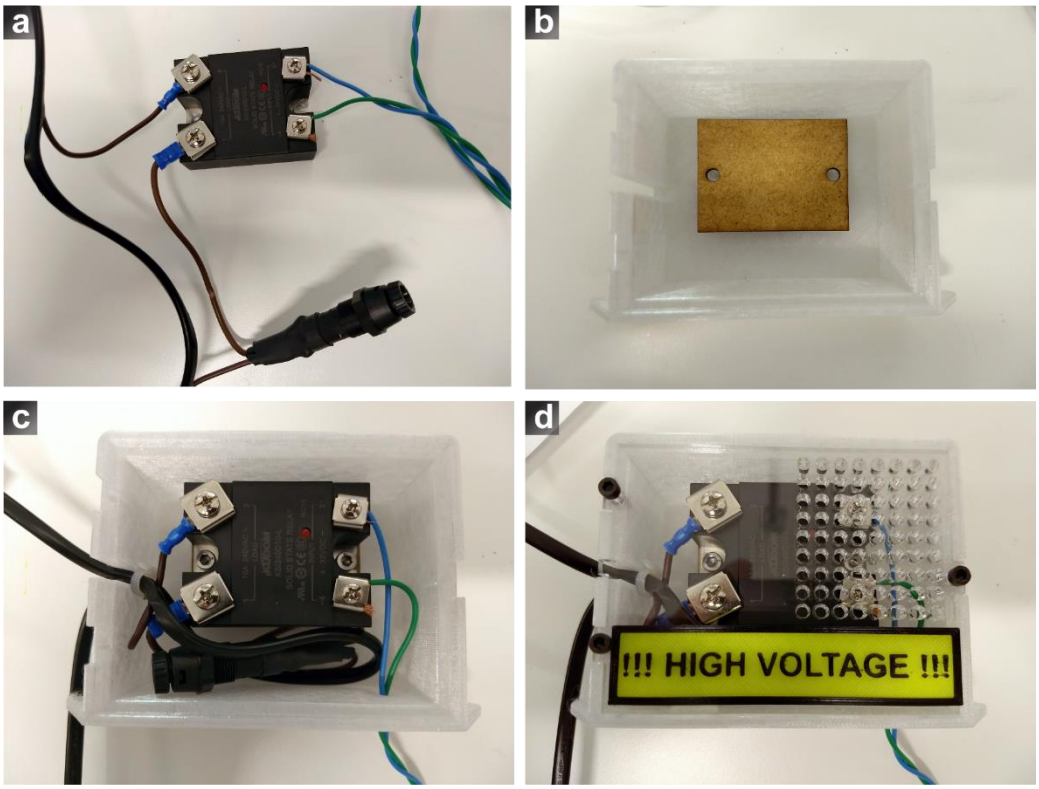

Figure 13 *Assembly of solid-state relay in solid-state relay housing. (a) Connection of solid-state relay with fuse holder and power socket of the heat lamp. (b) Insertion of wooden protection plate. (c) Placing of solid-state relay and fuse holder in housing. (d) Installation of acrylic cover and warning sign.*

Figure 14 *Wiring of solid-state relay to fuse, heat lamp and RAMPS 1.4 Arduino shield.*

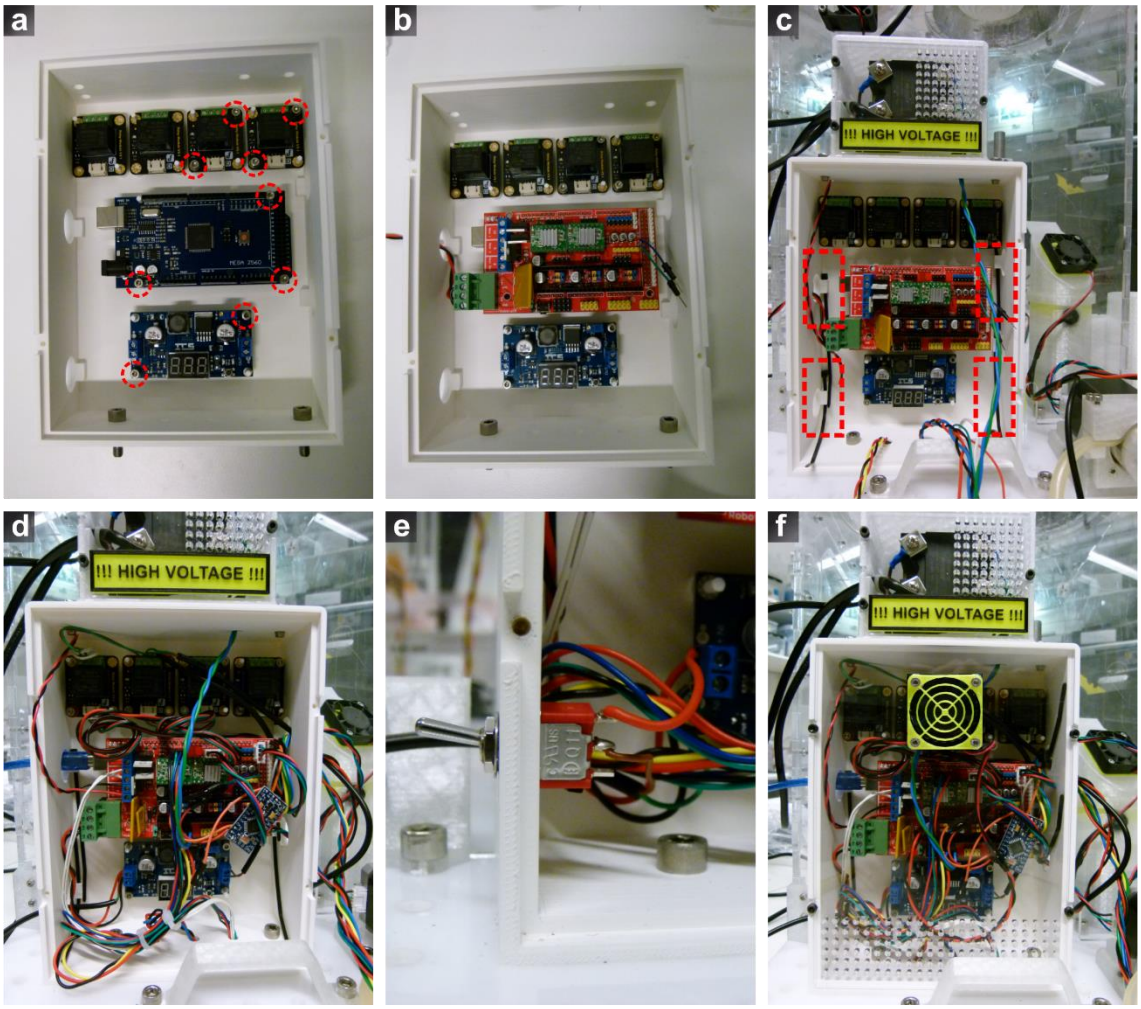

Figure 15 *Assembly of electronic components in electronics housing. (a) Placement of relays, Arduino and DC/DC boost converter in electronics housing and fastening with M3x8 hex head cap screws. (b) RAMPS 1.4 Arduino shield stacked on top of Arduino. (c) Mounting of electronics housing on baseplate with two M6 nuts and two M6x20 hex head cap screws and of solid-state relay housing on electronics housing with two M6x10 hex head cap screws. The picture also shows how the cables are routed into the electronics housing. (d) Connection of cables to RAMPS 1.4 Arduino shield. (e) Installation and connection of power switch. (f) Attachment of acrylic cover with four M3x10 hex head cap screws and mounting of fan with four M3x10 hex head cap screws.*

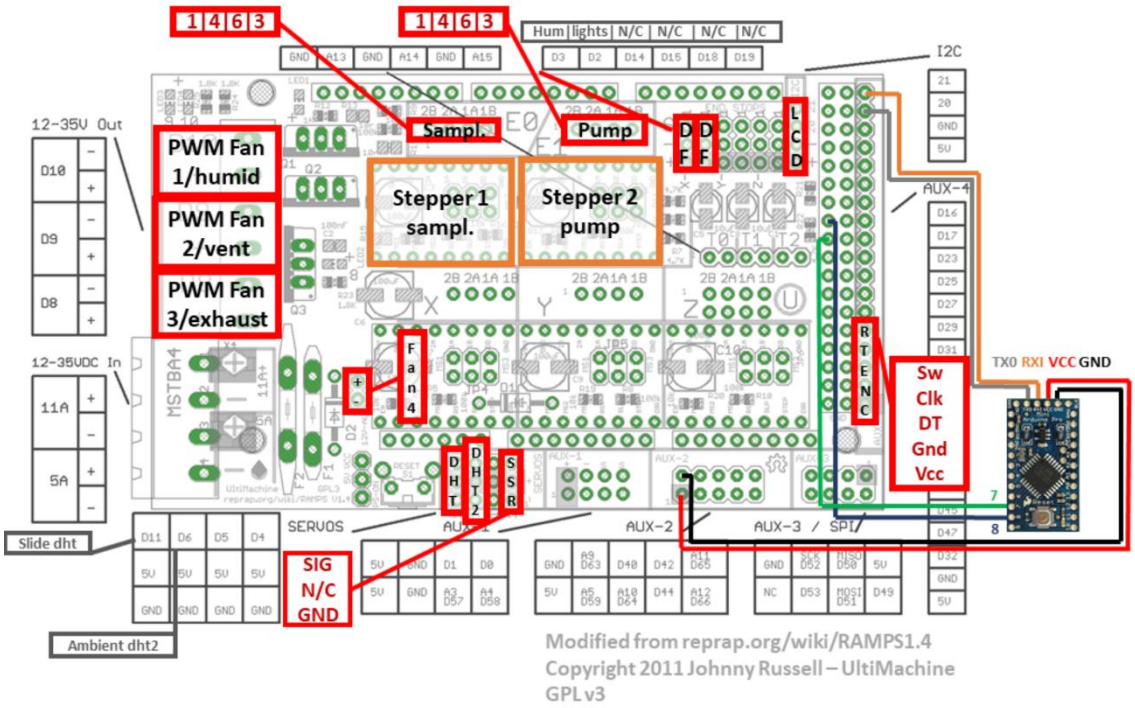

Figure 16 *Wiring of electronic components to RAMPS 1.4 Arduino shield.*

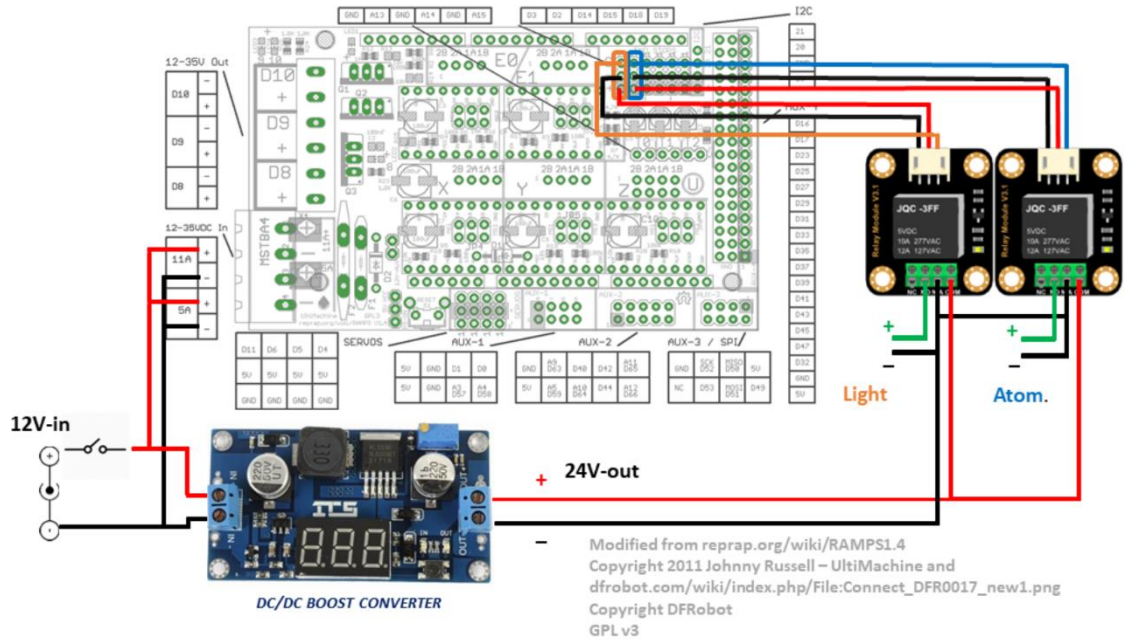

Figure 17 *Wiring of power supply, DC/DC boost converter and relays.*

5.12 Insertion of tubing and final setup

To finalize the construction of the retention model setup, insert a peristaltic pump/lab silicone tubing with an inner diameter of 4 mm and a wall thickness of 1.6 mm into the peristaltic pump and attach the ends to the slide (tissue holder) and a beaker (**Figure 18**). The 3D printable mesh (*mesh.stl*) possesses a hole with which the tube can be held in place.

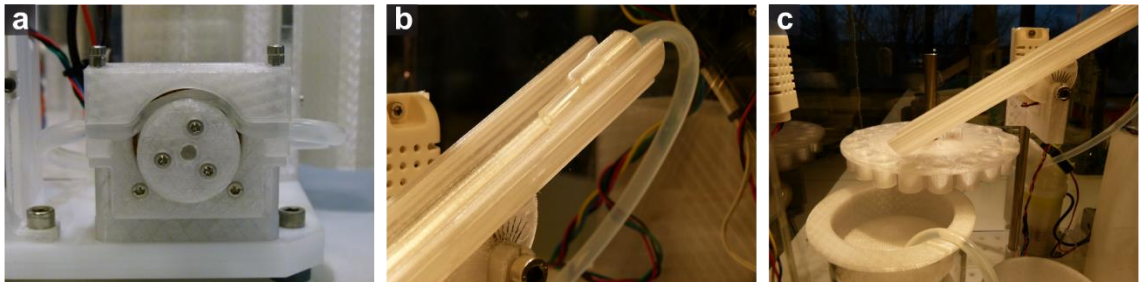

Figure 18 Installation of peristaltic pump tubing. (a) Tube inserted into peristaltic pump. (b) Tube connection to slide. (c) Tube entering a beaker through a 3D printed mesh.

A fully constructed retention model setup is depicted in **Figure 19.**

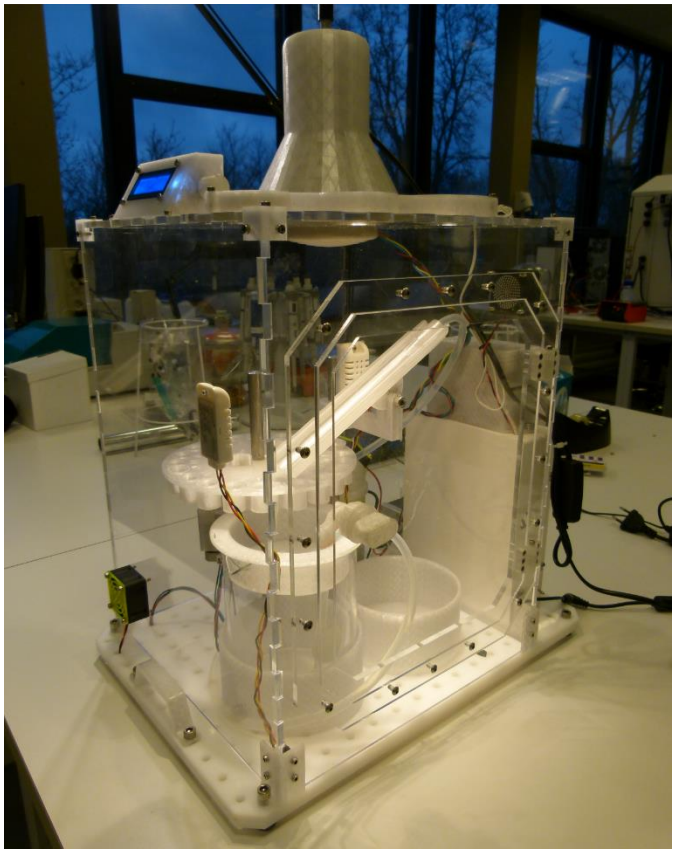

Figure 19 *Final setup of retention measurement system.*

6 Operation Instructions

6.1 Structure of Arduino sketch for control with Mega 2560

In this section, the structure of the code for the Arduino Mega 2560 microcontroller (*main.ino*) is explained. At each iteration of the "main loop" the microcontroller handles 3 tasks:

- Menu navigation:

  If an input from the user is detected (encoder rotated or clicked) the values of the "menu state variables" are modified and menu items are displayed accordingly. By navigating the menu as described in section 6.2, the user can manually enable/disable each of the functionalities of the system and configure all the parameters of the experiment.

- Climate-control:

  The control of temperature and humidity is disabled by default and the display shows "Temp/Hum control off". If enabled (manually through menu navigation or within the automated program), the value of the temperature from the slide sensor (T) and the value of the humidity from the ambient sensor (H) are read and compared to the *setpoints* giving $\Delta T = T - target\_T$ and $\Delta H = H - target\_H$, respectively. Then the ambient control devices are actuated depending on the values ΔT and ΔH:

  - if $\Delta H < 0$, the humidifier is turned ON by setting the digital signal driving the relay to high
  - if $\Delta H < 0$, the humidifier fan is turned ON and its speed is controlled by a PWM (pulse width modulation) signal with a duty cycle proportional to ΔH
  - if $\Delta T < 0$, the infrared heat lamp is turned ON by setting the digital signal controlling the solid-state relay to high
  - if $\Delta H > 0$ or $\Delta T > 0$, the ventilation and exhaustion fans are turned ON and their speeds are controlled by PWM signals with duty cycles which are dependent on both ΔH and ΔT.
  - Finally, the temperature of the ambient sensor (amb_T) is measured: if amb_T > 45°C or the temperatures measured by the two sensors differ more than 15°C (meaning that at least one of the sensors is not working properly) all the devices are turned OFF and the system stays in an ERROR state until it is restarted.

- Automated program execution:

  If the automated program function is enabled, a single instruction of the automated program is executed (a more detailed description of the automated program is proposed in section 6.3).

6.2 Structure of LCD/rotary encoder controller menu

The menu is structured in four layers, identified by different colors in **Figure 20**: *Home → layer1 → layer2 → parameters*. By default, the LCD displays one of two possible home pages, depending on whether the ambient control is disabled ("*temp hum control OFF*") or enabled (displaying temperature and humidity values).

By clicking the push-button of the rotary encoder, the user enters the menu navigation mode: the first row of the LCD displays the current section of the menu while the second row displays the subsections/items of that section. By rotating the button, the users can scroll through the items and by clicking the push-button the user selects the displayed item and enters the corresponding subsection.

The current state of the menu navigation is uniquely identified by a pair of variables: *P* and *C* (Figure 20). In the last layer of subsections (green blocks) the first row of the LCD displays the name of the parameter and the second row displays the current value of the selected parameter: the user can scroll through the possible values of the parameter by rotating the button and as the push-button is clicked the selected value of the parameter is stored and the menu moves back to the previous subsection.

Special cases:

- *Sel func → temp/hum control → enable*: by clicking the push-button while the "*enable*" item in the "*temp/hum control*" section is displayed, the ambient control will be enabled if it was previously disabled and disabled if it was previously enabled.
- *Sel func → pump → start/stop*: by clicking the push-button while the "*start/stop*" item in the "*pump*" section is displayed, the pump will be turned ON if it was previously OFF and turned OFF if it was previously ON.
- *Sel func → autosampler → next sample*: by clicking the push-button while the "*next sample*" item in the "*autosampler*" section is displayed, the autosampler will move to the next sample right away.
- *Sel func → autosampler → manual pos → X*: by rotating the knob while in the position parameter of the "*manual pos*" item of the "*autosampler*" section, the autosampler will move according to the rotation of the button to fine-tune the position of the autosampler. The user can exit the manual positioning mode by clicking the push-button at any point and the menu will return to the autosampler section.
- *Sel func → prog start/stop*: by clicking the push-button while the "*prog start/stop*" item of the "*sel func*" section is displayed, the automated program algorithm will start if it was previously disabled or it will stop if it was running.

By clicking on the "*Home*" item, present in any section and subsection, the user will exit the menu navigation and the LCD will display the home page.

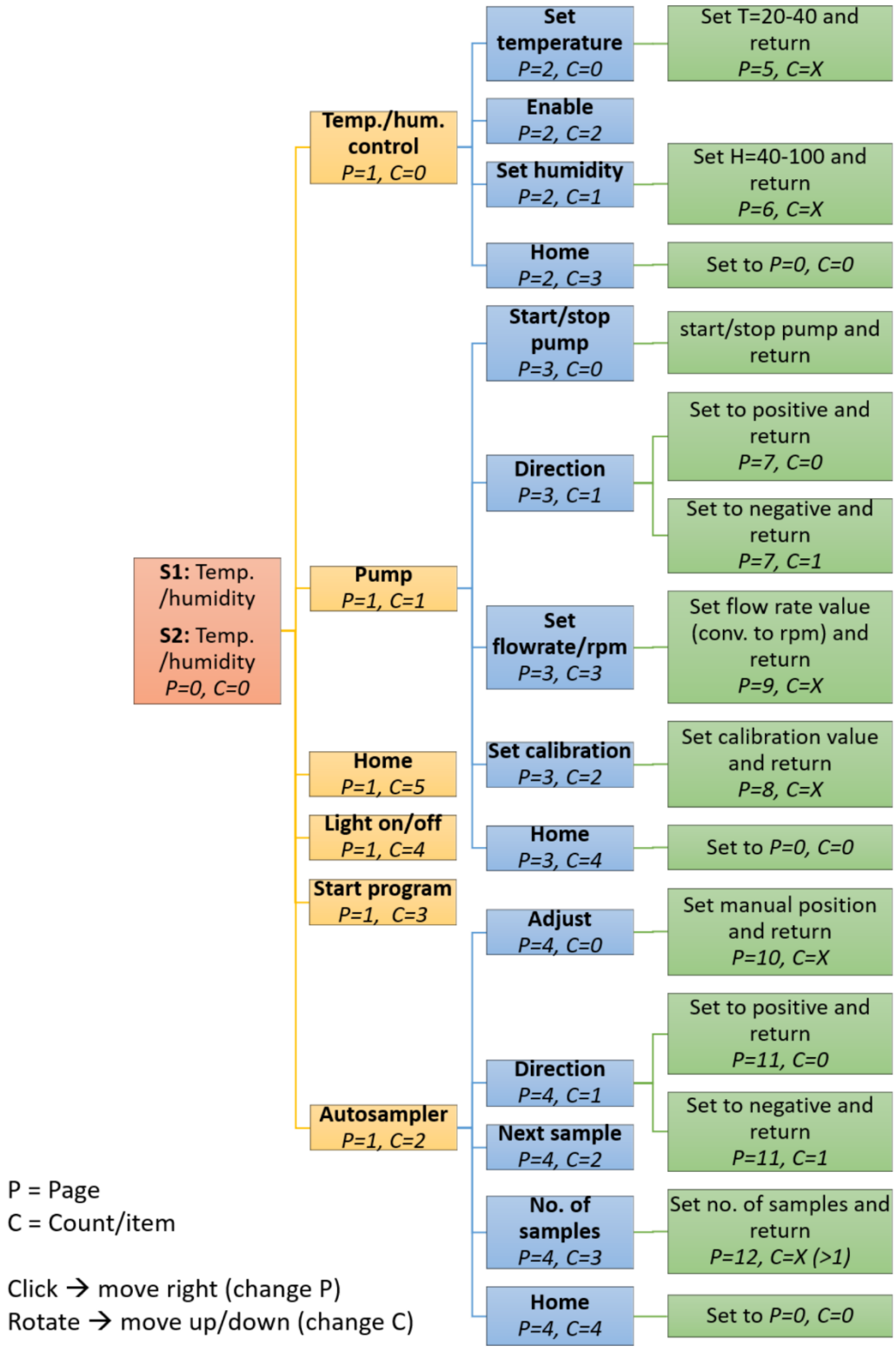

Figure 20 *Organigram of all menu points in the controller menu. Different colors correspond to different layers of the menu structure.*

6.3 Instructions for generation of customized automated program sequences

In order to build a custom designed automated program, the user must modify the "*my_program ()"* function that can be found at the very end of the arduino code (*main.ino*). The "*my_program*" function is a case structure in which each case corresponds to one step of the desired sequence of operations. Each step (case) must contain only one instruction from the provided instruction set (**Figure 21**). The default instruction must always be the "*stop_program ()"* function.

set_pump (rpm, direction, enable) controls the peristaltic pump. The function accepts values of byte-type (0-255). For the "*enable*" parameter, 0 corresponds to stop while any other positive integer corresponds to start. For the "*direction*" parameter, 0 corresponds to clockwise while any other positive integer corresponds to counterclockwise (the actual direction of the flow depends on the tube placement). The value of the "*rpm*" parameter controls the actual speed of the pump in RPM (revolutions per minute).

next_sample (N_of_samples, direction) controls the stepper motor of the autosampler. The function accepts values of "integer" type. For the "direction" parameter, 0 corresponds to clockwise while any other positive integer corresponds to counterclockwise. The autosampler rotates 1/*N_of_samples* of a full rotation.

s*et_temp_hum (target_T, target_H, enable)* stores the setpoints for *T* and *H* and enables/disables the climate-control. The function accepts values of integer-type. For the "*enable*" parameter, 0 corresponds to stop, while any other positive integer corresponds to start.

reach_target_temp_hum () causes the sequence to stall until both temperature and humidity reach the setpoints within a range of ± 2°C for *T* and ± 3% for *H*.

wait_milliseconds (x) causes the sequence to stall for x milliseconds before moving to the next instruction (ongoing active operations such as ambient control or pump rotation will keep being active). The function accepts values of unsigned_long-type.

instruction_loop (instr_number,number_of_cycles) is used to perform loops of several instructions. The program will jump back to the instruction indicated by "*instr_number*" for a number of times specified by "*number_of_cycles*".

stop_program () is the "default" instruction, meaning that it is performed any time at the end of the program routine. This function disables the automated program and restores all values to default.

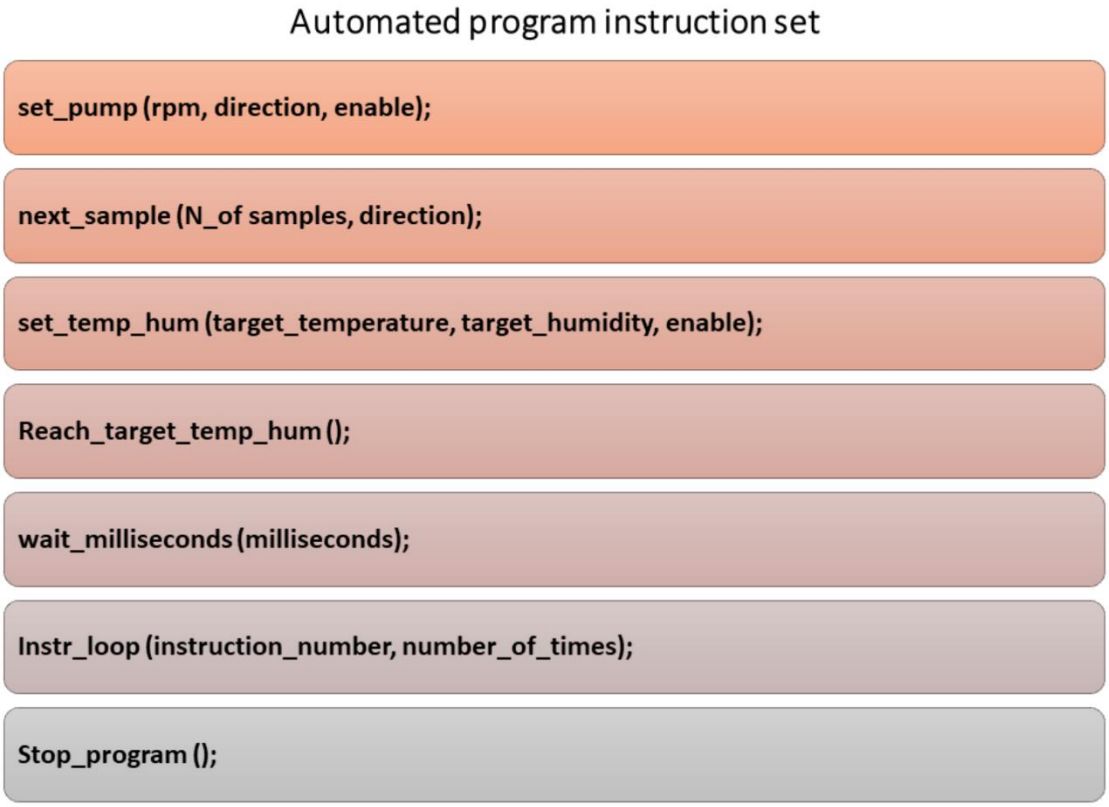

Figure 21 *Graphical overview of commands for customized automated programs.*

6.4 Structure of Arduino sketch for Pro Mini pump control

The Arduino Pro Mini has the only task to control the stepper motor of the peristaltic pump. It reads speed, direction and state values sent by the Arduino Mega 2560 from the serial bus and generates the digital signal for direction as well as the square wave signal required to control the stepper motor. This additional external microcontroller is required to provide accurate speed control of the pump, independently from the other functions which are handled by the main microcontroller (Arduino Mega 2560) to avoid critical timing issues. The code for the Arduino Pro Mini (*mini_pump_control.ino*) must be uploaded before connecting it to the circuit as it will not be accessible from the outside.

7 Cost Analysis

The cost analysis for this project estimates a total cost of 492 USD for a complete retention model setup. As pricing of the various components can be heterogeneous depending on the source, the total cost is expected to vary depending on where the parts are purchased. However, we estimate that the cost is more likely to be reduced as in some cases parts were purchased that were more expensive than necessary. When looking at the cost analysis overview in the table, it becomes clear that the acrylic sheets as well as the electronics contribute the main expenses to the project.

Component groups	Cost (USD)
3D printed parts	45
Acrylic sheets	108
Electronics	246
Screws and other mechanical parts	88
Pump tubing	7
Total Cost	**494**

8 Validation and Characterization

The functionality of the constructed retention model setup was tested. In this regard, we investigated the climate control over time, the performance of the peristaltic pump and the automation of the system.

8.1 Performance of climate control feedback loop

The capability of the climate control feedback loop using a ceramic heat lamp, an ultrasonic mist fogger, three fans, two DHT22 sensors and an Arduino Mega 2560 was tested by measuring temperature and relative humidity over time (**Figure 22**). As experimentally relevant target values, we chose a temperature of 37°C and a relative humidity of 90%. The results show that the humidity fluctuates right below the target value in a much faster frequency than temperature fluctuates around the target value. Furthermore, the target humidity can be reached much faster than the target temperature, which is reached after approximately 10 minutes. All in all, the control feedback loop shows a very robust behavior which can also be observed when the door of the chamber was opened for a specific amount of time. While the temperature stays unaffected after these short interruptions, the humidity decreases as an extreme down to 50% relative humidity but reaches the target value again within one minute after the event. The temperature exhibits a fluctuation in range of 5.3°C with an average of 37.9°C and a standard deviation of ± 1.5°C. The fluctuation of relative humidity takes place in a range of 12% with an average of 88% and a standard deviation of ± 2%.

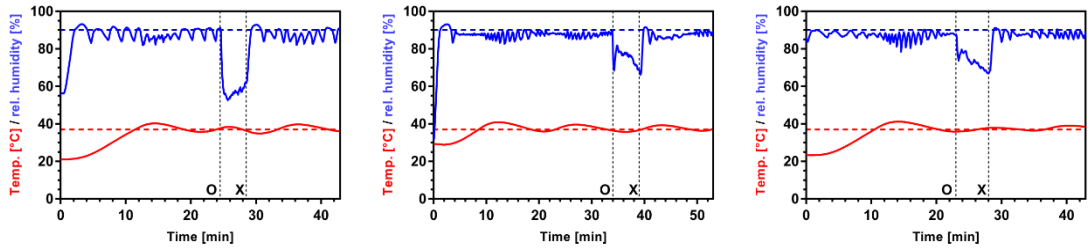

Figure 22 *Replicated measurements of temperature and relative humidity over time. Dotted lines represent the programmed target values. Events "O" and "X" mark when the door of the climate chamber was opened ("O") and closed ("X").*

8.2 Peristaltic pump calibration

The peristaltic pump was adapted from a previously posted project in which it was characterized in detail [18]. As the pump was introduced to a modified setting and modified control, a calibration curve was determined (**Figure 23**). Within the examined RPM-range, the pump exhibits a precise linear relationship to the flowrate.

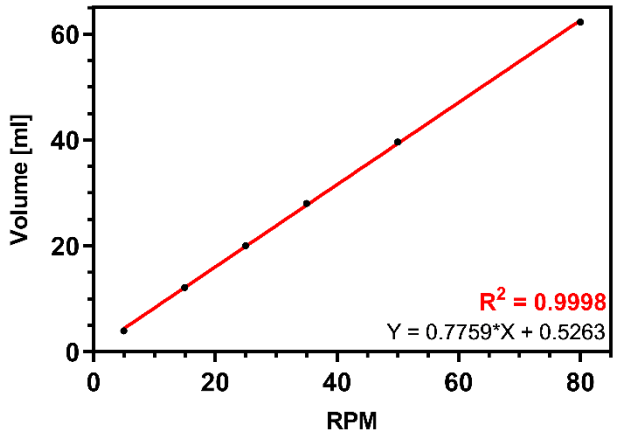

Figure 23 *Calibration curve of peristaltic pump. Error bars representing standard deviation are not depicted as they are smaller than the individual points of the plot. N = 3.*

8.3 Demonstration of retention experiment using automated program sequence and autosampler

To demonstrate the extended capabilities by means of automation of the presented retention model setup, a demonstration experiment with two differently shaped 3D printed specimens was performed (**Figure 24**). A piece of untreated porcine intestinal tissue was placed on the tissue holder as soon as the climate control reached the target values of 37°C and 90% relative humidity. Then the tissue was flushed with Dulbeccos' phosphate buffered saline for 5 minutes at 50 RPM to remove loose pieces of mucus. The 3D printed cones and cylinders (Figure 24a and b) had a diameter of 1 mm and were placed simultaneously and randomly in a number of 25 each onto the intestine and left for incubation for 10 minutes (Figure 24c). With expiration of the incubation time, a customized program as visualized in **Table 1** was started.

As indicated, the program started the pump at 10 RPM, then rotated the autosampler to the next sample (small filter mesh; Figure 24d) four times after two minutes of flow each. Then the flow was increased consecutively three times to 30, 40 and 50 RPM in order to increase stress conditions. After the program stopped, the cone and cylinder samples in the fractions of the autosampler as well as the samples remaining on the tissue were counted. Plotting the results of the replicated experiments as relative amount of samples left on the tissue (relative retention) against the number of autosampler fractions (Figure 24e) shows that in all replicates there is a tendency of the cones to exhibit slightly higher retention than the cylinders. This could be caused by the fact that the cones encounter less drag force than the cylinders and also as they might penetrate into the mucus layer more easily due to their sharp tip. Since the experiment was fully automated, the number of autosampler fraction correlates with time as well as with flowrate.

In summary, the demonstration and validation of the instrument shows:

- Stable control of temperature and humidity over time
    - Fluctuation of temperature in range of 5.3°C over time (mean of 37.9°C; standard deviation of ± 1.5°C over time)
    - Fluctuation of relative humidity in range of ~12% over time (mean of 88%; standard deviation of ± 2% over time)
- Precise peristaltic pump calibration with linear correlation of RPM to flowrate ml/min in a physiologically relevant range of flowrate
- Capability to run fully automated mucoadhesion assays using an autosampler and a customized controller program

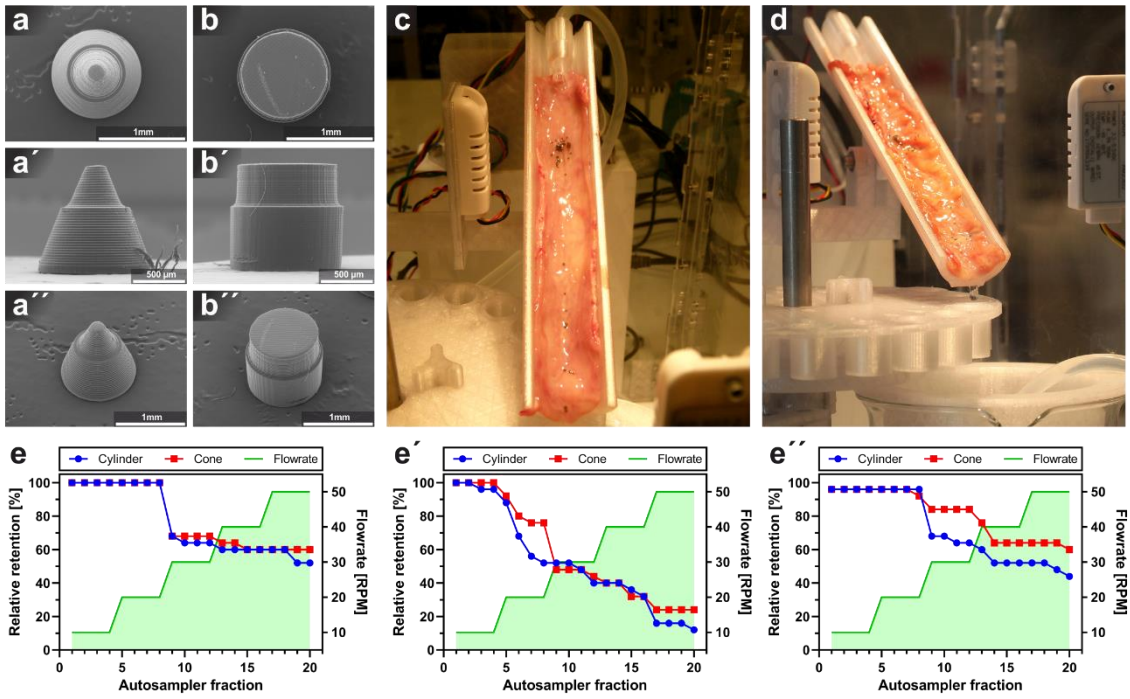

Figure 24 *Example retention measurement experiment using customized program automation. (a) Top view of millimeter sized 3D printed cone-shaped sample. (b) Top view of millimeter sized 3D printed cylinder-shaped sample. (') side view and (") 45 degree tilted view in both cases. (c) Photograph of running experiment with both types of samples placed on the tissue. (d) Photograph of experimental setup with rotational autosampler and porcine intestinal tissue on 30 degree tilted tissue holder. (e) Graphical analysis of the data obtained from counting the samples remaining in the different fractions of the autosampler after three replicates (e – first replicate, e' – second replicate, e" – third replicate).*

Table 1 *Example instruction loop used for retention experiment in Figure 24. Climate control is set to a temperature of 37°C and a relative humidity of 90%. After a waiting time of 5 seconds, the flow of the pump is started at a flowrate of 10 RPM. After 2 minutes, the sample in the autosampler is changed. The latter procedure is repeated 4 times, then the flowrate is increased. The flow rate is increased 4 times in total until the program stops.*

```
void my_program()
{

switch (k) {

 case 0:
 set_temp_hum(37,90,1);
 break;
 case 1:
 wait_milliseconds(5000);
 break;

 case 2:
 set_pump(10,1,1);
 break;
 case 3:
wait_milliseconds(120000);
 break;
 case 4:
 next_sample(20,0);
 break;
 case 5:
 instruction_loop(3, 3);
 break;
 case 6:
 set_pump(20,1,1);
 break;
 case 7:
wait_milliseconds(120000);
 break;
 case 8:
 next_sample(20,0);
 break;
 case 9:
 instruction_loop(7, 3);
 break;

 case 10:
 set_pump(30,1,1);
 break;
 case 11:
wait_milliseconds(120000);
 break;
 case 12:
 next_sample(20,0);
 break;
 case 13:
 instruction_loop(11, 3);
 break;
 case 14:
 set_pump(40,1,1);
 break;
 case 15:
wait_milliseconds(120000);
 break;
 case 16:
 next_sample(20,0);
 break;
 case 17:
 instruction_loop(15, 3);
 break;

 case 18:
 set_pump(50,1,1);
 break;
 case 19:
wait_milliseconds(120000);
 break;
 case 20:
 next_sample(20,0);
 break;
 case 21:
 instruction_loop(19, 3);
 break;
 default:
 stop_program();
  break;

  }

}
```

9 Potential modifications

Potential modifications of the system include a more precise control of the slide angle. Increased repeatability of the angle will possibly lead to increased repeatability of the experiments. As the RAMPS 1.4 Arduino shield has three more slots for stepper motor drivers, a motor could be used to precisely control the angle of the slide.

Further, the design of the peristaltic pump could be altered in order to more easily fit tubes of different diameters and thereby achieve different ranges of flowrates.

Another desirable modification would be the optimization of 3D printed parts to reduce the amount of required screws and to adapt the parts to the use of the same size and type of screws as they contribute a substantial fraction of the cost of the setup.

Acknowledgements

The authors would like to acknowledge the Center for Intelligent Drug Delivery and Sensing Using Microcontainers and Nanomechanics (IDUN) whose research is funded by the Danish National Research Foundation (DNRF122) and Villum Fonden (Grant No. 9301).

References

[1] K.V.R. Rao, P. Buri, A novel in situ method to test polymers and coated microparticles for bioadhesion, Int. J. Pharm. 52 (1989) 265–270. doi:10.1016/0378-5173(89)90229-9.

[2] V. V. Khutoryanskiy, Advances in Mucoadhesion and Mucoadhesive Polymers, Macromol. Biosci. 11 (2011) 748–764. doi:10.1002/mabi.201000388.

[3] K. Albrecht, E.J. Zirm, T.F. Palmberger, W. Schlocker, A. Bernkop-Schnürch, Preparation of thiomer microparticles and in vitro evaluation of parameters influencing their mucoadhesive properties, Drug Dev. Ind. Pharm. 32 (2006) 1149–1157. doi:10.1080/03639040600712334.

[4] K.D. Madsen, C. Sander, S. Baldursdottir, A.M.L. Pedersen, J. Jacobsen, Development of an ex vivo retention model simulating bioadhesion in the oral cavity using human saliva and physiologically relevant irrigation media, Int. J. Pharm. 448 (2013) 373–381. doi:10.1016/j.ijpharm.2013.03.031.

[5] Y.A.L. Lee, S. Zhang, J. Lin, R. Langer, G. Traverso, A Janus Mucoadhesive and Omniphobic Device for Gastrointestinal Retention, Adv. Healthc. Mater. 5 (2016) 1141–1146. doi:10.1002/adhm.201501036.

[6] J.M. Pearce, Building Research Equipment with Free, Open-Source Hardware, Science (80-.). 337 (2012) 1303–1304. doi:10.1126/science.1228183.

[7] T. Baden, A.M. Chagas, G. Gage, T. Marzullo, L.L. Prieto-Godino, T. Euler, Open Labware: 3-D Printing Your Own Lab Equipment, PLoS Biol. 13 (2015) 1–12. doi:10.1371/journal.pbio.1002086.

[8] J. Hollander, MakerCase - Easy Laser Cut Case Design, (2014). www.makercase.com (accessed December 29, 2018).

[9] J.G. Nascimento, Door lock, (2018). https://www.thingiverse.com/thing:2795624 (accessed December 29, 2018).

[10] R. Gosling, Parametric Hinge, (2017). https://www.thingiverse.com/thing:2187167 (accessed December 29, 2018).

[11] J. Janssen, Gears Library for OpenSCAD, (2016). https://www.thingiverse.com/thing:1604369 (accessed December 29, 2018).

[12] iGEM_Team-Aachen, Precise Peristaltic Pump, (2017). https://www.thingiverse.com/thing:2619479 (accessed December 29, 2018).

[13] D. Lee, Mini Desktop Humidifier, (2015). https://www.thingiverse.com/thing:768693 (accessed December 29, 2018).

[14] Capitaenz, 40mm fan grill, (2012). https://www.thingiverse.com/thing:20081 (accessed December 29, 2018).

[15] Adafruit, Adafruit Unified Sensor Driver, (2015). https://github.com/adafruit/Adafruit_Sensor (accessed December 29, 2018).

[16] Adafruit, Adafruit DHT Humidity & Temperature Unified Sensor Library, (2016). https://github.com/adafruit/DHT-sensor-library (accessed December 29, 2018).

[17] F. Malpartida, New LiquidCrystal, (2017). https://bitbucket.org/fmalpartida/new-liquidcrystal/downloads/ (accessed December 29, 2018).

[18] iGEM_Team-Aachen, iGEM Aachen 2017, (2017). http://2017.igem.org/Team:Aachen/Hardware (accessed December 31, 2018).